FUNCTIONAL ANALYSIS OF THE *FLNC* W2164C MISSENSE VARIANT ASSOCIATED WITH HYPERTROPHIC CARDIOMYOPATHY

by

AMAR JOSEPH SINGH AZAD

A thesis submitted to

The University of Birmingham

for the degree of

DOCTOR OF PHILOSOPHY

Institute of Cardiovascular Sciences

College of Medical and Dental Sciences

University of Birmingham

November 2022

Declaration of own work and attribution

Unless otherwise stated, this thesis consists of my own work. All live handling of animals and collection of animal measurements were done by either Dr Austin Jiang or Dr Sophie Broadway-Stringer. The generation of adenoviruses for SarcTrack analysis was done by Dr Violette Steeples.

Part of Chapter 1 (1.5) has been adapted from previously published work: The Role of Z-disc Proteins in Myopathy and Cardiomyopathy.

ABSTRACT

Hypertrophic cardiomyopathy (HCM) is an inherited cardiac condition associated with diastolic dysfunction and sudden cardiac death. Disease genes for HCM are traditionally coding for proteins involved in force generation. More recently, it has emerged that variants in genes coding for proteins involved in biomechanical stress-signalling can also cause HCM.

One such protein is filamin C, with proposed mechano-sensing functions in the heart. Within the protein, the immunogloblulin-like domain 20 (Ig20) may play a crucial role in mediating biomechanical stress responses. While the mechano-sensing functions of filamin C have been investigated well in skeletal muscle, the underlying cardiac disease mechanisms are not completely understood. A multi-generational family affected by cardiomyopathy were found to carry a *FLNC* variant located in the mechano-sensing Ig20 – *FLNC* W2164C.

Aim: This work attempts to provide insights into the role of filamin C in cardiac mechano-sensing and dissect disease pathways leading to HCM in the presence of the *FLNC* W2164C variant.

Methods: Using mass spectrometry, a detailed analysis of the proteome of mice carrying the filamin C variant, using ventricular tissue samples from 14wk old homozygous mice. An induced pluripotent stem cell-derived cardiomyocyte (iPSC-CM) model which harbored the *FLNC* W2164C variant was also investigated. Molecular biology techniques were utilized to determine the molecular phenotype of the *FLNC* W2164C variant in both mice and iPSC-

CMs. iPSC-CMs were developed for improved characterization by fabricating culturing surfaces of physiological stiffness.

Results: Mice carrying this variant recapitulate molecular features of HCM and restrictive cardiomyopathy in the homozygous setting and showed evidence of protein redistribution to the intercalated disc. An HCM molecular phenotype was also described in the iPSC-CM model.

Conclusion: This work supports the pathogenic role of the *FLNC* W2164C variant in cardiomyopathy. This thesis highlights the importance of using both mice and iPSC-CMs for modelling cardiovascular disease in order to overcome individual model deficiencies.

ACKNOWLEDGEMENTS

These are the last written words of this thesis, though personally, they are the most important. Written in the lab where this thesis was conducted, it is with pleasure that I reflect on these years and give thanks to you all.

Firstly, I cannot express enough gratitude to Dr. Katja Gehmlich, your continued support and guidance has been invaluable. Thank you for all the advice, teachings and patience over the years, which has allowed me to grow as a scientist. Thank you Dr. Davor Pavlovic for many helpful discussions throughout this journey.

This thesis is dedicated to my family, in particular my parents, Glenys and Harv Azad, as well as my sister, Holly Azad, who have been an encouraging shoulder from as early as I can remember. They have given me the freedom to make my own decisions and have nurtured my curiosity. I do not appreciate you enough. My beloved cat, Chilli, cannot be forgotten. A quiet but ever-present furry companion in my life.

I would like to express my eternal gratitude to Amy Jones for putting my well-being (and lab demands) before her own during my academic years. Her belief in me has always kept my spirits and motivation high.

Last (but not least), the completion of this project could not have been accomplished without the support from every member of the Gehmlich group and all of those around me in both a professional and personal setting, whether for one day or for four years, you all deserve my sincere thanks.

In the end, all was well.

TABLE OF CONTENTS

LIST OF FIGURES

LIST OF TABLES

ABBREVIATIONS

ABD	Actin binding domain
Ang-II	Angiotensin-II
APD	Action potential duration
ARVC	Arrhythmogenic right ventricular cardiomyopathy
ATP	Adenosine triphosphate
BW	Body weight
CASA	Chaperone-assisted selective autophagy
CHD	Coronary heart disease
CMs	Cardiomyocytes
CRISPR-cas9	Clustered regularly interspace short palindromic repeat-associated protein 9
DCM	Dilated cardiomyopathy
DEP	Differentially expressed protein
DMSO	Dimethyl sulfoxide
ECG	Electrocardiogram
ECM	Extracellular matrix
EHT	Engineered heart tissue
ESCs	Embryonic stem cells
ESC-CM	Embryonic stem cell-derived cardiomyocytes
ETC	Electron transport chain
FACS	Fluorescence-activated cell sorting
FC	Fold change

FDR	False discovery rate
FLNC	Filamin C
F-actin	Filamentous actin
GAPDH	Glyceraldehyde-3-phosphte dehydrogenase
HCM	Hypertrophic cardiomyopathy
Het	Heterozygous
HSPs	Heat shock proteins
HW	Heart weight
Hz	Hertz
IB	Immunoblotting
ICD	Intercalated disc
IF	Immunofluorescence
Ig	Immunoglobulin
iPSCs	Induced pluripotent stem cells
iPSC-CMs	Induced pluripotent stem cell-derived cardiomyocytes
ISO	Isoprenaline
LA	Left atria
LC-MS	Liquid-chromatography Mass spectrometry
LV	Left ventricle
LVAW	Left ventricular anterior wall thickness
LVID	Left ventricular internal diameter
LVNC	Left ventricular non-compaction
LVPW	Left ventricular posterior wall thickness
MFM	Myofibrillar myopathy

M-line	Middle line
mRNA	Messenger ribonucleic acid
PBS	Phosphate buffered saline
PCR	Polymerase chain reaction
PDMS	Polydimethylsiloxane
qPCR	Quantitative PCR
RA	Right atria
RCM	Restrictive cardiomyopathy
RV	Right ventricle
SEM	Standard error of mean
sHSPs	Small heat shock proteins
SL	Sarcomere length
SR	Sarcoplasmic reticulum
T2DM	Type-2 diabetes mellitus
TL	Tibia length
WT	Wild-type
Z-disc	Zwischenscheibe disc

Chapter 1 : INTRODUCTION

1.1 Cardiomyopathies

By definition, heart failure is the inability of the heart to pump an appropriate volume of blood around the body, usually because the heart is either too weak or too stiff (1). Reduced cardiac output can be caused by abnormalities in contraction, anatomy of the muscle and valves, heart rhythm and conduction. This primarily results in systolic and/or diastolic dysfunction.

Systolic dysfunction is the reduced ejection of blood from ventricular contraction, whereas diastolic dysfunction is a result of improper ventricular filling during cardiac relaxation. If left untreated, compromised cardiac function is the result in both cases.

In the United Kingdom, an average of one person dies every 3 minutes due to cardiac and vascular diseases (2). This accounts for more than a quarter of all national deaths. While lifestyle choices such as diet, exercise and smoking can be a major influencer on the development of cardiac and vascular diseases, in contrast cardiomyopathy is influenced primarily by genetic factors (3). Cardiomyopathies (*cardio* – heart, *myo* – muscle, *pathy* – suffering) are inherited diseases of the cardiac muscle that affect the structural and electrical characteristics of the heart, and can ultimately result in heart failure (4,5). Patients can present with features of cardiomyopathy from birth to upwards of 80 years of age (6).

Varying morphological presentations split cardiomyopathy classification into four major subtypes: hypertrophic cardiomyopathy (HCM), dilated cardiomyopathy (DCM), restrictive cardiomyopathy (RCM) and arrhythmogenic cardiomyopathy (ACM). Although each are considered as distinct diseases, cardiomyopathies have phenotypic overlap which makes diagnosis by clinical features alone difficult: e.g. HCM and RCM both are characterised by

diastolic dysfunction (7). HCM is primarily characterised by left ventricular hypertrophy whereas DCM is defined by left ventricular dilation leading to systolic dysfunction (8). ACM is defined by irregular electrical signals in the heart, usually the right ventricle, sometimes due to abnormal levels of fatty fibrous tissue (9). Of all cardiomyopathies, HCM is the most prevalent affecting up to 1:344 individuals (10–14).

1.1.1 Hypertrophic cardiomyopathy

In 1868, initial HCM characteristics were first described by A. Vulpian as an anomaly in sub-aortic structure and was first termed HCM by Teare, 1958 (15,16). It was not until the latter half of the following century that HCM was clinically characterised as a familial cardiac syndrome causing hypertrophy in the ventricles and diastolic dysfunction (17–19). HCM is a disease that rarely manifests in the right ventricle (20) and primarily affects the left ventricular cardiac myocytes, defined by unexplained hyperplasia and hypertrophy, with myofiber disarray and fibrosis at histology level (21–24). Cardiac hypertrophy in HCM is due to an increase in cardiomyocyte cell size rather than an increase in cell number. In addition to whole cell cardiomyocyte disarray, myofilamentous disarray within the cells themselves is also observed in HCM (25).

Although HCM is the most common genetic cardiovascular disease, many people do not present with significant symptoms and are often undiagnosed. The symptoms a diagnosed HCM patient can experience are as follows: chest pain, shortness of breath, fainting and can even develop heart murmurs and palpitations. Left ventricular outflow tract (LVOT) obstruction is also a significant pathological feature of HCM (26,27). LVOT obstruction is the result of systolic contact between the mitral valve and interventricular septum (27). HCM patients with LVOT obstruction are more likely to experience more severe symptoms such as heart failure and sudden death (28).

Lacking targeted drug therapies that cure cardiomyopathy, the only treatments available to patients are pharmacological treatment (with beta-blockers, diuretics and ACE inhibitors), myectomy or septal ablation, but no specific therapies addressing the underlying molecular causes are routinely used. Mavacamten, a myosin ATPase inhibitor, has been developed and recently approved for use in the US (29). Uncovering the disease mechanisms in HCM caused by genetic factors is instrumental in understanding and treating HCM patients specifically and effectively.

HCM is a genetically inherited disease that can be caused by a single genetic variant. Shortly after Jarcho *et al* and Solomon *et al* reported genetic associations in HCM patients (30,31), the first *de novo* pathogenic variants were found in the gene encoding β-myosin heavy chain (*MYH7*) (32,33). Since this initial discovery, more than 1400 pathogenic variants implicated in HCM have been identified in major cardiac sarcomere genes (e.g. *MYH7, MYBPC3, TNNT2*) thus postulating that HCM is a disease of the sarcomere (34–37).

Variant type (missense/truncation) that affects protein conformation can give rise to different clinical outcomes. Clinically found variants such as missense mutations in *MYH7* or truncating variants in *MYBPC3* result in altered contractility due to differences in transcription and protein incorporation into the sarcomere. Some variants however, result in pathology due haploinsufficiency in response to truncating variants of sarcomere proteins (38–40). In comparison with thick filament variants (e.g. myosin-binding protein C), patients with variants in thin filament proteins (e.g. troponin I and actin) are more likely to have left ventricular dysfunction (41).

Genetic identification allows for greater diagnostic resolution when combined with clinical identification. However, many variants which are found in similar regions of the same protein can result in a different clinical presentation. To increase the understanding of these

disease genes and aide eventual HCM-specific treatments it is worth considering the cardiac biomolecular mechanisms that enable a healthy, functioning sarcomere and result in disease manifestation.

1.1.2 HCM molecular mechanisms

On a molecular level, there are three overlapping perspectives on the mechanisms behind HCM: abnormal contractility (hypocontractility and hypercontractility), energy efficiency and calcium handling (42). For instance, HCM patients with *MYBPC3* variants display hypercontractility which results in hypertrophy, however, this hypercontractility is caused by ATPase cycle alterations or the overly accessible myosin heads for contraction to occur (43). Sarcomere variants may also impair cardiac output and hence contractility becomes load-dependent (43). On an energetic front, the mitochondrial role in cardiac disease has been well studied (44) and HCM has even been characterised as a disease of energetic deficiency (45,46). Calcium handling abnormalities are reported in HCM and are associated with arrhythmogenesis and diastolic dysfunction due to increased calcium concentration during diastole (47).

1.2 Cardiomyocyte function

1.2.1 Contraction

The cardiovascular system is indispensable for human body to function. The delivery of essential oxygen and nutrients and the removal of metabolic waste is driven by the cardiovascular system alongside the lungs, kidney and liver. The heart is the centrepiece of this system acting as the bodies mechanical pump. The heart is made up of four chambers: the left and right atrium and left and right ventricles (Figure 1-1). The right atria receives

deoxygenated blood from the body and is transferred to the right ventricle to be pumped through the pulmonary arteries towards the alveoli of the lungs to exchange carbon dioxide for oxygen (known as the pulmonary circulation). This newly oxygenated blood passes into the left ventricle via the left atrium. Within the left ventricle, the muscular walls contract to create pressure gradients hereby ejecting blood throughout the body into thin capillaries where the diffusion limits between circulation and surrounding tissues allow for gas and nutrient exchange.

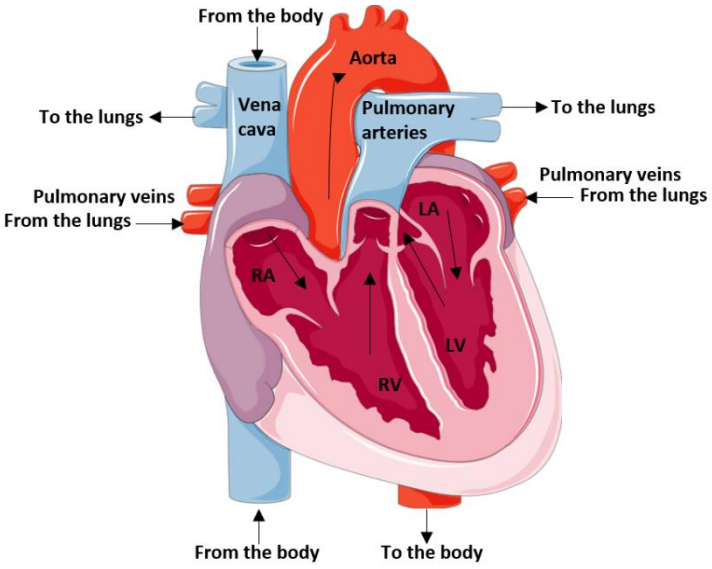

Figure 1-1 Diagram of the direction of blood flow through the veins, chambers and arteries of the heart. Deoxygenated blood from the body enters the RA heart via the vena cava and is pumped into the RV. The deoxygenated blood gets pumped out of the RV into the pulmonary arteries to undergo gas exchange at the lungs before returning to the LA of the heart via the pulmonary veins. The oxygenated blood enters the LV and is ejected into the aorta for delivery to the body. RA, right atria; RV, right ventricle; LA, left atria; LV, left ventricle.

Regulating the blood flow between the chambers of the heart is instrumental for heart and bodily functions. Blood flow must be unidirectional, from the atria to the ventricles and out to the body and lungs. This is achieved by valves. During muscle relaxation (diastole), the valves which separate the atria and ventricles (mitral and tri-cuspid valves) open due to the negative pressure generated from ventricular relaxation. To prevent back-flow into the atria, these valves close during systole when the ventricle contracts. During cardiac contraction (systole), the ventricular pressure is greater than within the aorta or pulmonary circulation

and hence the aortic and pulmonary semilunar valves open to allow blood flow to the body and lungs.

All four chambers contract and relax in a coordinated fashion to allow steady blood flow into and out of the heart (Figure 1-2). Contraction is initiated via the sinoatrial node, which is located in the right atria. The sinoatrial node is comprised of pacemaker cells that spontaneously depolarise and induce atrial contraction allowing the atria chambers to transfer the blood from the atria into the ventricles (48). The activation of the atrioventricular node leads to the depolarisation and contraction of the ventricles. Atrioventricular activation leads to signal propagation through the Bundle of His and to the Purkinje fibres that stimulate ventricular wall contraction to allow for the ejection of blood to the lungs and body (49). This ensures that the contraction cascade is initiated on a whole-heart level to allow coordinated blood flow through the heart.

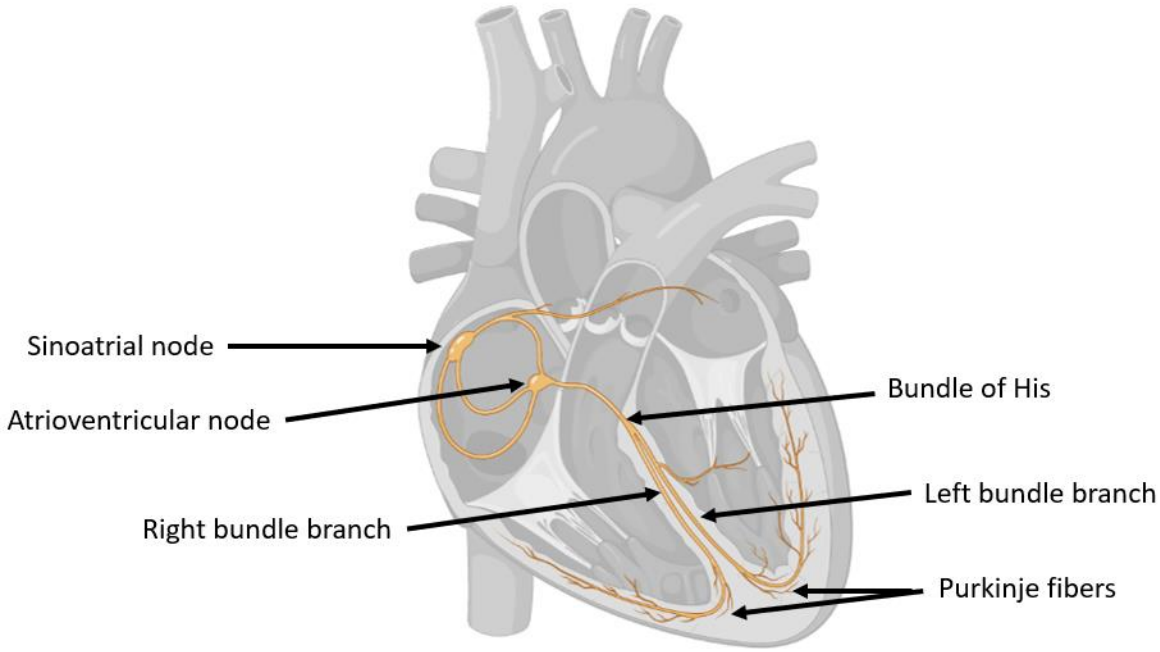

Figure 1-2 Cardiac electrical conduction pathway. The conduction pathway of the heart from the sinoatrial node to the atrioventricular node, down the Bundle of His and through the Purkinje fibres.

Between cells, contraction stimulation is regulated through electrical conduction mediation in stimulatory cells and between individual cardiomyocytes (CMs). Conduction is achieved between CMs via the intercalated discs (ICD) which form porous junctions (gap junctions) which permit direct ionic transmission (50). This electric coupling allows for rapid action potential transmission, thus aiding in coordinated cardiac contraction.

The ventricles have thicker muscular walls compared to the atria, and the left ventricular wall is thicker than the right. The atria only need to move blood into the next chamber. The ventricles, however, are required to generate enough pressure during systole to move blood to the lungs and body hence why the muscular walls are thicker. The left ventricle is thicker than the right for a similar reason. The right ventricle is only required to deliver blood to the lungs, whereas the left ventricle is tasked with delivering blood around the body. Out of all four chambers, left ventricular performance is of particular importance when ventricular arrhythmia or fibrillation occurs. Dysfunctional ventricular contractile performance is of concern in cardiomyopathies.

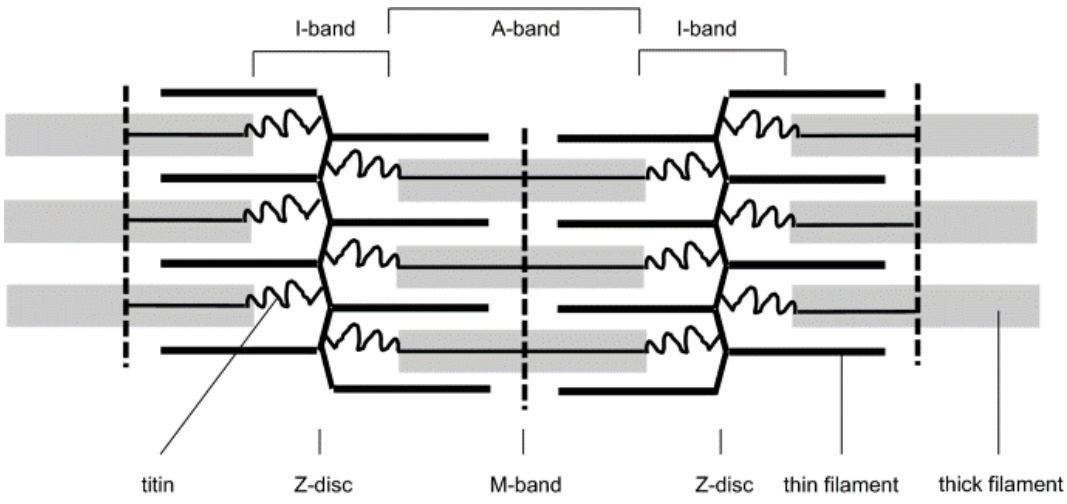

Figure 1-3 Schematic drawing of the sarcomere. The positions of the Z-disc, M-band, I-band and A-band are indicated. Taken from *Azad., et al 2019.*

1.2.2 The cardiomyocyte

The heart muscle is composed of cardiomyocytes, cardiac fibroblasts, endothelial cells, smooth muscle cells, conduction cells and resident immune cells (51). Cardiomyocytes make up approximately 70% of the heart by volume (52). The cardiomyocyte consists of myofibril bundles which possess contractile properties. Within each myofibril lies the contracting unit of cardiac and striated muscle: the sarcomere. The sarcomere is composed of aligned and repeating units of myosin and actin that form thin and thick filaments giving rise to a striated appearance (Figure 1-3). Many sarcomeres lined into a series make up myofibrils which combine to make a muscle fibre. The sarcomere is defined as the contractile unit, being located between two Z lines and is composed of distinct areas. Myomesin is the key protein at the M-line within the A-band and the Z-disc splits down the middle of the I-band. Within these bands, the sarcomere is composed of the thick filament myosin, extending across the A-band and connected at the M-line whereas the thin actin filaments, stretch from the I-band and into the A-band. Although actin is the main constituent of the thin filament, there are other proteins that also make up the thin filament (e.g. α-tropomyosin, troponin C and troponin I) (Figure 1-4).

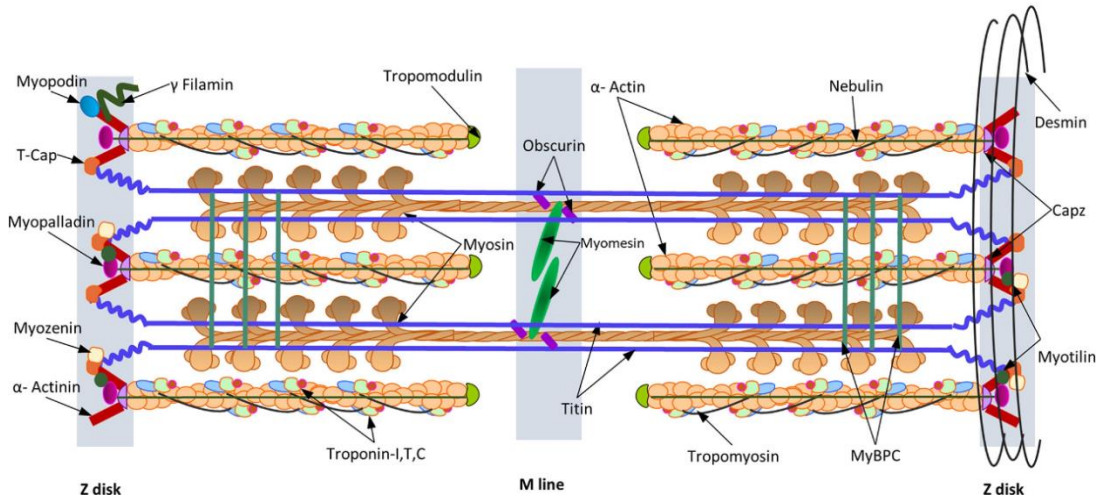

Figure 1-4 Detailed schematic diagram of the sarcomere, displaying the organisation and location of major proteins along the sarcomere. *Taken from Mukund and Subramaniam, 2019.*

During contraction, the globular heads on myosin (also displayed in Figure 1-4) attach and break from the corresponding actin binding sites to pull the thin filaments from the Z-disc towards the sarcomere's centre, the M-line (cross-bridge cycles). Cell-cell contacts are the ICD, structurally they resemble an "end Z-disc" as they anchor thin filaments at the cell membrane. The ICD forms a cellular bridge between adjacent cardiomyocytes allowing the exchange of chemical and electrical stimuli and thus enabling cardiomyocytes to coordinate its function (53). The force generated by the sarcomere is transmitted via structural proteins (titin, filamin C, integrins, dystrophin and others) through the cytoskeleton, sarcolemma and to the surrounding myocardium (54,55). These proteins are implicated in mechanical load-sensing and are also associated with hypertrophic signalling (54,55) .

1.3 Mechano-sensing and mechano-transduction

1.3.1 Mechano-sensing

As previously mentioned, sarcomere genes make up the majority of clinically-found HCM disease genes, but a small subset affects proteins involved in mechano-sensing (BAG3, OBSCN, FHL1, FHL2, ANKRD1 and heat shock proteins) (56,57). Mechano-sensing is defined as the responsivity that a cell or cellular components may have to a mechanical stimulus (58). Through contraction the sarcomere is under continuous mechanical, heat and oxidative stress (59). Considering that the heart is estimated to beat approximately two and a half billion times during the average lifetime of a human, it is crucial that the heart is able to withstand the physical forces which are exerted on it (60). Changes in mechanical force can be due to increased atrial or ventricular blood volume, fibrosis leading to stiffness, extracellular matrix deposits. Mechanical forces change during contraction. Cardiomyocytes

stretch through diastole and contract during systole as pressure is generated in order to eject blood (61).

Stress generated during contraction is spread from the actin-myosin complex, through the sarcomere and cytoskeleton to the sarcolemma. Within the sarcomere, the Z-disc and I-band consists of mechano-responsive complexes which respond to changes in the cardiac mechanical environment and influence gene regulation and proteostasis (62,63). From the sarcomere, force is transmitted towards the ICD and cardiomyocytes can undergo ultrastructural changes in response to increased force due to volume overload (64). ICDs are a key site for sensing and processing mechanical stress via the fascia adherens and desmosomal junctions (65).

Cardiac muscle can sense and respond to mechanical stress conditions in order to deliver consistent volumes of oxygenated blood to the body as well as ensuring the stability and thus function of the cardiomyocyte. During contraction, mechanical forces are translated into chemical signals, known as mechano-transduction (66). Proteins with mechano-sensitive properties localise at adhesions, e.g. ICD, costamere, where active contractile and passive stiffness forces are sensed (Figure 1-5) (67–69). The mitochondria are also proposed to be involved in mechano-transduction and mechano-sensing as it adapts activity and structure based on the environmental mechanical forces to regulate calcium homeostasis (70). Impaired structural integrity between the mitochondria and the sarcomere can directly result in mechanically-induced calcium release and abnormal impulse propagation (44,70). Mechano-sensing adaptive responses convert perceived mechanical force into actions such as inducing the activation of transcription factors that regulate the expression of proteins to cope with the mechanical demands of the cell (71,72).

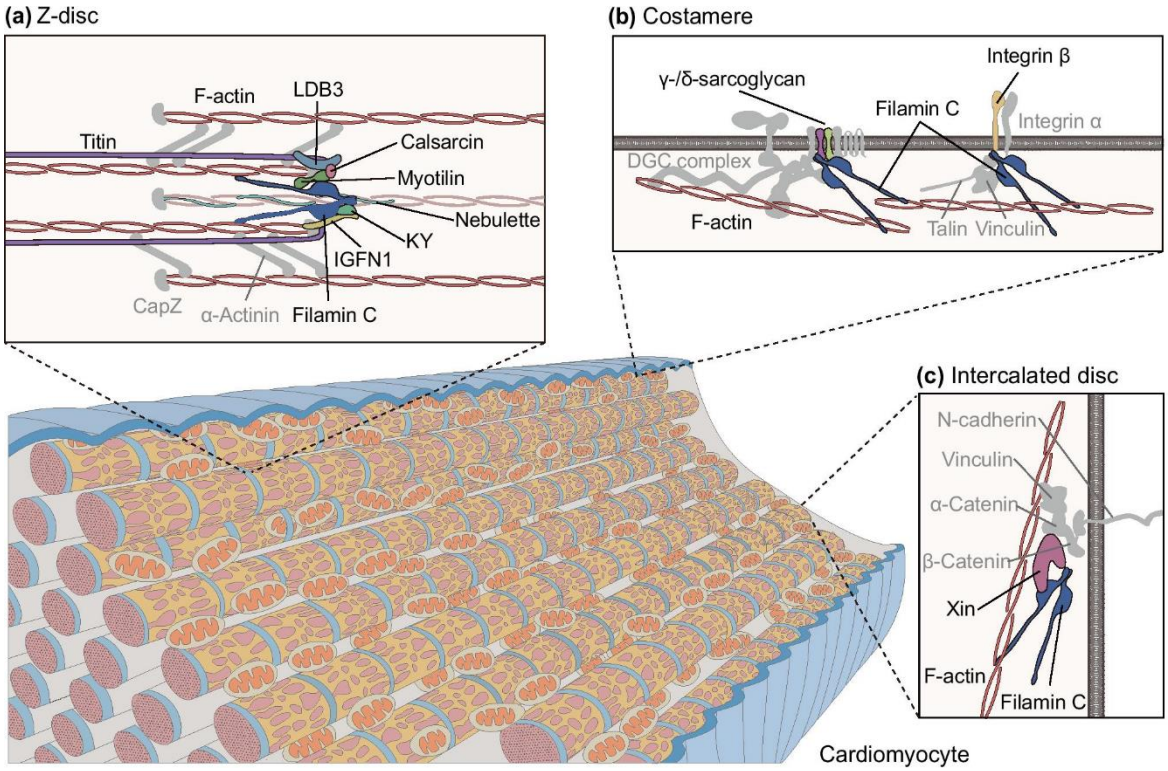

Figure 1-5 Key sites of mechano-sensing in cardiomyocytes. (a) Z-disc, filamin C is located at the Z-disc periphery with other proteins (titin, nebulette, myotilin, calsarcin, LDB3, IGFN1, KY) also interacting here (b) the costamere is involved in cell-extracellular matrix interactions (c) intercalated discs where cardiomyocytes are longitudinally connected have filamin C, Xin and membrane-related proteins located here. *Taken from Song et al. 2022*

The underlying mechanisms behind cardiac mechano-transduction are not well understood, however, a number of proteins and protein complexes have been associated with mechano-transduction. Unlike mechano-sensing which directly responds to mechanical stimuli, mechano-transduction is the conversion of mechanical stimuli into a biochemical response (73). Here, proteins, such as stretch-sensitive ion channels, respond directly to the mechanical stress during contraction and produce an appropriate functional, structural and/or signalling cellular response (73). Responses can include electrophysiological and calcium regulation, fibrosis and altered contractile function.

1.3.2 Mechano-sensing and mechano-transduction in pathology

Mechano-transduction has been labelled as a unifying molecular mechanism in the development of HCM phenotypes (74). Abnormal contractility can influence the gene

expression of epicardial cells and lead to the development of structural abnormalities and responses that lead to cardiac muscle growth via hypertrophy (74). Mechano-sensors are found in different locations of the cardiac myocyte: the sarcomere, the intercalated disc, the sarcolemma and even the mitochondria (70). Dysfunctional mechano-sensing processes are believed to result in altered cellular responses to mechanical force. A failure by mechano-sensors to recognise and clear mechanically-compromised proteins may lead to cardiac disease. Mechano-sensitive structures (sarcomere, ICD, sarcolemma) appear to be central to this process and need to be explored further to elucidate its function in disease.

1.4 Chaperone-assisted selective autophagy (CASA)

Sarcomere and cytoskeletal proteins changes their conformational state to a closed state and unfolds upon mechanical stress in order to protect the membrane to cytoskeleton linkage (75,76) and accommodate the mechanical stress required for actin contraction (75,77). This continuous mechanical unfolding and refolding can result in irreversible damage due to this exerted mechanical stress. In skeletal muscle, damaged proteins are recognised, disposed of, via autophagy, and replaced with a newly synthesised protein. Autophagy is carried out by molecular chaperones and is vital for protein homeostasis. This muscle homeostasis is done via a mechanism called chaperone-assisted selective autophagy (CASA) (78).

The CASA chaperone complex recognises protein misfolding and translates it into biochemical signals (76,79). This chaperone complex consists of BAG3, the key cochaperone that initiates CASA and is coupled to e.g. the ubiquitin ligase, CHIP (80), and the molecular chaperones: the heat shock proteins (HSPs) HSPB8 and HSC70 (59,81,82). The BAG3 complex, along with an interaction between BAG3 and myopodin (SYNPO2),

monitors the conformational state of filamins (and other sarcomere proteins) to recognise damaged proteins (83). During contraction, the conformation of filamin is open and extended with hidden binding sites now revealed and accessible for ligand interactions (84,85). Upon recognition of the damaged protein and the complex triggers filamin to be released from the myofilament to the cytosol for lysosomal autophagic degradation via CHIP/STUB-mediated ubiquitylation (Figure 1-6) (86). This induces the recruitment of p62, an autophagic ubiquitin adaptor, for protein clearing through the formation of an autophagosome (59). An upregulation of transcription and translation activity is induced to create a new filamin for incorporation into the Z-disc (59,83).

1.4.1 A cardiac CASA

An impaired CASA pathway has been implicated in diseases of the skeletal muscle such as myofibrillar myopathy, finding filamin C protein aggregates that deplete myofibrillar components from the myofilament (87,88). Although the CASA pathway is activated, it cannot maintain protein homeostasis due to an inability to clear the aggregates (88,89). Though CASA has been found specifically in the skeletal muscle, the mechano-signalling mechanisms may not be limited to skeletal muscle and its myopathies.

A growing amount of evidence points to autophagy as a key regulator of cardiac homeostasis and function. There are numerous forms of cardiac autophagy, some of which have specific targets for degradation, such as mitophagy targeting the mitochondria (90). Chaperone-mediate autophagy is the most similar to CASA, with much of the machinery appearing to also be dominated by modulatory co-chaperones, such as Hsp40 and Bag1 (90,91). With both cardiac filamin C and small HSPs (sHSPs) present in cardiomyopathies and known to

interact with each other (92), these mechanosensitive domains and proteins may lay the basis of chaperone-mediated mechano-signalling in the heart.

In cardiac stress conditions, autophagy acts to prevent the accumulation of toxic protein aggregation (93–95). Recent evidence suggests that impaired autophagy is involved in the pathophysiology of cardiomyopathy (especially considering the impact of misfolded proteins), however it is unclear whether autophagy is inhibited or enhanced (96,97). A CASA-like autophagy system may be present in the cardiac muscle and may provide insights in understanding the development of pathologic cardiac conditions from due to filaminopathies and may even be an option to treat cardiomyopathy in patients.

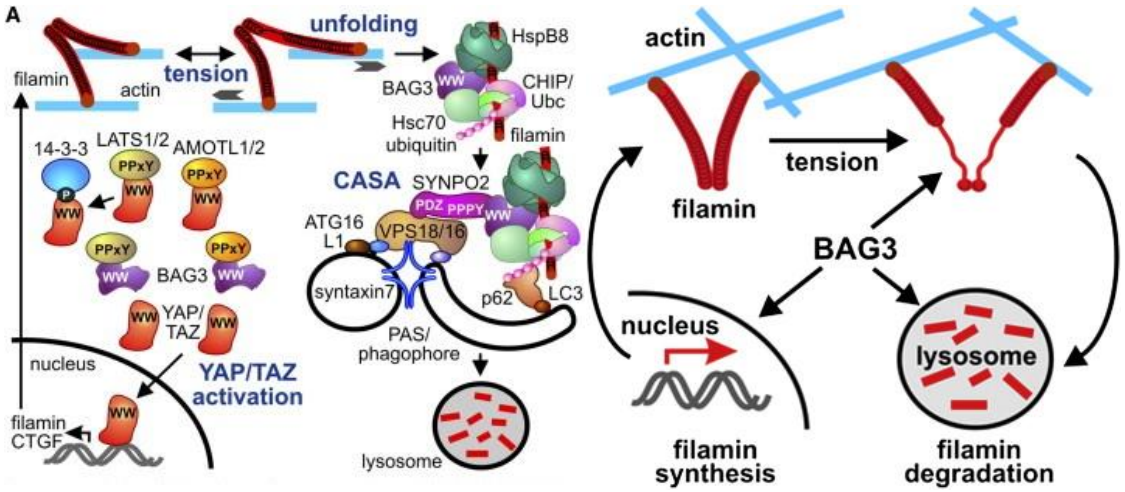

Figure 1-6 Scheme displaying the tension-induced activation of the BAG3 complex and how it leads to filamin synthesis and lysosomal degradation. *Taken from Ulbricht et al 2013.*

1.5 Filamin C

Although the majority of familial HCM patients possess variants in genes encoding key sarcomere proteins, nearly 10% of all measured familial cases are not caused by defects in the major sarcomere proteins (98). This, along with advances in next generation sequencing technologies, has led to the identification of *FLNC*-associated cardiomyopathies independent of variants in the well-established cardiomyopathy disease genes (99–101). The

structure, function and clinical relevance of filamin C, the transcribed protein from the *FLNC* gene, will be discussed in this section.

1.5.1 Structure and function of filamin C

Filamin C is a member of the actin-binding filamin family, consisting of three members: filamin A, B and C. Filamin C is expressed in cardiac and striated muscle sarcomeres and is found at load-bearing sites of the muscle: Z-disc, myotendinous junctions, intercalated discs and costameres (Figure 1-5). Known to bind to more than 90 different binding partners, filamins provide structure stability and mediate crucial signalling functions to the muscle. Filamin C is also proposed to play a role in mechano-sensing and is a client target for the pre-described CASA maintenance processes in skeletal muscle (102–107).

Encoded on chromosome 7q32.1, filamin C consists of an amino-terminal actin binding domain followed by 24 immunoglobulin-like (Ig) domains (Figure 1-7A - showing a shorter filamin from *Drosophila* with actin-binding domain displayed as Ig22) (108,109). Following from the actin-binding domain, 24 large Ig-like domains form part of the rod regions (Ig1-15 ROD1, Ig16-24 ROD2) (109). These flexible rod regions regulate the spacing and orientation of F-actin cross-linkages through protein-protein interactions with cytoskeletal, transmembrane and cell signalling proteins (110,111). There are two filamin C isoforms – the shorter one lacks exon 31 which encodes for the hinge region and is thought to be a less flexible protein (112).

Of the 24 Ig-like domains and unique only to filamin C in the filamin family, is domain 20 (Ig20). Ig20 contains an 82 amino acid insertion which is presumably a site for muscle-specific ligand interactions e.g. with myotilin, myopodin, xin for myofibrillogenesis and HSPB1, aciculin for sarcomere organisational and structural (84,85,103,104,107,113–115). These ligand interactions include but are not necessarily limited to roles such as Z-disc organisation and chaperone-mediated autophagy control due to its ability to change between conformational states during sarcomere relaxation and contraction (Figure 1-7B) (88,116–118). The carboxy-terminal portion of the protein consists of the dimerisation domain 24 (Ig24), which contains membrane glycoprotein-binding properties, allowing for the homodimerization of FLNC to form and maintain a network of cross-linking F-actin filaments that binds membrane proteins to actin (108,119). Ig24 is also the site for ligand interactions with HSPB7 and calpain 1 (120–123).

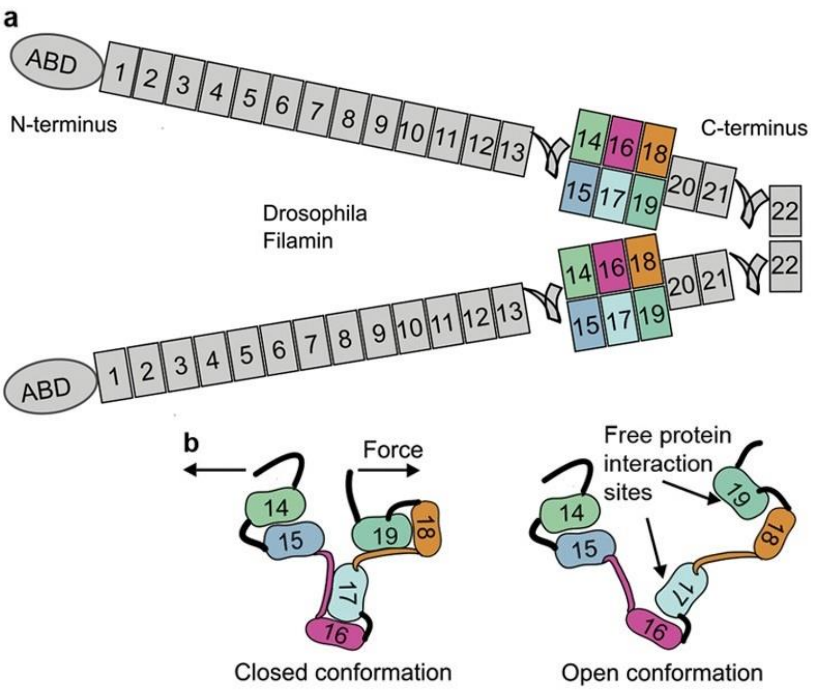

Figure 1-7 Schematics of *Drosophila* filamin during open and closed states. (a) Schematic of the conserved *Drosophila* filamin, Cheerio. Numbers represent the immunoglobulin-like domains and the mechanosensory region (MSR) is coloured (Ig14-19) although in humans it is between 18-21, actin binding domain (ABD). (b) The closed and open conformation of the MSR. *Image adapted from Huelsmann et al. 2016*

Signalling roles of filamin C include regulating the morphology and cell migration via binding to cell-matrix adhesion protein migfilin (124). These processes of the protein can modulated by phosphorylation events (125–127). In addition, filamin C plays a role in maintaining structural stability of the sarcolemma via interactions with sarcoglycans on the dystrophin-glycoprotein complex at the actin-binding domain of filamin C (128).

Skeletal muscle functions of filamin C are well established, highlighting its role in CASA (mentioned in 1.4). However, the function of filamin C within the cardiac muscle is relatively unknown. In part this could be due to early-stage lethality in animal models potentially masking any cardiac implications (129,130). With the increased use of human genetics studies (98,131), mouse and cellular models this protein is being interrogated for its cardiac specific functions (132). One such example is the use of an inducible cardiomyocyte specific *FLNC* knockout mouse, which displays high rates of lethality along with cardiac defects, including heart dilation and systolic dysfunction.

1.5.2 Filamin C in mechanosensing

Evidence of cardiac mechano-sensing mechanisms has been demonstrated by the upregulation of sHSPs, HSPB1 and HSPB7, alongside *FLNC* upregulation under mechanical stress (107,133) (and unpublished data). HSPB1 and HSPB7 offer mechanical stress cardio-protection to cardiac proteins, including filamin C by stabilising Ig20 and Ig24 of filamin C respectively, both regions suspected of mechanosensitive mechanisms (107,133). In addition, a phosphorylated HSPB1 plays cardioprotective roles of filamin C by preventing further protein unfolding during mechanical stress (107). Due to these and many more interactions, filamin C is therefore proposed as a central protein in cardiac mechano-sensing and mechano-signalling processes.

1.5.3 Filamin C in pathology

Pathogenic variants of *FLNC* have been identified in patients with skeletal and cardiac myopathies as well as being closely linked to neurodegeneration (134,135). These conditions are termed as filaminopathies. Due to much higher levels of *FLNC* expression in the skeletal muscle compared to cardiac muscle (3.5-fold (59)), variants found in this protein have been predominantly been associated with neuromuscular conditions such as myofibrillar myopathy (MFM) (119,134,136,137). Most studies on skeletal muscle-related filaminopathies, however, did not thoroughly characterise cardiac phenotypes and therefore cardiac involvement cannot be excluded in these cases (137,138). In 2005, Vorgerd and team discovered the first pathogenic *FLNC* variant (p.Trp2710X) in patients with MFM of which one-third of patients present with cardiac abnormalities (137,138). Since then, *FLNC* variants have been identified in familial cardiomyopathy patients independent of MFM (Figure 1-8).

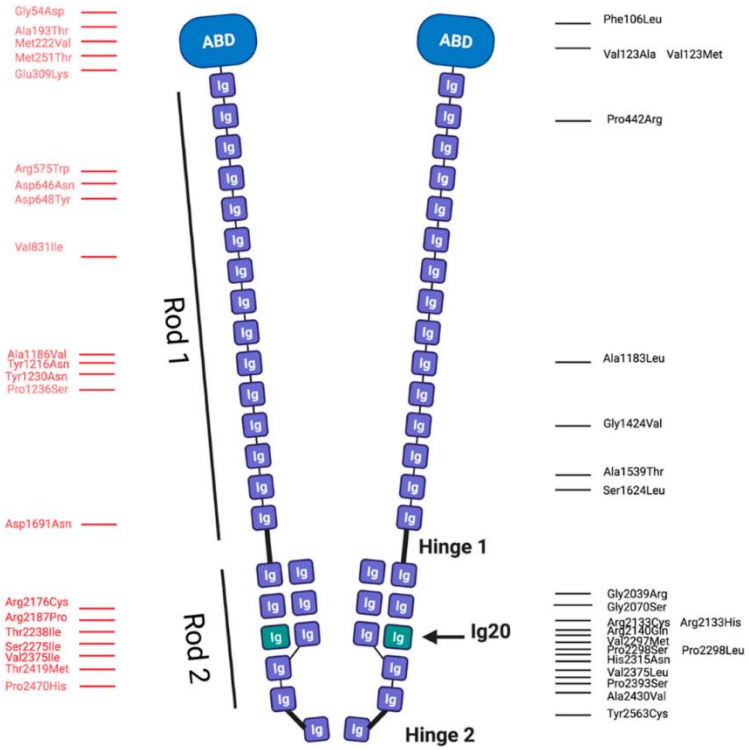

Figure 1-8 Schematic of the dimeric filamin C and its associated missense variants. Variants are shown vertically, correlating with their relative position in rod 1 and rod 2. Variants in red, represent variants found in individuals with myopathy and black represent individuals with cardiomyopathy. *Image taken from Wadmore et al., 2021*

Large cohort screening and family studies utilising the advancements of whole genome sequencing found that in addition to skeletal muscle system pathology association, *FLNC* variants also manifest in inherited cardiomyopathies (99–101,139–141). Overall, 101 variants have been identified by sequencing in familial DCM, RCM, ARVC, LVNC, cardiac arrhythmias and arrhythmogenic bileaflet mitral valve prolapse, thus providing greater evidence of the involvement of *FLNC* to cardiomyopathy (101,134,140,142). Understanding the way a *FLNC* variant may present can help improve the management of patients, especially considering patients carrying truncating *FLNC* variants have shown a higher proportion of sudden cardiac deaths compared to patients without *FLNC* variants (98,100).

1.5.3.1 *FLNC* variant type and location

There is a broad clinical spectrum of *FLNC* variant carrying patients, with some variants determining which organ is affected and how. The genetic location and type of variant in the *FLNC* gene may explain the different phenotypes patients present with (Figure 1-9). Cardiomyopathy subtype determination by variant type and site location is seen in other cardiomyopathy-associated genes (*DES*, *LDB3* (143), *BAG3* (144), *FHL1* (145)). To date, 95% of all *FLNC* variants found in HCM are missense variants whilst frameshift, in-frame, nonsense and splice variants resulting in a loss of function contribute to 81% of DCM-related filaminopathies (131). The relationship to variant type and clinical phenotype is strengthened when understanding the shared pathomechanisms of *FLNC* truncating variants. Truncating variants primarily result in haploinsufficiency and weaker structural adhesion which lead to DCM and cardiac arrhythmias (142,146,147).

Despite these links, it is not currently clear why some *FLNC* truncation and missense variants can cause skeletal muscle defects yet others result in exclusive cardiac phenotypes (131). These differences have been partially linked to the variant location determining the clinical phenotype. For instance, variants which affect the folding or the dimerization regions of filamin C often result in aggregate presentation and are found in HCM and MFM (87,98,137,148–150) (Figure 1-9). While this can partially explain the differences in phenotypes observed in filaminopathies, there are exceptions to this with many variant hotspots covering the same variant type but a different clinical outcome (131). Other possibilities are important to consider, such as the tension-based model, which infers that the disease phenotype may be determined by the effect of a variant on calcium flux via altered sarcomere tension generation (23).

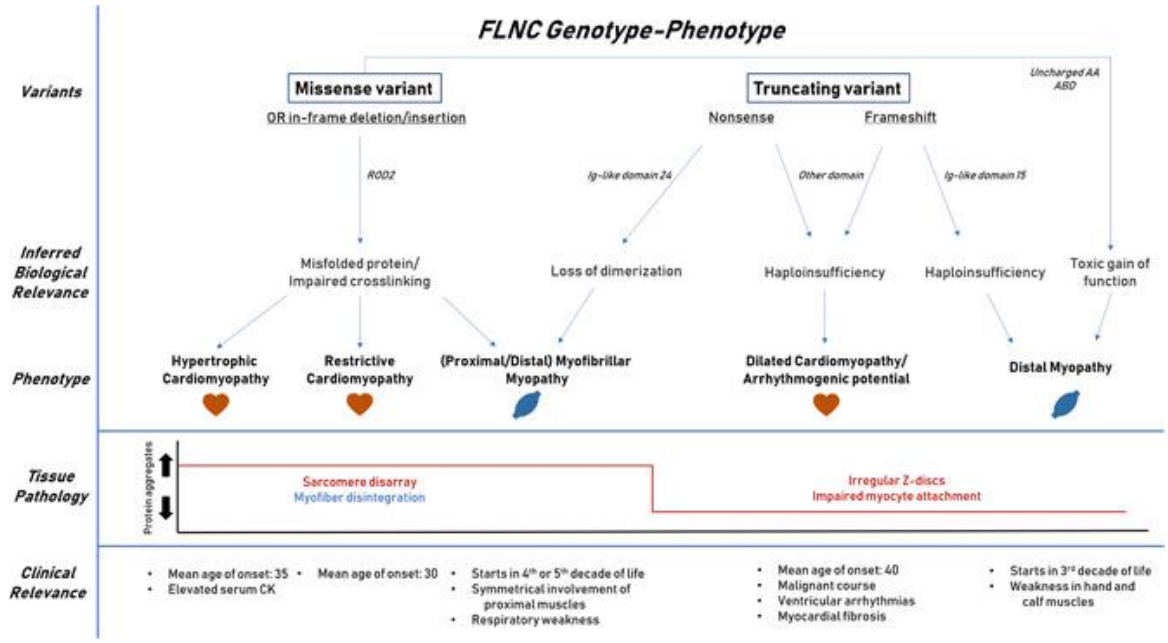

Figure 1-9 A summary of *FLNC* genotype-phenotype relations. The type of *FLNC* variant leads to different disease mechanisms and hence different clinical phenotypic outcomes which correspond with structural changes which are specific to the variant subtype. *Taken from Verdonschot et al. 2020*

1.5.3.2 *FLNC* variants and aggregation

The common presence of protein aggregation in patients harbouring *FLNC* missense variants is indicative of autophagy pathways being unable to maintain homeostasis. The activation of CASA and CASA-like pathways have been studied in cases of protein aggregation in MFM and report that autophagy is activated but cannot clear aggregation (88,89). Further studies have also observed the dispersion of FLNC binding partners which interferes with the stability of ligand interactions between the cytoskeleton and the membrane (151–153). The resultant aggregation, combined with the depletion of myofilament components is a major contributor to fibre disintegration (87,89,154). The exact mechanisms which cause a *FLNC* variant to result in protein aggregation is not fully elucidated, however, further studies have identified additional proteins that regulate FLNC via autophagy (e.g. HSPB7) that may help the overall understanding of FLNC proteostasis (133).

Although this work has primarily been carried out in *FLNC* variants affecting the skeletal muscle, aggregation is also observed in cardiac filaminopathies (98,100), though not as universally in cardiac disease (101,140,155). Since filamin C is client target of CASA, the presence of protein aggregation in a cardiac context may be similarly due to an impaired CASA (or CASA-like process) being deficient in maintaining FLNC proteostasis.

Interestingly, immunohistochemical assessments of cardiomyopathy patients with *FLNC* missense variants reported the loss of filamin C from the ICD (99,100,149). Evidence of filamin C redistribution to the ICD has been observed in models of biomechanical stress and may be an adaptive response in order to resist greater mechanical strain (156). As discussed

previously, the amino acid change and location of a *FLNC* variant may render it susceptible to unfolding and aggregation or redistribution (98–101,139–141,155).

1.6 HCM-related FLNC W2164C variant

As discussed in 1.5.2, filamin C and its genetic variants have been identified as a key player in the pathology of cardiomyopathies. Despite the promise of next-generation sequencing, assigning causality to *FLNC* variants identified in a clinical genetic setting remains a challenge. Since cohort sizes of family studies are often small, extensive segregation analysis is required along with the functional investigation of these variants with a lack of patient cardiac tissue (157).

By combining whole genome sequencing and linkage analysis (158), a heterozygous *FLNC* W2164C missense variant was identified in a three-generation family affected by cardiomyopathy (159). Patients presented with HCM with features of RCM and displayed electrocardiogram (ECG) changes (Figure 1-10). Affected patients were identified as early as 15 years old. A variety of cardiac phenotypes (elements of non-compaction cardiomyopathy, long QT syndrome, ventricular and atrial septal defects) is observed in some family members.

An ECG registers the action potentials of the heart via an ECG wave. The P wave is the result of atrial depolarisation with abberations associated with left atrial alterations in size, conduction and hypertension (160). The QRS complex represents the average depolarisation waves of the endocardial and epicardial cardiomyocytes (161). The T wave is the repolarisation of the ventricles, abnormalities related to the T wave usually involve the ST segment and can indicate alterations in myocardial electrophysiology (161). The recording

of electrical activity through the heart is done by using external electrodes places on the skin, the two used in these readings were both placed in the 4th intercostal space, V1 (right of the sternum) and V2 (left of the sternum) (161).

In the patients possessing the *FLNC* W2164C variant, a partial right bundle branch block (RBBB) was observed due to a QRS duration of greater than 120 milliseconds and an "bunny ear" pattern. This prolonged QRS duration also shows a lower action potential peak and can indicate delays in electrical stimulation between ventricles and, thus, contraction. T wave inversion, as observed in V1 measurements, is correlated with apical hypertrophy, coronary heart disease and death (162). A bifid p-wave can assess disrupted atrial conduction and can indicate left atrial dilation or hypertrophy (163). The R wave represents the electrical signal as it is transmitted through the ventricular walls (164). Left ventricular hypertrophy has been reported to be the cause of R-wave abnormalities and hence may explain the dominant R-wave in V1 (164). The evidence of a prolonged QT interval (the electrical duration of ventricular systole) may reflect electrical disturbances in the ventricles and is associated with increased risk of death (165). The ST segment represents the time between ventricular depolarisation and ventricular repolarisation (166). An elevation of the ST segment may be indicative of electrical remodelling due to left ventricular hypertrophy and can be caused by myocardial infarction and scarring (167).

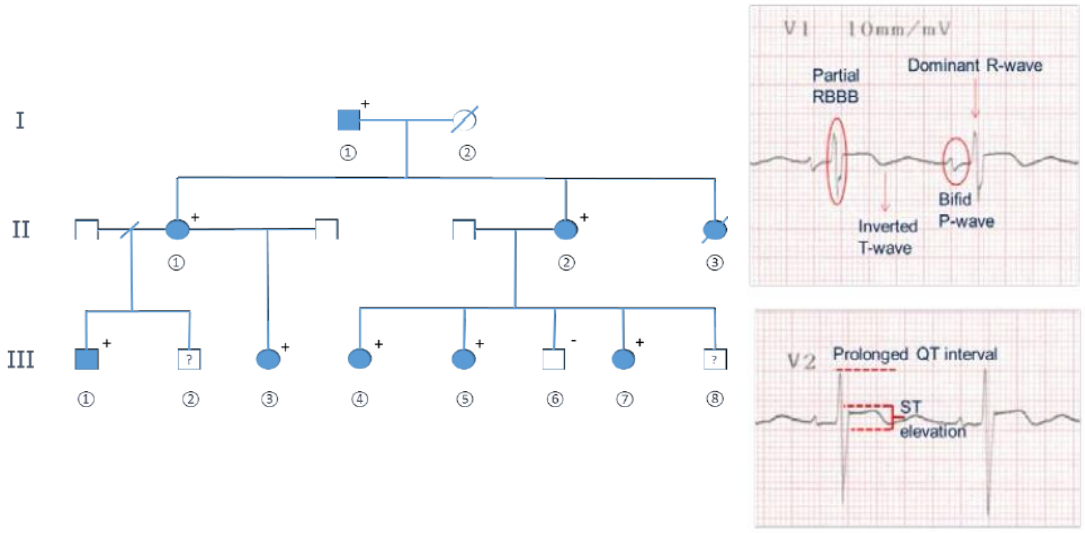

Figure 1-10 Pedigree of a three-generation family carrying the FLNC W2164C missense variant. (+) variant, (–) variant absent. Unpublished data by H. Watkins. Key: Males (squares), females (circles), deceased individual (/), unaffected individuals (white), clinically affected (blue), unknown disease/genetic status (?). Abbreviations: RBBB, right bundle branch block.

1.7 Cardiomyopathy disease modelling in animal models

Since suitable human cardiac samples are not readily available for research purposes (especially healthy controls), there is a need to use alternative methods to study cardiovascular disease. Models for disease characterisation can either be whole organisms or *in vitro*. While both have benefits and caveats, it is important that the model is able to recapitulate phenotypes that exist within human cardiac pathophysiology.

Animal models (in particular mice) can offer valuable insights into cardiovascular function, providing detailed *in vivo* parameters such as echocardiography. The cardiac tissue from the mice can further be used for molecular analyses for identification of pathological pathways. The mouse is the model organism of choice due to 99% of human genes having direct murine orthologues and can recapitulate some phenotypes observed in human cardiac diseases such as hypertrophy. Rodent models are typically used for cardiomyopathy research in-part due to their shorter lifespan which allows the study of disease progression at an accelerated pace. Although rodents have been used in order to corroborate what is seen in the human patients,

some studies have discovered additional data that may have relevance to human disease mechanisms (168). Filamin C-associated cardiomyopathy studies have utilised mouse models considerably to give mechanistic insight into the cardiac roles of filamin C (98,132,155). Knockout models have shown the importance of filamin C in cardiac development and cardiomyopathy in adult mice (132). Key species-related differences in physiology (heart rate), electrophysiology (lack of certain ion channels) and protein isoform expression (e.g. MYH7 is dominant in human ventricles, while MYH6 is dominant in mouse ventricles allowing for an increased contractility rate), however, can render results non-translatable to the human condition (169,170). The dominant *FLNC* isoform expressed may be different between models and hence influence the study of *FLNC* variants. Choosing the best disease model to answer a biological question is multifaceted and requires one to understand the advantages and limitations of each one.

1.7.1 Cellular models

To compliment rodent mice whole organism studies, *in vitro* models have been used: rat and mouse cardiac myoblasts, rat and mouse embryonic stem cells, primary adult murine cardiomyocytes, neonatal rat cardiomyocytes (171,172). These models enable researchers to gain morphological, biochemical and electrical readouts and have been used in studies for drug cardiotoxicity screening, cardiac development and disease modelling (171–173). Studies employing cellular models have been used to probe for the composition of aggregates observed in HCM-related *FLNC* variants (98). Despite the wide-use of these models, there are issues regarding scalability as well as rodent-human differences, without the advantages of being a whole organism multi-cellular organism.

1.8 Cardiomyopathy disease modelling in human cellular models

Embryonic stem cells (ESCs) are pluripotent stem cells derived from embryos that are able to be used to generate all somatic cell types and have proved as a valuable tool for disease modelling (174). The emergence of the embryonic stem cell line (ESC) and its derived cardiomyocytes allowed for the continuous generation and long-term culture of theoretically human cardiomyocytes, considering human cardiac tissue does not survive in culture for long. The possibility to study specific variants proposed to be implicated in mechano-sensing or mechano-signalling however has been limited due to ethical limitations in genetically modifying ESCs.

In 2006, the ethical boundaries to ESC cell-type research was overcome with the reversal of terminally differentiated cells of human-induced pluripotent stem cell (iPSC) technology (175). Takahasi *et al*. were able to induce pluripotency in mouse fibroblasts using as few as four transcription factors (cMyc, Klf4, Sox2, and Oct3/4) which have since become known as the "Yamanaka Factors" (175). Due to the ease of use, only one year after this publication, the same group generated the first human iPSCs from human endothelial fibroblasts (176). Similar to ESCs, iPSCs can be directed towards a specific cell-type. For studying cardiomyopathies, iPSCs would undergo directed differentiation into cardiomyocytes (iPSC-CMs). The successful generation of iPSC-CMs is reliant on upon the developmental pathways which are activated or inactivated during the differentiation process. Alterations of such pathways may lead to the differentiation into different cell types. The manipulation of these pathways is dependent on the use of defined factors which have been developed in ESCs and adapted for iPSC-CMs (176,177). Protocols drive differentiation initially towards a mesoderm lineage before cardiac specification by modulating the Wnt/β-catenin signalling pathway. This is achieved by either employing the use of Activin A and Bone Morphogenic

Protein 4 to enhance pathway activation or by relying on chemical inhibition of Wnt signalling proteins. The latter is a popular approach due to the relative ease in manipulating a single pathway (Figure 1-11).

Most protocols for chemical inhibition rely on a GSK3 inhibitor (CHIR99021) which results in increase β-catenin production and promotes canonical Wnt signalling leading to mesoderm differentiation (178). To push cardiac specification, the Wnt signalling pathway is then suppressed by a Wnt inhibitor (IWR-1) which stabilises the β-catenin destruction complex (179). Further to this, the removal of insulin from culturing medium was found to improve the yield of generated iPSC-CMs (180).

iPSC-CMs have been used to improve our understanding of the structure and function of human cardiomyocytes. Common readouts in iPSC-CM models are changes in calcium handling, cell size, contractility, only to name a few. Tucker et al. used the iPSC-CM model to show that a *FLNC* Ig20 variant resulted in reduced fractional shortening (155).

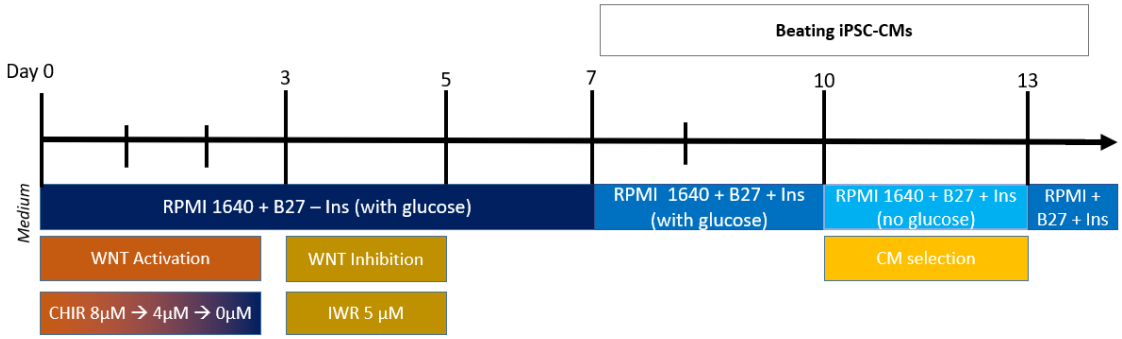

Figure 1-11 The differentiation protocol of iPSCs to iPSC-CM. Initiation begins by the activation of WNT signalling pathway at day 0 to day 2 to force iPSCs into mesoderm differentiation, before cardiac specification via WNT signalling pathway inhibition from day 3 to 5. iPSC-CMs are enriched in glucose deprivation between days 10 and 13. Each line represents a media change unless otherwise stated. MD = media dilution.

1.8.1 Genetic manipulation of iPSCs

Some earlier studies utilising patient-derived iPSCs harbouring a variant did not have patient mutant corrected control lines, instead using control lines from a completely different genetic background (181,182). Since cardiomyopathies are believed to be influenced by a

combination of common variants, it is vital that the control iPSCs have the same genetic background as the mutant.

Combined with the use of clustered regularly interspace short palindromic repeat-associated protein 9 (CRISPR-cas9) or transcription activator-like effector nucleases (TALENs), specific cardiac variants can be genetically engineered into isogenic control iPSCs or iPSCs can be derived from patients and have their genetic abnormality repaired as a control (183,184). CRISPR-cas9 edits genes by using a guide RNA sequence to direct the cas9 enzyme to specifically cut the DNA at the precise target location, introducing double-strand DNA breaks (185). Genome editing is then stimulated in the damaged DNA as it undergoes either nonhomologous end joining or homology-directed repair (Figure 1-12) (185,186).

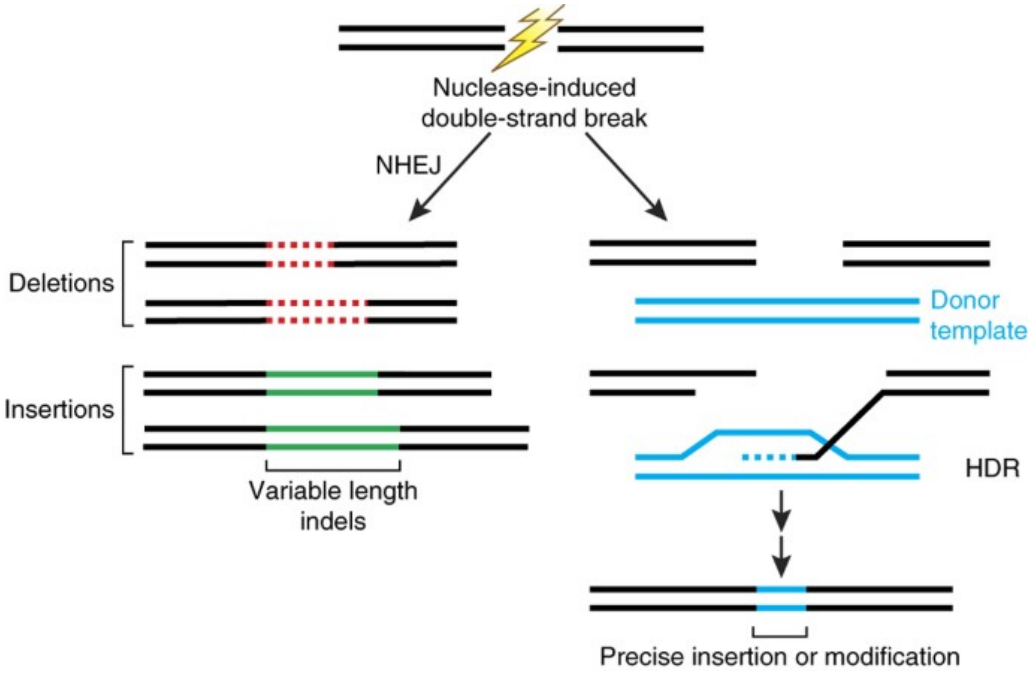

Figure 1-12 Scheme of CRISPR/Cas9-assisted genome editing mechanisms. A nuclease-induced double-strand break is generated by Cas9 and repaired either by non-homologous end joining (NHEJ) or homology-directed repair (HDR). NHEJ introduces either insertion or deletion mutations at the double-strand break site. HDR precisely introduces sequence replacement and insertion based on a donor DNA template. *Image taken from Sander and Joung, 2014*

Since its arrival, iPSC-CMs have been used to investigate key cardiomyopathy disease genes and their patient-specific variants utilising the following functional outputs: contractility, sarcomere length and organisation, calcium and voltage signals etc (187). In addition to now being able to study rare inherited diseases by isolated iPSCs from patients, iPSC-derived cells have enabled targeted drug development, opening the door to personalised medicine which is tailored to the genetic signature of the patient (89,99,155,188).

1.9 A combined approach

Rodent and iPSC-CM models for studying inherited cardiomyopathies both carry significant advantages and disadvantages themselves (Table 1-1).

Rodent models are able to display adult cardiac features whereas although iPSC-CMs are human, they display very immature phenotypes (189–191). By using both models, reported phenotypes can be validated and be more likely corroborated in adult humans.

Table 1-1 Comparative Pros and Cons list for rodent and iPSC-CM models for modelling cardiomyopathy.

Model	Pros	Cons
Rodent	Ease of genetic modification Low cost	Differences in electrophysiology High resting heart rate Shortened APD Different gene expression profile (N2B/N2BA, MYH6/MYH7)
iPSC-CM	Ease of genetic modification Patient-specific investigation – direct genotype-phenotype association Comparable calcium handling properties	Disorganised sarcomere structure Reduced cell size Immature gene expression (N2B/N2BA, MYH6/MYH7)

1.10 Hypothesis and Aims

Investigating a specific variant will uncover information about how that variant causes HCM and the underlying disease mechanisms that may inform better personalised medicines. The current thesis focuses to elucidate the underlying mechanisms of HCM in a *FLNC* W2164C variant by (*i*) utilising a novel *Flnc* W2165C (equivalent to W2164C in humans) mouse model of HCM and (*ii*) a human iPSC line carrying the *FLNC* W2164C variant.

The central hypothesis is that the *FLNC* W2164C missense variant causes cardiomyopathy and results in over-activated mechano-sensing processes.

It is hypothesised that the combined use of a mouse model and the iPSC-derived cardiomyocyte model carrying the W2164C variant in *FLNC* will allow for insight into combined phenotypes of HCM, which may have relevance to patients carrying this mutation.

1.10.1 Study of HCM in the *Flnc* W2165C mouse model

Chapter three presents a characterisation of the mouse model harbouring this variant. By measuring the morphological, functional and molecular parameters of mutant mice, a cardiomyopathy phenotype was probed for. It is hypothesised that the mice will display a cardiomyopathy phenotype.

1.10.2 Generation and characterisation of *FLNC* W2164C iPSC-CMs

In the fourth chapter, the impact of this variant was characterised in the iPSC-CM model. A cardiomyopathy phenotype was also be probed for at a morphological, functional and molecular level and was predicted to result in a phenotype indicative of HCM. Due to model limitations, the cells will be characterised in regular 2D plastic culturing conditions, in the presence of a drug known to induce hypertrophy and on surfaces of a physiological stiffness. By culturing human iPSC-CMs on surfaces of physiological stiffness, it is hypothesised that

the model will be matured and hence display a phenotype which is more comparable with what is observed in patients harbouring this variant.

1.10.3 Assessing mechano-sensing properties of *FLNC* W2164C

The fifth chapter was conducted in parallel to both Chapter 3 and 4 and is dedicated to specifically probing for the impact of this filamin C variant on mechano-sensing in both genetically-edited mouse and iPSC-CM models. Since the clinically-relevant *FLNC* variant is located in the supposed mechano-sensing hub, Ig20, disruptions to mechano-sensing can be interrogated. The aim of this work is to aid in the elucidation of the mechano-sensing role filamin C may have and its relevance to inherited cardiomyopathies. To achieve this, the mouse tissue was molecularly probed and iPSC-CMs underwent functional and molecular interrogation. For this chapter, all iPSC-CMs were cultured on PDMS of a physiological stiffness, as it was hypothesised that it would unmask any mechano-sensing phenotype by ensuring the cells were not mechanically compromised. It is hypothesised that the *FLNC* variant alters the dynamic properties of filamin C and, thus results in constitutively active mechano-sensing processes.

Chapter 2 : MATERIALS AND METHODS

All buffers and solutions are included in the Appendix (Table S1). Commercial kits and other commercial products are also summarised in the Appendix (Table S2). Instruments used are mentioned throughout the methods.

2.1 Materials

2.1.1 iPSC line

KOLF2-C1 iPSC line (WTSIi018-B-1) was derived from health male skin fibroblasts, given as a gift from the Wellcome Sanger Institute.

[http://www.hipsci.org/lines/#/lines/HPSI0114i-kolf_2]

2.1.2 Antibodies

All antibodies used in this thesis are listed in Table 2-1.

Table 2-1: List of antibodies. The concentrations used for each application are stated. Abbreviations: IF, immunofluorescence; WB, immunoblot; IP, immunoprecipitation; FACS, fluorescence assisted cell sorting.

Primary antibbodies				
Antigen	**Host**	**Source**	**Catalogue No.**	**Concentration**
GAPDH	Rabbit	Cell Signalling technology	D1H11	1: 10 000 (WB)
ACTN2	Rabbit	Abcam	Ab68167	1: 5000 (WB), 1:500 (IF)
ACTN2	Mouse	Abcam	Ab9465/Ea53	1:500 (IF)
Vinculin	Rabbit	ProteinTech	26520-1-AP	1: 2000 (WB)
FLNC	Rabbit	Medical Research Council, Protien Phosphorylation and Ubiquitinylation	S661B	1: 2000 (WB) 1:100 (IP)
FLNC	Rabbit	Cell Signalling Technologies	D1K3J	1:100 (IF)
F-actin (Alexa Fluor 633 conjugated phalloidin)	-	Invitrogen	A22284	1:500 (IF)
Connexin-43	Rabbit	Abcam	Ab11370	1: 3000 (IB)

MYOT	Mouse	Insight Biotechnology	SC-393957	1:200 (IF)
AIF	Rabbit	ProteinTech	17984-1-AP	1:1000 (IB)
NDUFV1	Rabbit	ProteinTech	11238-1-AP	1:500 (IB)
UQCRC2	Rabbit	ProteinTech	14742-1-AP	1:500 (IB)
FBLIM1	Rabbit	ProteinTech	13349-1-AP	1:1000 (IB)
BAG3	Rabbit	ProteinTech	10599-1-AP	1:1500 (IB)
MYOT	Rabbit	ProteinTech	10731-1-AP	1:3000 (IB), 1:100 (IF)
MYOT	Mouse	Leica	NCL-MYOTILLIN	1:100 (IF)
LC3	Rabbit	Cell Signalling Technologies	2775	1:500 (IB)
p62	Rabbit	ProteinTech	66184-1-IG	1:1000 (IB)
XIRP1	Rabbit	ProteinTech	11896-1-AP	1:1500 (IB)
MYH7	Rabbit	ProteinTech	22280-1-AP	1:3000 (IB)
HSPB7	Rabbit	ProteinTech	15700-1-AP	1:500 (IB), 1:100 (IF)
HSP27 (HSPB1)	Mouse	Cell Signalling Technologies	2442	1:1000 (IB), 1:100 (IF)
HSP70	Rabbit	Cell Signalling Technologies	4872	1:1000 (IB)
Cadherin	Mouse	BD Transduction Laboratories	610254	1:2000 (IB), 1:400 (IF)
Tropoinin T (cTnT)	Rabbit	Abcam	Ab45932	1:2000 (IB) 1:100 (FACS)
MLC2V	Rabbit	ProteinTech	10906-1-AP	1:100 (FACS)
Secondary antibodies				
Specificity	**Host**	**Source**	**Catalogue No.**	**Concentration**
anti-Rabbit IgG IRDye 800CW	Goat	LI-COR	926-32211	1: 10 000 (WB)
anti-Mouse IgG IRDye 680RD	Goat	LI-COR	926-68070	1: 10 000 (WB)
Alexa Fluor 488-conjugated anti-rabbit IgG	Goat	Invitrogen	A11034	1:500 (IF)

Alexa Fluor 488-conjugated anti-mouse IgG	Goat	Invitrogen	A11029	1:500 (IF)
Alexa Fluor 568-conjugated anti-rabbit IgG	Goat	Invitrogen	A11036	1:500 (IF)
Alexa Fluor 647-conjugated anti-rabbit IgG	Donkey	Invitrogen	A31573	1:500 (IF)
Alexa Fluor 647-conjugated anti-mouse IgG	Donkey	Invitrogen	A31571	1:500 (IF)
DAPI	-	Sigma-Aldrich	28718–90–3	1:500 (IF)

2.1.3 Probes and primers for qPCR

Probes and primers for qPCR are listed in Table 2-2.

Table 2-2 Assays for qPCR. All assays were FAM-MGB TaqMan Assays (Applied Biosystems) unless stated otherwise.

TaqMan Probes		
Transcript	**Species**	**Assay ID**
ACTA1	Human Mouse	Hs05032285_s1 Mm00808218_g1
ACTN2	Human Mouse	Hs00153809_m1 Mm00473657_m1
ANKRD1	Human Mouse	Hs00923600_m1 Mm00496512_m1
ANKRD2	Human Mouse	Hs00220469_m1 Mm00508030_m1
BAG3	Human Mouse	Hs00188713_m1 Mm00443474_m1
COL1A1	Human Mouse	Hs00164004_m1 Mm00801666_g1
COL3A1	Human Mouse	Hs00943809_m1 Mm00802300_m1
CRYAB	Human Mouse	Hs00157107_m1 Mm00515567_m1
CSRP3	Mouse	Mm00443379_m1
FBLIM1	Human Mouse	Hs01036329_g1 Mm00505298_m1
FHL1	Human Mouse	Hs00793641_g1 Mm04204611_g1
FHL2	Human Mouse	Hs00991865_m1 Mm00515781_m1
FLNC	Human Mouse	Hs00155124_m1 Mm00471824_m1
GAPDH (VIC-MGB labelled)	Human Mouse	4626317E 4352339E
GJA1	Mouse	Hs00748445_s1

HK2	Human	Hs00606086_m1
HSPA8	Human Mouse	Hs03044880_gH Mm01731394_gH
HSPA1A	Human Mouse	Hs03044880_gH Mm01159846_s1
HSPB1	Human Mouse	Hs00356629_g1 Mm00834384_g1
HSPB7	Human Mouse	Hs00205296_m1 Mm04210487_m1
LOX	Mouse	Mm00495386_m1
MYH6	Human	Hs01101425_m1
MYH7	Human Mouse	Hs01110632_m1 Mm00600555_m1
MYL2	Human	Hs00166405_m1
MYL7	Human	Hs01085598_g1
MYOT	Human Mouse	Hs00199016_m1 Mm00498877_m1
NPPA	Human Mouse	Hs00383230_g1 Mm01255748_g1
NPPB	Human Mouse	Hs00173590_m1 Mm01255770_g1
PDK4	Human	Hs01037712_m1
PGM5	Human Mouse	Hs00222671_m1 Mm02031187_s1
RCAN1	Mouse	Mm00627762_m1
TNNT	Human	Hs00943911_m1
TTN	Human	Hs00399225_m1
SYBR Green		
Transcript	**Species**	**Sequence (5' – 3')**
TTN N2BA (spanning exons 11-12)F7-R7	Human	CCGGGAGCTCAAGAAGAAA TGACTTTGGGTGTGGCAACT
TTN N2BA and N2B (exons 49-50) F9-R9	Human	TGAGGCCTTGAATGACAGCG GATCACTGGGGCAGCTCTTT

2.2 Methods

2.2.1 Mouse model

2.2.1.1 Generation of mouse model

C57BL/6J mice carrying the *W2165C* variant in the *Flnc* gene (the murine equivalent of the human W2164C) at a homozygous and heterozygous level were generated by CRISPR-Cas9 techniques at The Transgenic Core (Dr Ben Davies), Wellcome Centre for Human Genetics, University of Oxford. The mouse *W2165C* variant is equivalent to the human *W2164C* variant in the identified HCM family. Mice were bred, maintained and culled at The Wellcome Trust Centre for Human Genetics, University of Oxford. Mice were culled in accordance with HO schedule 1 regulations by cervical dislocation followed by confirmation of death (cessation of circulation by cutting major blood vessel or removal of the heart).

2.2.1.2 Echocardiography of mouse model

Mice were initially anesthetised using 2 % isoflurane supplemented with 100 % oxygen in an anaesthesia box. Once suitably unconscious, the mouse was transferred to a warming platform with nose cone supplying anaesthesia in a supine position. Conductance gel was placed onto the four electrodes within the warming and paws were subsequently taped to monitor heart rate and ensure it is maintained at 450±50 BPM. Eye cream was applied to the eyes to keep them lubricated while anesthetised. A rectal probe was inserted with the aid of lubricant to measure core body temperature throughout the procedure. Depilatory cream (Nair) was applied to the chest area to remove hair from the area to be imaged. Once hair was been removed and area was been cleaned with warm water, pre-warmed ultrasound gel was applied to the area to be imaged. The system used was a Vevo 2100 system (VisualSonics) with a 550XD transducer.

The platform was tilted slightly downward and the transducer was made parallel to the sternum. Once the aorta was in view, the transducer was turned anti-clockwise until the left ventricular apex was in line with the aorta. Next the transducer was rotated 90^{o} to visualise the short axis view of the left ventricle at the level of the papillary muscles. Motion mode (M-mode) was used to analysed the left ventricular posterior wall (LVPW), left ventricular internal diameter (LVID) and left ventricular anterior wall (LVAW) at both diastole and systole. These measurements were quantified offline using Vevolabs software (VisualSonics) and used to calculate the following parameters; ejection fraction, fractional shortening, left ventricular mass, left ventricular volume in diastole and systole.

Left ventricular mass was also calculated using anterior wall thickness (LV mass AW corrected) in M-mode from measurement for the short axis view of the heart. These measurements were corrected by a factor of 0.8.

Note: This method was carried out by Austin Jiang.

2.2.1.3 Mouse gravimetry

Mice were culled as described above. Mouse tibia length was measured and used to correct heart weight. Heart weight (HW), body weight (BW), and tibia length (TL) measurements were taken post-treatment of saline/ang-II and also at baseline.

Mouse tibia length was measured using digital callipers following incubation of tibiae overnight with 0.8M sodium hydroxide (Scientific Laboratory Supplies, CHE3416) and removal of excess muscle, patella, and foot. Body weight and height weight were measured to calculate ratios of heart weight to tibia length (HW/TL), heart weight to body weight (HW/BW), and tibia length to body weight (TL/BW).

2.2.1.4 Angiotensin-II treatment

Method for angiotensin-II (Ang-II) treatment was followed as according to ISO/PE treatment in Jiang et al. (192) but with Ang-II instead. On day 0, mice underwent 2% isofluorane anaesthesia and maintained in 100% oxygen. A small dorsal area was shaved to reveal an area between the shoulder blades and the mouse was covered in large tegaderm drape. A small, straight incision was made with blunt-ended scissors and the skin was dissected to make a pocket. The prepared mini-pump was inserted into the incision, and pushed through the skin pocket to reach the desired position. Once the mini-pump reached the desired location, the incision was sutured closed. The post-operative recovery of the mice was then measured.

Mice were given Ang-II at a concentration of 1.1 mg/kg BW per day and the mice were monitored daily. Echo measurements made at baseline was conducted 2-3 days before the implant, then again following 2-weeks of osmotic minipump treatment. Mice were then culled for recording heart weight, body weight and tibia length.

Note: Ang-II treatment and tissue collection was carried out by Austin Jiang.

2.2.2 iPSC culture

2.2.2.1 iPSC maintenance

The KOLF2 isogenic human induced pluripotent stem cell (iPSC) line derived from a healthy individual was cultured, passaged and underwent differentiation into iPSC-derived cardiomyocytes (iPSC-CMs). All iPSC and iPSC-CM cell cultures (including differentiation protocols) were maintained in a humidified incubator at 37^{o}C, 5% CO_2, 20% O_2.

Tissue culture wells were pre-coated with an extracellular matrix to allow improved adhesion. Matrigel (Corning) or GelTrex (Life Technologies) was incubated in DMEM/F12

(Life Technologies) at a ratio of 1:200 for 4 hours at 37ºC. These were for iPSC maintenance and iPSC-CM differentiation.

iPSCs were maintained in mTeSR Plus (StemCell Technologies). Medium was changed every other day until the cells had reached 90-95% well confluence. Once confluent, cells were dissociated using 0.5 mM EDTA/PBS (ThermoFisher Scientific). iPSCs were collected and plated in mTeSR Plus with 10 μM Rho Kinase (ROCKi) inhibitor, Y-27632 (Selleck). ROCKi containing mTeSR Plus medium was replaced with mTeSR Plus within 20 hours of passage.

For cryopreservation, 0.5 mM EDTA/PBS was used to dissociate iPSCs and resuspended in mFreSR (StemCell Technologies). The cell suspension was transferred into a cryovial in a dropwise manner at approximately 10^6 cells per cryovial. iPSCs were moved into the cooling unit "Mr Frosty" and stored at -80 ºC overnight before long-term preservation in liquid nitrogen.

Frozen cells were thawed at 37 ºC for approximately 1 minute until a small ice crystal remained. The cell solution was then gently added to culturing medium and centrifuged at 200 g for 3 minutes. The collected cell pellet was resuspended in mTeSR Plus supplemented with 10 μM ROCKi and plated in Matrigel/GelTrex coated tissue culture wells.

2.2.2.2 iPSC-CM differentiation

iPSC-CMs were generated in house based on a chemically defined differentiation protocol (Figure 2-1) (179). Three days prior to differentiation initiation, iPSCs were passaged and seeded at 100,000 cells per 6-well dish.

Induction of cardiac differentiation began when iPSC well confluence reached approximately 90%. mTeSR Plus medium was replaced with RPMI 1640 medium (Gibco) with a B27 supplement lacking insulin (Gibco) (RPMI-MinIns) on Day 0. Parallel to the media change, the WNT signalling pathway was activated by the inclusion of 8 µM CHIR99021 (Selleck) in the medium solution, this was then diluted with RPMI-MinIns to 4 µM the following day (Day 1). On day 3, addition of 5 µM IWR-1 (Selleck) to the medium change stimulated the inactivation of the WNT signalling pathway. A medium change of RPMI–MinIns was done on day 2 and day 5 to remove CHIR99021 and IWR-1. A medium change at day 7 of RPMI 1640 medium with B27 supplement containing insulin (Gibco) (RPMI-PlusIns) indicates the end of directed differentiation and spontaneous contractions are expected from this day. All media changes from day 0 until day 7 were supplemented with 30 µM L-ascorbic acid. At day 10 iPSC-CMs underwent glucose deprivation until Day 12 in glucose-lacking RPMI 1640 (Gibco) + B27 + Ins to enrich the iPSC-CM population.

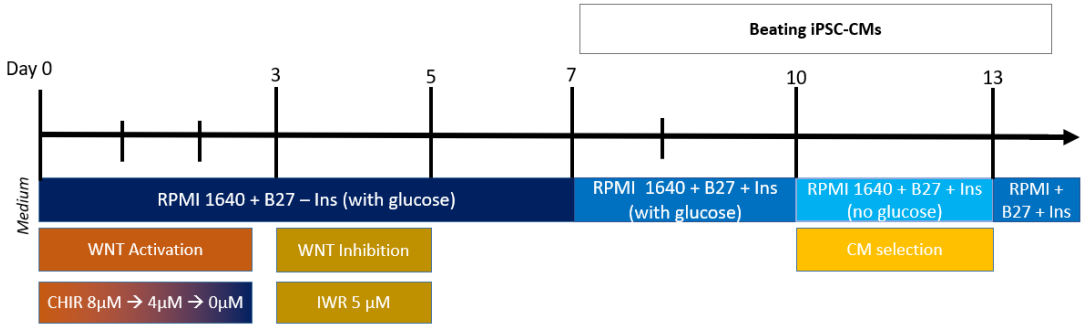

Figure 2-1 The differentiation protocol of iPSCs to iPSC-CM. Initiation begins by the activation of WNT signalling pathway at day 0 to day 2 to force iPSCs into mesoderm differentiation, before cardiac specification via WNT signalling pathway inhibition from day 3 to 5. iPSC-CMs are enriched in glucose deprivation between days 10 and 13. Each line represents a media change unless otherwise stated. MD = media dilution.

2.2.2.3 iPSC-CM maintenance and passage

Cardiomyocytes were maintained in glucose containing RPMI+B27+Ins media, changing media once every two days.

When necessary (e.g. for passage onto coverslips), iPSC-CMs were passaged. Cells were dissociated in TrypLE Select 10X (Life Technologies) was added to each well and incubated twice for 4 minutes, gently shaking the plate in between. Plating media (90 mL

RPMI+B27+Ins, 10 mL knock-out serum replacement, 20 μl thiazovivin) inactivates the dissociating reagent and further dissociation was done. The cell-containing media was transferred into a falcon tube via 50 μm^3 filter cap. Cardiomyocyte solution was centrifuged at 215G for 3 minutes at room temperature. Plating media was aspirated, and the cell pellet was resuspended for plating onto Matrigel/GelTrex DMEM/F12 (Life Technologies) coated 6-well plates (Corning) at appropriate densities (approximately 1 million per well of 6-well plate).

2.2.2.4 Isoprenaline treatment

iPSC-CMs at 27-days old, underwent DMSO or 10 μM isoprenaline treatment daily for two days before being harvested at day 30 for protein and transcript analyses (193). On the day of harvesting, the beating frequency of iPSC-CMs was recorded by manual counting in a temperature uncontrolled environment.

2.2.2.5 Treatment of iPSC-CMs for autophagic flux

Autophagic flux was measured by treated iPSC-CMs at day 29 with either DMSO or 50 μM chloroquine (CQ) diluted in RPMI-B27+Ins for 24 hours. Samples were harvested after 24 hours (day 30). iPSC-CMs were starved of glucose 48 hours before CQ treatment.

2.2.3 Proteomics of murine cardiac tissue

To analyse the proteomics profiles of wild-type and *Flnc* W2165C mutant cardiac tissue, proteins were extracted from ventricular tissue (n = 6 per group: 3 male, 3 female), subjected to subcellular fractionation and methanol/chloroform protein precipitation prior to protein quantification via mass spectrometry techniques.

Organ harvest: Mice were sacrificed by cervical dislocation, the heart excised and rinsed in ice cold PBS. Atria were removed and ventricular tissue snap frozen in liquid nitrogen.

Hearts were later transported to the University of Birmingham where the molecular characterisation discussed in this report took place.

2.2.3.1 Subcellular fractionation

At 14 weeks old, ventricular tissue were excised and snap frozen to be stored at -80^{o}C until needed. The frozen tissue was pulverised using the BioPulverizer (BioSpec) in liquid nitrogen. Powdered tissue (approx. 5 mg) was homogenised with Lysis Buffer 1 (LB1) (Table S1) followed by a 15 min incubation at 4^{o}C. The volume of LB1 used was at a ratio of 10 µL per 1 mg tissue. The homogenate was centrifugated at 17 000 g for 30 minutes at 4 ^{o}C. The supernatant consisting of the cytosol-enriched fraction was removed. The remaining pellet was resuspended with the same volume of Lysis Buffer 2 (LB2) (Table S1), incubated for 15 minutes at 4^{o}C and centrifugated at 17 000 g for 30 minutes at 4^{o}C. The supernatant containing the membrane-enriched fraction was collected. The myofilament-enriched fraction was extracted by resuspending the insoluble pellet in LB2 and underwent an additional 15 minutes incubation at 4^{o}C. All three fractions contained equal volumes. This was validated by immunoblot analysis.

2.2.3.2 Chloroform-methanol protein precipitation

Due to the incompatibility of the high salt content of the lysis buffer, LB2, with mass spectrometry equipment, the fractionated protein samples underwent chloroform-methanol precipitation. Per 200 µL of LB2 containing fractionated protein sample 600 µL methanol was added and mixed thoroughly followed by the addition of 150 µL chloroform and 450 µL H_2O. After vortex the solution which becomes cloudy with precipitate was centrifuged for 1 minute at 14 000 g. The precipitate forms a protein flake separating two aqueous layers. The top aqueous layer was removed prior to the addition of 450 µL methanol and vortex

before an additional centrifugation for 5 minutes at 20 000 g. Methanol was removed and the remaining protein pellet dried under a vacuum.

2.2.3.3 Protein digestion, identification and quantification

The chloroform/methanol enriched proteins were sent to the School of Biosciences, University of Birmingham for trypsin protein to peptide digestion, liquid chromatography with tandem mass spectrometry and protein identification and quantification.

Trypsin digestion was performed using 10 µL of samples (up to 10 µg of protein) and added 40 µL of 100 mM ammonium bicarbonate (pH 8). The samples were then incubated with 50 µL 10 mM dithiothreitol (DTT) at 56ºC for 30 minutes. After cooling to room temperature, cysteines were alkylated by the addition of 50 µl 50 mM iodoacetamide, mixed and incubated at room temperature in the dark for 30 mins. Finally, 50 µl of trypsin gold (Promega, 6 ng/µl) was added to the samples, which were then incubated at 37ºC overnight. The samples were desalted using Millipore C18 ZipTips after pre-wetting in 100 % acetonitrile and rinsed in 2X 10 µL 0.1 % formic acid. Samples were then repeat pipetted through the volume of the samples ten times. The tip was then washed 3 times with 10 µL 0.1% formic acid to remove excess salts. Peptides were eluted in 10 µL 50% acetonitrile/water/0.1% formic acid and dried to remove acetonitrile. All desalted samples were resuspended in 0.1% formic acid solution in water.

UltiMate® 3000 HPLC series (Dionex) was used for peptide concentration and separation. Samples were trapped on precolumn, Acclaim PepMap 100 C18, 5 um, 100A 300um i.d. x 5mm (Dionex) and separated in Nano Series™ Standard Columns 75 µm i.d. x 15 cm, packed with C18 PepMap100, 3 µm, 100Å (Dionex). The gradient used was from 3.2% to 44% solvent B (0.1% formic acid in acetonitrile) for 30 min. The column was then washed

with 90 % mobile phase B before re-equilibrating at 3.2% mobile phase B. Peptides were eluted directly (~ 350 nL min-1) via a Triversa Nanomate nanospray source (Advion Biosciences) into a QExactive HF Orbitrap mass spectrometer (ThermoFisher Scientific). The spray voltage of QE HF was set to 1.7 kV through Triversa NanoMate and heated capillary at 275°C. The mass spectrometer performed a full FT-MS scan (m/z 360−1600) and subsequent higher-energy collisional dissociation (HCD) MS/MS scans of the 20 most abundant ions with dynamic exclusion setting 15S. Full scan mass spectra were recorded at a resolution of 120,000 at m/z 200 and automatic gain control (AGC) target of 3×106. Precursor ions were fragmented in HCD MS/MS with resolution set up at 15,000 and a normalized collision energy of 28. AGC target for HCD MS/MS was 1x105. The width of the precursor isolation window was 1.2 m/z and only multiply-charged precursor ions were selected for MS/MS. Spectra were acquired for 56 mins.

2.2.3.4 Downstream analysis and visualisation

Label-free quantification was determined from raw data outputs via the MaxLFQ workflow(194) on the quantitative proteomics platform MaxQuant version 1.6.14. Downstream analysis on the free bioinformatics-based computational platform Perseus version 1.6.12.0 was used to uncover biologically relevant information(195). This dataset was split to isolate the membrane and myofilament data and subjected to false hit filtration (removing potential contaminants, reverse sequences and hits only identified by one site), median subtraction normalisation and logarithmic transformation. Since some proteins go unquantified due to technical and/or biological reasons, proteins with at least 3 valid quantified values in at least one group (*WT*/*FLNC W2165C*) were kept. All remaining unquantified samples were replaced with imputed values from the normal distribution. Statistical quantification was determined by a 2-sample T-test whereby the permutation-

based false discovery rate (FDR) was used. An FDR threshold of 0.05 was set. Perseus outputs for membrane and myofilament datasets were visualised using RStudio version 1.2.1335. Since the permutation-based FDR value has been shown to overestimate the FDR value, setting a relaxed threshold was also used (Fold change<2, q-value < 0.05 thus -logP < 1.301)(196,197), STRING analysis was performed alongside using the Functional Annotation Tool (DAVID Bioinformatics Resources 6.7) to pull out KEGG pathway and gene ontology information and visualised via REVIGO.

2.2.4 Protein extraction and immunoblotting

Cells were harvested as cell pellets before further use at day 30. TryPLE Select 10X was used as the dissociation reagent before collecting cells in PBS in an Eppendorf tube. iPSC-CM containing Eppendorfs were centrifuged at 13 000 g for 5 minutes at 4 ^{o}C. PBS was aspirated and cell pellet was stored in -80 ^{o}C freezer until needed.

Cell pellets were denatured in 2X SDS-SB and fractionated tissue solutions were denatured with equi-volume of 2X SDS-SB for 3 minutes at 100 ^{o}C. Protein samples underwent sonication.

Protein samples were separated by 4-15% polyacrylamide SDS-PAGE gel (Biorad) and transferred to nitrocellulose membranes via iBlot 2 Gel Transfer Device (Invitrogen). Ponceau S solution (Sigma-Aldrich) was applied to the membrane to allow visualisation of total protein for imaging. Ponceau S solution was washed off in deionised water.

The membranes were blocked in 5% semi-skimmed milk powder in tris-buffer saline (Sigma-Aldrich) supplemented with 0.1% Tween-20 (VWR) (TBST) for 1 hour. Subsequently, primary antibodies were incubated in fresh 5% milk supplemented TBST for

16 hours at 4 ºC. The membrane was washed with 0.1% TBST 5 times for 5 minutes each on a rocking platform. Bound primary antibodies were detected by fluorescently labelled goat anti-rabbit or anti-mouse secondary antibodies diluted in the 1% semi-skimmed milk powder in TBST at room temperature for 1 hour (concentrations found in Table 2-1). Protein bands were detected on the Odyssey Fc Imaging System (LI-COR) by fluorescence at 700 nm and 800 nm. Protein bands were quantified by densitometry on ImageJ software (version 1.53c).

2.2.5 RNA extraction, cDNA synthesis and quantitative polymerase chain reaction (PCR)

Cells were harvested as cell pellets before further use at day 30. TryPLE Select 10X was used as the dissociation reagent before collecting cells in PBS in an Eppendorf tube. iPSC-CM containing Eppendorfs were centrifuged at 13 000g for 5 minutes at 4ºC. PBS was aspirated and cell pellet was stored in -80ºC freezer until needed.

Total RNA was extracted from iPSC-CMs using TRIzol Reagent (Invitrogen) in a fume-cupboard and followed the Directzol RNA MiniPrep Kit (Cambridge Bioscience) protocol. Potential contaminant genomic DNA was removed by RNase-Free DNase Set (Qiagen) with 400 µL wash buffer.

Reverse transcriptase-PCR was used to synthesise cDNA by following the High-Capacity cDNA Reverse Transcription Kit protocol (Applied Biosystems).

Quantitative real-time PCR was carried out using TaqMan™ probes Fast Advanced Master Mix 2X (Thermo Fisher) protocol on the Applied Biosystems 7500 Fast Real-Time PCR system. Analysis of transcripts *N2B* and *N2BA* was performed using PowerUP SYBR Green Master Mix (Applied Biosystems). Transcript expression was displayed as a fold change,

calculated by means of ΔΔCt ($2^{-\Delta(\Delta Ct)}$ using either *GAPDH*, *ACTN2*, or *cTnT*, as normalisation genes. TaqMan and SYBR green probes are presented in Table 2-2.

2.2.6 Immunofluorescence

Cells and cryo-sectioned tissues were washed in PBS, fixed in 4% paraformaldehyde for 15 minutes at room temperature. The cells were then washed with PBS and were stored in 0.01% sodium azide at 4 ^{o}C.

Fixed samples were permeabilised in 0.2% triton-X-100/PBS for 15 minutes at room temperature and blocked for 1 hour in 5% bovine serum albumin (BSA) (Sigma-Aldrich). Primary antibodies were diluted (as according to Table 2-2) in 5% BSA and applied to the sample overnight at 4 ^{o}C. The primary antibodies were subsequently washed off in PBT 3 times and incubated with secondary antibodies diluted in 5% BSA for 1 hour. Stained wells were washed in PBT and mounted onto a lean glass slide containing Hydromount mounting medium (National Diagnostics).

All samples were assessed and imaged by confocal microscopy (Zeiss LSM780) with the solid-state laser illumination sources using either a 40X water-immersion and 63X oil-immersion objective lens at 1024*1024-pixel resolution with 7.5X zoom factor.

2.2.6.1 CellPose 2.0

Cell area was determined by CellPose 2.0, a deep-learning algorithm (198). iPSC-CMs were stained with a sarcomere marker (ACTN2/F-actin) and underwent automatic segmentation on CellPose 2.0. Segments were corrected manually and images were processed again to train the model. Cell segment masks were processed on ImageJ to obtain the estimated cell area.

2.2.6.2 Z-line detection

For measurements pertaining Z-line length and myofibrillar skewness, the iPSC-CMs were stained with ACTN2/F-actin and underwent instruction of the script 'ZlineDetection' on MATLAB version 9.5.0.1033004 (R2018b) (199).

2.2.7 Flow cytometry

To maximise cell numbers for flow cytometry analysis, iPSC-CMs were cultured for a maximum of day 30.

iPSC-CMs underwent dissociation by incubating in accutase (Life Technologies) for 4 minutes at 37.5 ^{o}C, swirling and incubating for a further 4 minutes prior to inactivation with 1 mL PBS and forceful dissociation via P1000 tip. After dissociation, iPSC-CMs underwent a 3-minute 200 g centrifugation and the cell pellet was resuspended in 200 μL PBS. Samples were washed with 200 μL 1% BSA/PBS, transferred into assigned 96-wel Eppendorf tubes and was centrifuged for 5 minutes at 500 g at 4 ^{o}C.

Fixation took place on ice, using 2% PFA/0.1% Triton-X-100/PBS for a 20-minute incubation. This was followed by addition of 0.1% Triton-X-100/PBS solution and centrifuged as described. An additional 0.1% Triton-X-100/PBS solution and centrifugation were done before 50 μL 0.1% Triton-X-100/PBS solution resuspension.

The primary antibodies were added directly to the Eppendorf tube (concentrations found at Table 2-2) and incubated for approximately 16 hours at 4 ^{o}C. The secondary antibodies were incubated for 30 minutes on ice after 3 washes in 0.1% Triton-X-100/PBS solution. Secondaries were then washed three times in 0.1% Triton-X-100/PBS solution. Fixed cells were run on the Beckamn Coulter Cytoflex and analysed on FlowJo version 10.8.1.

2.2.8 Live-cell imaging

2.2.8.1 Adenoviral transduction and SarcTrack contractility analysis

At least 7 days before contractility measurement, iPSC-CMs were seeded at approximately 1 x 10^5 cells per 3.5 cm glass bottomed culture dish. The cells were transduced with adenoviral vectors containing a *mScarlet-ACTN2* cassette for 1 hour at a dilution of 1: 10 000 (from stock) before changing medium to RPMI-PlusIns. After 48 hours, medium was changed to Tyrode's HEPES solution. Contraction videos were acquired on the Olympus IX81 microscope using a 100X oil-immersion lens at 37 ^{o}C at 50 frames per second. The *mScarlet-ACTN2* adenoviruses used were generated by Dr Violetta Steeples. Contractility of the sarcomere was analysed by SarcTrack scripts in collaboration with Professor Chris Toepfer, Dr Yiangos Psaras and Dr Violetta Steeples (200).

2.2.8.2 Mitochondrial membrane potential

JC-10 Mitochondrial Membrane Potential Kit (Sigma-Aldrich), was used to measure potential across membrane potential in live iPSC-CMs. Prior to JC-10 incubation, cells were seeded at roughly 40 000 cells/well of a 4-chamber Ibidi slide. JC-10 Dye was added to RPMI-PlusIns for 1-hour incubation. Fluorescence intensity was measured at λ_{ex} = 490 nm, λ_{em} = 525 nm and λ_{ex} = 540nm, λ_{em} = 590 nm for ratio analysis. The ratio of red/green fluorescence intensity was used to measure mitochondrial membrane potential. Videos were acquired in an incubation chamber (37 ^{o}C, 5% CO_2) using the LSM880 confocal microscope with the 63X oil-immersion objective lens. Image data was processed using ImageJ software.

2.2.8.3 Lysosomal assessment

The LysoTracker red DND-99 fluorescent probe (Invitrogen) was incubated for 1 hour at 75 nM in RPMI-PlusIns. Videos were acquired in an incubation chamber (37 ^{o}C, 5% CO_2) using the LSM880 confocal microscope with the 63X oil-immersion objective lens.

2.2.9 Autophagic flux assessment

iPSC-CMs were treated with either DMSO or with 20 uM of chloroquine for 24 hours. Protein was extracted from cells as described above and immunoblotting was performed to determine the p62, LC3-I and LC3-II expression relative to GAPDH. Quantitation was performed using densitometry on ImageJ.

2.2.10 Polydimethylsiloxane generation

Polydimethylsiloxane (PDMS) substrates with tuneable stiffnesses were prepared using Sylgard 184 and Sylgard 527 (Dow Corning) used at 2 different Sylgard 184:527 mass ratios (1:10 and 1:20). These were blended and applied to plasma-treated coverslips by vacuum assisted spin coating (Spin150i, Polos) at 1000 rpm for 40 seconds to create a thin PDMS layer on the coverslip (Figure 2-2). PDMS-coated coverslips were cured at 65^{o}C for 8-12 hours before undergoing ethanol sterilisation and PBS leeching washes to remove unpolymerized silicone.

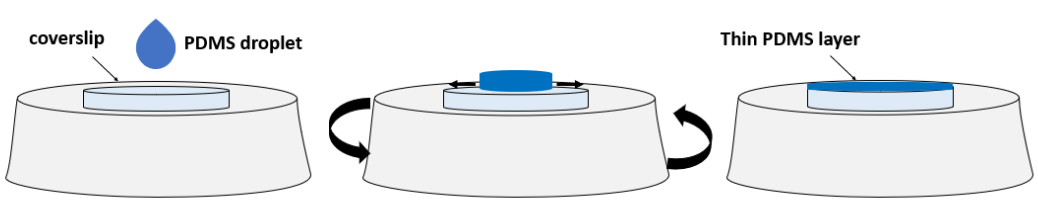

Figure 2-2 Schematic of spin-coating a PDMS mixture of defined stiffness from droplet to a thin even PDMS layer.

Standard ECM coating procedures beforementioned were followed prior to seeding. iPSCs were cultured and differentiated into iPSC-derived cardiomyocytes on standard tissue culture plastics. Post-glucose starvation, iPSC-CMs were passaged onto PDMS-coated or uncoated coverslips and cultured until day 30 in this environment.

Due to the practicalities of characterisation by immunofluorescence, iPSC-CMs on PDMS-coated coverslips were compared with glass coverslips as a control with an estimated stiffness to be in the GPa range.

2.3 Data analysis and statistics

All statistical analyses were performed using GraphPad Prism software (version 9.4.1). For a two-group comparison, a Student *t*-test was used on normally distributed data. If not normally distributed, then a Mann-Whitney U-test was used. When measuring 2 groups of more, a one-way ANOVA. When testing the effect of two or more treatments, normal distributed data underwent a two-way ANOVA with multiple comparisons. Non-parametric data underwent a Kruskal-Wallis test.

Chapter 3 *Flnc* W2165C IN THE MOUSE MODEL

3.1 Introduction

As outlined in Chapter 1, *FLNC* has emerged as a novel HCM disease gene and contains a region (Ig18-Ig21, including the insertion in domain 20) which is proposed to play a role in mechano-sensing and signalling (102–107). By combining WGS and linkage analysis, a heterozygous *FLNC* W2164C missense variant was identified in a three-generation family affected by cardiomyopathy (158). These patients displayed HCM with features of restrictive cardiomyopathy and displayed electrocardiogram (ECG) changes indicative of remodelling. This tryptophan to cysteine amino acid change at position 2164 is located in the insertion within the Ig-domain 20 which is involved in targeting the protein to the Z-disc (201). The variant is predicted to render filamin C to be less structured and result in misfolding, hence altering the structure and function of the cardiomyocyte, potentially through hypertrophic remodelling. Along with structural roles, this region is predicted to have additional functions in aiding how cardiomyocytes sense and respond to changes in mechanical stress by engaging with molecular chaperones (98).

With advances in next-generation sequencing, more genetic testing is done in clinical settings and more genetic variants in *FLNC* are identified. However, assigning causality to *FLNC* variants identified in such clinical genetic settings remains a challenge. Family cohort sizes are often small due to the extensive segregation analysis required (157). Also, determining the functional significance is limited due to a lack of available, variant-relevant patient cardiac tissue. This challenge remains when assigning causality and functional relevance to the *FLNC* W2164C variant. Therefore, relevant disease models are required for in-depth functional investigation.

The mouse is the model organism of choice due to 99% of human genes having direct murine orthologs and can recapitulate some phenotypes observed in human cardiac diseases such as hypertrophy.

3.1.1 Hypothesis and Aims

The *FLNC* W2164C missense variant is hypothesised to cause a cardiomyopathic phenotype in mutant mice and will display molecular features of hypertrophy and structural remodelling.

The objective therefore was to elucidate the cardiomyopathic role of the HCM-disease associated *Flnc* W2165C variant in an adult mouse model (3-months). A mutant mouse model harbouring the *Flnc* W2165C variant (the mouse equivalent of the human *FLNC* W2164C variant) was previously generated by employing homology directed repair-based CRISPR-Cas9 methodology. The presence of the mutation in the edited mouse model was validated by Sanger sequencing.

In this chapter, the hypotheses are tested through the following:

1. To measure the *in vivo* cardiac phenotype of 3-month old mutant mice at baseline and in response to chronic AngII stimulation.
2. To assess alterations of proteins involved in filamin C related mechano-signalling by unsupervised proteomics and validate these findings.
3. To perform follow-up molecular characterisation of these changes in the mutant mouse at transcript level, at protein level and with regards to protein localisation.

Note: Live mouse work was carried out by Austin Jiang and Sophie Broadway-Stringer. Molecular characterisation and data handling were carried out by myself.

3.2 Analysis approach for the proteomics data set

Liquid chromatography mass spectrometry-driven proteomics (LC-MS) generates large amounts of high-quality data which allows for the identification and relative abundance determination of individual proteins. As described in the materials and methods section, proteins were digested into peptides which were in turn analysed by mass spectrometry. Based on the unique set of tryptic peptide patterns, the protein sequence was assembled and identified from MS/MS data in a process called peptide mass mapping. The subsequent dataset produced from the LC-MS experiments requires downstream analysis methods to extract the biological meaning from these datasets. Bioinformatics tools enable this large-scale data processing.

3.2.1 Data filtering

Downstream analysis on the bioinformatics-based computational platform Perseus version 1.6.12.0 was used to uncover biologically relevant information (195). The dataset was split to isolate the membrane and myofilament data and subjected to false hit filtration: removing potential contaminants, reverse sequences and hits only identified by one site. The abundance of a protein identified by LC-MS quantitation may be determined by as few as one peptide. Therefore, a cut-off is required to improve reliability - proteins with at least 3 valid quantified values in at least one group (WT or Hom) were kept. Normalisation of the raw quantitative data removed non-biological related variations and aligned the data across the samples. Since the distribution of protein abundance is significantly skewed towards zero, logarithmic transformation on the intensity values was performed prior to normalisation by median subtraction (202). Due to stochasticity in sampling during the LC-

MS experiment, the raw quantitative data may possess missing values (203). Missing values were replaced with imputed values based on the normal distribution of all proteins detected (204). MA plots (microarray plot) and hierarchical clustering were evaluated individually to determine the effectiveness of the data filtering and cleaning pre-processing steps.

3.2.2 Determining significance

To determine the significant protein level changes between WT and Hom fractionated tissue, statistical analysis by a 2-sample student *t*-test was performed. However, due to limited multiplexity, the sample sizes in proteomics data is small hence reducing the statistical power of the commonly used t-test. Since multiple hypotheses were being tested simultaneously, a false discovery rate (FDR) threshold was set up to reduce the number of false positives detected in this statistical analysis (205). The Benjamini-Hochberg adjusted FDR was chosen.

3.2.2.1 Setting significance thresholds

A minimum fold change (FC) was determined at >2 selecting a threshold at the inflection point of the graph to ensure the fold-change cut-off was neither too permissive or restrictive and Benjamini-Hochberg adjusted FDR (FDR<0.05). Since the -log(FDR) has been shown to overestimate the FDR value, setting a relaxed threshold was also used (Fold change<2, FDR < 0.05 thus -logP < 1.301) – the relaxed threshold (196,197). Perseus outputs for membrane and myofilament datasets were visualised using RStudio version 1.2.1335.

3.2.3 Enrichment analysis

Enrichment analysis was performed to identify pathways which are over- or underrepresented which may share common functions or have a role in the same pathway. Enrichment analysis was determined using the hits from the relaxed threshold of both

fractions combined and run on Gene Ontology (GO) Resources with Panther 17.0 to pull out GO Enrichment Analysis.

Prior to analysis, a subset of proteins of interest was defined (Table 3-1). These proteins were chosen based on their location to the Z-disc, where filamin C is located, as well as proteins which have shown to interact with filamin C. HCM-associated proteins and those involved in the mechano-sensitive process of chaperone-assisted selective autophagy were also selected.

Table 3-1 Proteins of interest prior to proteomics mass spectrometry experiment. Proteins displayed in the table came under four categories: Z-disc proteins, filamin C interactors, HCM-associated proteins and proteins involved in chaperone-assisted selective autophagy. HCM, hypertrophic cardiomyopathy.

Z-disc proteins	Filamin C Interactors	HCM-associated proteins	Chaperone-assisted selective autophagy
Titin (TTN)	Myopodin (SYNPO2)	FHL1, FHL2	Heat shock proteins (HSPs, HSPBs)
Alpha actinin (ACTN2)	Myotilin (MYOT)	ACTA1	Cochaperones: CHIP, STIP1, BAG3
Muscle LIM Protein (MLP)	Aciculin (PGM5)	MYH7	Transcriptional co-activators: YAP, TAZ
Myopalladin	Xin actin-binding protein (XIRP1/2)	ANKRD1/2 (CARP)	Autophagy-related: NBR1, LC3, p62, LATS
Z-disc stability: ZASP, Cypher, FATZ	Filamin interacting protein (FILIP-1)	RCAN (DSCR1)	Alpha crystallin B (CRYAB)

3.3 Results

3.3.1 Assessing the baseline cardiac phenotype of heterozygous and homozygous mice

The cardiac phenotype of heterozygous (Het) and homozygous (Hom) *Flnc* W2165C mice was assessed relative to their wild-type (WT) littermates by echocardiography and gravimetry. Data derived from both male and females were combined for this section.

At baseline, Hom *Flnc* W2165C mice displayed no significant trend in systolic function with fractional shortening unchanged (WT = 30.1±0.9 %; Hom = 28.9±1.1 %) (Table 3-2). Left ventricular volumetric dimensions did not appear to be affected at systole or diastole (Table 3-2). Interestingly, the mean corrected left ventricular mass was lower in the HCM-associated Hom mutant mice (97±4 mg) than in WT (101±3 mg) and Het (102±3 mg) mice, though this was not significant. When the heart weight was corrected to tibia length, the heart weight and ventricular weight was significantly reduced in Hom mice (HW/TL, 7.80±1.42 mg/mm; VW/TL 5.93±01.08 mg/mm) compared to WT mice (HW/TL, 8.70±1.47 mg/mm; 6.57±1.18 mg/mm). Atrial weight relative to tibia length was significantly increased in Hom mice (WT = 0.42±0.09 mg/mm; Hom = 0.48±0.09 mg/mm).

Table 3-2 Echocardiographic and gravimetry parameters of WT, Het and Hom W2165C mouse hearts at baseline at 3 months. Asterisks are shown if significant relative to WT ($p<0.05$, *). Parameters shown as a mean ± SEM, at 3 months old. All parameters underwent a one-way ANOVA, except for gravimetry results which underwent an unpaired t test. Abbreviations: LVID.D, left ventricular internal diameter end-diastole; LVID.S, left ventricular internal diameter end-systole; LVAW.D, left ventricular anterior wall thickness end-diastole; LVAW.S, left ventricular anterior wall thickness end-systole; LVPW.D, left ventricular posterior wall thickness end-diastole; LVPW.S, left ventricular posterior wall thickness end-systole; LV mass AW corr, left ventricular mass corrected to anterior wall thickness; LV vol.D, left ventricular volume end-diastole; LV vol.S, left ventricular volume end-systole; HW/TL, heart weight/tibia length ratio; BW/TL, body weight/tibia length; VW/TL, ventricular weight/tibia weight; AW/TL, atrial weight/tibia length; SEM, standard error of the mean.

		3 months		
		WT	**Het**	**Hom**
Number	n	19	29	21
Body weight	g	24.5±0.7	24.4±0.5	23.9±0.6
Heart rate	bpm	462±6	466±5	470±3
Baseline				
Fractional shortening	%	30.1±0.9	29.1±0.9	28.9±1.1
LVID.D	mm	3.92±0.05	3.91±0.05	3.82±0.05
LVID.S	mm	2.74±0.06	2.78±0.07	2.73±0.06
LVAW.D	mm	0.84±0.03	0.85±0.02	0.80±0.02
LVAW.S	mm	1.29±0.02	1.28±0.03	1.23±0.03
LVPW.D	mm	0.88±0.02	0.89±0.02	0.92±0.03
LVPW.S	mm	1.23±0.03	1.22±0.03	1.25±0.04
LV mass AW corr	mg	101±3	102±3	97±4
LV vol.D	µl	67±2	67±2	63±2
LV vol.S	µl	28±2	29±2	28±2
Gravimetry				
HW/TL	mg/mm	8.70±1.47	-	7.80±1.42 *
BW/TL	mg/mm	1.63±0.32	-	1.52±0.30
VW/TL	mg/mm	6.57±1.18	-	5.93±1.08 *
AW/TL	mg/mm	0.42±0.09	-	0.48±0.09 *

3.3.2 Assessing the cardiac phenotype of heterozygous and homozygous mice under hypertensive stimulation

Body weight and heart rate remained consistent across genotypes both under saline and Ang-II treatment (Table 3-3). Ang-II challenge was designed to increase mechanical demand via pressure overload.

3.3.2.1 Assessing the cardiac phenotype of heterozygous and homozygous mice under hypertensive stimulation

In the presence of chronic hypertensive stimulation by Ang-II for 2 weeks (1.1mg/kg per day, osmotic pump), Het and Hom mice displayed a significant hypertrophic response to Ang-II compared to the WT as indicated by LV mass differences between saline and Ang-II treatment (WT = +27mg, Het = +39mg, Hom =+42mg) (Table 3-3). When the heart weight was corrected to tibia length, all mice treated with Ang-II had increased heart weights.

All left ventricular wall thickness and internal diameter measurements trended towards an increase when mice were exposed to Ang-II relative to saline treated mice. This reached significance in LV posterior wall thickness end-diastole (LVPW.D) (Het and Hom vs WT) and LV anterior wall thickness end-diastole (LVAW.D (Het vs WT).

Fractional shortening trended towards reduction in both WT (28.4% → 19.4%) and mutant hearts (Het, 29.7%→ 23.4%; Hom, 25.7% → 20.0%) in response to hypertensive stimulation. Left ventricular volume end of systole was also increased in Ang-II mice, correlating with reduced fractional shortening percentages, indicating a trend towards impaired systolic function in Ang-II treated mice.

Table 3-3 Echocardiographic and gravimetry parameters of WT, Het and Hom W2165C saline and Ang-II treated mouse hearts at 3 months. Parameters shown as a mean ± SEM and underwent a two-way ANOVA. Abbreviations: LVID.D, left ventricular internal diameter end-diastole; LVID.S, left ventricular internal diameter end-systole; LVAW.D, left ventricular anterior wall thickness end-diastole; LVAW.S, left ventricular anterior wall thickness end-systole; LVPW.D, left ventricular posterior wall thickness end-diastole; LVPW.S, left ventricular posterior wall thickness end-systole; LV mass AW corr, left ventricular mass corrected to anterior wall thickness; LV vol.D, left ventricular volume end-diastole; LV vol.S, left ventricular volume end-systole; HW/TL, heart weight/tibia length ratio; BW/TL, body weight/tibia length ratio. Asterisks are shown if significant relative to WT of the same treatment. # is shown if significance is found between treatments Sal vs Ang-II in the same genotype.

		Saline			**Ang-II**		
		WT	**Het**	**Hom**	**WT**	**Het**	**Hom**
Number	n	8	15	9	11	14	12
Body weight	g	25.9±0.9	25.9±0.7	25.5±1.1	25.1±0.7	25.0±0.6	23.9±0.6
Heart rate	bpm	484±4	477±6	484±8	486±6	482±6	484±5
Fractional shortening	%	28.4±2.2	29.7±1.4	25.7±1.5	19.4±2.6	23.4±2.2	20.0±1.8
LVID.D	mm	4.02±0.08	3.84±0.07	3.80±0.13	3.92±0.09	3.84±0.08	4.07±0.07
LVID.S	mm	2.88±0.12	2.69±0.08	2.83±0.13	3.17±0.15	2.95±0.11	3.26±0.11
LVAW.D	mm	0.81±0.03	0.86±0.03	0.81±0.03	0.97±0.03	1.06±0.05 ###	0.95±0.05
LVAW.S	mm	1.24±0.06	1.33±0.04	1.23±0.04	1.32±0.06	1.47±0.05	1.35±0.06
LVPW.D	mm	0.80±0.03	0.89±0.04	0.98±0.04	1.02±0.03	1.14±0.07 ###	1.16±0.06 #
LVPW.S	mm	1.14±0.05	1.26±0.05	1.27±0.06	1.24±0.02 *	1.43±0.06	1.34±0.06
LV mass	mg	97±6	100±5	101±6	124±8	139±8 ###	143±8 ##
LV vol.D	µl	71±3	64±3	63±5	67±4	64±3	73±3
LV vol.S	µl	32±3	27±2	31±3	41±4	35±3	44±3
Gravimetry							
HW/TL	mg/mm	7.2±0.1	7.2±0.1	7.0±0.2	9.1±0.5 ##	9.3±0.3 ####	8.6±0.4 ##
BW/TL	mg/mm	1.46±0.04	1.44±0.03	1.37±0.02	1.52±0.05	1.56±0.05 #	1.48±0.06 #

3.3.3 Assessing the gender-based differences in cardiac phenotype in the presence of the FLNC variant

Studies have reported significant sex differences in the cardiac phenotype that is observed in genetically modified mice (206). With both sexes included, this might disguise sex-related differences in the cardiac response therefore sexes were separated and compared in the following figures (Figure 3-1 to Figure 3-4).

3.3.3.1 Gravimetry

When separating female and male mice, significant Ang-II differences emerged in corrected heart weight tibia length (Figure 3-1), though differences in genotype were not present in left ventricular mass. All Ang-II treated males had an increased heart weight to body weight ratio, whereas this only reached significance in Ang-II Het female mice. Interestingly, mutant male mice had a greater reduction in body mass (relative to tibia length) in response to Ang-II than WT male mice (Figure 3-1).

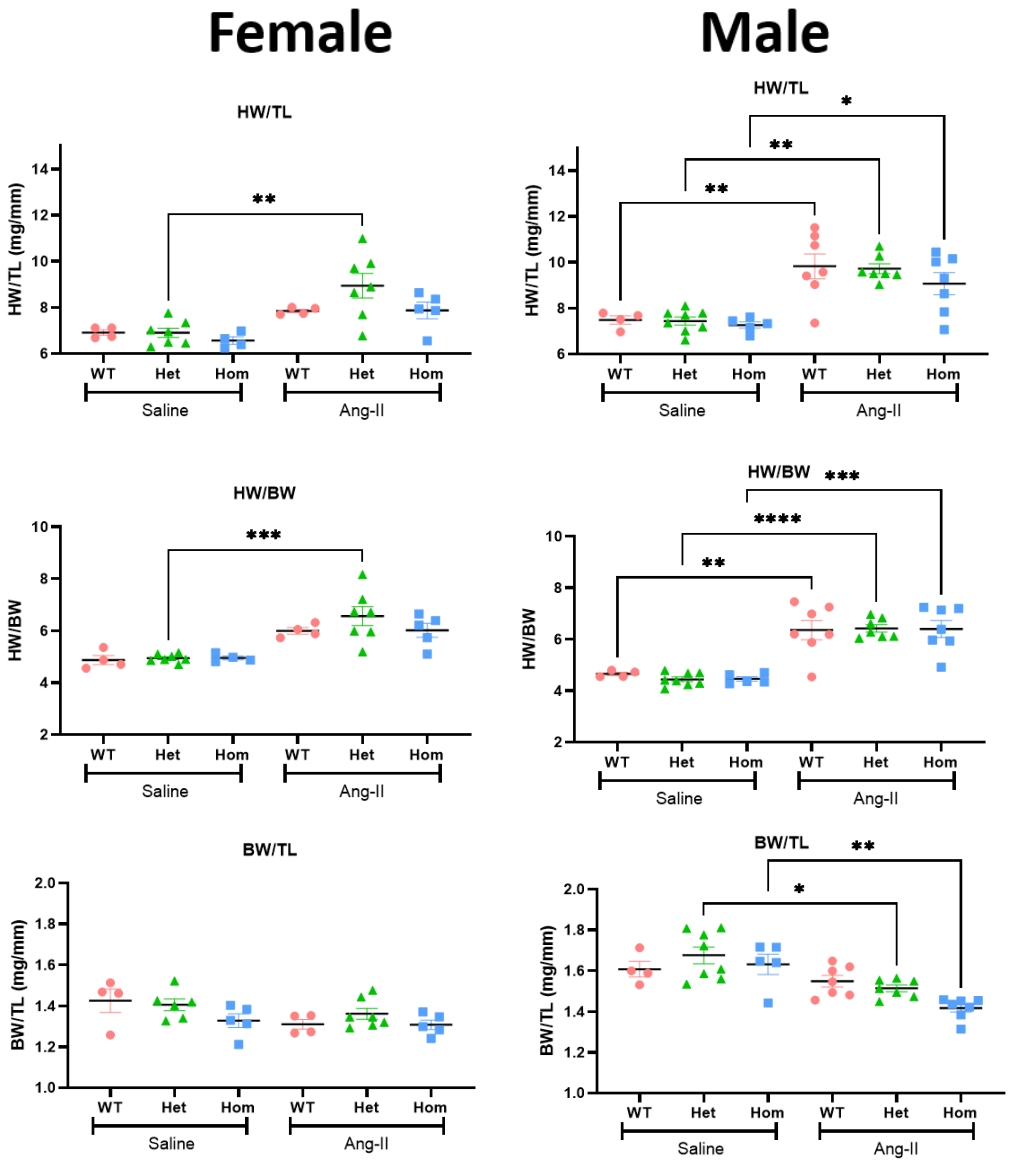

Figure 3-1 Comparing the corrected heart and body weights when treated with saline or Ang-II. The data displayed separates both female and male data. Hearts were investigated at 3-months old, n=4-7 per group. 2-way ANOVA multiple comparisons test was conducted on normally distributed samples. Significant changes are observed in the hearts of W2165C mice ($p<0.05$, *; $p<0.01$, **; $p<0.001$, ***, $p<0.0001$, **** versus WT). Abbreviations: HW/TL, heart weight/tibia length ratio; HW/BW, heart weight/body weight ratio; BW/TL, body weight/tibia length ratio.

3.3.3.2 Dimensions, wall thicknesses and fractional shortening

In both sexes, the left ventricular wall thicknesses showed varied genotype effects when treated by Ang-II as seen in Figure 3-2. There were no significant trends observed in fractional shortening, though relative to females, the males had a larger percentage drop in Ang-II treatment compared to saline (Figure 3-2). No differences in internal diameters were observed in either female or male mice, regardless of treatment.

The LVAW.d increased significantly in Ang-II treated Het female mice but did not reach significance in any other parameters (Figure 3-3). The LVPW.d measurements showed an increasing trend when under Ang-II treatment, but this only reached significance in Het female mice (Figure 3-3).

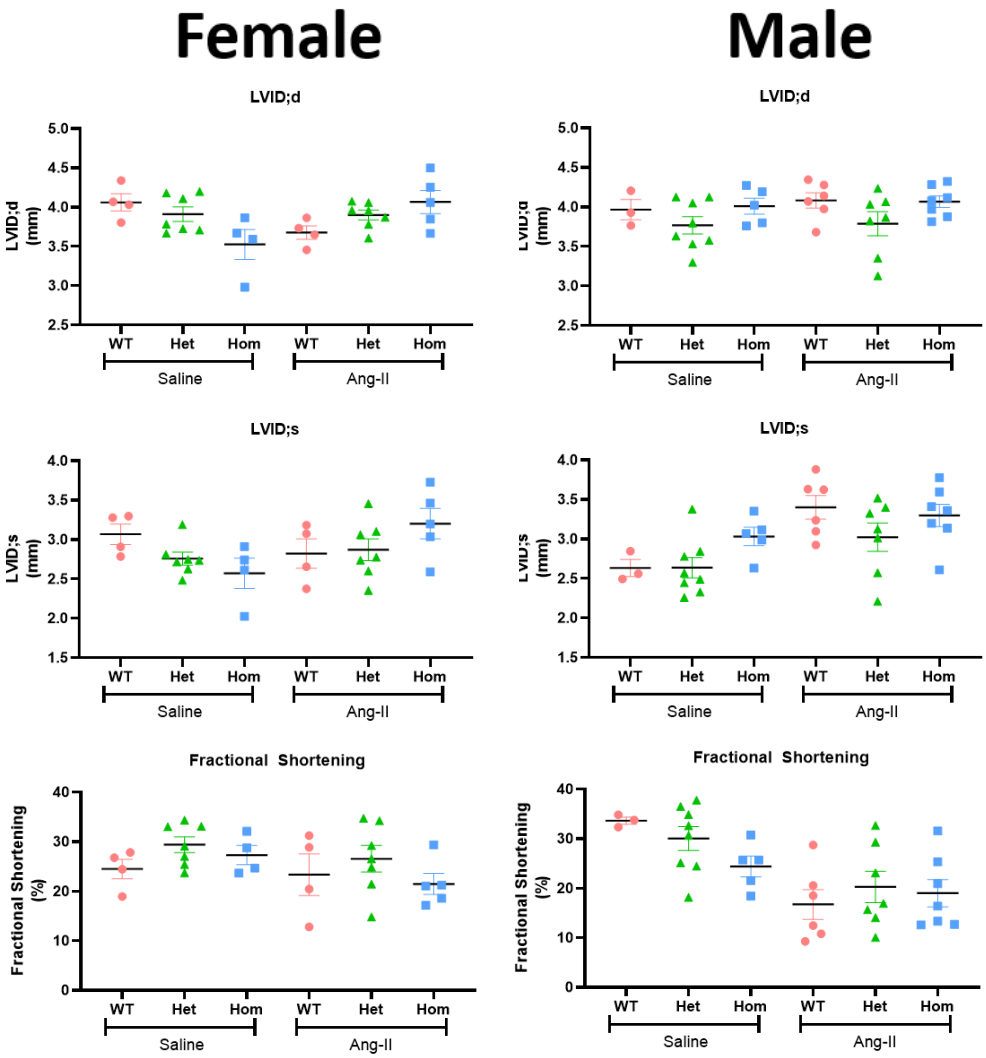

Figure 3-2 Comparing the internal diameters and fractional shortening of the left ventricle during diastole and systole when treated with saline or angiotensin-II. The data displayed separates both female and male data. Hearts were investigated at 3-months old, n=3-7 per group. 2-way ANOVA multiple comparisons test was conducted on normally distributed samples. Significant changes are observed in the hearts of W2165C mice ($p<0.05$, *; $p<0.01$, **; $p<0.001$, ***, $p<0.0001$, **** versus WT). Abbreviations: LVID.D, left ventricular internal diameter end-diastole; LVID.S, left ventricular internal diameter end-systole.

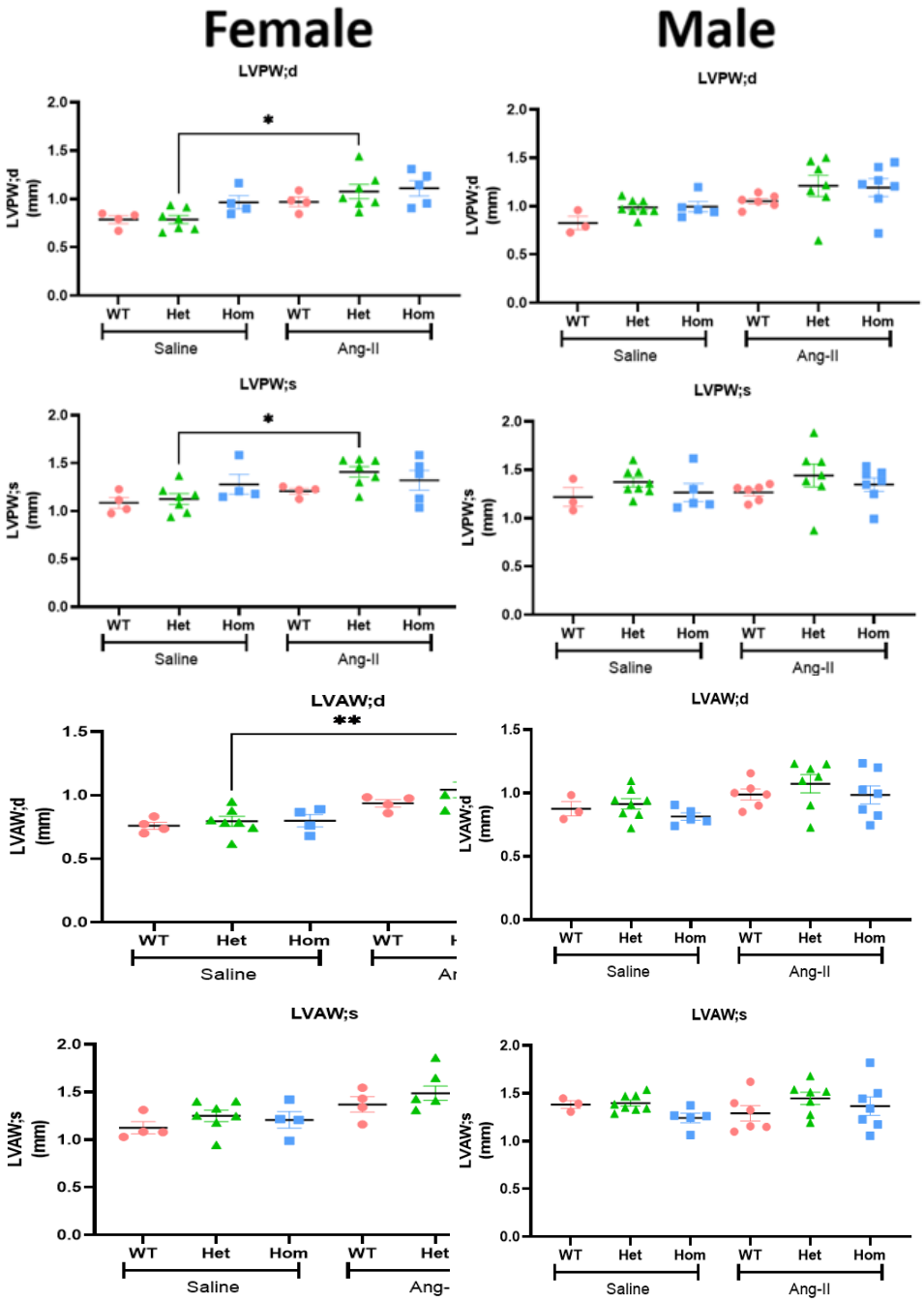

Figure 3-3 Left ventricular wall thicknesses during diastole and systole when treated with saline or angiotensin-II. The data displayed separates both female and male data. Hearts were investigated at 3-months old, n=4-7 per group. 2-way ANOVA multiple comparisons test was conducted on normally distributed samples. Significant changes are observed in the hearts of W2165C mice ($p<0.05$, *; versus WT). Abbreviations: LVPW.D, left ventricular posterior wall thickness end-diastole; LVPW.S, left ventricular posterior wall thickness end-systole; LVAW.D, left ventricular anterior wall thickness end-diastole; LVAW.S, left ventricular anterior wall thickness end-systole.

3.3.3.3 Volumes and left ventricular mass

Left ventricular volumes in diastole and systole showed no trends between genotype or treatment (Figure 3-4). There was a positive non-significant treatment- female mice, though there was a significant increase between saline and related trend in corrected LV mass for male mice (Figure 3-4). The same is true for Ang-II treated Het mice.

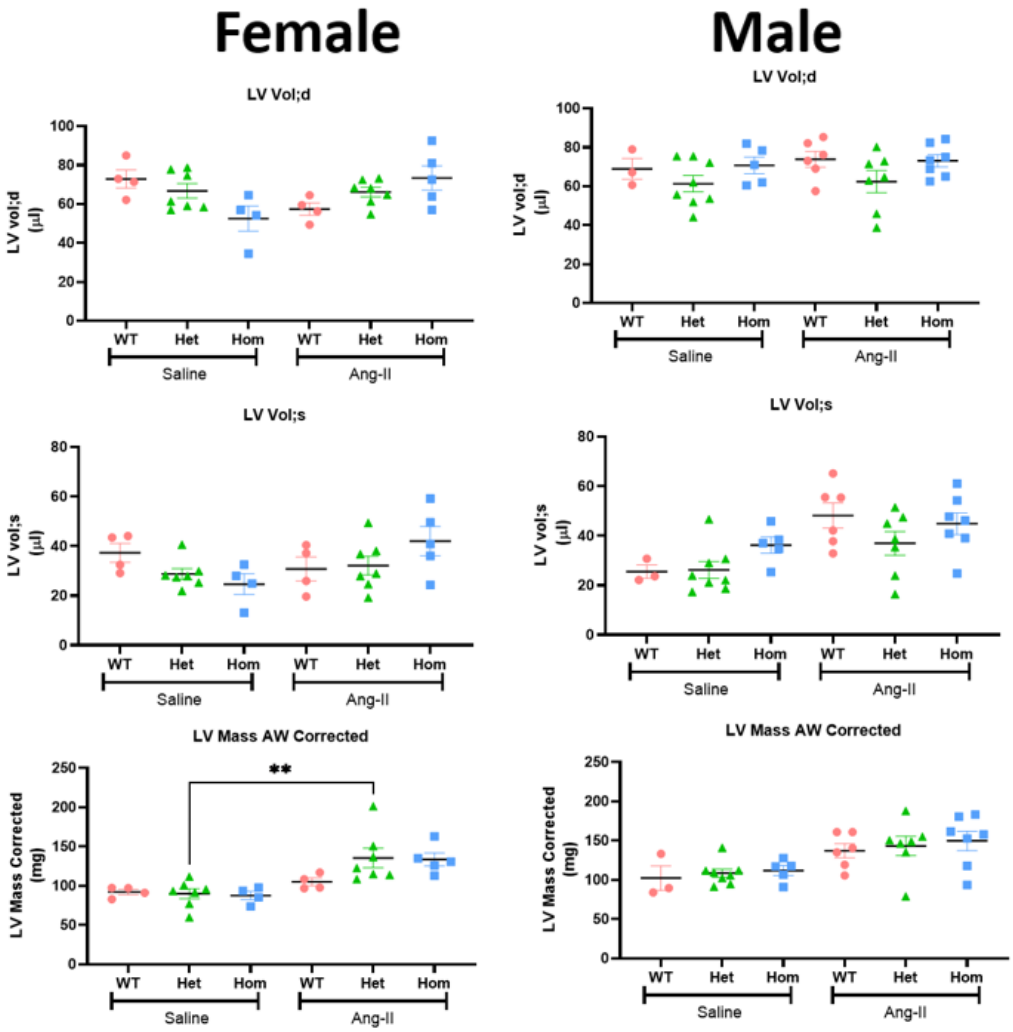

Figure 3-4 Comparing the left ventricular wall volume during diastole and systole and the corrected LV mass when treated with saline or angiotensin-II. The data displayed separates both female and male data. Hearts were investigated at 3-months old, n=4-7 per group. 2-way ANOVA multiple comparisons test was conducted on normally distributed samples. Significant changes are observed in the hearts of W2165C mice ($p<0.01$, **; versus WT). Abbreviations: LV vol.D, left ventricular volume end-diastole; LV vol.S, left ventricular volume end-systole; LV, left ventricular.

3.3.4 Proteomics profiling and pathway analysis of whole heart tissue in mutant mice

The goal of performing liquid chromatography mass spectrometry (LC-MS) of WT and Hom murine ventricular tissue was to identify proteins which were differentially expressed, here known as differentially expressed proteins (DEPs). LC-MS on both membrane- and myofilament-enriched samples (n = 6 per group: 3 male, 3 female) revealed a number of proteins to be significantly expressed differentially between WT and mutant mouse hearts that met the fold-change cut-off criteria (>2) described in methods.

3.3.4.1 Validation of fractionation

Immunoblot validation was needed to confirm that the subcellular fractionation was successful prior to the LC-MS experiment. The detergent-based subcellular fractionation approach on ventricular tissue was chosen to highlight any protein redistribution and increase detection coverage of complex samples during detection. The protocol resulted in 3 subcellular fractions: cytosol-enriched fraction, membrane-enriched fraction and myofilament-enriched fragment (Figure 3-5).

As expected, the sarcomeric protein, α-actinin, appears to be expressed in both whole tissue and notably the myofilament-enriched fraction was present. γ-catenin, a membrane protein localised at adheren junctions, appears to be absent from all fractions except in the membrane-enriched fraction. As expected, the cytoplasmic protein, Gapdh, was found exclusively in the cytoplasmic-enriched fraction and whole tissue samples.

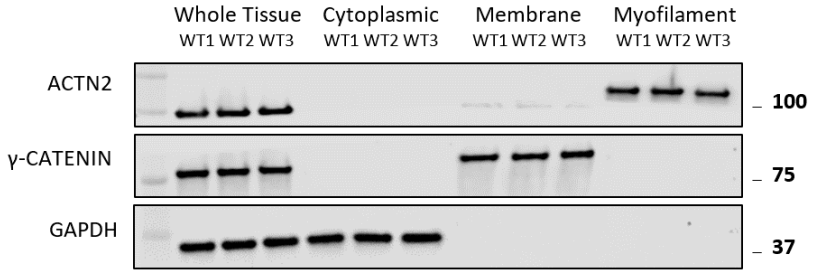

Figure 3-5 Protein expression of 14-week old WT mouse hearts after subcellular fractionation. α-actinin (ACTN2), γ-catenin and GAPDH were blotted due to their localisation to the myofilament, membrane and cytoplasmic fractions respectively.

3.3.4.2 Membrane-enriched fraction

In the membrane-enriched fraction 11 out of 850 total proteins were significant DEPs as according to the stringent FDR cut-off criteria described in *3.2.2.1* (Figure 3-6). In total 90 proteins were significant as according to the relaxed significance criteria.

Analyses of the significant membrane DEPs showed a reduced comparative abundance of mitochondrial proteins and an enrichment in filamin binding (Figure 3-6). 8 of the 9 comparatively downregulated DEPs were mitochondrial proteins: NADH dehydrogenase [ubiquinone] flavoprotein 1 (*Ndufv1*), NADH dehydrogenase [ubiquinone] 1 α subcomplex subunit 10 (*Ndufa10*), NADH dehydrogenase [ubiquinone] iron-sulfur protein 3 (*Ndufs3*), NADH dehydrogenase [ubiquinone] 1 subcomplex α subunit 3 (*Ndufa3*), NADH dehydrogenase [ubiquinone] 1 β subcomplex 5 (*Ndufab1*), ubiquinol-cytochrome C reductase core protein 2 (*Uqcrc2*), Apoptosis-inducing factor 1 (*Aifm1*), monoamine oxidase B (*Maob*). The 2 filamin-binding proteins, filamin-binding LIM protein 1 (*Fblim1*) and aciculin (*Pgm5*) were the only positively expressed DEPs in this comparison. The remaining DEP revealed in the Membrane-enriched fraction was reticulon 2 *(Rtn2*) found to be decreased in mutant mice.

Out of the pre-identified proteins (Table 3-1), 6 proteins (HCM: Calm1, Csrp3; FLNC-binding partner: Pgm5; Z-disc protein, Actn2; CASA, Bag3, Hspb2) were identified to be differentially expressed as according to the relaxed threshold (LogFC=+2, LogFDR=+1.301) with Pgm5 (aciculin) (LogFC=4.307, LogFDR = 3.28) being the only one to reach the strict thresholds (Table 3-4).

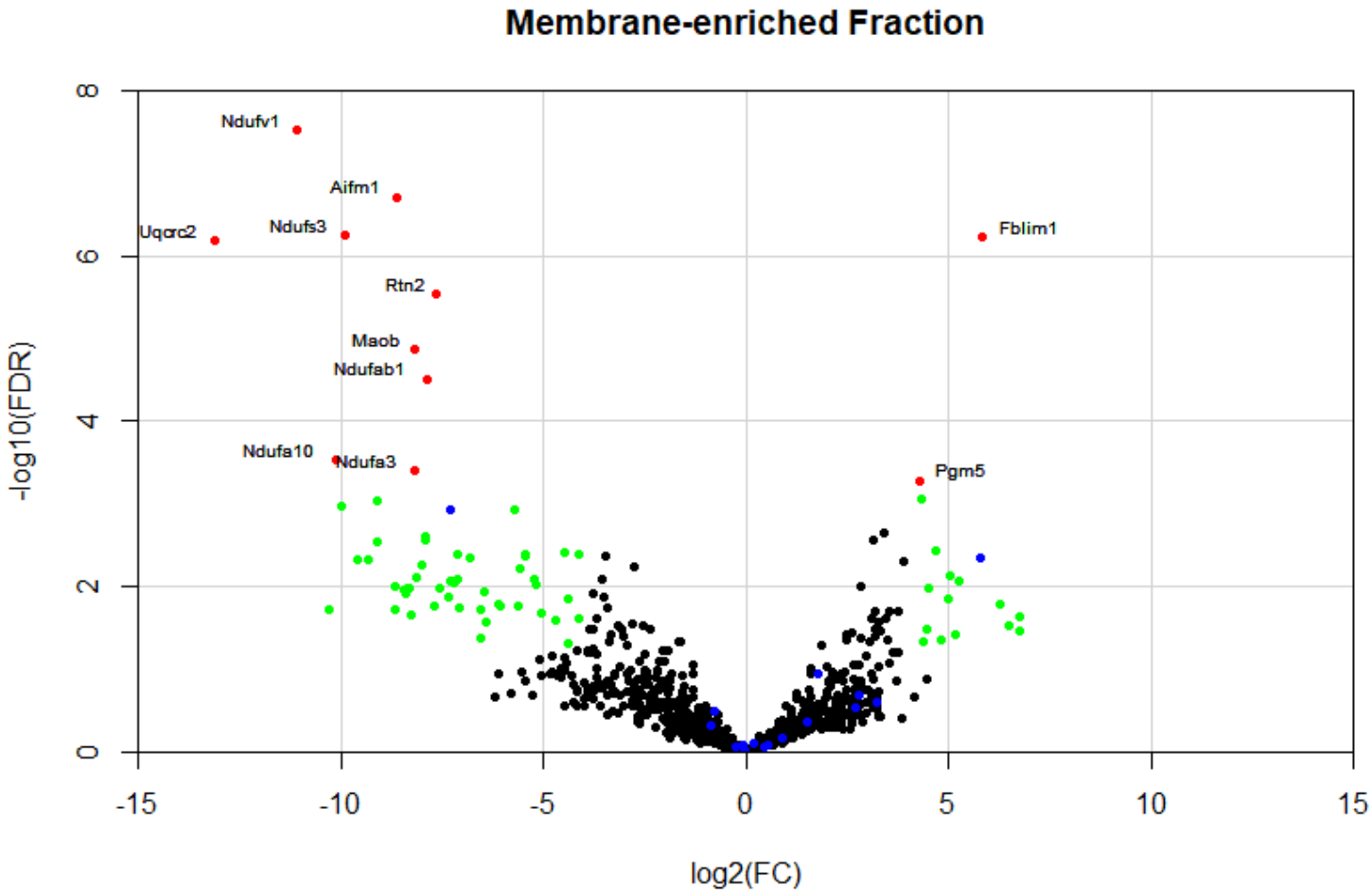

Figure 3-6 Volcano plot visualising unsupervised proteomics results of the membrane-enriched fraction comparing protein quantity between WT and mutant mouse hearts. At Difference = 0 it is expected that there is no difference between the WT and mutants. Data is taken from the membrane-enriched fraction, displaying 11 proteins to be significantly differentially expressed compared to the WT. Key: Significance = Red, Relaxed threshold = Green, Proteins of interest = Blue (as indicated in Table 1). n=6 per genotype.

Table 3-4 List of proteins down or upregulated in both the Membrane-enriched Fraction. Proteins were selected by their T-test fold change and -LogP value. The localisation, function and pathology association as according to Pubmed searches. Red highlighted protein symbols represent the proteins that Perseus data handling deemed significant as according to the BH-based false-discovery rate (FDR). Significant proteins as according to the relaxed criterion are highlighted in *italics*. Abbreviations: LQTS, long QT syndrome; MFM, myofibrillar myopathy; AD, Alzheimer's disease; PD, Parkinson's disease; T2DM, Type-2 diabetes mellitus; CHD, coronary heart disease;

Protein symbol	Protein Name	Expression location	Function	Pathology association	Interaction with Filamins	Log2 (Fold Change)	-log10 (FDR)	Ref
Significant proteins								
Ndufv1	Ubiquinone Oxidoreductase Core Subunit V1	Mitochondria	Mitochondrial respiration	Cardiomyopathy Leigh syndrome Leukodystrophy	No known direct interactions	-11.071	7.52	(207–209)
Aifm1	Apoptosis-inducing factor 1	Mitochondria	Regulates apoptosis Mitochondrial respiration	Cardiomyopathy MFM Mitochondrial disease	No known direct interactions	-8.627	6.71	(210–212)
Ndufs3	Ubiquinone Oxidoreductase Core Subunit S3	Mitochondria	Mitochondrial respiration	Leigh Syndrome Cancers	No known direct interactions	-9.903	6.26	(213,214)
Uqcrc2	Cytochrome b-c1 complex subunit 2	Mitochondria	Mitochondrial respiration	Mitochondrial diseases Cancers	No known direct interactions	-13.114	6.23	(215)
Ndfuab1	NADH-ubiquinone oxidoreductase complex subunit ab1	Mitochondria	Mitochondrial respiration	Mitochondrial diseases	No known direct interactions	-7.889	2.27	(207–209)
Ndufa10	NADH-ubiquinone oxidoreductase complex subunit a10	Mitochondria	Mitochondrial respiration	Mitochondrial diseases	No known direct interactions	-10.129	1.72	(216)
Ndufa3	NADH-ubiquinone oxidoreductase complex subunit a3	Mitochondria	Mitochondrial respiration	Mitochondrial diseases Cancer	No known direct interactions	-8.167	3.40	(217)
Rtn2	Reticulon 2	Endoplasmic reticulum	Intracellular vesicular transport	Spastic paraplegia MFM	Co-localised in MFM plaques	-7.637	5.54	(218)
Maob	Monoamine oxidase B	Mitochondria	Catabolises neuroactive amines	Heart failure AD & PD	No known direct interactions	-8.181	4.87	(219,220)

Fblim1	Filamin binding Lim protein 1 (Migfilin)	Cell-ECM and cell-cell adhesion sites	Interacts with filamin to aid integrin-cytoskeleton linkages	Cardiomyopathy Esophageal cancer	Interaction at the N terminal domain	5.847	6.23	(76,221,222)
Pgm5	Aciculin	Cell junctions	Myofibril assembly and maintenance	Liver cancer	Interaction in ICD and Z-discs	4.307	3.28	(113,223,224)
Proteins of interest								
Acta1	Actin alpha-1	Cytoplasm	Actin cross-linking	Cardiomyopathy MFM	No known direct interactions	1.776	0.94	(225)
Actn2	Alpha-actinin 2	Z-disc	Crosslinks actin and titin from Z-disc	Cardiomyopathy	Interaction via myopodin at Ig20-21	-7.284	2.93	(91,226,227)
Bag3	Bcl2-associated athanogene 3	Cytosol Sarcomere	CASA co-chaperone for Hsp70 and Hsc70.	Skeletal and cardiac myopathies	Filamin C proteostasis	5.782	2.34	(228,229)
Calm1	Calmodulin-1	Skeletal muscle	Calcium – binding messenger protein. Controls Ca across SR thus affects contraction	Arrhythmia Long QT syndrome	Regulates filamin-actin binding	-5.701	2.93	(230–232)
Capza2	Capping actin protein of muscle Z-line subunit alpha 2	Z-disc	Actin network maintenance	Neurodevelopmental	No known direct interactions	-0.884	0.32	(233)
Capzb	Capping actin protein of muscle Z-line subunit beta	Z-disc	Actin network maintenance	Cardiomyopathy	No known direct interactions	-0.238	0.06	(234)
Cryab	Crystallin alpha B	Cytosol Sarcomere	Molecular chaperone activity Cardioprotection	MFM Cardiomyoapthy Cataracts Neurodegeneration	Interaction found in Drosophila	0.4644	0.05	(137,235)
Csrp3	Muscle LIM Protein	ICD	Positive regulator of myogenesis	Cardiomyopathy	No known direct interactions	6.767	1.47	(55,236,237)
Fhl2	Four and a half LIM domains 2	Myocardium	Anti-hypertrophic adaptor	Cardiomyopathy	No known direct interactions	2.700	0.54	(238)
Gja1	Connexin-43	ICD	Intercellular communication	Arrhythmia, DCM	Enhance actin network	0.802	0.14	(239,240)

Hspb1	Heat shock protein beta 1	Cytosol Sarcomere	Molecular chaperone activity Cardioprotection	Neuropathy Cardiomyopathy MFM	Interaction at Ig18-21	2.767	0.69	(241–243)
Hspb2	Heat shock protein beta 2	Cytosol Sarcomere	Molecular chaperone activity Cardioprotection	Mitochondrial disease	Interaction at Ig24	3.395	2.65	(244,245)
Hspb7	Heat shock protein beta 7	Cytosol Sarcomere	Cardiac development	Cardiomyopathy	Interaction at Ig24	1.503	0.36	(133,246)
Hspb8	Heat shock protein beta 8	Cytosol Sarcomere	Cardioprotection Molecular chaperone activity	Cardiomyopathy Motor neuropathy	Filamin C proteostasis	-0.786	0.49	(247)
Hspa8	Heat shock protein family A member 8	Cytosol Sarcomere	Molecular chaperone activity	CHD Immune disorders Myopathy	Filamin C proteostasis	3.220	0.58	(248)
Ldb3	LIM domain binding 3	Sarcomere	Z-disc structural integrity	MFM Cardiomyopathy	Interacts at mechano-sensing domain	0.540	0.07	(249)
Nebl	Nebulin	Sarcomere	Actin-binding protein	Cardiomyopathy	Interaction at Ig20-24	-0.094	0.08	(250)
Stip1	Stress-induced-phosphoprotein 1 (Hsp70/Hsp90-organising protein)	Nucleus Cytosol	Regulates chaperones	Cardiomyopathy	No known direct interactions	-0.048	0.01	(251)
Ttn	Titin	Sarcomere	Structural support	Cardiomyopathy	Enhance sarcomere stability	0.908	0.17	(92,106,252)
Xirp1	Xin-actin binding repeat-containing protein 1	ICD	Protects actin filaments from depolymerisation	Cardiomyopathy	Interaction at Ig20-21	0.211	0.09	(87,113,253)

3.3.4.3 Myofilament-enriched fraction

Data from the Myofilament-enriched fraction found 10 significant DEPs (out of a total of 681 proteins) which met the stringent cutoff criteria to be considered significantly different in mutant mice compared to WT (Figure 3-7). When relaxing the significance criteria 46 proteins were classified as a significantly DEP. The results show enrichment of proteins involved in actin binding: filamin C (Flnc), myotilin (Myot), β-myosin heavy chain (Myh7), leiomodin-2 (Lmod2), synaptopodin-like protein 2 (Synpo2l) and α-II spectrin (Sptan1). In addition, many of the DEPs localise at the Z-disc Flnc, Myot, Myh7, Synpo2l, Sptan1, obscurin (Obscn) and ArgBP2 (Sorbs2). Cardiac gap junction protein, connexin-43 (Gja1) was the final DEP in the Myofilament-enriched fraction which was found downregulated.

Out of the pre-identified proteins (Table 3-1), 5 proteins (HCM: Csrp3, Fhl2; CASA: Hspb7; FLNC-binding protein: Synpo, Xirp1) were identified to be differentially expressed as according to the relaxed threshold (LogFC=2+, LogFDR=+1.301) (Table 3-5).

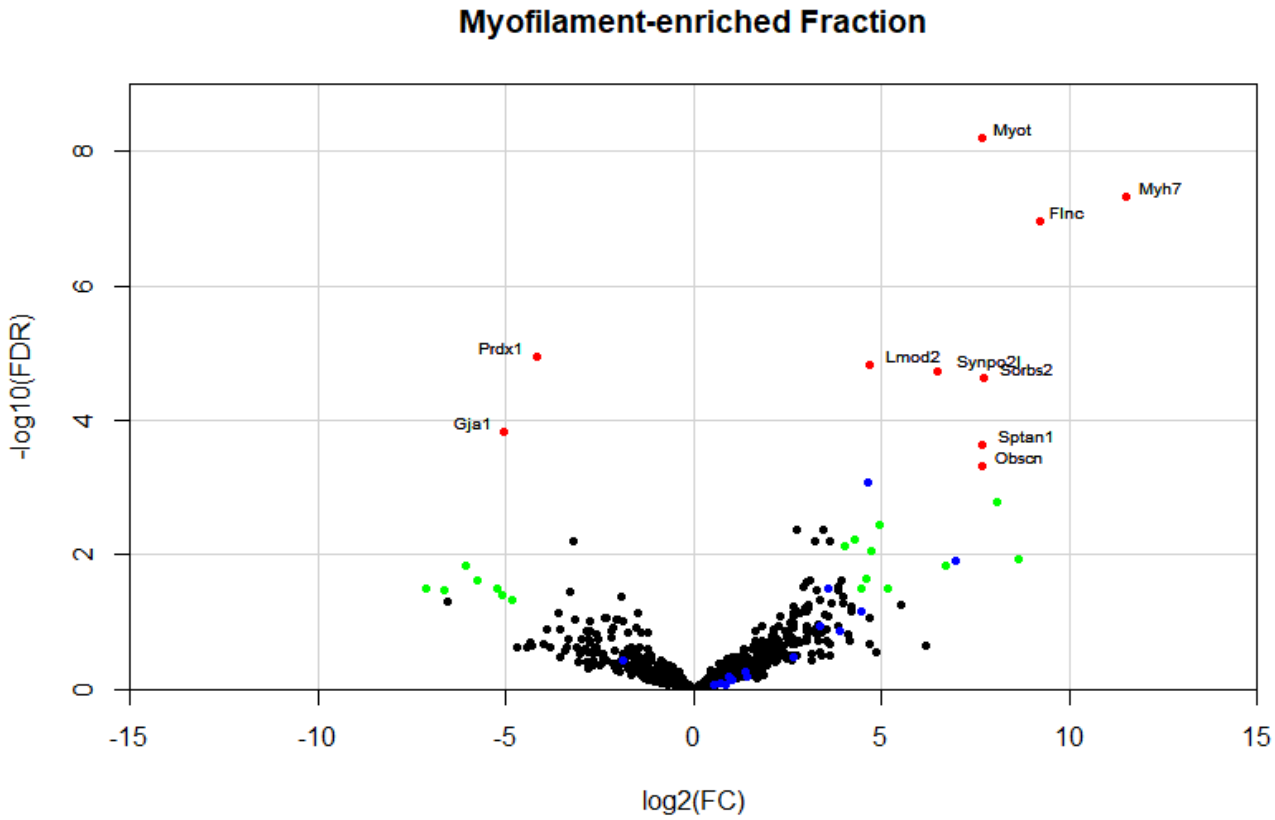

Figure 3-7 Volcano plot visualising unsupervised proteomics results of the myofilament-enriched fraction comparing protein quantity between WT and mutant mouse hearts. At Difference = 0 it is expected that there is no difference between the WT and mutants. Data is taken from the myofilament-enriched fraction, displaying 10 proteins to be significantly differentially expressed compared to the WT. Key: Significance = Red, Relaxed threshold = Green, Proteins of interest (as indicated in Table 1) = Blue. n=6 per genotype.

Table 3-5 List of proteins down or upregulated in both the Myofilament-enriched Fraction. Proteins were selected by their T-test fold change and -LogP value. The localisation, function and pathology association as according to Pubmed searches. Red highlighted protein symbols represent the proteins that Perseus data handling deemed significant as according to the BH-based false-discovery rate (FDR). Significant proteins as according to the relaxed criterion are highlighted in *italics*. Abbreviations: DCM, dilated cardiomyopathy; T2DM, type-2 diabetes mellitus; MFM, myofibrillar myopathy; ICD, Intercalated Disc.

Protein symbol	Protein Name	Expression location	Function	Pathology association	Interaction with Filamin C	Log2 (Fold Change)	-log10 (FDR)	Ref
Significant proteins								
Myh7	Myosin heavy chain 7	Z-disc	Actin-cross-linking, reorganising actin cytoskeleton	Skeletal myopathy Cardiomyopathy	Co-localised in the sarcomere	11.508	7.31	(254,255)
Flnc	Filamin C	Z-disc	Actin-cross-linking	Skeletal myopathy Cardiomyopathy	N/A	9.210	6.96	(98,100,136,137)
Myot	Myotilin	Z-disc	Actin network organisation	Skeletal myopathies	Direct interaction within the Z-disc	7.682	8.20	(256–258)
Sorbs2	Sorbin and SH3 Domains-containing Protein 2	Costamere	Cell adhesion and cytoskeletal formation	Cardiomyopathy Cancer	Co-localised in the ICD	7.738	4.63	(259)
Obscn	Obscurin	Sarcoere	Myofibrillogenesis of A-bands	Skeletal myopathy Cardiomyopathy Cancer	Co-localised in the Z-disc	7.664	3.32	(260,261)
Sptan1	Spectrin alpha chain	Cytoskeleton	Actin crosslinking and molecular scaffold.	Cardiac defects Encephalopathy	No known interactions	7.662	3.62	(262,263)
Synpo2l	Synaptopodin 2-like protein	Z-disc	Interacts with actin and alpha actinin proteins at Z-disc	Heart failure Atrial fibrillation	Interaction with actin filaments in the Z-disc	6.508	4.74	(264)
Lmod2	Leiomodin-2	Sarcomere	Actin filament regulation	DCM	No known direct interactions	4.680	4.83	(265)

Prdx1	Peroxiredoxin-1	Cytosol Nucleus	Cytoprotective antioxidant in the myocardium	Heart failure T2DM	No known direct interactions	-4.188	4.94	(266)
Gja1	Connexin-43	ICD	Intercellular communication	Arrhythmia, DCM	Enhance actin network	-5.050	3.83	(239,240)
Proteins of interest								
Acta1	Actin alpha-1	Cytoplasm	Actin cross-linking	Cardiomyopathy MFM	No known direct interactions	3.873	0.86	(225)
Actn2	Alpha-actinin 2	Z-disc	Crosslinks actin and titin from Z-disc	Cardiomyopathy	Interaction at Ig20-21	1.403	0.18	(91,226,227)
Bag3	Bcl2-associated athanogene 3	Cytosol Sarcomere	CASA co-chaperone for Hsp70 and Hsc70.	Skeletal myopathy Cardiomyopathy	Filamin C proteostasis	4.478	1.15	(228,229)
Capza2	Capping actin protein of muscle Z-line subunit alpha 2	Z-disc	Actin network maintenance	Neurodevelopmental	No known direct interactions	-1.860	0.43	(233)
Capzb	Capping actin protein of muscle Z-line subunit beta	Z-disc	Actin network maintenance	Cardiomyopathy	No known direct interactions	1.400	0.25	(234)
Cryab	Crystallin alpha B	Cytosol Sarcomere	Molecular chaperone activity Cardioprotection	MFM Cardiomyopathy Neurodegeneration	Interaction found in Drosophila	2.672	0.46	(137,235)
Csrp3	Muscle LIM Protein	ICD	Positive regulator of myogenesis	Cardiomyopathy	No known direct interactions	5.185	1.50	(55,236,237)
Fhl2	Four and a half LIM domains 2	Myocardium	Anti-hypertrophic adaptor	Cardiomyopathy	No known direct interactions	6.992	1.92	(238)
Hspb1	Heat shock protein beta 1	Cytosol Sarcomere	Molecular chaperone activity Cardioprotection	Neuropathy Cardiomyopathy MFM	Interaction at Ig18-21	0.942	0.19	(241–243)
Hspb6	Heat shock protein beta-6	Cytosol	Molecular chaperone activity	Heart failure AD	Indirect interaction via BAG3	2.450	0.53	(267)
Hspb7	Heat shock protein beta 7	Cytosol Sarcomere	Cardiac development	Cardiomyopathy CHD	Interaction at Ig24	4.640	3.07	(121,133,246,268)

Hspb8	Heat shock protein beta 8	Cytosol Sarcomere	Cardioprotection Molecular chaperone activity	Cardiomyopathy Motor neuropathy	Filamin C proteostasis	3.358	0.95	(247)
Hspa8	Heat shock protein family A member 8	Cytosol Sarcomere	Molecular chaperone activity	CHD Immune disorders Myopathy	Filamin C proteostasis	0.703	0.10	(248)
Ldb3	LIM domain binding 3	Cytosol Sarcomere	Z-disc structural integrity	MFM Cardiomyopathy	Interacts at mechano-sensing domain	0.354	0.08	(249)
Nebl	Nebulin	Cytosol Sarcomere	Actin-binding protein	Cardiomyopathy	Interaction at Ig20-24	0.543	0.07	(250)
Synpo	Myopodin	Z-disc	Actin binding	Cardiomyopathy MFM	Interaction with actin filaments in the Z-disc	4.611	1.65	(103,269)
Ttn	Titin	Sarcomere	Structural support	Cardiomyopathy	Enhances sarcomere stability	0.865	0.07	(92,106,252)
Xirp1	Xin-actin binding repeat-containing protein 1	ICD	Protects actin filaments from depolymerisation	Cardiomyopathy	Interaction at Ig20-21	3.570	1.50	(87,113,253)

3.3.4.4 Combined analysis

Individually the fraction-specific data provides useful information – however, the fractions within the cardiomyocyte do not function completely independently. Using the relaxed criteria threshold, proteins from both membrane (91 out of 850 proteins) and myofilament fractions (46 out of 681 proteins) which reached the relaxed criteria threshold were used for GO pathway enrichment analysis (Figure 3-8). A large proportion of downregulated membrane proteins that reached the relaxed criteria threshold were mitochondrial subunits and hence resulting in a negatively significant enrichment in activities related to the electron transport chain (ETC). When DEPs from both fractions were combined, a significant positive enrichment in sarcomere proteins and sarcomere-relative activities (SC) was observed. The remaining data displayed were grouped as "mixed function" (MF).

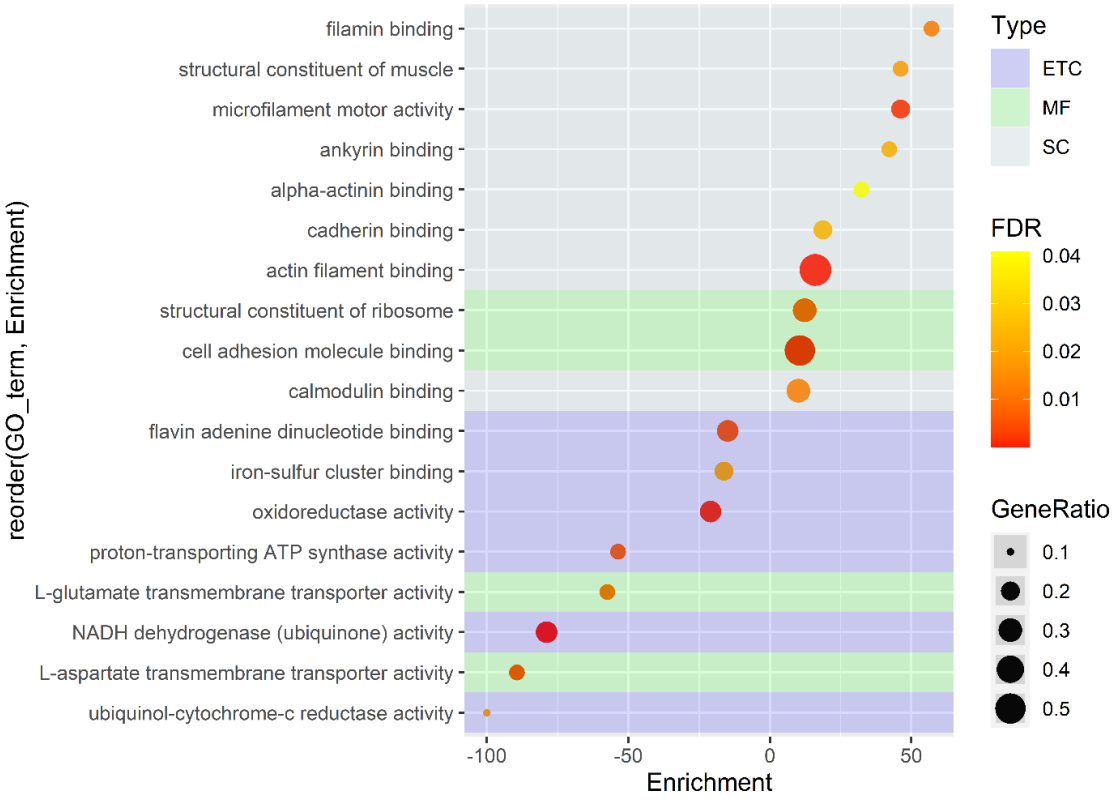

Figure 3-8 GO pathway enrichment analysis for proteomics hits based on the relaxed threshold. Y-axis represents the enriched GO terms; X-axis represents the enrichment of each activity. The colour and size of each bubble represents enrichment significance (FDR) and gene ratio. Each activity is coloured by functional type – ETC is electron transport chain. MF is mixed function, SC is sarcomere.

3.3.5 Validation of proteomics findings

Findings from the proteomics were validated by immunoblot. By performing immunoblots on targets in cytoplasmic, membrane and myofilament fractionated samples as well as whole tissue, additional information on whether DEPs were fraction-specific or globally changed were probed for.

3.3.5.1 Cytoplasmic fraction immunoblots

Although the cytoplasmic fraction did not undergo proteomics, the samples were used to understand if changes in protein abundance was fraction-specific. In the cytoplasm, Flnc was significantly upregulated, and Myot and Hspb7 showed no significant changes (Figure 3-9).

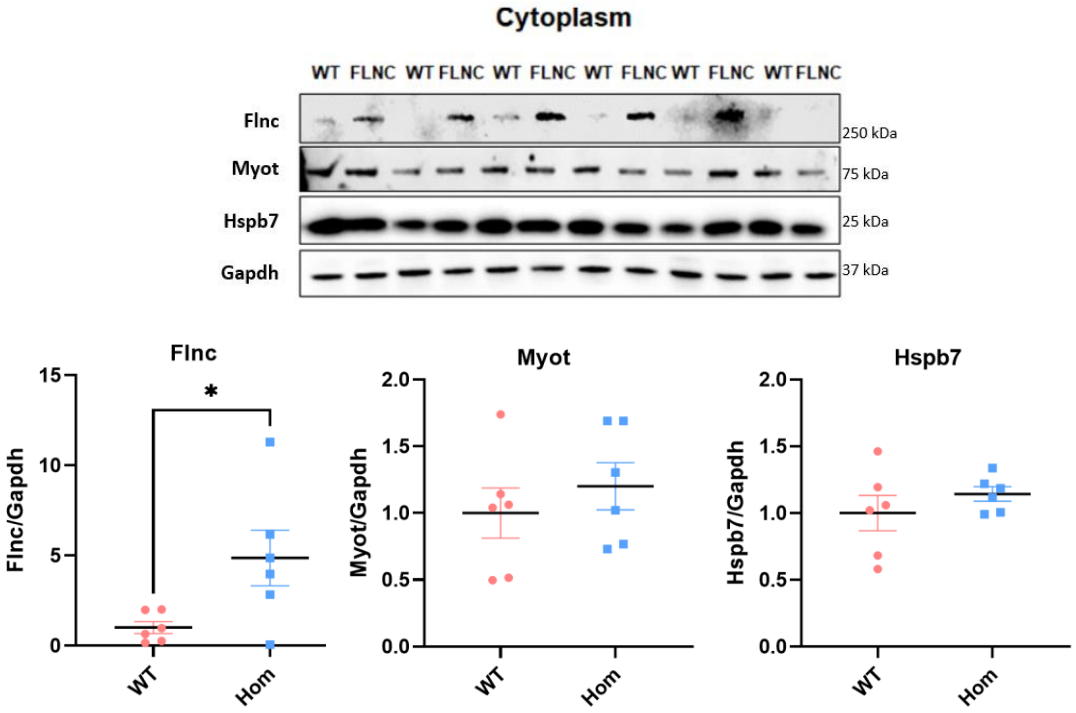

Figure 3-9 Immunoblotting and quantification of mouse tissue. Displayed are immunoblots conducted on the cytoplasmic fraction, normalised to Gapdh. Samples were normally distributed and underwent a t-test. ($p<0.05$, *; versus WT). n = 6 mice per genotype, 14-weeks old.

3.3.5.2 Membrane fraction immunoblots

Of the membrane proteins analysed, none had significantly different expression between WT and Hom samples (Figure 3-10). Aifm1, Uqcrc2, Ndufv1 and Fblim1 which were found to be differentially expressed to a significant degree, were unchanged when membrane fractions underwent immunoblotting. There were no visual trends observed in any of the parameters which reached significance in membrane-enriched fractionation (Figure 3-10).

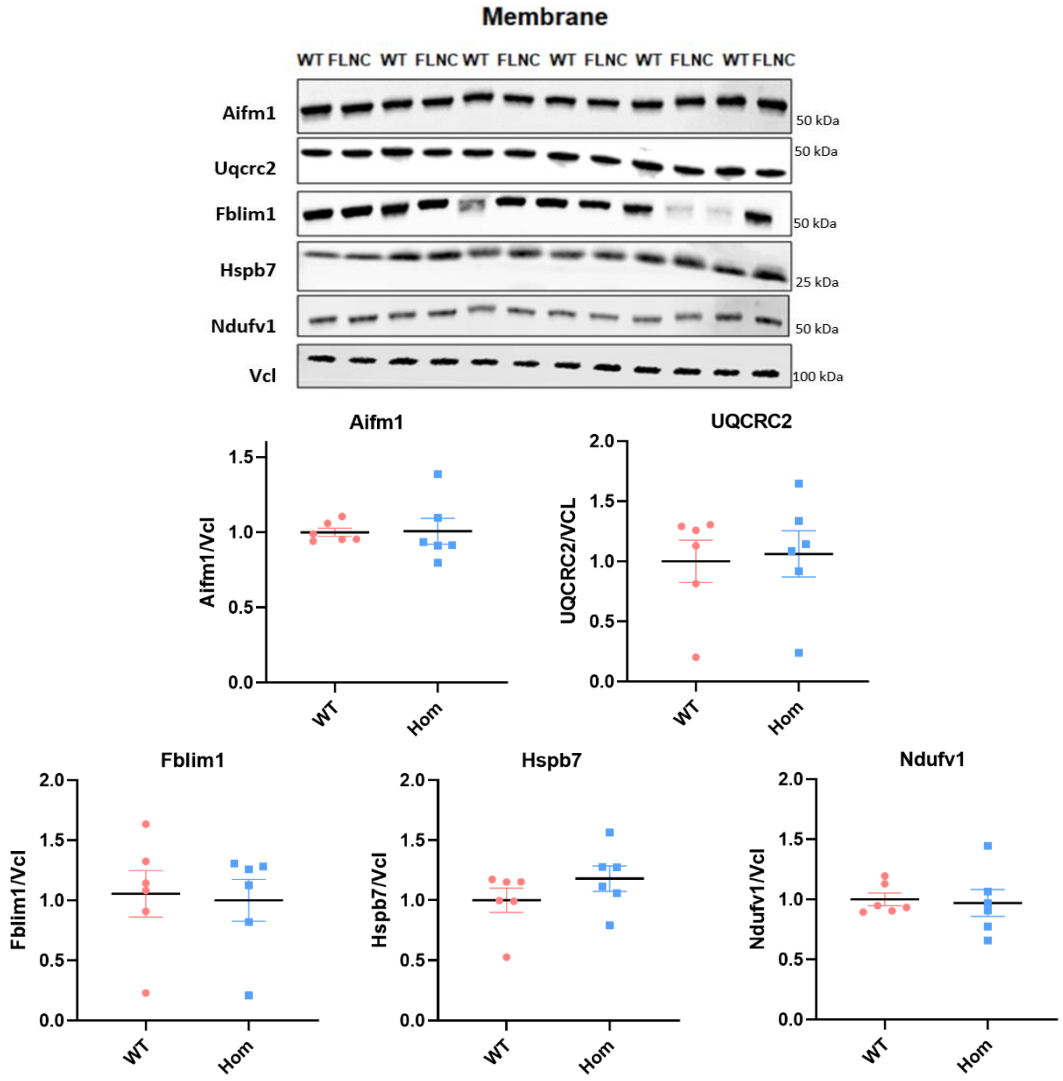

Figure 3-10 Immunoblotting and quantification of mouse tissue. Displayed are immunoblots conducted on the membrane fraction, normalised to Vcl, vinculin. Samples were normally distributed and underwent a t-test. n = 6 mice per genotype, 14-weeks old.

3.3.5.3 Myofilament fraction immunoblots

Consistent with the validation of subcellular fractionation, the sarcomere based filamin C was not found in the membrane fraction in WT or Hom tissue. In the myofilament fraction, Myot, and Myh7 were significantly upregulated, however, in contract to the proteomics findings there were no significant differences in FLNC expression in the myofilament immunoblots (Figure 3-11). Hspb7 was also found to be significantly upregulated.

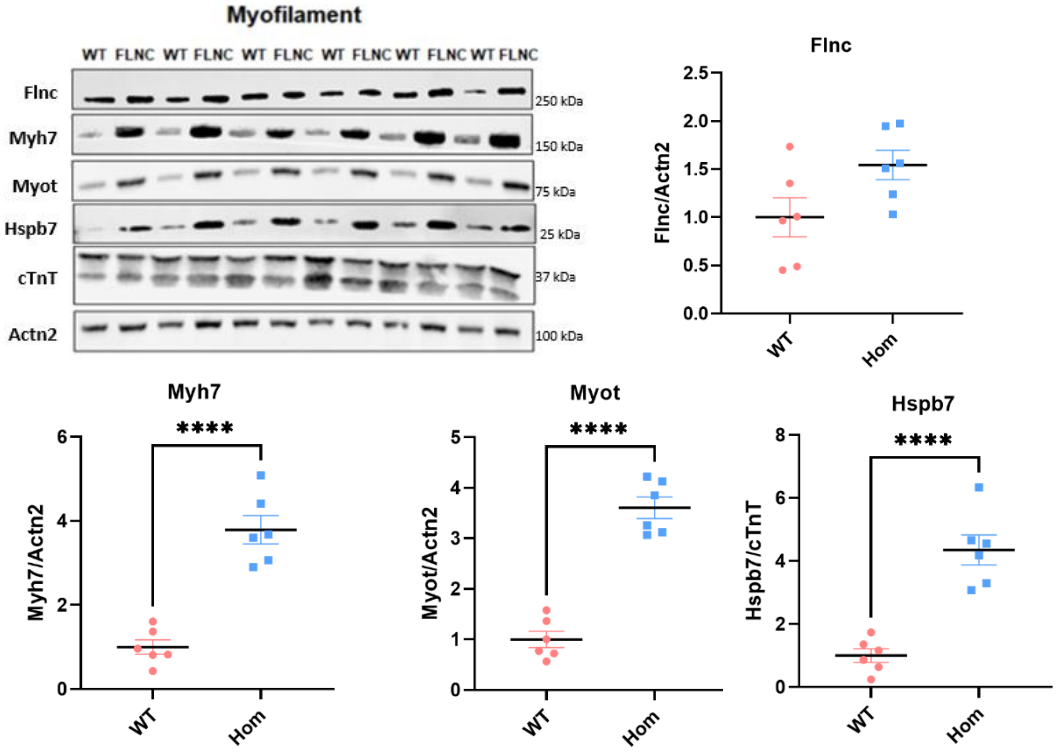

Figure 3-11 Immunoblotting and quantification of mouse tissue. Displayed are immunoblots conducted on the myofilament fraction, normalised to Actn2 except for HSPB7 which was normalised to cTnT. Samples were normally distributed and underwent a t-test. (<0.0001, **** versus WT). n = 6 mice per genotype, 14-weeks old.

3.3.5.4 Whole tissue immunoblots

Complementing the myofilament upregulations, in the whole tissue, Flnc, Myh7 and Myot were significantly upregulated. Both Flnc and Myh7 had negligible expression in the WT samples (at times undetectable) (Figure 3-12).

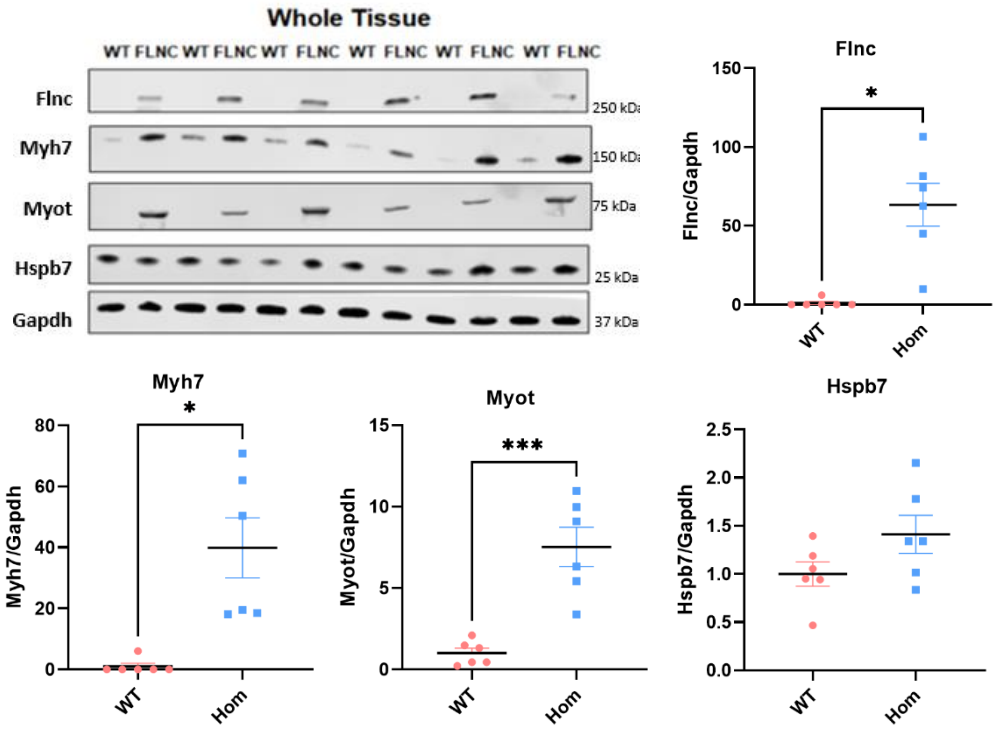

Figure 3-12 Immunoblotting and quantification of mouse tissue. Displayed are immunoblots conducted on whole tissue, normalised to Gapdh. Samples were normally distributed and underwent a t-test. ($p<0.05$, *; <0.001, *** versus WT). n = 6 mice per genotype, 14-weeks old

3.3.6 Analysis of protein localisation in cardiac muscle sections

In models of biomechanical stress, filamin C relocalises towards the intercalated disc and the Z-disc, both load-bearing sites (270). Frozen sections of ventricular tissue from WT and Hom mice were stained for the protein of interest (Flnc, Myot, Hspb1, Hspb7) and counterstained to visualise sarcomeric structures (F-actin) and either the Z-disc (Actn2) or the intercalated discs (γ-catenin).

In Hom hearts, Flnc was located at intercalated discs at a greater abundance than WT based on fluorescence intensity – consistent with previous studies of Flnc localisation (Figure 3-13) (107,156).

Sporadically, Myot was also found to localise towards the intercalated disc at a greater abundance in Hom mice but this was not omnipresent (Figure 3-14).

The localisation of Hspb7 was analysed in cardiac sections to test which heat shock protein associated with Flnc changed localisation in cardiac tissue (271–273). At the intercalated disc, Hspb7 was found at a relative greater abundance in Hom cardiac sections (Figure 3-15).

Both Flnc and Myot were shown to be expressed at the intercalated disc in both WT and Hom sections (Figure 3-16).

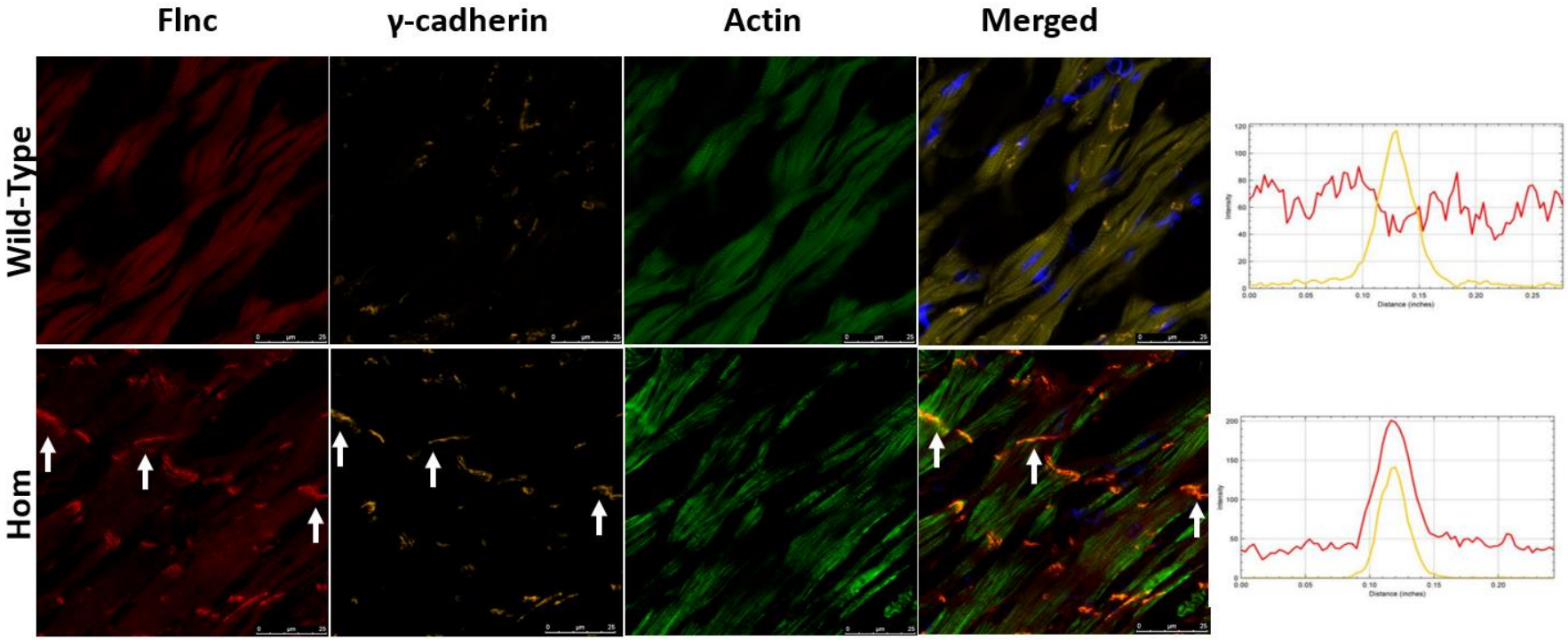

Figure 3-13 Frozen sections of ventricular tissue from WT and Hom *Flnc* W2165C mice with line intensity plots. Sections were stained for Flnc (rabbit, D1K3J) and counterstained to visualize sarcomeres (phalloidin 488) and intercalated discs (mouse, γ-cadherin 610154). FLNC is primarily localized at intercalated in the Hom tissue. Line intensity plots for WT and Hom displaying the fluorescence intensity for both channels

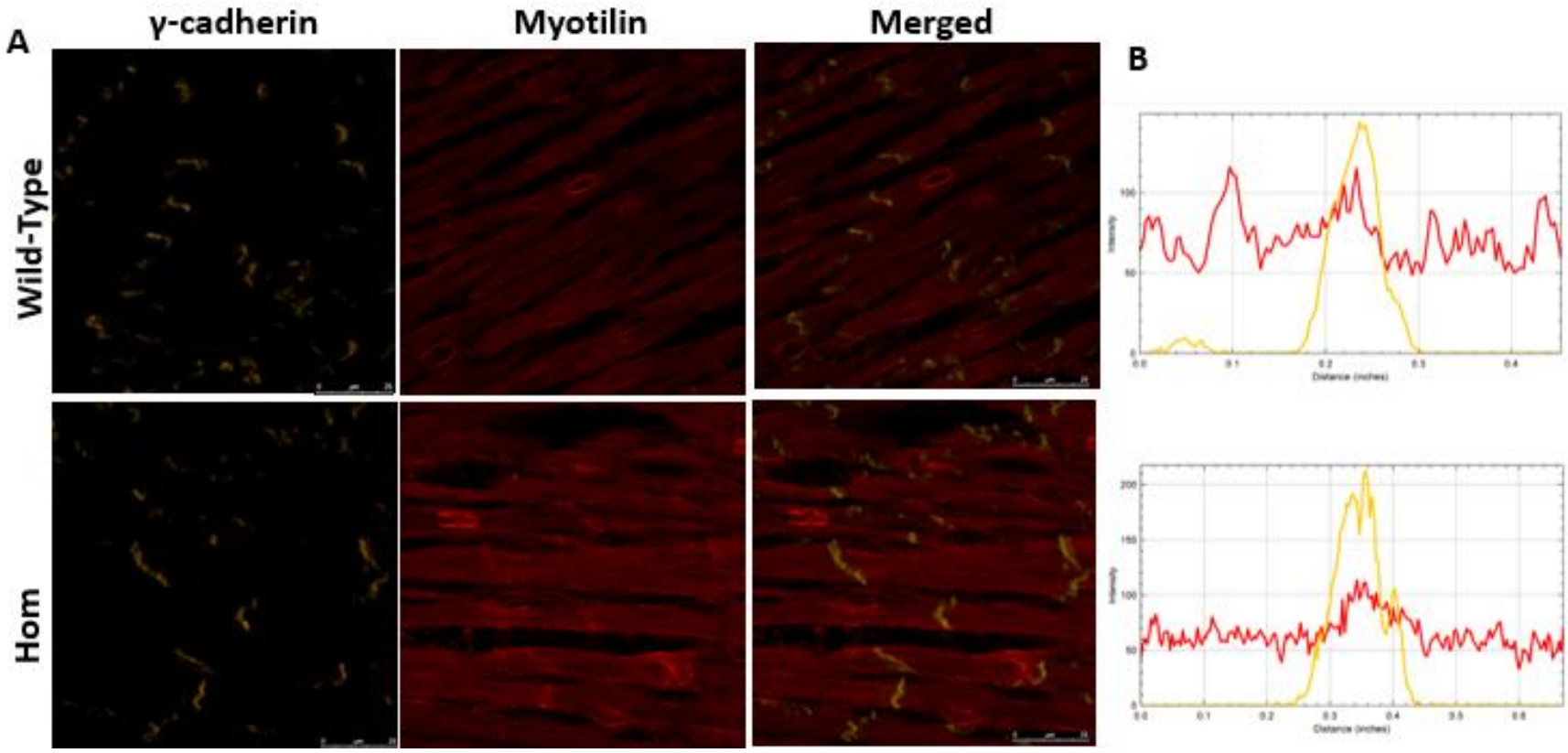

Figure 3-14 (A) Frozen sections of ventricular tissue from WT and Hom *Flnc* W2165C mice with line intensity plots. Sections were stained for Myot (rabbit, 10731-1-AP) and counterstained to visualise the intercalated discs (mouse, γ-cadherin 610154, orange). Myot is primarily localized at intercalated discs in the Hom tissue. (B) Line intensity plots for WT and Hom displaying the fluorescence intensity for both channels. Line intensity plots for WT and Hom displaying the fluorescence intensity for both channels.

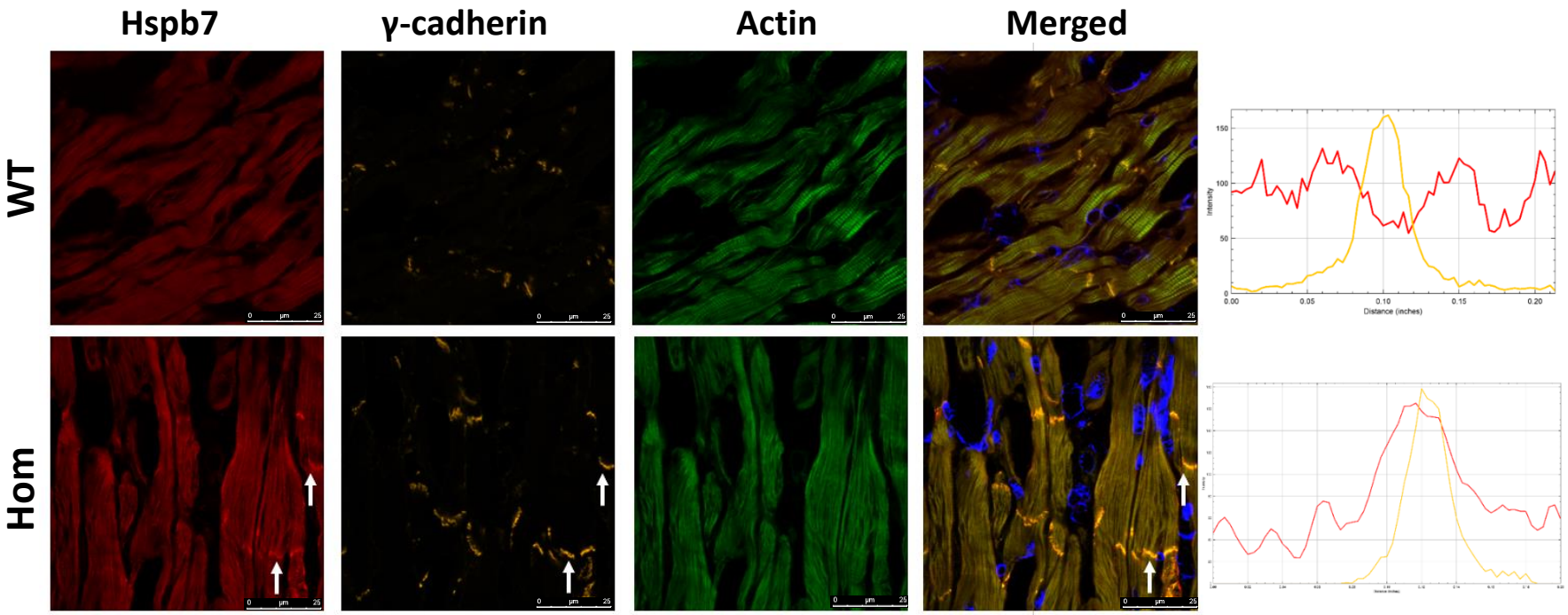

Figure 3-15 Frozen sections of ventricular tissue from WT and Hom *Flnc* W2165C mice with line intensity plots. Sections were stained for Hspb7 (rabbit, 15700-1-AP) and counterstained to visualize sarcomeres actin) and intercalated discs (mouse, γ-cadherin 610154). HSPB7 is primarily localized at intercalated discs and appears more abundant in the Hom tissue. Line intensity plots for WT and Hom displaying the fluorescence intensity for both channels.

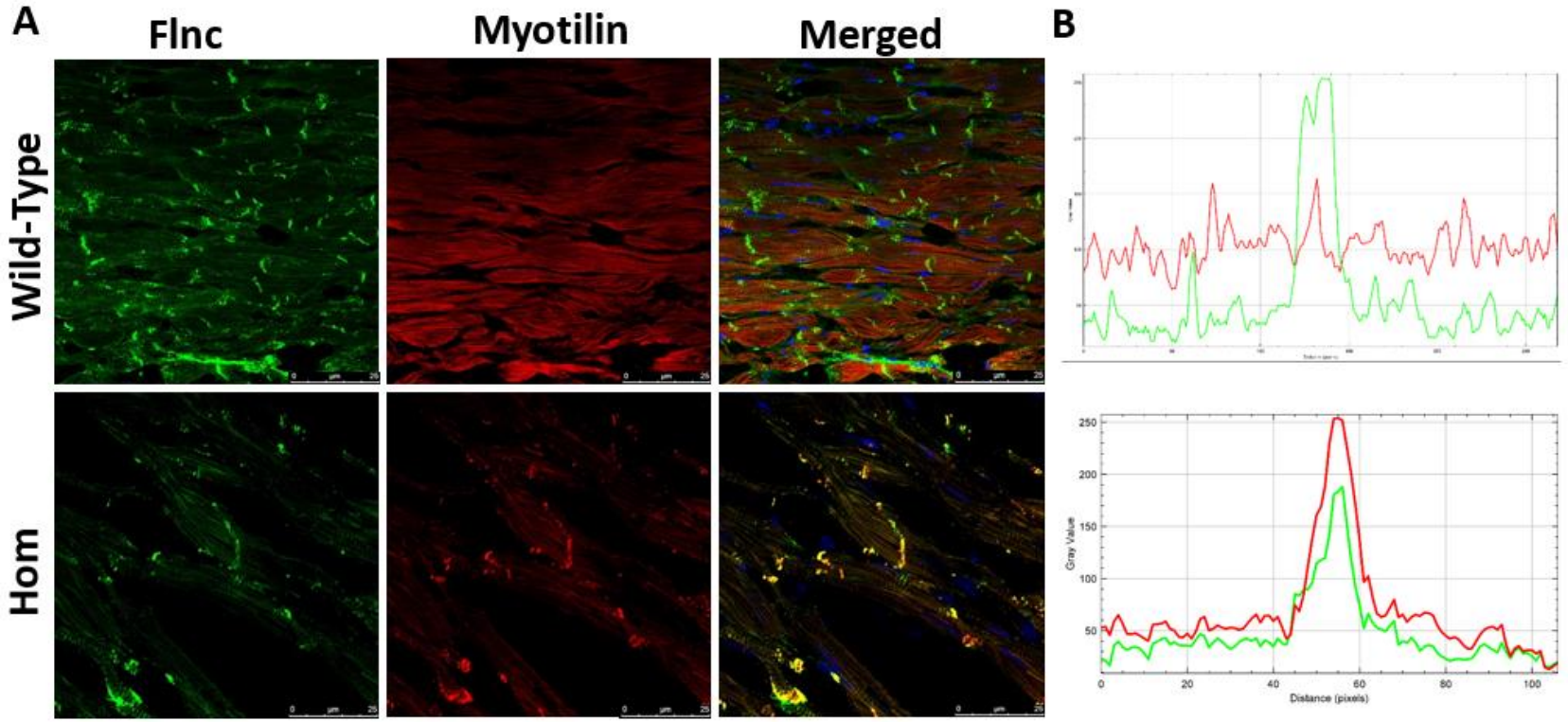

Figure 3-16 Frozen sections of ventricular tissue from WT and Hom *Flnc* W2165C mice. Sections were stained for FLNC (mouse RR90) and MYOT (rabbit 10731-1-AP). In Hom mice there is greater colocalization of Flnc and Myot at the intercalated disc. (B) Line intensity plots for WT and Hom displaying the fluorescence intensity for both channels.

3.3.7 Transcriptome profile of W2165C mice

3.3.7.1 Baseline transcript profile

A targeted approach in addressing the transcriptome level of WT and mutant mice was used to gain specific insight into the molecular changes underlying the *Flnc* W2165C phenotype. At baseline, the induction of the fetal gene programme in W2165C hearts (induction of *Nppa*, *Acta1*, *Myh7*) was also observed. Transcripts implicated in hypertrophic signalling (*Fhl1*, *Ankrd1*) also displayed significant increased expression profiles in mutant mice (Figure 3-17). However, incongruous with the proteomics data, *Flnc* was not statistically significantly changed at transcript level.

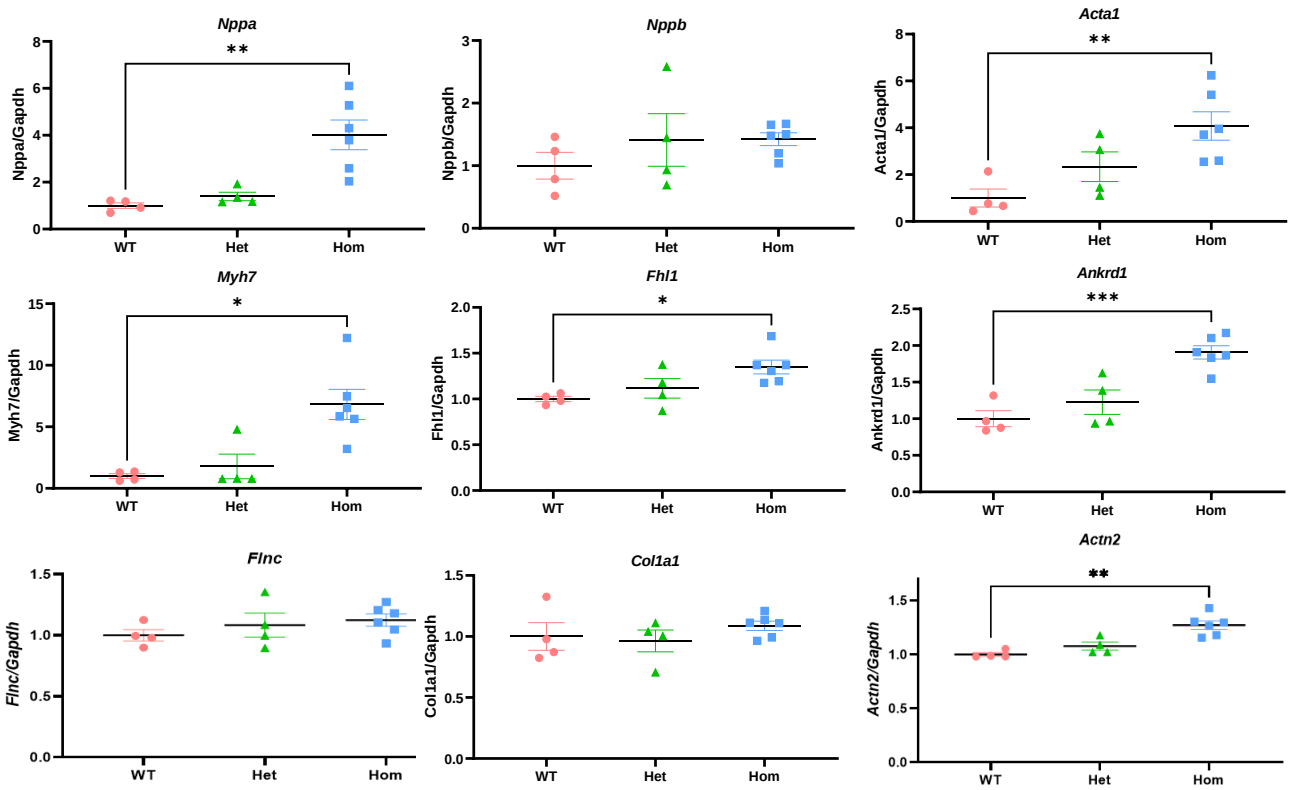

Figure 3-17 qPCR indicating the baseline induction of the fetal gene programme, a hallmark of cardiomyopathy, and hypertrophic signalling, in 3-month old WT and Hom *Flnc* W2165C mice. Values are normalised to *Gapdh* and made relative to WT group. Hearts were investigated at 3-months old, n=4-7 males per group. A one-way ANOVA was conducted on all samples except for Myh7 and Actn2 which underwent a Kruskal-Wallis multiple comparisons test as they were not normally distributed. Significant changes are observed in the hearts of W2165C mice ($p<0.05$, *; $p<0.01$, **; $p<0.001$, ***, versus WT).

3.3.7.2 Ang-II transcript profile

Next, the molecular response of mice which underwent saline or chronic Ang-II treatment were investigated at transcript level. In agreement with the proteomics data (increased Myh7), a targeted RNA expression approach revealed a trend towards the induction of the fetal gene programme in Ang-II treated mice, with an upregulation of *Nppa*, *Nppb*, *Myh7*, and *Acta1* (Figure 3-18). *Myh7* was also increased in saline-treated Hom mice. WT and Het mice showed a significant treatment effect in these markers, all increasing in respond to Ang-II.

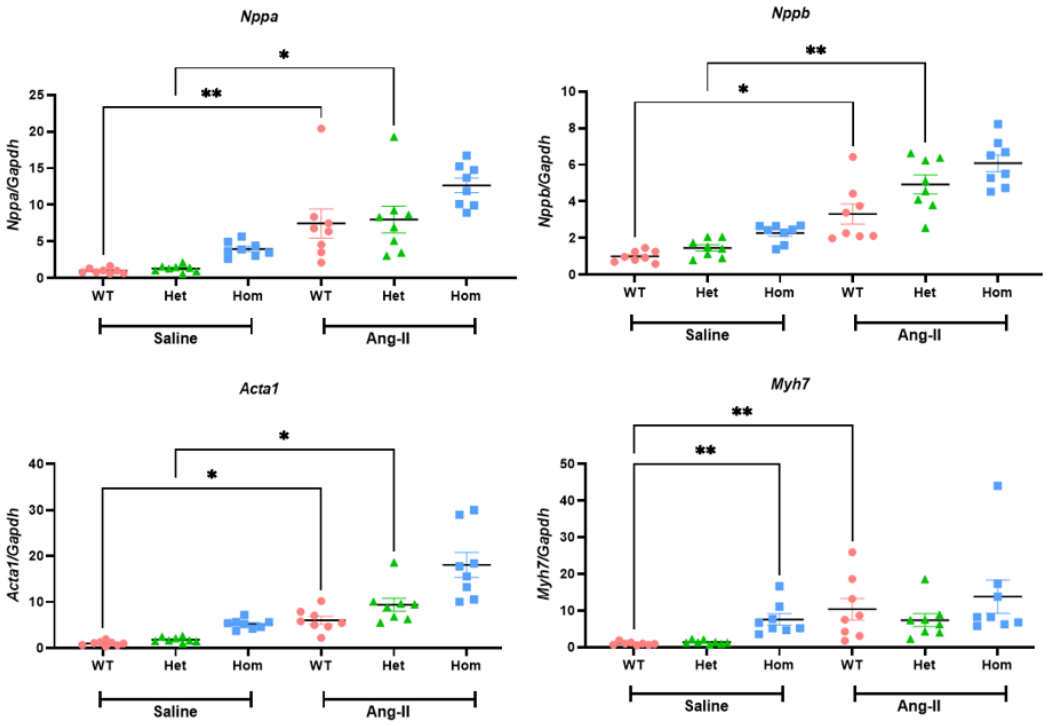

Figure 3-18 qPCR of fetal gene programme markers in 3-month old WT and Hom *Flnc* W2165C mice treated with either saline or Ang-II. Values are normalised to *Gapdh* and made relative to the saline WT group which was set to 1 hearts were investigated at 3-months old, n=8 per group. A Kruskal-Wallis multiple comparisons test was conducted on these samples since they were not normally distributed. 2-way ANOVA multiple comparisons test was conducted on normally distributed samples. Significant changes are observed in the hearts of W2165C mice ($p<0.05$, *; $p<0.01$, **; versus WT).

Contrary to baseline transcript expression of *Flnc*, this data revealed statistically significant increases in *Flnc* at a transcript level in both saline and Ang-II treatment in Hom mice relative to WT (Figure 3-19A). A significant positive induction *of Myot* was shown in Hom mice in both saline and Ang-II treatment (Figure 3-19B). *Pgm5* was found to decrease in WT and Hom mice after Ang-II treatment (Figure 3-19C). *Actn2* showed a positive induction in Hom saline treated mice relative to WT mice, however, this difference was not seen in Ang-II treated mice (Figure 3-19D). No differences were observed in *Fblim1* expression (Figure 3-19E). Compared to saline treated Het mice, Ang-II treated Het mice displayed a significant increase of the gene for the FLNC-binding protein Xirp1 (*Xirp1*) (Figure 3-19F).

In response to Ang-II stimulation, WT and Het mice displayed a positive induction of fibrotic signalling transcripts (WT and Het: *Col1a1*, *Col3a1*, WT only: *Lox*) (Figure 3-20A-C). Hypertrophic signalling proteins, Fhl1 and Rcan1 showed significant differences (Figure 3-20D&F). *Fhl1* was significantly induced in Ang-II treated Het and Hom mice, while *Rcan1* was increased in Ang-II treated WT and Het mice relative to their saline-treated counterparts.

Overall, the use of Ang-II helped to unmask genotype responses to the treatment at transcript level, however, a strong HCM molecular phenotype was not observed in the Hom mice, likely due to variability. Differences were also seen in saline treated mice.

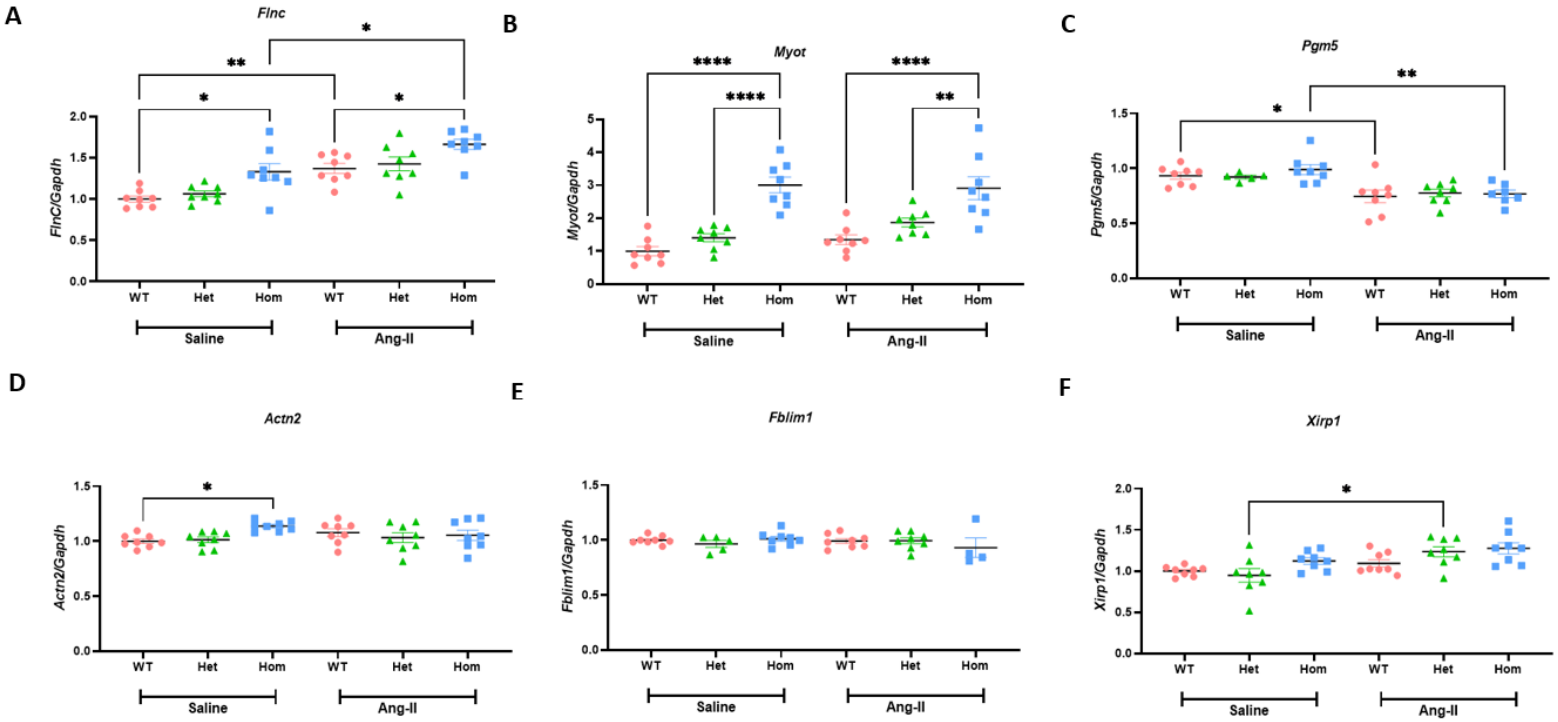

Figure 3-19 Targeted assessment of transcriptional changes of filamin C and binding partners of filamin C interactors by qPCR in 3 month old WT, Het and Hom W2165C mice with Saline/Ang-II treatment. Values are normalised to *Gapdh* and made relative to the saline WT group which was set to 1. Hearts were investigated at 3-months old, n=8 per group. A 2-way ANOVA multiple comparisons test was conducted. Significant changes are observed in the hearts of W2165C mice ($p<0.05$, *; $p<0.01$, **; $p<0.0001$, **** versus WT)

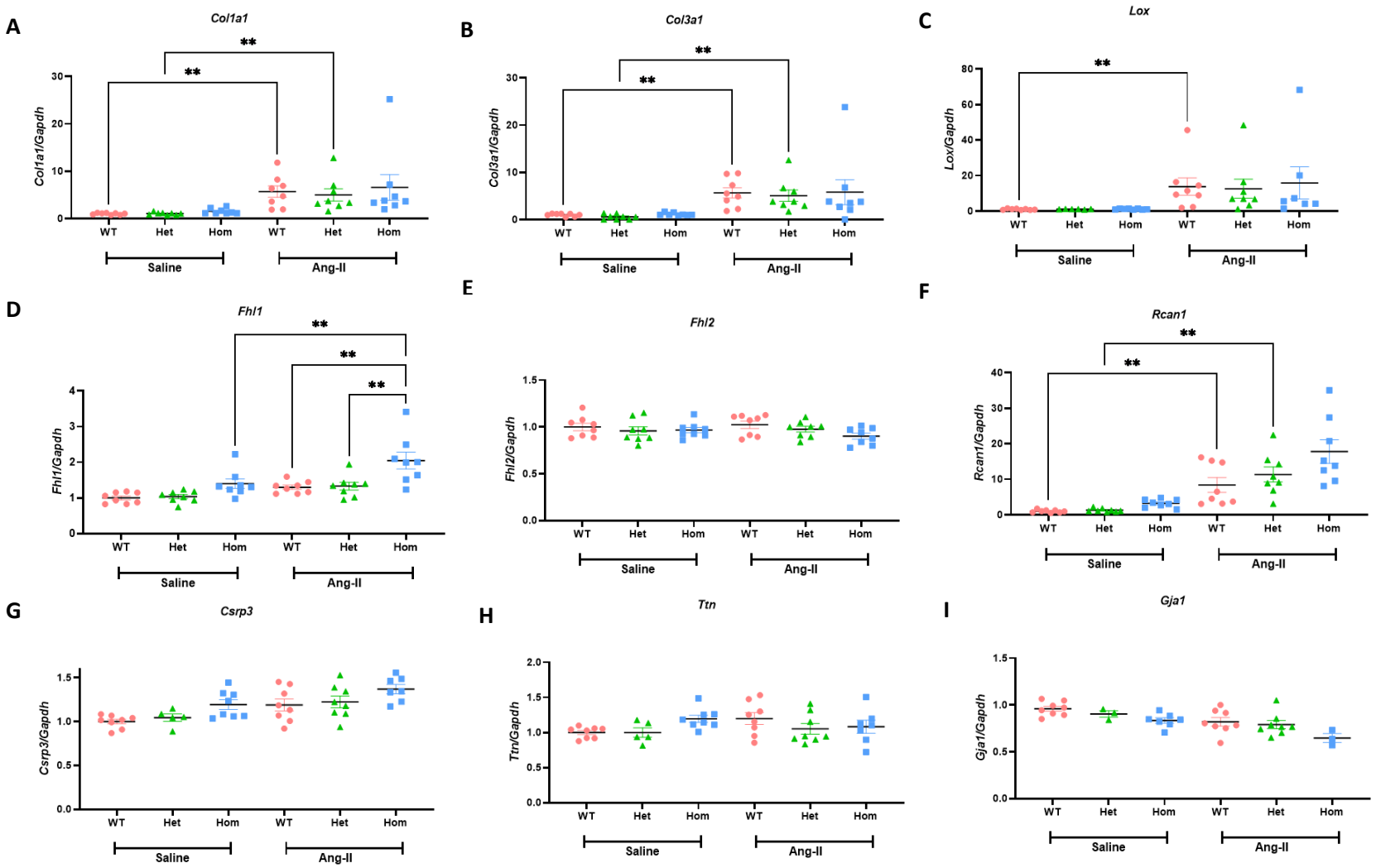

Figure 3-20Targeted assessment of transcriptional changes of hypertrophic signalling markers by qPCR in 3 month old WT, Het and Hom W2165C mice with Saline/Ang-II treatment. Values are normalised to *Gapdh* and made relative to the saline WT group which was set to 1. Hearts were investigated at 3-months old, n=8 per group. A Kruskal-Wallis multiple comparisons test was conducted on not normally distributed data (*Col1a1, Col3a1, Lox, Fhl2, Rcan*). 2-way ANOVA multiple comparisons test was conducted on normally distributed samples. Significant changes are observed in the hearts of W2165C mice ($p<0.01$, **; versus WT).

3.4 Discussion

3.4.1 Aims of chapter

Numerous pathogenic variants in a variety of genes coding for sarcomere proteins are HCM-causing, however, the contribution and mode of action of HCM-linked *FLNC* variants are currently unknown. The *FLNC* variant W2164C was found to co-segregate in a HCM family. Patients presented with electrocardiogram features and structural cardiac abnormalities typical of HCM with features of restrictive cardiomyopathy. A mouse model previously generated carrying the HCM-variant W2165C in the *Flnc* gene was used for both in vivo and ex vivo investigation.

This chapter presents a physiological and molecular characterisation of this mouse model. Key readouts to assess the *in vivo* cardiac function were performed: mouse heart volumes and gravimetry measurements, echocardiography. These measurements were taken at baseline and with saline/Ang-II treatment to measure the response to chronic pressure overload. Additional *ex vivo* experiments were done to measure the molecular phenotype in the presence of this *FLNC* missense variant.

3.4.2 Cardiac structure

While at baseline there were no genotype-related cardiac phenotypes observed, Ang-II stimulation resulted in an altered diastolic ventricular wall thicknesses in heterozygous and homozygous mice. In the presence of Ang-II treatment, *FLNC* variant-carrying mice displayed more drastic increases in ventricular wall thicknesses (LVPW.d and LVAW.d) (Table 3-3), indicating an aggravated hypertrophic response.

It is known that there are sex-related differences in heart disease from diagnosis to mortality (274). For instance, females have lower ventricular wall thicknesses and have higher levels

of diastolic dysfunction compared to males (275,276). Females also display lower mortality rates relative to males and have less severe evidence of hypertrophy (277). This is likely due to the differential regulation of estrogen which acts as a cardiac protector but also along with testosterone level results in reduced physical activity for female mice – hence reducing cardiac stress (278–280).To understand whether the phenotypes observed are driven by one sex, data was separated by sex.

Interestingly, although significance was lost – likely due to reduced n numbers – most of the observed trends remained (Figure 3-1 to Figure 3-4) such as increased LV wall thicknesses (Figure 3-4) and corrected LV mass in response to Ang-II treatment. In female mice, ang-II treatment-related significance was only found in the heterozygous mice, although this could be due to variability in the Homs obscuring significance. However, some variables, such as LVID.s (Figure 3-3), had trends which were conflicting between sexes suggesting sex may be a relevant biological variable for some measurements in this *FLNC* missense variant dataset, at least upon Ang-II stimulation.

Although sex differences were observed in this chapter, there was no indication that one sex had a more pronounced genotype-phenotype relationship compared to another sex. This is not wholly surprising since the variant presents itself in both female and male patients affected by cardiomyopathy. As mentioned earlier, females do have lower rates of cardiovascular mortality, however, post-menopause females have an acceleration to mortality (281). This is likely due to the reduction of estrogen-induced cardiac protection in post-menopause females – therefore, it would be interesting to see if there are any sex-related differences in older mice (12-month) (Figure 3-21) (282).

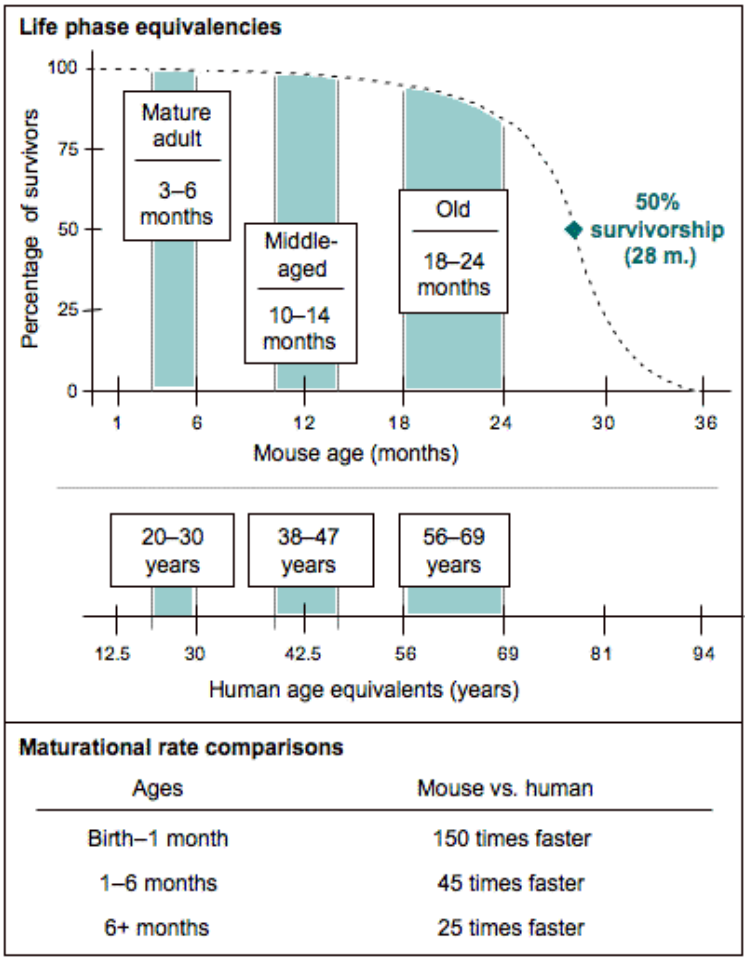

Figure 3-21 Scheme comparing human and mouse lifespan. *Taken from: https://www.jax.org/news-and-insights/jax-blog/2017/november/when-are-mice-considered-old*

3.4.3 Proteomics-led findings

One of the main advantages of using LC-MS is the ability to compare alterations of protein abundance across multiple samples without requiring isotopic labels. Proteome quantitation by unsupervised LC-MS allows for a greater understanding of the often-complex protein dynamics in biological systems. By performing label-free proteomics on both the myofilament-enriched and membrane-enriched fractions, potential affected molecular pathways were identified: proteins involved in sarcomere protein binding was upregulated, while proteins involved in the electron transport chain were downregulated (Figure 3-8). Fraction-specific molecular changes in homozygous mice were found, which is particularly

important due to the highly compartmentalised structure of many proteins residing in the cardiomyocyte.

Due to the statistical measures applied to the data to produce a list of protein identifications, the data quality can vary despite metrics such as the FDR being in place to minimise false positives. There is no standardised way of treating proteomics data, with papers electing for considerably lower thresholds than used in this thesis (p-value threshold = 0.05; no fold change threshold) (91). For this reason, comparative quantitative validation by immunoblot for LC-MS data is instrumental in tying the exploratory approach of LC-MS with an informed and targeted validation method. Targeted immunoblotting confirmed some upregulations, such as Myh7, but also indicated whether protein relocalisation was occurring between cardiomyocyte fractions, as was the case for Hspb7. Given the sensitive nature of LC-MS, performing these follow-up immunoblotting experiments in all three fractions (cytoplasm, membrane and myofilament), as well as whole tissue, allowed for altered proteins to be shown as false hits, such as Flnc upregulation in the myofilament fraction.

The interpretation of these findings will be discussed in the following sections: energetic deficiency, myofilament role, and stress-induced adaptive responses.

3.4.3.1 Energetic deficiency

The heart is an energy demanding tissue which requires an abundance of mitochondria occupying almost one third of the cardiomyocyte volume in order to produce ATP through oxidative phosphorylation to sustain cardiac contraction and relaxation (283). HCM is a disease of inefficient energy usage (45,284). In heart failure and HCM there is an energy deficiency which is in part contributed by a partial metabolic shift from fatty acids to glucose as its metabolic substrate of use (285).

Proteomics of the Hom membrane-enriched fraction, which is expected to contain cell membranes as well as the mitochondria, showed a reduction in numerous mitochondrial proteins (Figure 3-6). Many of the downregulated proteins are involved in the mitochondrial respiratory chain – a crucial ATP synthesis process. Identified mitochondrial respiratory chain proteins, such as Ndufv1, Ndufs3, and Uqcrc2, have been linked to a cardiomyopathic phenotype due to a dysfunctional ATP synthesis process leading to hypoxic conditions and poor contractile performance (208,209,211,286).

The changes observed in this proteomics data may reflect a compensatory mechanism to an energetic imbalance (244). Reduced expression of these proteins may affect the stability of mitochondrial complex I, resulting in inefficient oxidative phosphorylation and hence result in ATP depletion. ATP depletion in-turn contributes to the prolonged opening of the mitochondrial permeability transition pore resulting in altered myocardial function and structure. Decreased expression has also been found to increase the production of reactive oxygen species, which can further inhibit complex I activity (209,287,288). These changes lacked immunoblot validation and would require comprehensive analysis to confirm the functional effect of the *FLNC* W2164C variant on mitochondrial function i.e. Seahorse metabolic assay or metabolomics (289).

3.4.3.2 Myofilament role

Myh7 is the predominantly expressed isoform in the developing mouse heart, however, *Myh6* is the dominant isoform in the adult mouse with *Myh7* only expressed in mice during disease (290). These *Myh* genes encode for myosin heavy chains which are actin-based motor proteins that drive motile processes, such as muscle contraction, via mechanical force (291). Myh7 was highly upregulated in proteomic and immunoblot analysis in whole tissue verifying that it was a global upregulation and indicating a shift from the predominant adult

isoform *Myh6* (290). *Myh7* re-expression is part of the fetal gene programme and is consistent with earlier studies which found a shift in MHC isoforms (*MYH7* → *MYH6* in humans) in response to cellular stress (292,293). This finding is suggestive of a maladaptive cardiac response when under cardiac stress conditions which has been linked cardiac hypertrophy and heart failure (294,295).

A protein previously identified, Hspb7, might play a role in the turnover and localisation of filamin C. Increased levels of Hspb7 were reported by immunoblotting in the Myofilament-enriched fraction. Along with this, both Hspb7 and Flnc were upregulated and appeared to show increased abundance at the intercalated disc. Hspb7 may bind to mutant Flnc between Ig18 and Ig21, in addition to the binding domain, Ig24, where Hspb7 typically binds (133). When overstretched, mutant W2164C filamin C could expose Ig18-21 recognition for Flnc-Hspb7 binding and subsequently could competitively inhibit Flnc-Hspb1 binding, therefore interrupting the refolding and degradation functions Hspb1 has on Flnc. This is correlated with changes found at transcript level, mutants display higher levels of *Flnc* at transcript level whether under hypertensive Ang-II stimulation or not. If the *Flnc* missense variant results in altered incorporation into the sarcomere, it would make sense that at transcript level, *Flnc* increases to meet the demand. Due to increased levels of *Flnc* at transcript level, protein turnover cannot keep up. Transcript expression were not measured for *Hspb1* or *Hspb7*, though would be of interest to observe this effect.

With evidence of altered protein localisation in Flnc and its binding partners, as well as an upregulation in Hspb7, it is attractive to assume that altered proteostasis is occurring in the presence of the *Flnc* W2165C variant in mice. Proteins linked to stress-related responses appeared to be upregulated in the proteomics data, supporting the hypothesis of an altered cardiac mechano-sensing response in the presence of this *FLNC* variant: *Hspb7, Fblim1* and

Mlp (79,121,236). Binding to d24 of *FLNC,* an increase *HSPB7* has been associated with cardiomyopathy and also as a potential biomarker for myocardial infarction (296).

In pathogenic skeletal myopathies, *Flnc* and its binding partners (*Myot, Fblim1, Actn2*) are found in aggregates indicative of a dysfunctional proteostasis via CASA (79,148,153), however, aggregates have not been probed for in this study. To date, myotilin has only been associated with skeletal muscle pathologies, though myotilin aggregates were found in embryonic chick cardiomyocytes (297,298). In skeletal filaminopathies, an impaired CASA pathway results in aggregates of filamin C and myotilin and are predicted to result in loss-of-function at the Z-disc due to protein deficiency and hence impaired myofibrillar structural integrity (153). Though aggregates are not found in this mutant mouse and the Z-discs appear intact, both filamin C and myotilin translocate towards the intercalated disc (Figure 3-13 & Figure 3-14). As myotilin directly binds filamin C through domains 19-21, it is hypothesised that the interaction between myotilin and filamin C has increased affinity due to the W2165C variant, however, this was not tested (115).

Here we also present that filamin C and myotilin appear to be co-upregulated under models of biomechanical stress (Figure 3-16) indicating a relationship with filamin C and myotilin in cardiac conditions. Skeletal myopathies are often associated with features of cardiomyopathy so its role in HCM warrants further investigation (297). Although protein aggregation has not been observed in the mutant mouse yet, taken together, the proteins presented in this section suggest it is possible that these aggregate-associated proteins could be linked to a disrupted protein turnover mechanism. This mechanism may be related to a mechano-sensing system, and will be explored in Chapter 5 (299).

Filamin C is found in several cellular compartments: in the intercalated disc, in the plasma membrane, as well as in the Z-discs. These are all load bearing structures. In the data presented in this chapter, mutant Flnc appears to be significantly upregulated in the myofilament fraction proteomics, however, by immunoblot validation this was only significantly increased in the whole tissue and cytoplasm, indicating a cellular re-localisation of filamin C. Filamin C was observed to show a greater abundance at the membrane-associated intercalated disc by immunofluorescence (Figure 3-13), however, this was not found at detectable levels via membrane-enriched fraction immunoblotting. Since the *Flnc* W2165C variant is found in Ig20, close to the intradomain insert which aids filamin C in targeting it to the Z-disc (131), the variant may affect its ability to properly localise at the Z-disc. In models of biomechanical stress, increased localisation of filamin C to the intercalated disc is associated with its role in organising thin filaments which have to resist greater mechanical strain (156). This affected localisation could be acting by disrupting domain-related ligand binding to Ig20 of filamin C and hence result in the relocalisation of some FLNC-bound proteins (Myotilin and Hspb7). Together this data evidences a potential adaptive response towards biomechanical stress in homozygous mice, however, biomechanical stress itself was not directly tested.

3.4.3.3 Stress-induced adaptive responses

Cardiac hypertrophy is a morphological and functional adaptive response to stress induced from pressure and/or volume overload (300). At a molecular level, a network of stress-induced pathways are employed to compensate with the pressure and/or volume overload (300). The proteomics findings in this chapter displayed a molecular indication of a stress-induced adaptive response.

Unsupervised proteomics identified 11 proteins which were differentially expressed in the membrane-enriched fraction (Figure 3-6): Ndufv1, Ndufa10, Ndufs3, Ndufa3, Ndufab1, Uqcrc2, Rtn2, Aifm1 and Maob were all downregulated whereas Fblim1 and Pgm5 were found to be upregulated. No other membrane proteins, especially the mitochondrial ones, reported as significant in proteomic analysis have a known direct interaction with filamin C; therefore, expression changes are likely to be secondary, and may reflect an adaptive response. Immunoblotting also failed to validate the observed downregulation of the mitochondrial apotosis-inducing factor *Aifm1*, despite it supporting an earlier study which found expression to decrease with increasing severity of cardiac hypertrophy (301). The same study also found deficiency of this protein to stimulate maladaptive remodelling of the LV during mechanical stress, mediating cardiac hypertrophy and fibrosis, implicating it in HCM (301). Combined fraction GO term enrichment analysis of proteomics data highlighted a significant downregulation of GO term activities related to the electron transport chain. Whilst these mitochondrial hits individually may represent experimental noise given their abundance in tissues and lack of immunoblot validation, together the role the mitochondria cannot be completely discounted given the importance of the mitochondria in the healthy and diseased heart (302).

Interestingly, the only proteins to be significantly upregulated in Membrane-enriched fraction were filamin C binding partners migfilin (Fblim1) and aciculin (Pgm5). Otherwise known as filamin-binding LIM protein 1, migfilin binds to filamin C's domain 19, which neighbours the intradomain insert harbouring the variation (76). This protein has been reported to be upregulated in pressure overload to mediate hypertrophy and fibrosis, suggesting that it is increased in response to increased stress on the heart (303). In the intercalated disc, filamin C also interacts with aciculin, with which it is also co-localised in

Z-discs (113). Aciculin and filamin C have roles in myofibrillar repair and remodelling (113). Immunoblot data failed to validate the highly significant observation of Fblim1 or Pgm5 as found in proteomic analysis. This correlates well with no genotype differences in *Fblim1* and *Pgm5* observed at transcript level (Figure 3-19).

Adaptive proteins towards hypertrophy were also affected though to varying levels of significance: Synpo2l, Fhl2, Calm1 and Obscn. Synpo2l is essential in the developing skeletal and heart muscle and is linked to the induction of hypertrophy and could imply a translocation of the protein (264,304,305). Fhl2 is involved in the hypertrophic response, however, it is usually down-regulated in cardiac disease (265,306). Calcium handling proteins Calm1 and Obscn were also downregulated in the membrane-enriched fraction. Changes in calcium handling proteins may affect muscle contraction regulation via altered cardiac action potential generation (230). A downregulation of the major gap junction protein *Gja1* (Cx43) is found in heart failure and hypertrophic models (240,304). Cx43 regulates electrical signalling propagation, a reduction at the intercalated disc has been shown to slowdown conduction which could correlate with the ECG phenotype seen in *FLNC* W2164C patients however was normally expressed on immunoblots.

Collectively, this data would suggest that in the W2165C mouse heart, there is an activation of hypertrophic pathways and alterations in calcium handling. Thin filament proteins Lmod2 and Tnnt2 are both downregulated in proteomics findings. Lmod2 downregulation is associated with disrupted filament assembly and cardiac failure (265). Although Tnnt2 pathogenic variants account for around 3% of familial HCM, the pathomechanisms are not well understood (307,308).

3.4.4 Angiotensin-II treatment

Ang-II plays an important role in cardiovascular disease by acting within the renin-angiotensin-aldosterone system (309). Treatment in mice has been shown to induce premature senescence and promote cardiac hypertrophy and remodelling (310). Transcripts which encode proteins involved in the signalling (*Fhl1, Rcan1*) and structure (*Flnc, Xirp1*) of the sarcomere did appear to have a more pronounced increase in mutant mice. Chronic Ang-II stimulation of mice resulted in treatment-based changes, however, for most, treatment did not appear to aggravate a significant molecular phenotype in Hom mice on a transcript level. This is likely due to variability and the difference in the statistical measures used compared to baseline (baseline: one-way ANOVA, Saline/Ang-II treatment: two-way ANOVA).

Interestingly, there were differences between baseline and saline treatment (Table 3-2 & Table 3-3). Although unlikely, the differences may be in-part due to fluid overload or stress from surgery in the saline treated mice and hence also affect the Ang-II treatment - masking potential genotype-related differences induced by Ang-II treatment. Since mice around 3-months old are only young adults, it is reasonable to suggest that more mature mice (approx. 12-months) would have a greater phenotype, considering HCM pathology is often late-onset in humans (91,192).

3.5 Conclusion

This work demonstrates that the patient derived W2164C *FLNC* variant has a significant impact on a protein and transcript level in a mouse model. The homozygous expression of the variant was found to affect the total abundance and re-localisation of proteins involved in hypertrophic signalling. The impact of some of these changes are indicative of being protective mechanisms against increased cellular stress and contributing to an HCM phenotype. Although some findings were not validated by immunoblot, the proteome of the Hom mouse suggests dysfunctional mitochondria and cardiac-specific autophagy pathway could be a contributor to the *in vivo* observations. Guided by these findings, additional work has been done in the mutant iPSC-CM model and will be discussed in the next chapter.

Chapter 4 *FLNC* W2164C IN THE IPSC-DERIVED CARDIOMYOCYTE MODEL

4.1 Introduction

Humans are complex organisms. Through a highly regulated network of hormones, circulating factors, intercellular and intracellular cross talk, a distinct physiological function is achieved. Biological methods to interrogate function is largely done using disease models. Relevant disease models are vital to aid the understanding of cardiac physiology and pathology. The question "What is the most relevant disease model to study human cardiovascular disease?" is often posed as a discussion. It is a relevant one to the field in advancing the understanding of cardiovascular-focussed science (311).

Since suitable human samples are not readily available for cardiovascular research due to difficulties in obtaining primary cardiac myocytes, particularly from non-failing hearts, animal models (in particular, rodents) have been used. Animal models offer valuable insights into cardiovascular function, providing detailed *in vivo* and *ex vivo* parameters e.g. electrical and conduction activity by echocardiography and cardiac optical mapping respectively. Cardiac tissue from mice can be further used for molecular analyses which can help elucidate which pathways may be affected in a level of detail which is otherwise unavailable with the limited human material. The knowledge gained from studying rodent models in controlled environments has been instrumental in identifying and characterising the function of a large number of genes, many of which can be directly correlated to human pathology.

4.1.1 The iPSC-CM model

Large whole organism models, such as pigs, could provide more translational research due to their phenotypic resemblance to humans (anatomical, hemodynamic, electrophysiological), however these pose impractical hurdles regarding ethics, cost and

scalability (312). Although unable to completely recapitulate the organs physiological functions and systemic interactions between organs, the development of cell culture technology, which attempt to mimic the complex structures of cardiac tissue, represent significant scientific progress. The emergence of iPSCs and its derived cardiomyocytes has allowed the continuous generation and long-term culture of human cardiomyocytes, considering human cardiac tissue does not survive in culture for long (313–315). The opportunity to study specific patient-found variants proposed to be implicated in cardiomyopathy makes this cellular model potentially very insightful (175). Since its arrival, iPSC-CMs have been used to investigate key cardiomyopathy disease genes utilising the following functional outputs: contractility, calcium and voltage sensing as well as standard molecular biology outputs. iPSC-CMs have been shown to recapitulate key cardiac abnormalities found in cardiomyopathies (182,316–319).

4.1.2 Limitations of the iPSC-CM model

Limitations exist in all disease models. Optimising model selection and experimental design are instrumental. The field of iPSC-CM disease modelling is still in its infancy relative to animal models and there is potential to overcome its limitations in order to better answer the biological question in focus.

iPSC-CMs grown in standard culturing conditions express phenotypes that are characteristic of fetal human cardiomyocytes in terms of cardiac isoform expression and cell morphology (187). In humans, the mechanical and electrophysiological genes are expressed differentially throughout development to adulthood (181,320). Since most cardiac diseases present during adulthood, these immature iPSC-CM phenotypes raise questions over whether iPSC-CMs are comparable with adult cardiomyocytes, a similar issue seen for isolated cardiomyocytes from rodent models (321). Methods have been used to provoke a contractile and

hypertrophic phenotype through challenge e.g. the use of a beta-adrenergic agonist such as isoprenaline (ISO) has been used in iPSC-CM studies (322).

Many methods attempt to mature the iPSC-CM model through 3D culture (engineered heart tissue, engineered heart muscle, microtissues) (Table 4-1). A number of review discuss the efforts made to mature this model (323,324).

Table 4-1 Brief overview of some of the maturation methods used to improve iPSC-CM disease modelling.

Method	Effect of approach	Ref
Prolonged culture	Increased cell size and action potential amplitudes Improved sarcomere organisation Improved Ca^{2+} handling	(187,189)
Maturation media	Increases in aerobic respiration, sarcomere reticulum Ca^{2+}, force production Improved sarcomere structure Increased mitochondria number	(325–327)
Tuning substrate properties	Improved sarcomere alignment Improved sarcomere structure Expression of more mature sarcomere isoform ratio	(62,328–330)
Electrical stimulation	Improved sarcomere structure Increased intracellular Ca^{2+} levels Upregulation of cTnT	(331,332)
Biochemical cues	Increased cell size and sarcomere length Increased rate of Ca^{2+} release,	(325,333)
3D and co-culture approaches	Improved sarcomere structure and alignment Electrophysiological maturation Improved energy metabolism	(238,334–341)
In vivo maturation	Partially mature sarcomere structures	(342)

4.1.3 Use of iPSC-CM to study *FLNC* W2164C

In the previous chapter, the mutant *Flnc* W2165C mouse model was used to highlight the effects of this missense variant at a physiological and molecular level. The findings from this chapter showed some changes at a morphological level and a molecular phenotype indicative of cardiomyopathy via an induction of the fetal gene program. However, despite the mouse having approximately 95 % of genes in common with humans, key physiological differences in physiology, electrophysiology and protein isoform expression can render results non-translatable to the human condition (169,343,344). Species-related differences

between rodent and human compensatory mechanisms may result in a different molecular phenotype which may not be human-specific, as has been reported previously (345). Therefore, for robustness, the use of genetically-edited iPSC-CMs is required to validate the trends reported in the rodent.

As mentioned in the introduction chapter, to study patient-found variants in iPSC-derived cells two approaches can be employed: (1) using a patient-derived iPSCs with disease-associated variant being repairs to form a control iPSC or (2) using iPSCs derived from a healthy individual as a control and inserting the disease-associated variant into this line. In this thesis, the *FLNC* W2164C missense variant was introduced into iPSCs Kolfc2 line which were derived from a healthy individual by employing CRISPR-cas9. Silent mutations were also inserted into the *FLNC* W2164C edited and WT lines to ensure the effects observed are not due to off-target effects generated during CRISPR-cas9. The insertion of the variant in edited iPSC lines was validated by Sanger sequencing (Figure 4-1).

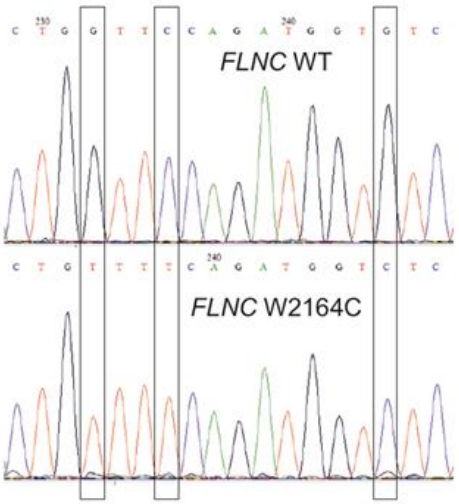

Figure 4-1 Sequencing of genomic DNA fragments from WT and FLNC W2164C iPSCs, displaying the presence of the knock-in missense variant (G→C). Additional silent variants were also inserted (G→T) and C→T).

4.1.4 Hypothesis and aims

As demonstrated in Chapter 3, the mouse model for the *FLNC* W2164C missense variant provided insights into the effect of this variant on morphology and at a molecular level. The previous chapter reported that the mutated filamin C was suggested to be implicated in a cardiomyopathic phenotype though it had no morphological pathology on echocardiography but did display a molecular phenotype.

It is hypothesised that in the human iPSC-CM model, the *FLNC* W2164C variant will show an overt cardiomyopathic phenotype in both Het and Hom iPSC-CMs both molecularly and functionally with evidence of altered proteostasis.

The objective of this chapter is to characterise the *FLNC* W2164C variant in the generated mutant human iPSC-CM model in an attempt to validate the reported findings from the mouse model.

In this chapter, the molecular and functional characterisation of the mutant iPSC-CM lines was achieved through the following:

1. To measure the *in vitro* cardiac phenotype of *FLNC* W2164C iPSC-CMs at baseline and in response to chronic isoprenaline stimulation in an attempt to induce cardiac hypertrophy
2. To follow-up characterisation of changes reported in the mutant mouse at a morphological, functional, transcript and protein level and with regards to protein localisation.
3. As a way to unmask hidden mechano-sensing *FLNC* W2164C phenotypes related to the immaturity and mechanical environment of regularly cultured 2D iPSC-CM monolayers, cells were cultured on PDMS surfaces of tuneable mechanical stiffness.

4.2 Methodological approach: Generation of surfaces of tuneable stiffness

Cardiac tissue is able to continuously respond to biophysical changes in order to regulate its growth and maintenance (346). Key components within the cardiomyocyte can sense mechanical cues from the extracellular matrix and consequently can trigger intracellular cascades for inducing proteostasis or pro-inflammatory/pro-fibrotic phenotypes (62).

The standard plastic *in vitro* environmental stiffness for culturing iPSC-CMs influences the structural and functional properties of the cell. The stiffness of an elastic material is measured by the Young's modulus by calculating the stress to strain ratio. The Young's Modulus of cell culture plastic is >1 GPa and in glass that figure can be in excess of 70 GPa, while the stiffness of the healthy myocardium is much lower, typically between 8-50 kPa (347,348). Given that increased myocardial stiffness is associated with a higher risk of cardiac pathologies, it is therefore vital that the culturing environment of iPSC-CMs is not mechanically compromised (71). The mechanical environment of the cell is hypothesised to play an important role in inducing iPSC-CM maturation and may mask any cardiomyopathic phenotype.

To produce an environment which mimics the native physiological and pathological mechanical stiffnesses, iPSC-CMs were cultured on polydimethylsiloxane (PDMS) mixtures of tuneable stiffness. PDMS was chosen due to ease of use regarding tuning its mechanical properties (349). PDMS is nontoxic, optically clear and is biocompatible (349,350). There is evidence of iPSC cardiac differentiation being enhanced when cultured on PDMS surfaces relative to conventional culturing conditions (351–353). A considerable limitation of PDMS, however, is that they have high hydrophobicity properties and require surface modification (via ECM coating) for cell attachment (354).

To mimic the adult healthy and cardiomyopathic physiological stiffness, PDMS mixtures were generated to have a Young's Modulus of 20 kPa and 130 kPa respectively. The healthy physiological stiffness of 20 kPa was chosen due to a reported human adult cardiac stiffness range between 8 kPa and 50 kPa (347,348). PDMS at 130 kPa was chosen based on cardiac wall stiffnesses reported to be in excess of 100 kPa in patients with congestive cardiomyopathy (355–358).

Prior to large-scale use, 3 batches of PDMS-coated coverslips of each desired stiffness (each made on 3 different days) underwent nanoindentation to test for reproducibility in production. Each specimen was indented at 3 different contact areas per coverslip at room

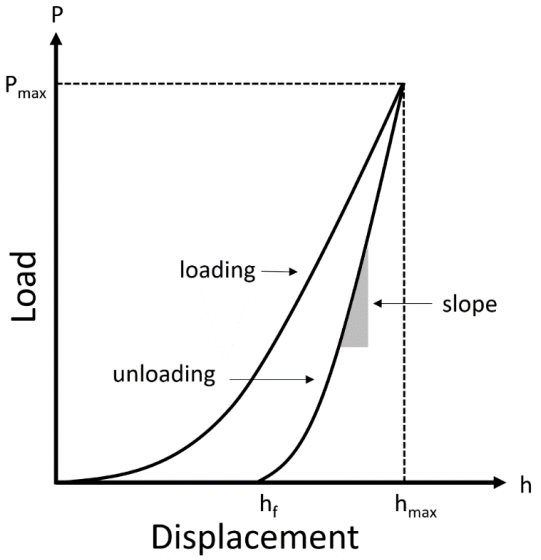

Figure 4-2 Curve of a typical load-displacement cycle during nanoindentation. The elastic modulus is derived from the slope of the unloading curve. Abbreviations: h, the indentation depth or displacement; P, the measure of load applied to the sample; hf, residual displacement depth.

temperature using the diamond spherical conical indenter of the NanoTest Vantage (MicroMaterials Ltd,UK) which pressed into the material up to a peak load of 1 mN and then was unloaded. Using the peak load over the contact area, the hardness of the specimen can be calculated and the slope of the unloading curve (slope = dP/dh) was used to determine the elastic modulus as only elastic displacements are assumed to be recovered during

unloading (Figure 4-2) (359). The measured Young's modulus for two predicted PDMS mixes (20 kPa and 130 kPa) was within an acceptable range for desired use thus confirming consistent PDMS fabrication (Table 4-2). At 130 kPa the range was 125.6±8.3 kPa which still is within fibrotic range (355,358).

Table 4-2 PDMS Sylgard-type composition mix ratios to generate a predicted Young's modulus. Nanoindentation was used to determine the mean measured modulus on 3 points of a coverslip. 3 coverslips were analysed per production batch with a total of 3 different production batches.

PDMS mix Sylgard 184:Sylgard 527	**Predicted Young's modulus**	**Mean Measured Modulus**
1:0	1 kPa	1.3±1 kPa
1:10	20 kPa	19.7±1 kPa
1:20	130 kPa	125.6±8 kPa

4.3 Results

4.3.1 Characterisation of generated iPSC-CMs

4.3.1.1 Proof of iPSC-CM generation

iPSCs were cultured and differentiated into iPSC-CMs successfully. iPSC-CMs demonstrated the expected simultaneous twitches and displayed the sarcomere marker α-actinin in well-organised sarcomeric structures (Figure 4-3).

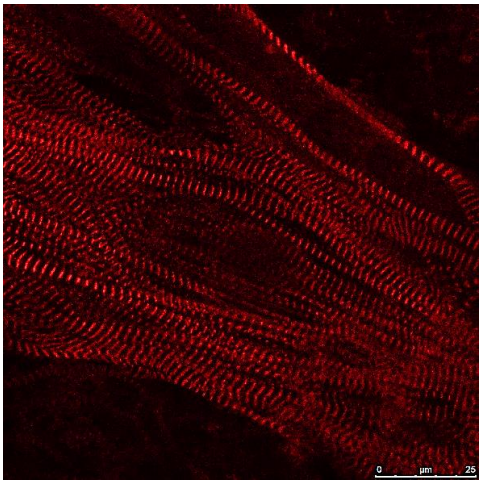

Figure 4-3 Myofibrillar organisation of a wild-type iPSC-CM clone stained at day 30 post-differentiation. α-actinin (red) is an indicator of the sarcomere.

Directed differentiation from iPSCs to iPSC-CMs was achieved with reasonable efficiency (Table 4-3). Out of all the clones, 2 clones of each genotype were found to have a comparable differentiation efficiency and started twitching around the same age. These clones were chosen for variant interrogation.

Table 4-3 Success rates for initial differentiation (characterised by the spontaneous twitching of cells). In bold are the clones which were used for further analysis.

	Clone	**Successful iPSC-CM differentiations**	**Age of twitching onset (days)**
Wild-type	**C3**	**82%**	**9.2**
	C8R	**89%**	**8.8**
FLNC W2164C Het	C4	75%	12.9
	C11	**85%**	**8.3**
	C26	**89%**	**8.7**
FLNC W2164C Hom	**C36R**	**84%**	**8.8**
	C72R	73%	13.5
	C82R	**80%**	**10.1**

Differentiation success is variable however, hence normalisation to sarcomere transcripts may be more accurate. Therefore, a relevant cardiac control is necessary. For instance, the conventional use of GAPDH may account for non-cardiomyocytes that may exist within a well of iPSC-CMs. When using cardiac markers, ACTN2 or TNNT2, compared to the conventionally used GAPDH control the spread of results can change (Figure 4-4). ACTN2 was chosen as the cardiac control for all iPSC-CM qPCR data presented in this due to the reduced variable distribution seen in Figure 4-4 and subsequent chapters as it aided in differentiation variability correction.

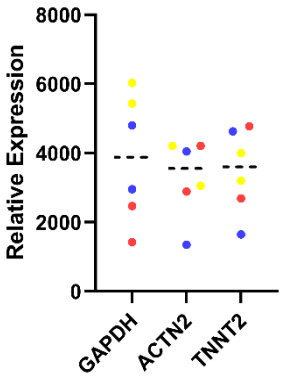

Figure 4-4 Quantitative RT-PCR of wild-type cardiac *TTN* transcript expression across three WT iPSC-CM differentiations (coloured appropriately). Transcript expression was normalised to either *GAPDH*, *ACTN2*, or *TNNT2* (cTnT) and expression of each marker was made relative to iPSC (Day 0). Each dot represents a result for an individual well.

4.3.1.2 Time course of differentiation in wild-type iPSC-CMs

The ventricular-specificity and maturity of generated iPSC-CMs was measured by the expression of specific cardiac transcripts and proteins in wild-type iPSC-CMs over time. The time-course experiment also presented an opportunity to determine the best point to conduct experiments on the mutant lines.

Undifferentiated wild-type iPSCs (Day 0) expressed no cardiac specific genes (Figure 4-5). At day 10, expression for all transcripts is observed. From day 20 onward, cardiac maturation and stabilisation is displayed. α-actinin (ACTN2), an indicator for sarcomere assembly activity, was expressed at a consistent rate post-differentiation. Both ventricular (*MYL2*, *MYH7*) and atrial (*MYL7, MYH6*) markers were expressed and enriched post-differentiation. Mirroring the differentiation success rates, there was no indication that the different iPSC WT clones had distinct iPSC-CM transcript profiles – validating the use of both iPSC-CM clones for further interrogation as a control. In contrast, there were distinct differences between individual iPSC-CM differentiation batches (Figure 4-5).

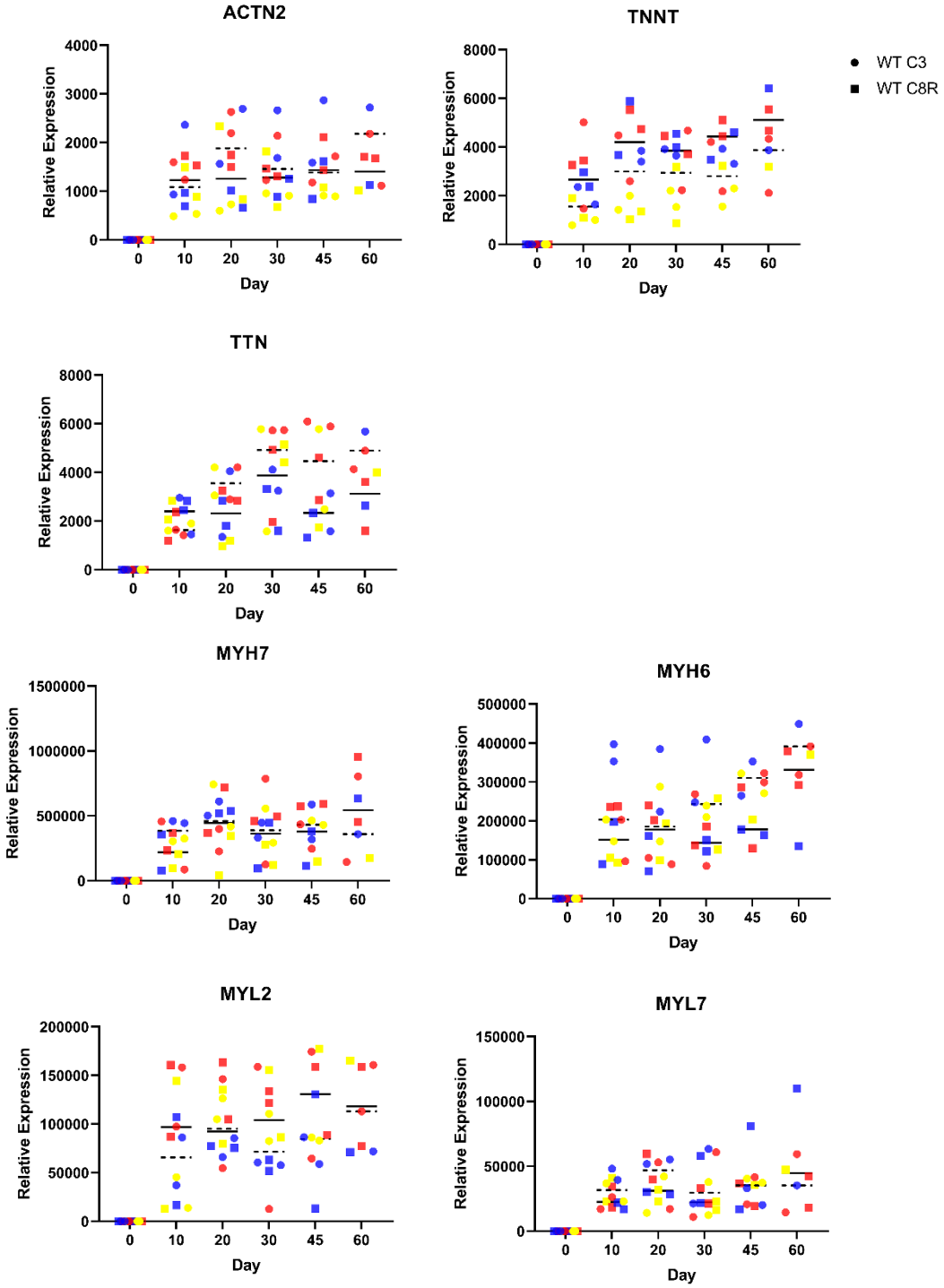

Figure 4-5 Quantitative RT-PCR of wild-type cardiac gene expression. WT C3 iPSC clones are shown as circles, WT C8R iPSC clones were shown as squares. Each colour represents a matched differentiation batch, the dotted line represents the mean of the WT C3 iPSC clone, the solid line represents the mean of the WT C8R iPSC line. n/d=2/3. Abbreviations: n/d = number of wells per differentiation/number of differentiations per genotype.

As with the transcript data, there was large variation between batches of iPSC-CMs at a protein level (Figure 4-6). The batch variability correlated with MLC2V and α-actinin expression – indicating the quality of the differentiations. From day 20, iPSC-CMs largely expressed proteins to the same level and hence day 20 and day 30 were chosen for reasonable time points for interrogating mutant iPSC-CMs. Day 20 represented early stage of sarcomerogenesis and day 30 as an accepted timepoint comparable with the literature (188,200,360).

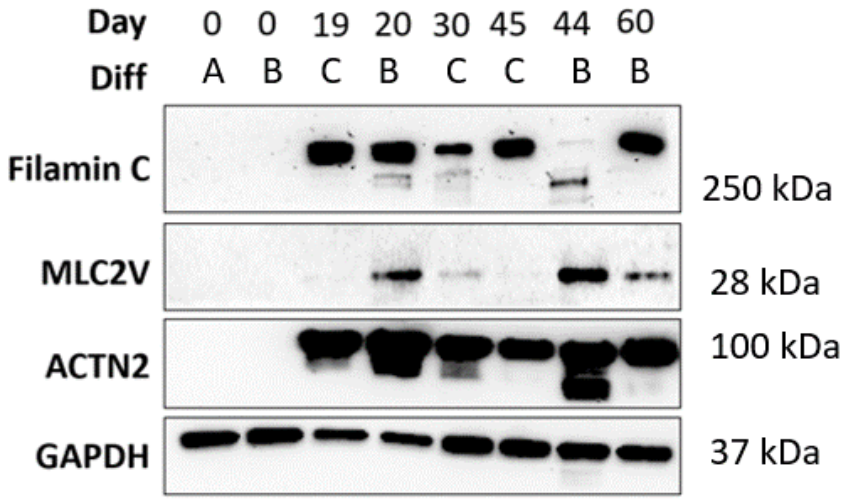

Figure 4-6 Protein expression in wild-type iPSC-CMs from Day 0 differentiation initiation and aged until 60 days. Samples are labelled as according to their differentiation batch (A, B, C) and age (Day 0 – iPSC). GAPDH was the control.

4.3.1.3 Flow cytometry characterisation

Flow cytometry analysis was done to quantify the expression of cardiac and ventricular-specific markers in 10 000 generated WT iPSC-CMs. Troponin T (cTnT), myosin light chain 2 (MLC2V) were present in all iPSC-CM lines at +90%, indicating a high iPSC-CM percentage purity. Data found 94 % positive staining for TNNT2 when compared to the negative control. Further flow cytometry data found the marker for MLC2V to be expressed in 96 % of cells (Figure 4-7).

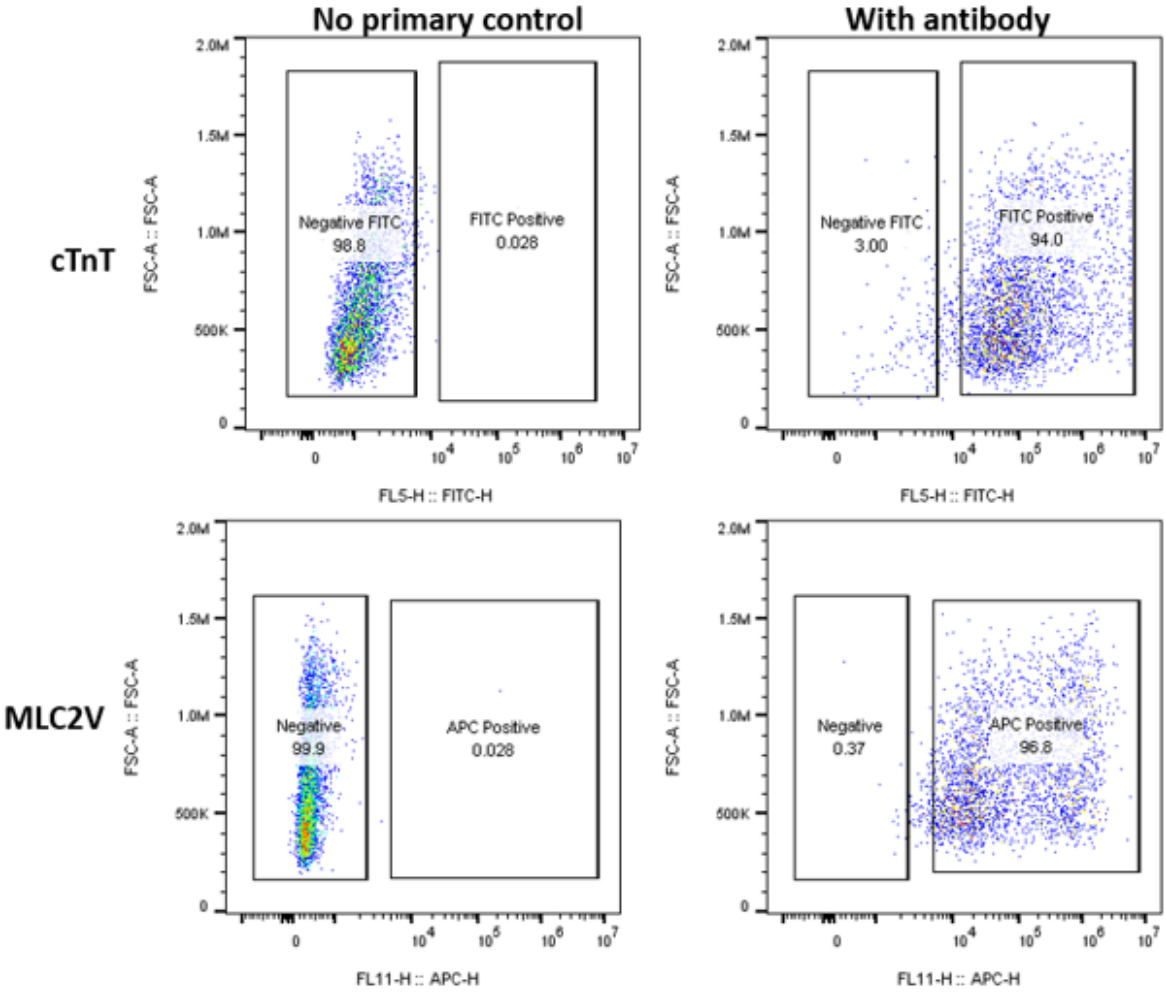

Figure 4-7 Fluorescent activated cell counting data in 30-day old WT iPSC-CMs. Cells were fixed and stained for TNNT (cTnT) and MLC2V.

4.3.1.4 Sarcomere and myofibrillar organisation

To confirm the structural integrity of the sarcomere and protein localisation relative to the sarcomere, WT iPSC-CM lines were immuno-stained for α-actinin, a marker for cardiomyocyte sarcomeres (Z-discs), which have a striated appearance. Regular α-actinin striations were observed in all generated cardiomyocytes with varied myofibrillar organisation within each well (Figure 4-8).

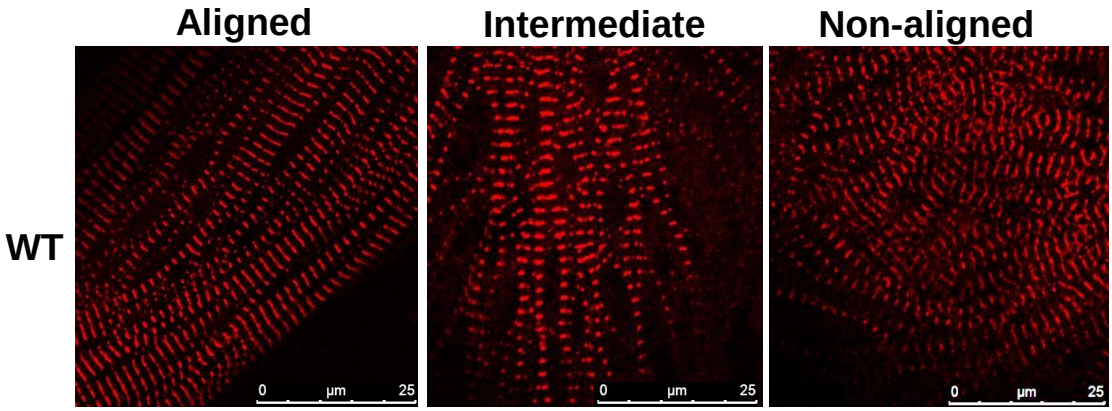

Figure 4-8 Myofibrillar organisation variation within the same WT iPSC-CM well. (α-actinin, red)

4.3.2 Interrogation of mutant iPSC-CMs

4.3.2.1 Changes at a transcript and protein level

Quantitative real-time PCR was done on WT, Het and Hom iPSC-CMs both at day 20 and at day 30. These dates were chosen as the mutant FLNC may interact differently with actin-rich pre-myofibrils (estimated to be at day 20) compared to the more mature sarcomeres at the widely used timepoint (day 30) (182,330,342,361).

Markers of the fetal gene programme: *MYH6, MYH7, ACTA1, NPPA* and *NPPB,* did not change between genotypes or age of iPSC-CM (Figure 4-9). *FLNC* W2164C variant carrying iPSC-CMs showed no differences of *FLNC* expression at transcript level at both day 20 and day 30 (Figure 4-10). Out of the remaining targets, *MYOT, HSPB1, HSPB7, FHL1* and

ANKRD1 showed no changes either at day 20 or day 30. There were no significant changes at transcript with differentiation day or genotype.

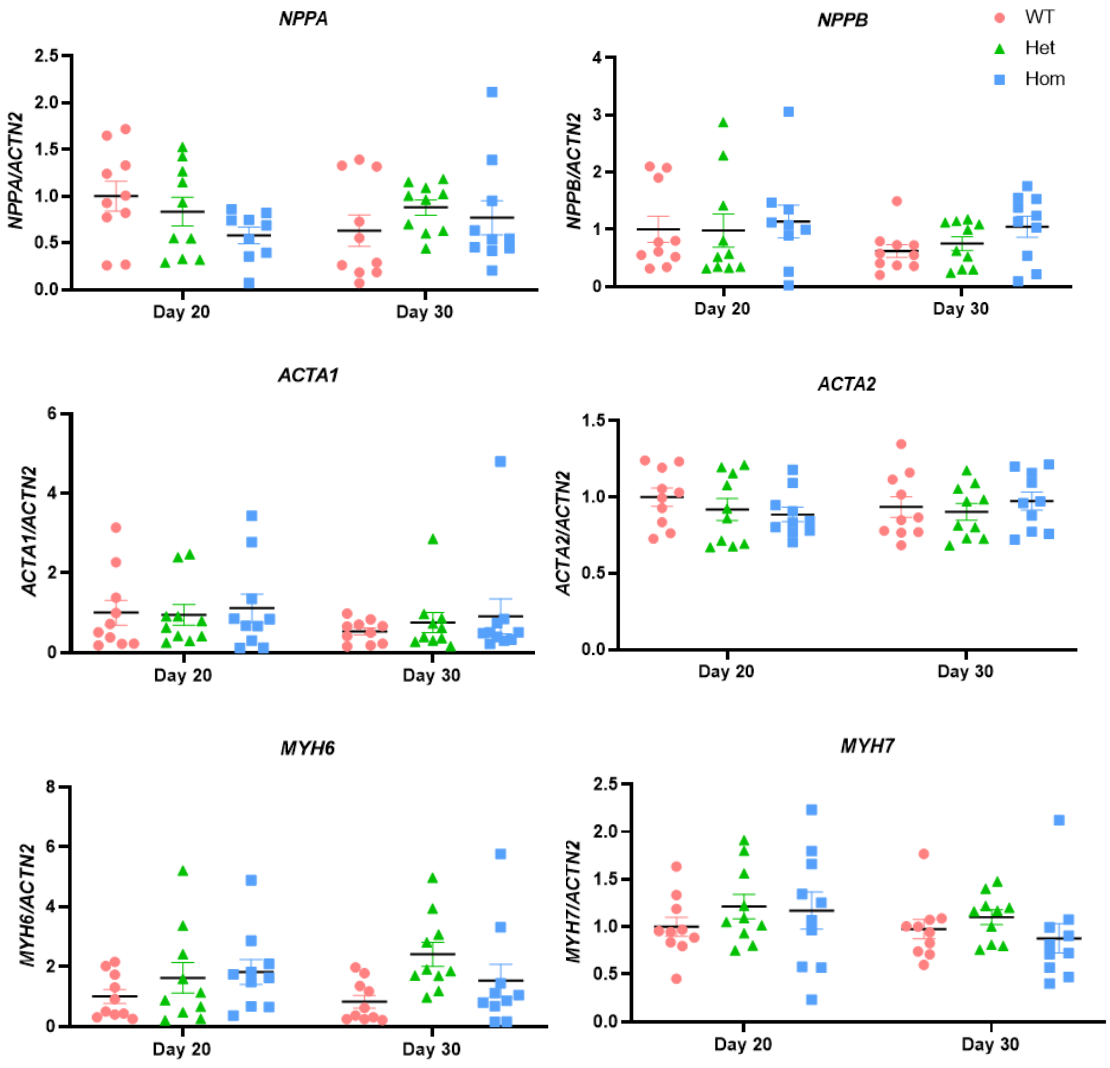

Figure 4-9 Targeted assessment of transcriptional changes of markers of the fetal gene programme in iPSC-CMs at day 20 and day 30. All measurements are normalised to *ACTN2* and presented as Mean+SEM; n/d=1-2/4-5 per group. 2-way ANOVA multiple comparisons test was conducted on normally distributed samples, no significant changes were observed. Abbreviations: n/d = number of wells per differentiation/number of differentiations per genotype.

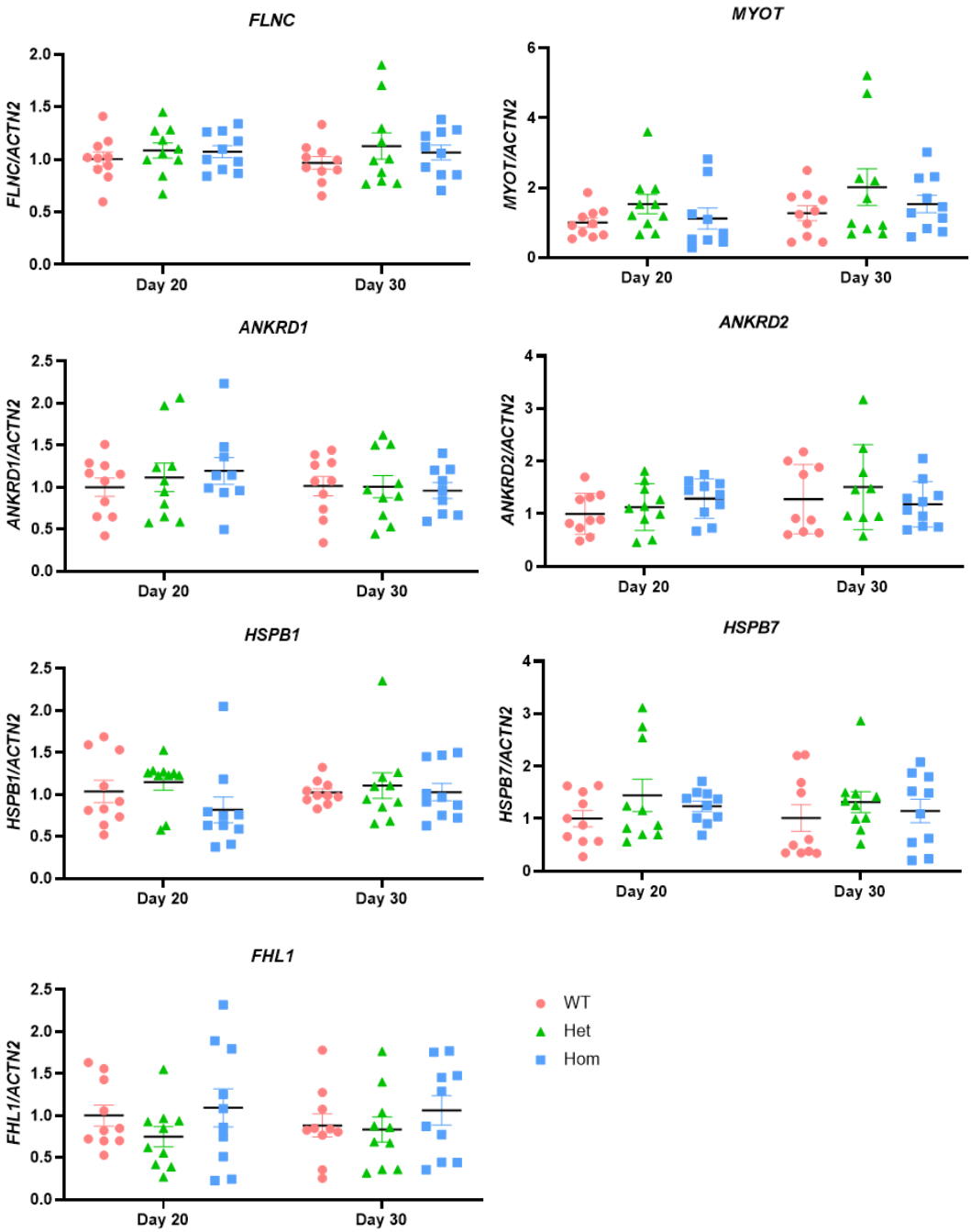

Figure 4-10 Targeted assessment of transcriptional changes of markers of FLNC, MYOT and hypertrophic markers in iPSC-CMs at day 20 and day 30. All measurements are normalised to *ACTN2* and presented as Mean+SEM; n/d=1-2/4-5 per group. 2-way ANOVA multiple comparisons test was conducted on normally distributed samples, no significant changes were observed . Abbreviations: n/d = number of wells per differentiation/number of differentiations per genotype.

Immunoblotting of cells at day 30 found only XIRP1 to be differentially expressed in mutant iPSC-CMs. XIRP1 was found to be significantly reduced in both Het and Hom iPSC-CMs relative to WT cells. Relative to ACTN2 abundance, the abundance of FLNC and MYOT in Het iPSC-CMs trended towards an increase, in agreement with the mouse model immuno-blots, though this was not significant (Figure 4-11). Significance was only found in the reduction of XIRP1 in Het and Hom iPSC-CMs. No significant differences were found in MYH7. Again, although not significant, HSPB1 and HSPB7 trended towards an upregulation in only Hom iPSC-CMs. To note, ACTN2 staining for Hom iPSC-CMs was not consistent and is likely to be skewing the results.

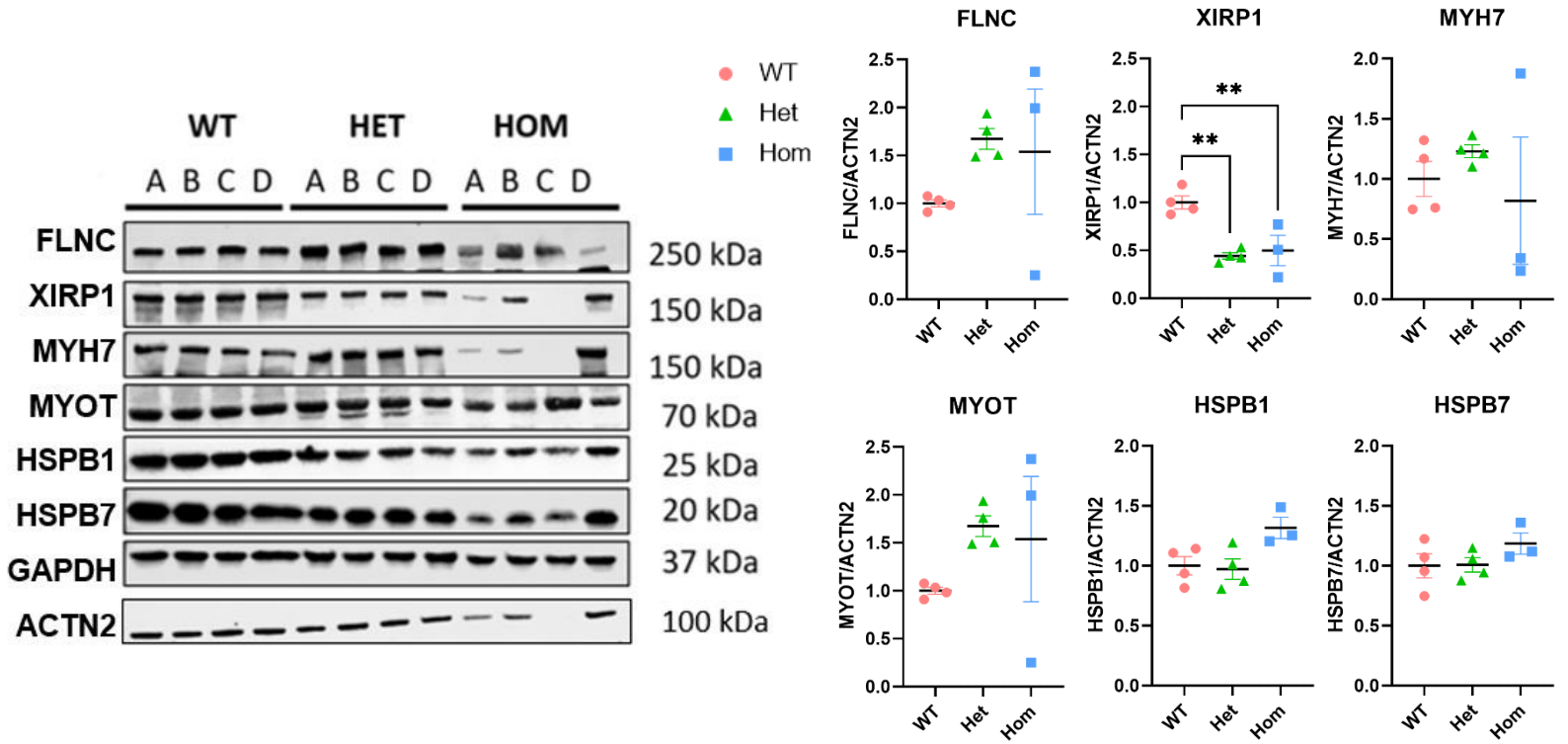

Figure 4-11 Immunoblots of WT, Het and Hom iPSC-CMs at day 30. Densitometry was used to quantify the values and was normalised to ACTN2. One-way ANOVA was used to analyse normally distributed data, n/d=1/4, Hom C has been excluded from analysis due to a lack of expression of the cardiac control marker Actn2. ($p<0.01$, **; versus WT). Abbreviations: n/d = number of wells per differentiation/number of differentiations per genotype.

4.3.2.2 Myofibrillar arrangement

The Z-line length represents the width of each singular Z-disc and the mean sarcomere length is the length between two Z-discs and is determined by α-actinin staining (red). Between WT, Het and Hom iPSC-CMs, both of these parameters were found to be unchanged (Figure 4-12). The regular α-actinin staining indicates that Z-disc sarcomere integrity is maintained between WT (1.10±0.08 µm), Het (1.10±0.11 µm) and Hom (1.11±0.08 µm) lines, though are much shorter than mature sarcomere length ~2 µm (362). The Z-line skewness, a measure of myofibrrilar arrangement, was unaffected in cells harbouring the *FLNC* W2164C variant.

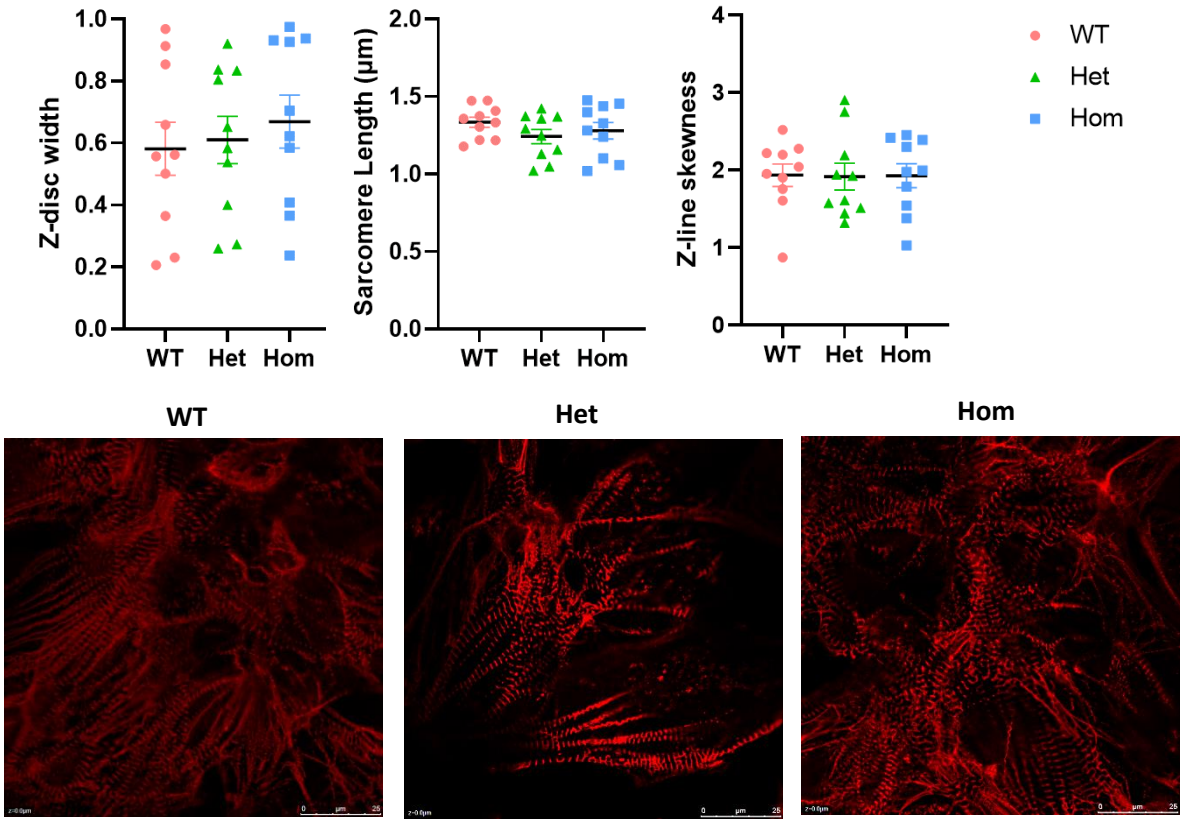

Figure 4-12 Z-line and sarcomere continuous lengths in WT, Het and Hom iPSC-CMs. iPSC-CMs were stained for alpha-actinin (red) at Day 30 and underwent a one-way ANOVA. n/d = 2-3/4. Abbreviations: n/d = number of wells per differentiation/number of differentiations per genotype.

4.3.2.3 Cell size

The FLNC W2164C variant results in HCM in patients. A hallmark of HCM is myocyte hypertrophy (363), therefore, performing cell size analyses using machine learning tools such as CellPose 2.0 on immunofluorescent images of iPSC-CMs can provide an unbiased and accurate determination of cellular hypertrophy (Figure 4-13).

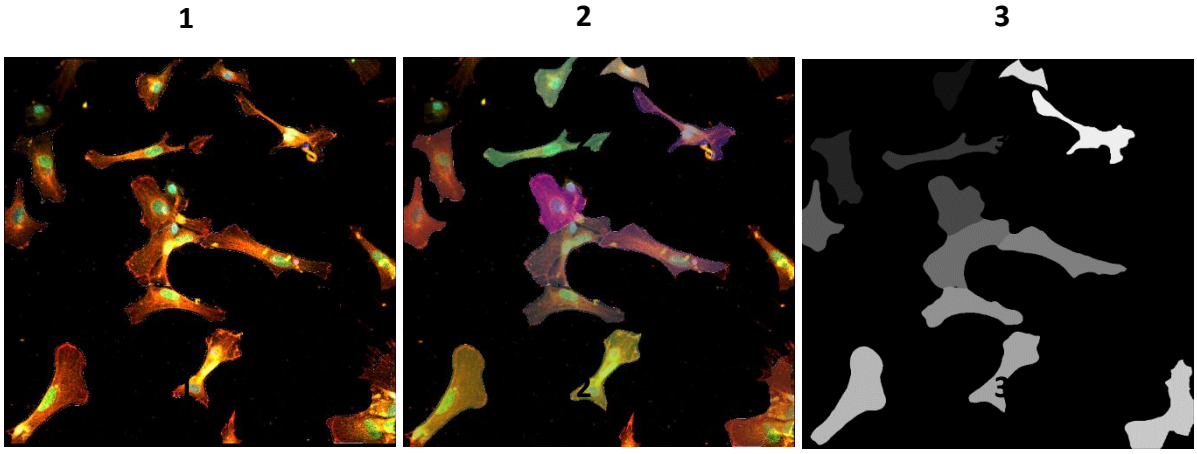

Figure 4-13 Example image of CellPose 2.0 data pre-processing from raw image (left) to full mask (right). (1) showing the input raw image. (2) using a neural network, a mask is predicted by CellPose to segment the cells and undergo gradient tracking. (3) All pixels that converged to an identical fixed point as identified by the gradient tracking are assigned to the same mask. Cells are stained with ACTN2, a sarcomere marker (red), myotilin (green) and DAPI (blue). CellPose 2.0 only used the sarcomere marker and DAPI as a reference point for data processing.

Across 153 WT and 147 Hom iPSC-CMs, there were no significant differences observed in cell size (Figure 4-14). A large variation in cell size was seen, with cell size ranging between 400 μm^2 and 2384 μm^2. iPSC-CMs generated in this thesis are mostly smaller than adult ventricular cardiomyocytes which have a cell area between 2000 μm^2 and 5250 μm^2 (364).

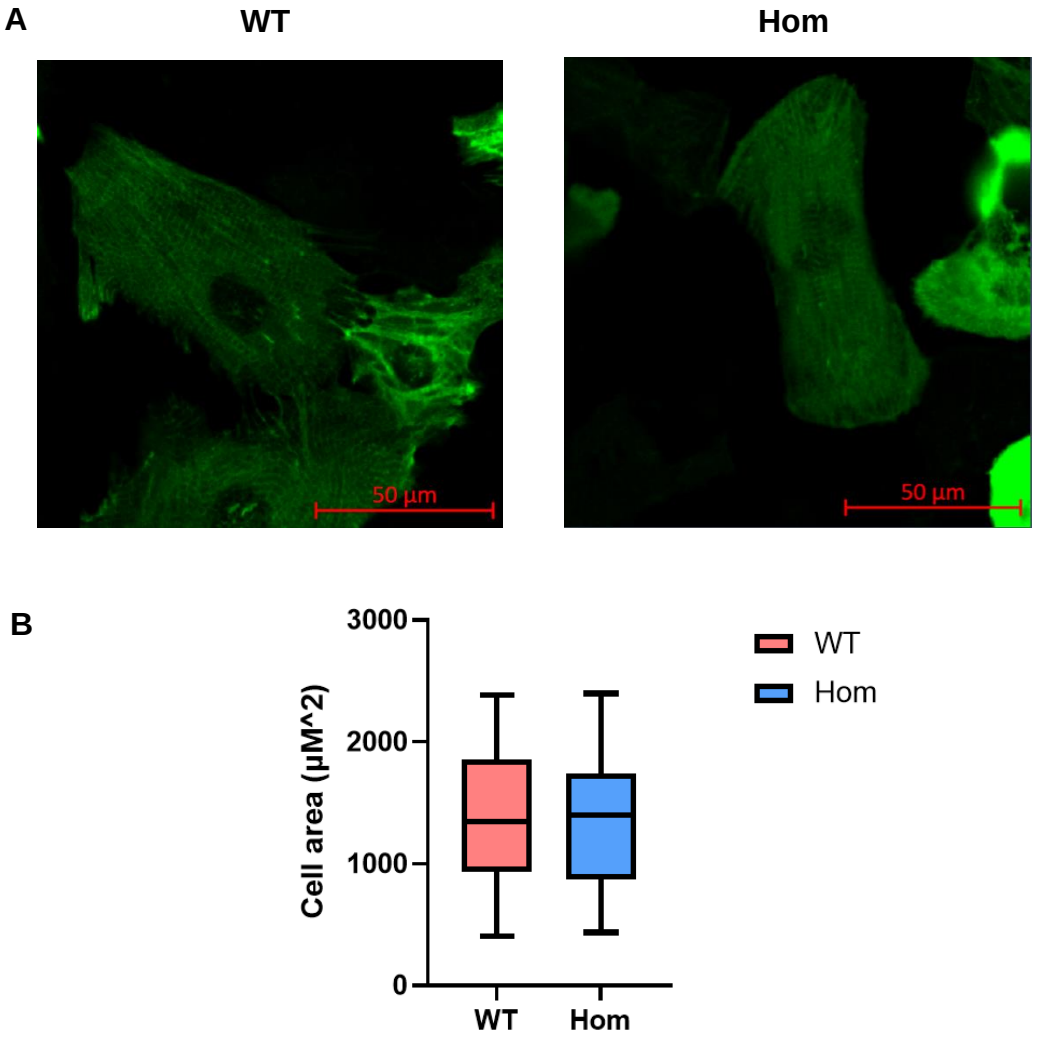

Figure 4-14 Image of WT and Hom iPSC-CMs and the CellPose 2.0 estimated cell area. (A) Raw image of a WT and Hom iPSC-CM for CellPose 2.0 data processing. (B) Box and whiskers plot to show the output of Cell Area as predicted by CellPose 2.0 between genotypes. iPSC-CMs were cultured on glass coverslips with GelTrex coating. Cells are stained with ACTN2, a sarcomere marker (green). CellPose 2.0 only used the sarcomere marker and DAPI as a reference point for data processing. N/n/d = 80-154/1-3/3. Significance was measured by a Student's t test. Abbreviations: N/n/d = number of cells anlysed per condition/number of wells analysed per differentiation/number of differentiations per genotype.

4.3.2.4 Analysis of contractile parameters

To assess whether iPSC-CMs harbouring the homozygous FLNC W2164C variant had altered function, the sarcomere lengths were tracked using SarcTrack (200) to measure the contraction and relaxation durations, peak contracted and peak relaxation SLs and percent contraction (Video 1). SarcTrack works by using a MatLab algorithm to track these parameters on live-cells which have undergone adenoviral transduction to express Actn2 GFP to visualise the Z-disc and hence measure contraction as the Z-discs are pulled.

Many of the iPSC-CMs reported a resting frequency above 1 Hz, therefore pacing was required at 2 Hz which may affect the cardiomyocyte when in relaxation. When comparing WT and Hom iPSC-CMs, there were no differences or observable trends reported in average contraction (WT = 276±58 ms, Hom = 279±55 ms) and relaxation times (WT = 291±51 ms, Hom = 290±50 ms) (Figure 4-15). The average contracted (WT = 1.73±0.09 µm, Hom = 1.73±0.08 µm) and relaxed sarcomere lengths (WT = 1.89±0.08 µm, Hom =1.89±0.08 µm) also showed no differences although were very different compared to the numbers observed by zline-detection (Figure 4-12). No trends between WT and Hom iPSC-CMs were reported by SarcTrack in contraction percentage (WT = 8.4±2.2 %, Hom = 8.2±2.3 %).

Video 4 QR code linking to a video of WT and Hom iPSC-CMs contracting with their sarcomeres tagged for Actn2 GFP visualising the Z-disc expressed via adenoviral transduction. Cells were paced at 2 Hz for recordings.

Thesis SarcTrack Video - YouTube

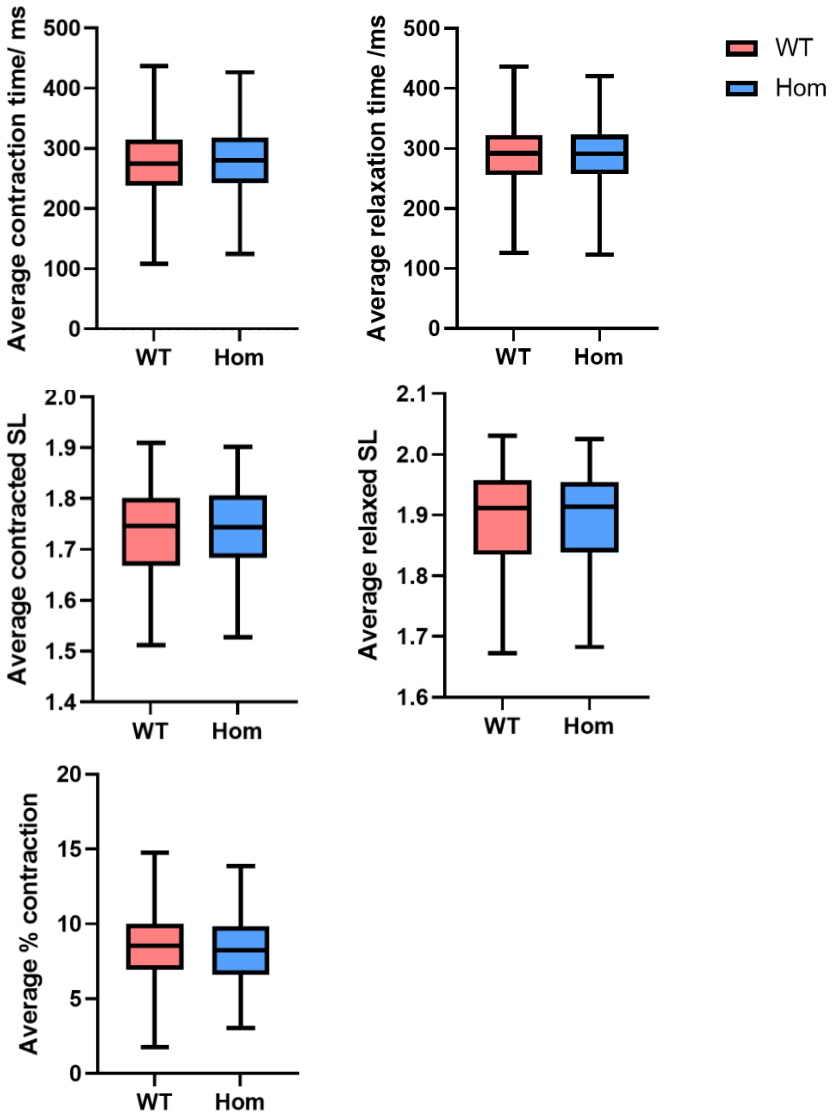

Figure 4-15 Contractile parameters between WT and Hom iPSC-CMs while being paced at 2 Hz and assessed via the SarcTrack algorithm. The average contraction and relaxation times were assessed as well as the average sarcomere lengths for both contraction and relaxed. The average percent contraction was also measured. n/d = Significance was determined by a Student's *t* test. Abbreviations: n/d = number of wells analysed per differentiation/number of differentiations per genotype.

4.3.2.5 Mitochondrial function of mutant iPSC-CMs

To follow-up the suggested downregulation of mitochondrial proteins in the membrane-enriched fraction of murine cardiac tissue (Figure 3-7), a basic mitochondrial function experiment was performed on live iPSC-CMs. The JC-10 dye detects mitochondrial membrane potential based on the formation of aggregates in the mitochondrial matrix where it fluoresces as red or stains cells green in apoptotic cells as the monomeric JC-10. Mutant iPSC-CMs showed comparable functional mitochondrial activity (displayed as red) with WT iPSC-CMs (Figure 4-16) and neither group showed relative increases in inactive organelles (displayed as green). As seen on the JC-10 fluorescence ratio plot (Figure 4-16B), iPSC-CMs showed a higher amount of low membrane potential compared to high membrane potential in the cells but between genotypes there was no difference in fluorescence ratio. This suggests normal mitochondrial activity in the mutant cells.

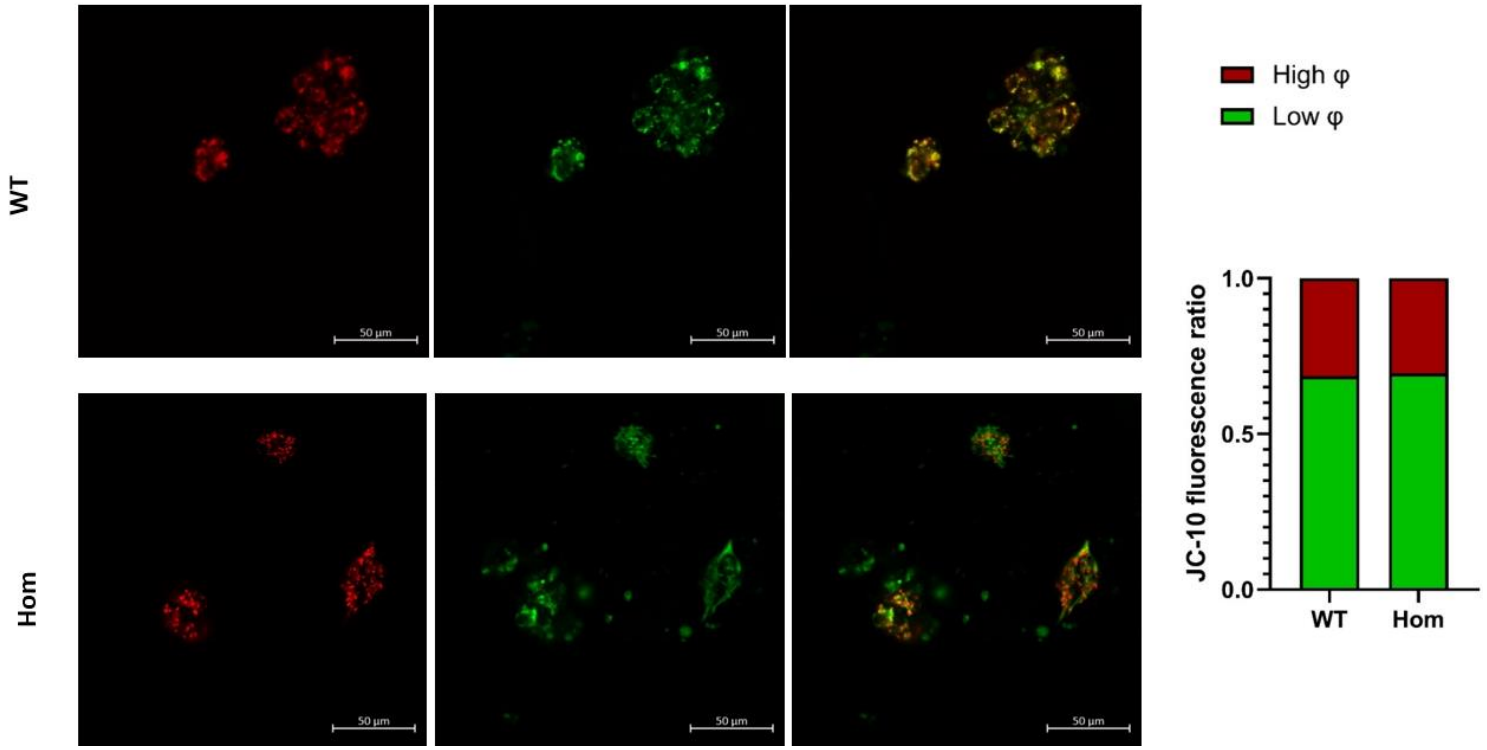

Figure 4-16 Mitochondrial staining with JC-10 dye on the 30th day of iPSC-CM in-vitro differentiation culture. High membrane potential is displayed red, while low membrane potential is shown as green. 6 cells of each of the 3 independent differentiation batches per genotype were tested.

4.3.3 Characterisation of mutant iPSC-CMs with isoprenaline treatment

Isoprenaline (ISO) is a nonselective beta-adrenergic agonist which is widely used to induce heart failure in mice and can mimic stress-induced cardiomyopathy (169,365). ISO (100 µM for 3 days) was used to unmask potential differences between genotypes. Basic characterisation was performed. This work was carried out in parallel to the decision to switch to use only WT and Hom iPSC-CMs for characterisation. Therefore, this work shows the characterisation of Het iPSC-CMs under ISO while some parameters in the previous and subsequent sections do not.

4.3.3.1.1 Beating frequency

Firstly, the beating frequency was characterised by counting the number of beats in a timed interval within 2 minutes of removing from the incubator. In the presence of ISO, there was no statistically significant difference in beating frequency across 4 batches of differentiations each (Figure 4-17). To note, a small increase in beating frequency was observed in ISO-treated cells compared to DMSO though this was not found to be statistically significant.

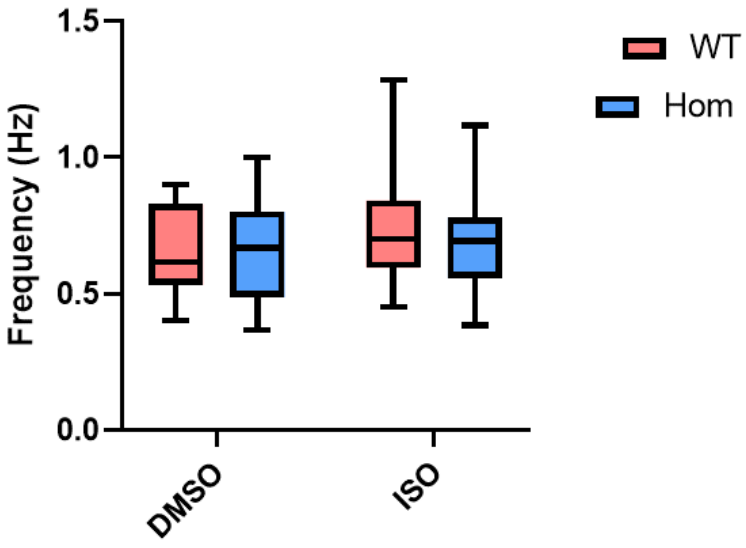

Figure 4-17 Beating frequency of WT and Hom iPSC-CMs at day 30 when under DMSO or ISO treatment. n/d=13/4. Abbreviations: n/d = number of wells per differentiation/number of differentiations per genotype.

4.3.4 Gene expression in iPSC-CMs under ISO

Transcript expression of the mutant iPSC-CMs after DMSO treatment (Figure 4-18 & Figure 4-19) showed no trends compared in iPSC-CMs at baseline (Figure 4-19 & Figure 4-20). Genes involved in the fetal gene programme (N*PPA, NPPB, MYH7 ACTA1*) remained unchanged as did *FLNC* and *MYOT*. Markers linked to hypertrophic signalling (*ANKRD1, ANKRD2, FHL1*) showed no significant trends.

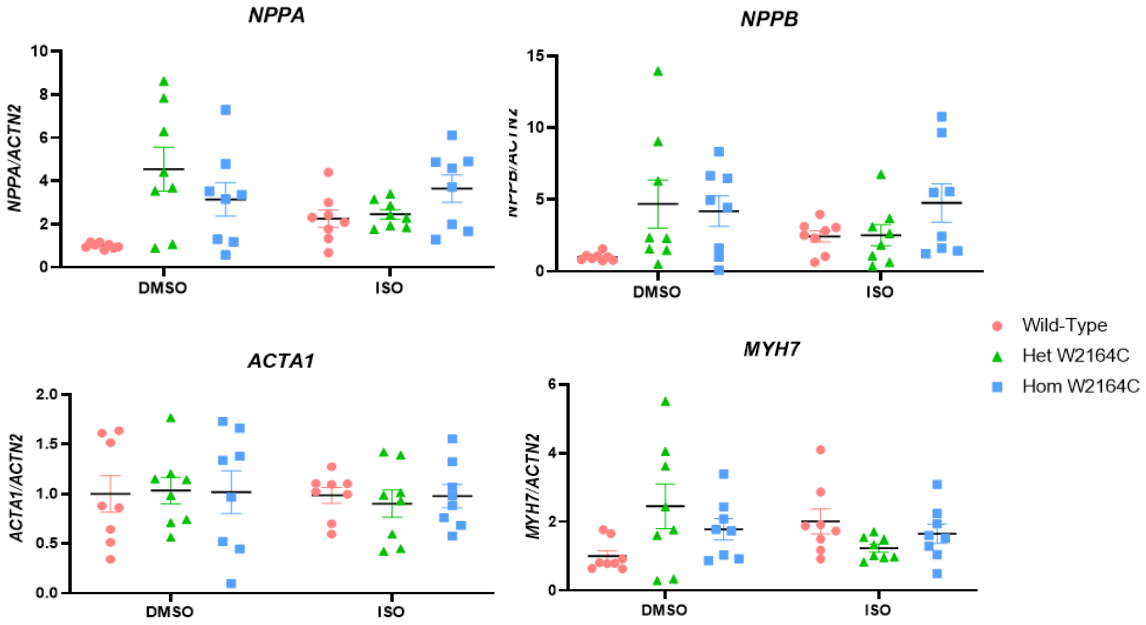

Figure 4-18 Targeted assessment of transcriptional changes of markers of the fetal gene programme in iPSC-CMs under DMSO or ISO treatment. All measurements are normalised to *ACTN2* and presented as Mean+SEM; n/d=1-2/4 per group. 2-way ANOVA multiple comparisons test was conducted on normally distributed samples. Abbreviations: n/d = number of wells per differentiation/number of differentiations per genotype.

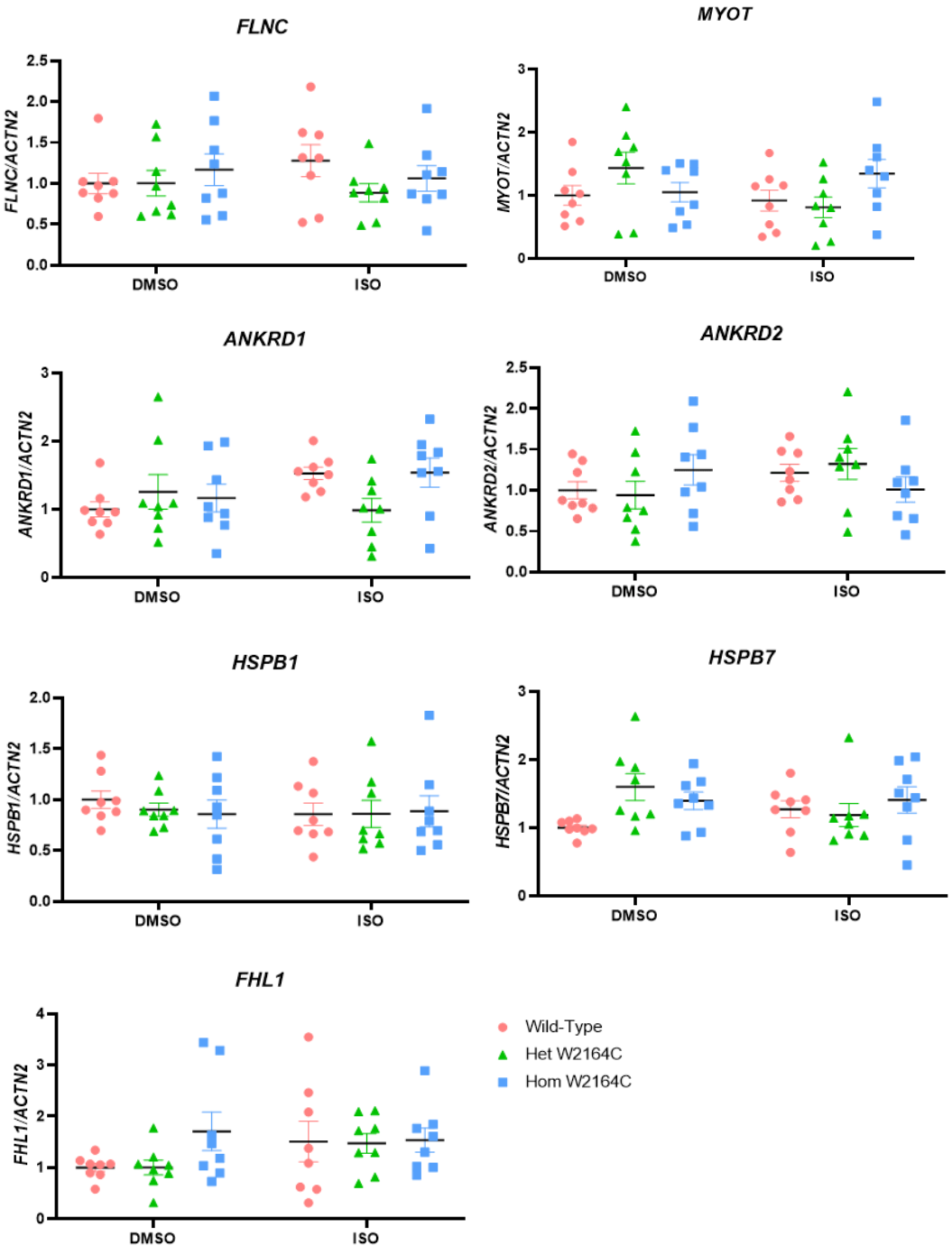

Figure 4-19 Targeted assessment of transcriptional changes of markers of hypertrophic markers and FLNC and MYOT. Normalised to *ACTN2* and presented as Mean+SEM; n/d=1-2/4 per group. 2-way ANOVA multiple comparisons test was conducted on normally distributed samples. Abbreviations: n/d = number of wells per differentiation/number of differentiations per genotype.

4.3.5 Protein levels in iPSC-CMs under ISO

At a transcript level there were no significant trends observed when iPSC-CMs were treated with ISO. Except for FBLIM1, the same was true when looking at immunoblots, no trends or differences in protein levels appear to be present in iPSC-CMs when treated with ISO compared to DMSO treatment (Figure 4-20). FBIM1, which was found to be significantly reduced in Hom mice by proteomics (3.3.4.2), was found to be significantly reduced in response to ISO in WT iPSC-CMs. Significant genotype differences were not observed in FBLIM1. The three significantly upregulated proteins from the proteomics in the myofilament fraction (Flnc, Myh7, Myot) were also measured at transcript level in iPSC-CMs with either DMSO or ISO treatment though no clear trends were observed in Het or Hom iPSC-CMs relative to WT counterparts.

Note: From this point onwards, all comprehensive characterisation was normalised to cardiac troponin T (cTnT), for both immunoblotting and transcript analysis.

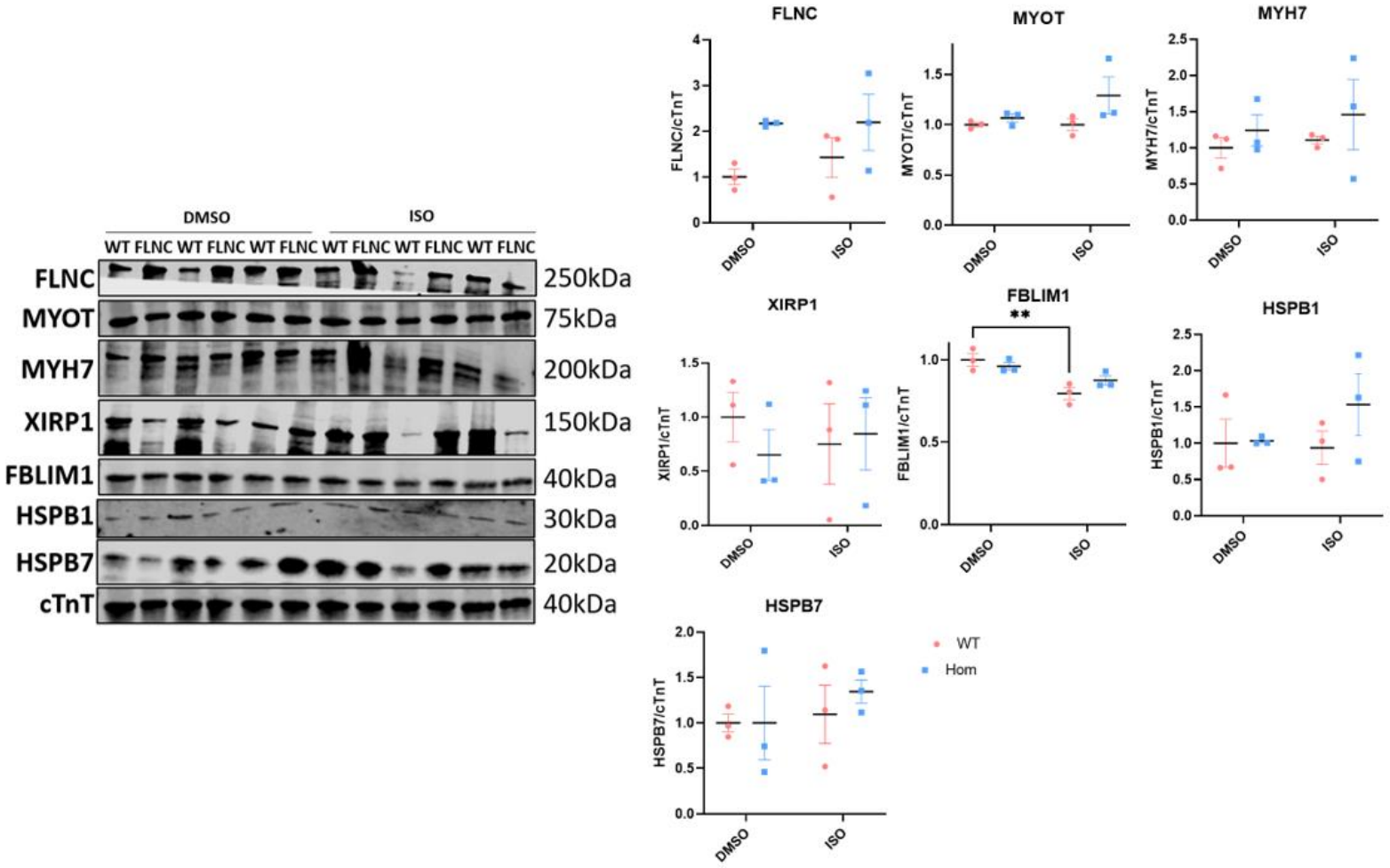

Figure 4-20 Targeted assessment of protein changes of markers of FLNC, MYOT, FBLIM1 and hypertrophic markers in iPSC-CMs under DMSO or ISO treatment in WT and Hom cells. All measurements are normalised to *cTnT* and presented as Mean+SEM; n/d=1/3 per group. Data was normally distributed and underwent a 2-way ANOVA. ($p<0.01$, **; versus WT). Abbreviations: n/d = number of wells per differentiation/number of differentiations per genotype.

4.3.6 Interrogation of mutant iPSC-CMs on physiological stiffness

In this part of the chapter, iPSC-CMs were cultured on PDMS substrates of physiological adult healthy (20 kPa) and fibrotic (130 kPa) stiffnesses. Glass coverslips were the chosen stiff control surface for all work for practical consistency. All work on iPSC-CMs cultured on PDMS was conducted on WT and Hom *FLNC* W2164C cell lines only. Cardiomyocytes underwent molecular and functional characterisation as described previously.

4.3.6.1 iPSC-CM maturation on PDMS substrates

To test if culturing iPSC-CMs on PDMS substrates of variable stiffness induced maturation, maturation markers at a transcript level were chosen to indicate the various maturation levels: ratios of the titin isoforms (*N2BA/N2B*) and myosin heavy chain isoforms (*MYH7/MYH6*) markers indicate sarcomere maturation and the decrease of *HK2* and increase of *PDK4* indicate metabolic maturity.

Wild-type iPSC-CMs cultured on PDMS still predominantly express the N2BA isoform of titin, though relative to cell culture on glass, the *N2BA/N2B* ratio was significantly reduced (Figure 4-21). Though not significant, the relative *MYH7/MYH6* ratio increasing when cultured on the less rigid PDMS surfaces. The mitochondrial enzyme linked to enhanced fatty acid oxidation, pyruvate dehydrogenase lipoamide kinase isozyme 4, encoded by the gene *PDK4,* increased significantly when on PDMS of 130 kPa. The gene *HK2,* encoding hexokinase 2, is reduced in mature cardiomyocytes, however, did not show any significant trend when cultured on soft substrates.

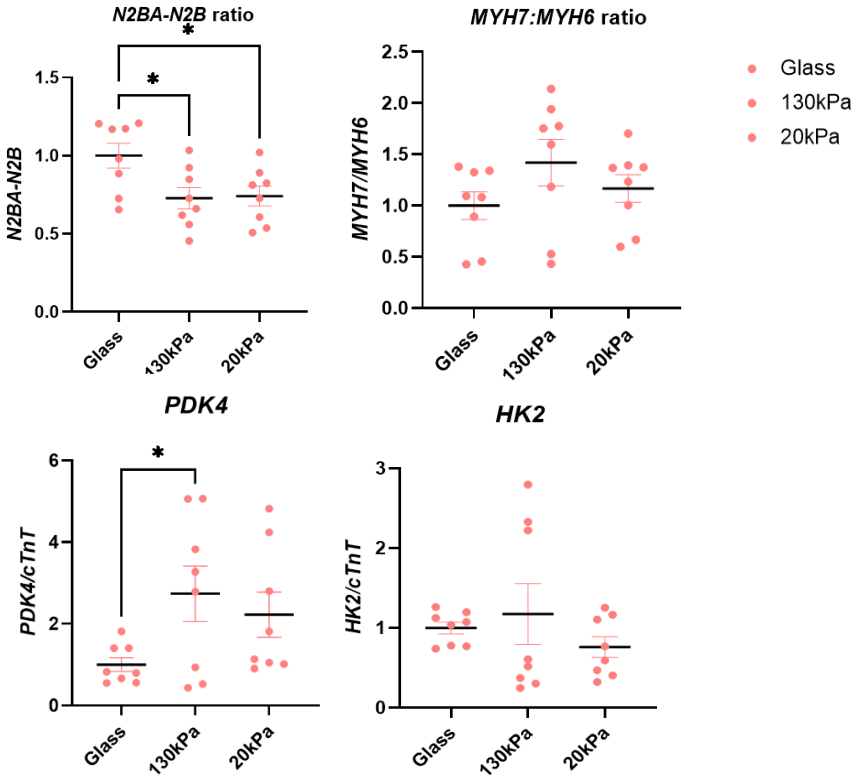

Figure 4-21 Transcript expression of cardiac maturity markers on 30-day old WT iPSC-CMs. Data was relative to glass WT and expression was relative to cTnT. Samples underwent a one-way ANOVA. n/d = 2/4. ($p<0.05$, *; versus WT). Abbreviations: n/d = number of wells per differentiation/number of differentiations per genotype.

4.3.6.2 Transcript expression of mutant iPSC-CMs on PDMS

The same targets were probed for in the iPSC-CMs on PDMS of varying stiffnesses to provide direct comparisons between other experiments used in this chapter. Additional targets were identified since initial characterisation on 2D plastics or ISO experiments, and were also probed for at transcript level. There was a significant induction in genes related to the fetal gene programme (Figure 4-22). Relative to glass-cultured cells, when cultured on 20 kPa, Hom iPSC-CMs showed an increased level of significance compared to the WT counterparts (*NPPA*, *MYH7*, *ACTA1*). Genes linked to hypertrophic signalling were unaffected on either glass or PDMS surfaces (*ANKRD1*, *ANKRD2*, *FHL1*) (Figure 4-23).

The expression of *MYOT* and *FLNC* did not change between genotypes or stiffness at a transcript level (Figure 4-23).

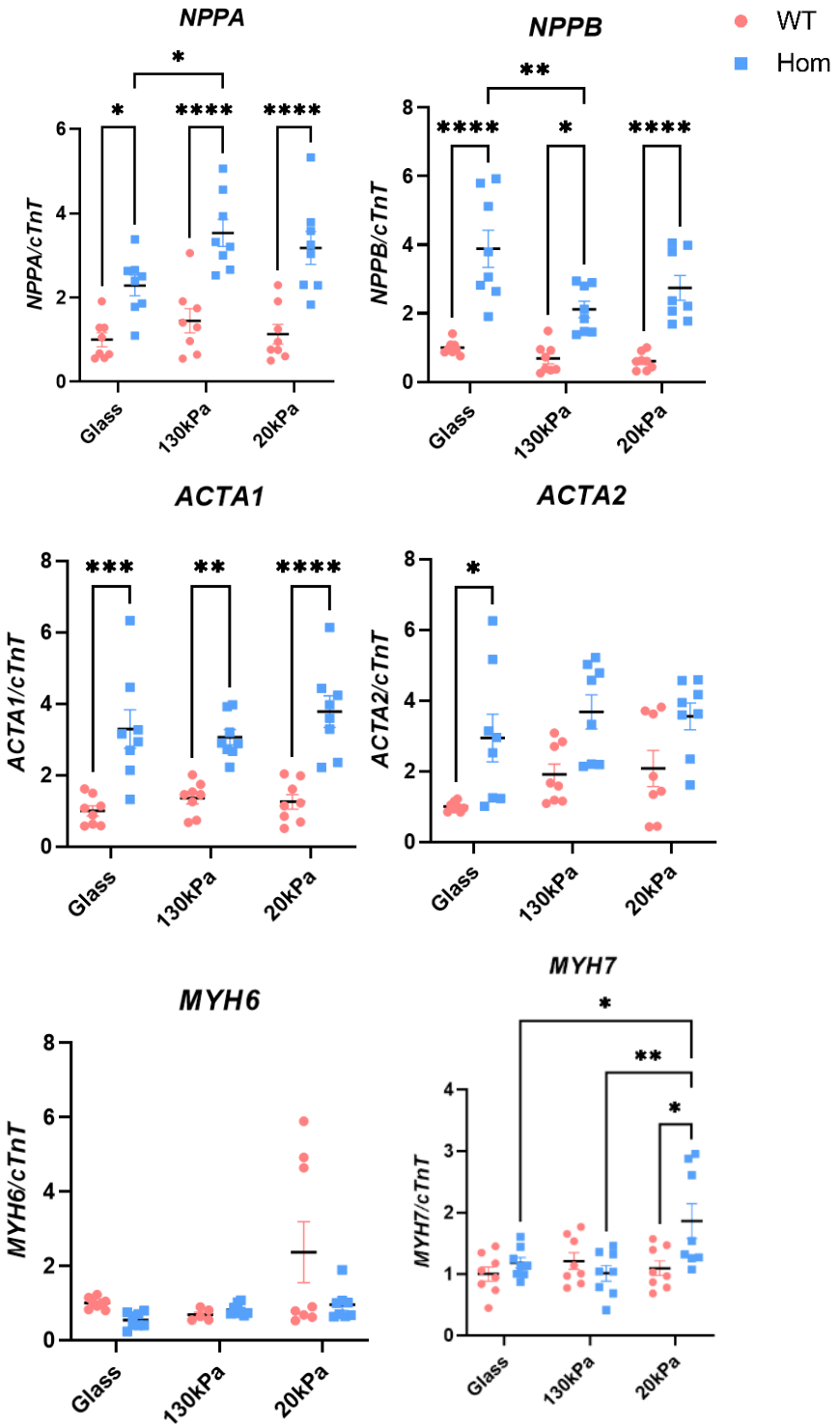

Figure 4-22 Targeted assessment of transcriptional changes of markers of the fetal gene programme in iPSC-CMs when cultured on either 130 kPa or 20 kPa PDMS surfaces. All measurements are normalised to cTnT and made relative to WT; n/d=1-2/4 per group. 2-way ANOVA multiple comparisons test was conducted on normally distributed samples. ($p<0.05$, *; $p<0.01$, **; $p<0.001$, ***; $p<0.0001$, ****; versus WT). Abbreviations: n/d = number of wells per differentiation/number of differentiations per genotype.

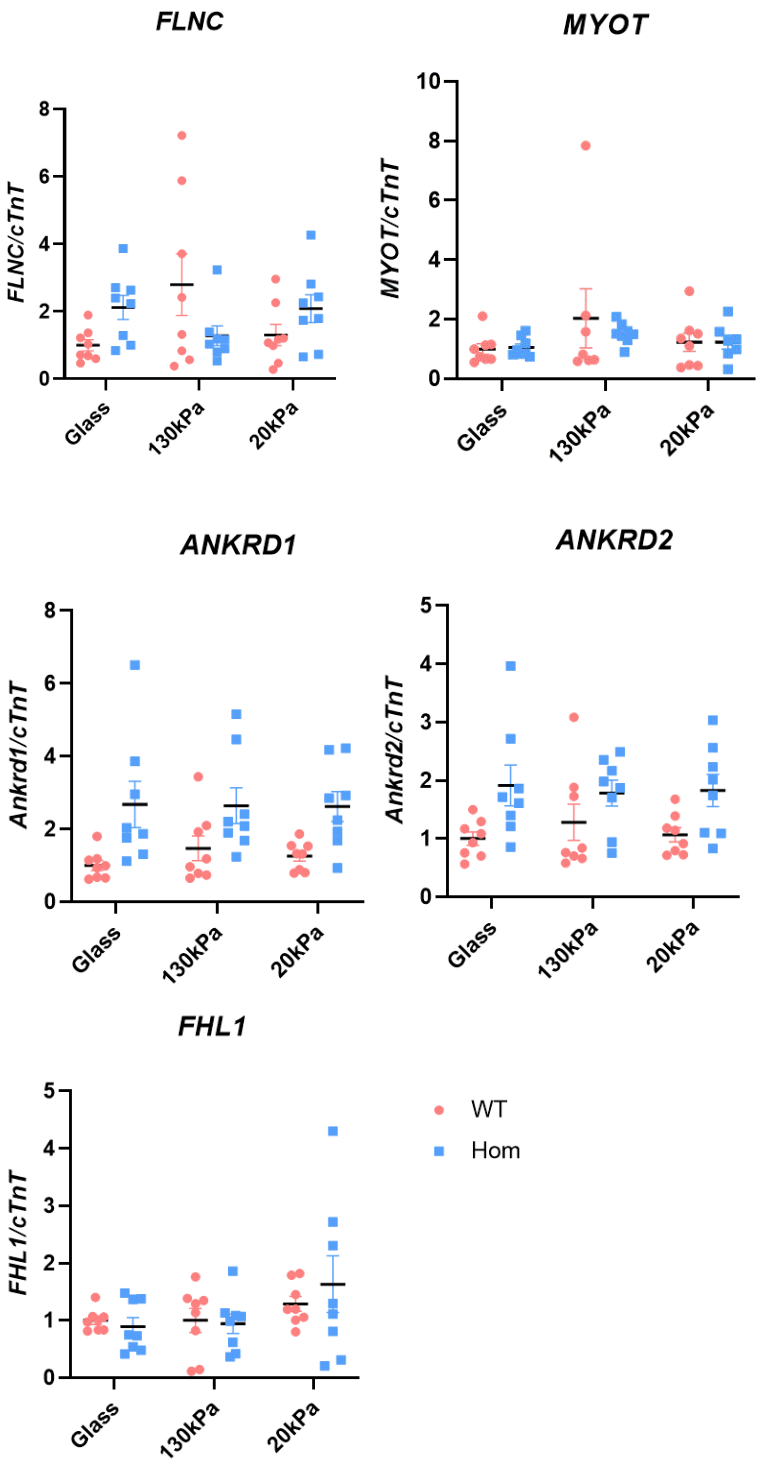

Figure 4-23 Targeted assessment of transcriptional changes of hypertrophic markers markers in iPSC-CMs when cultured on either 130 kPa or 20 kPa PDMS surfaces. All measurements are normalised to cTnT and made relative to WT; n/d=1-2/4 per group. 2-way ANOVA multiple comparisons test was conducted on normally distributed samples. Abbreviations: n/d = number of wells per differentiation/number of differentiations per genotype.

4.3.6.3 Protein expression of mutant iPSC-CMs on PDMS

Cells cultured on physiological healthy (20kPa) and fibrotic (130kPa) stiffnesses were immunoblotted for markers identified in Chapter 3. FLNC showed a trend towards increase in 20 kPa conditions, however, this did not reach significance (Figure 4-24). Significance was reached when measuring MYH7 at 20 kPa between WT and Hom cells, comparable to the mouse. Both HSPB1 and HSPB7 displayed significant increases between WT and Hom cells at 130kPa. As stiffness is reduced from 130 kPa to 20 kPa, Hom iPSC-CM protein expression of HSPB1 and HSPB7 is comparable with WT and significantly lower than Hom iPSC-CM expression at 130kPa. MYOT and FBLIM1 was not found to be altered between 130 kPa or 20 kPa in either genotype.

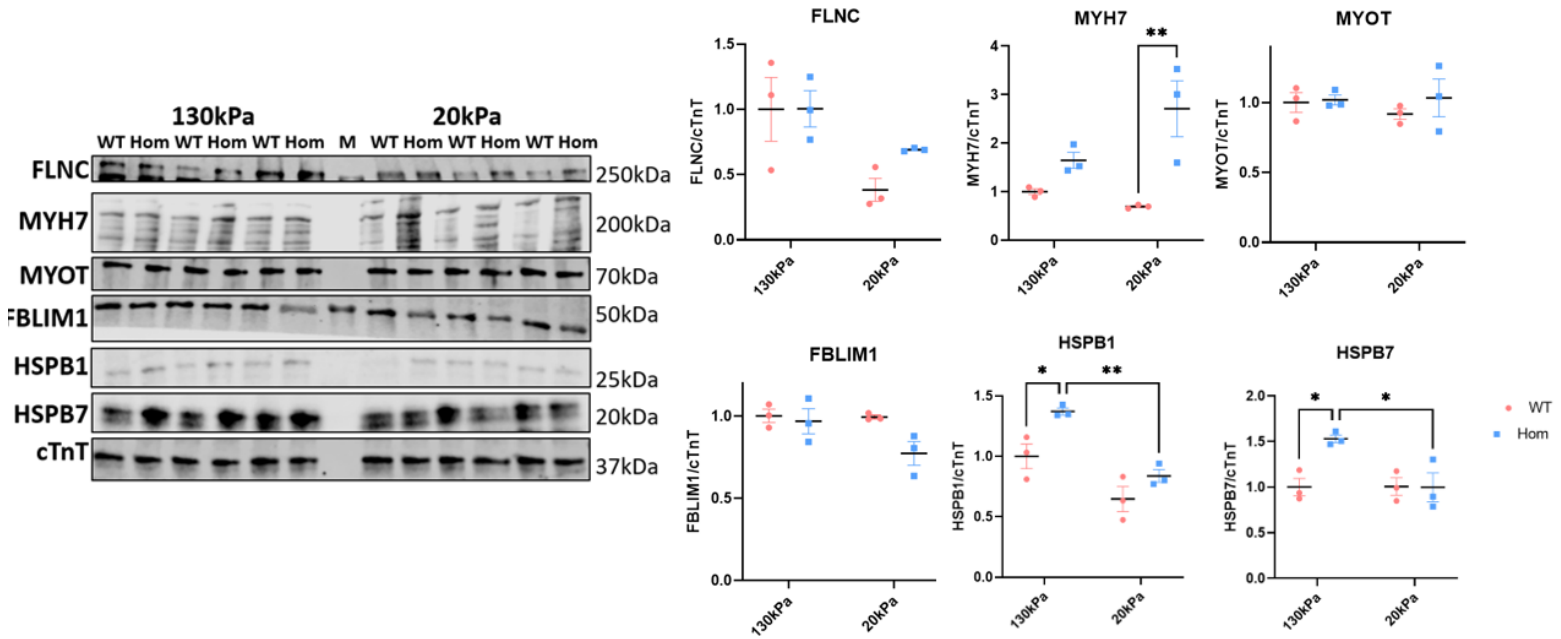

Figure 4-24 Targeted assessment of protein changes of markers FLNC, MYOT, FBLIM1 and hypertrophic markers in iPSC-CMs when cultured on either 130 kPa or 20 kPa PDMS surfaces. All measurements are normalised to *cTnT* and made relative to WT 130.kPa. Data is presented as Mean+SEM; n/d=1/3 per group. Data was normally distributed and underwent a 2-way ANOVA. ($p<0.05$, *; $p<0.01$, **; versus WT). Abbreviations: n/d, number of wells per differentiation/number of differentiations per genotype; PDMS, polymethyldioxysilone.

4.3.6.4 Beating rate of mutant iPSC-CMs on PDMS

The beating frequency of iPSC-CMs on PDMS was significantly reduced compared to glass-cultured iPSC-CMs (Figure 4-25). In a stiffness-dependent manner, both WT and Hom cells beat with a reduced frequency correlative with decreased surface stiffness as well as increased maturity.

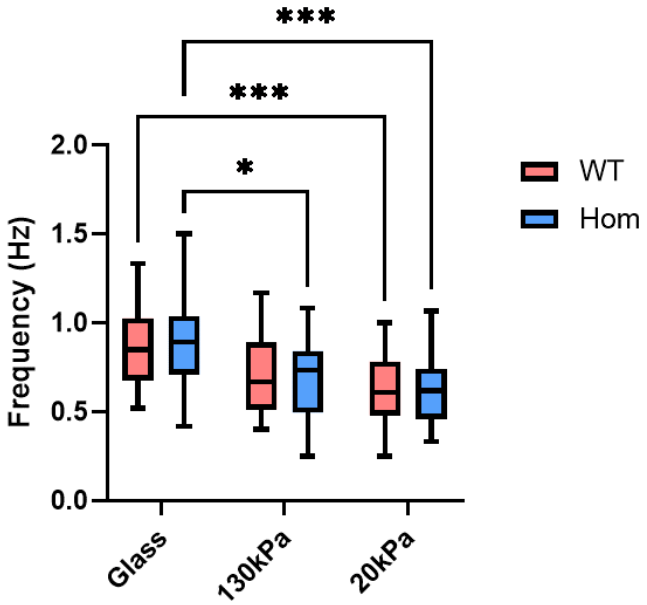

Figure 4-25 Beating frequency of WT and Hom iPSC-CMs cultured on different surfaces characterised by their Young's modulus. Frequency was recorded by counting on 30-day old cells, n/d = 6/4, data underwent a 2-way ANOVA, significance is shown by asterisks. Abbreviations: n/d, number of wells analysed per differentiation/number of differentiations per genotype.

4.3.6.5 Cell size of mutant iPSC-CMs on PDMS

As mentioned in 4.3.2.3, cell size is expected to change in HCM, however, in the HCM-related FLNC mutant cells, there was no significant change in cell size. Culturing iPSC-CMs on softer stiffnesses may allow the cells to grow in size and hence be more comparable to adult cardiac myocytes (190). iPSC-CMs cultured on glass, 130 kPa PDMS and 20 kPa PDMS had comparable cell sizes, with trend of size increase on the softest substrate (20 kPa) (Figure 4-26 & Figure 4-27). Hom *FLNC* W2164C iPSC-CMs cultured on 20 kPa were significantly larger than Hom cells cultured on glass.

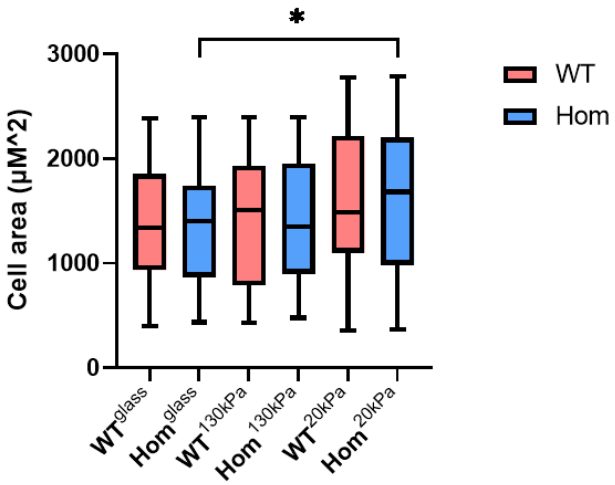

Figure 4-26 Box plot displaying the cell area of WT and Hom iPSC-CMs cultured on glass, 130 kPa PDMS and 20 kPa PDMS. Cell area was calculated via CellPose 2.0 on 30-day old cells, n/d = 1-2/4, data underwent a 2-way ANOVA, significance is shown by asterisks. ($p<0.05$, *; versus WT). Abbreviations: n/d, number of wells per differentiation/number of differentiations per genotype.

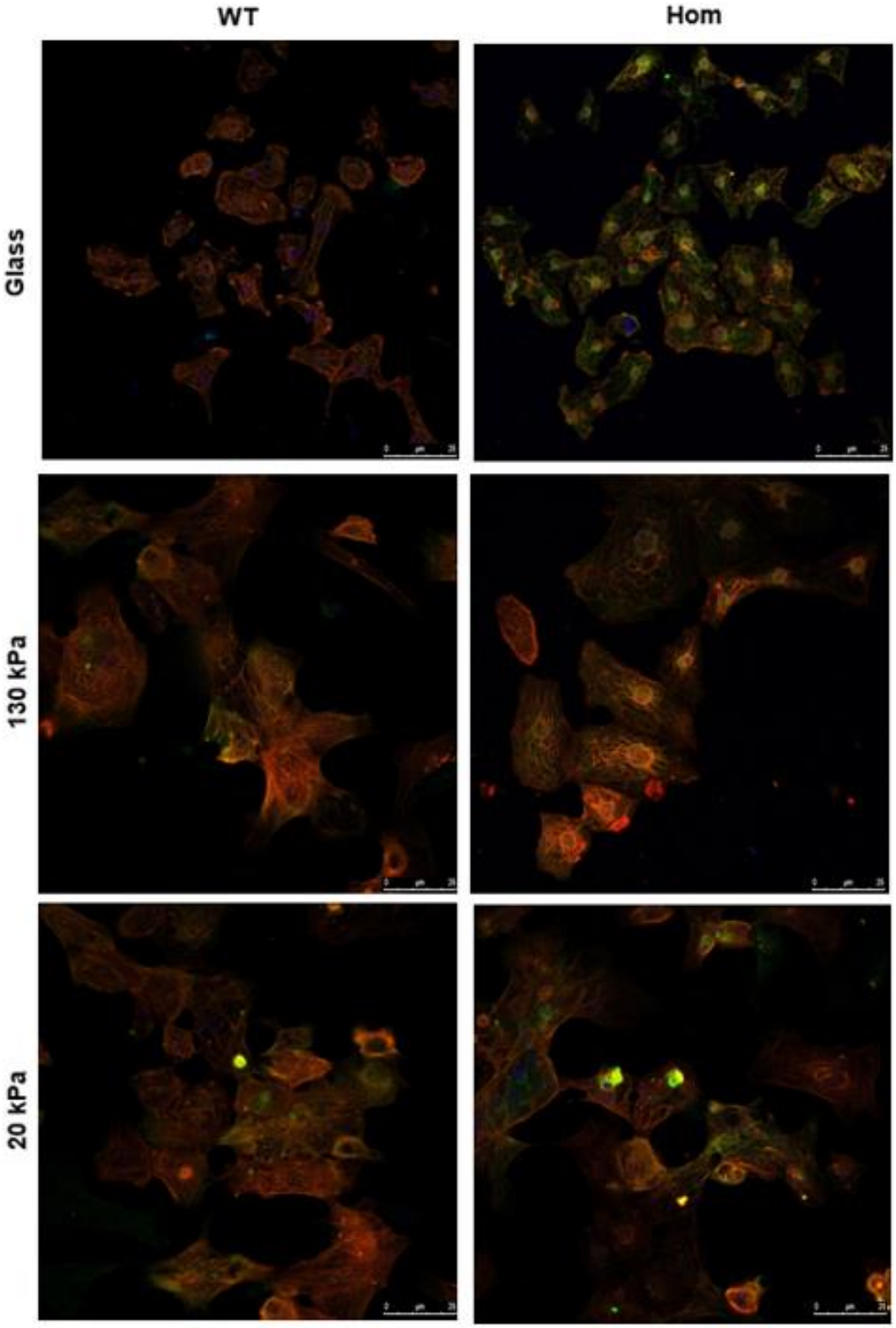

Figure 4-27 Immunofluorescent images used to calculate cell area via CellPose 2.0 of WT and Hom iPSC-CMs cultured on glass, 130 kPa PDMS and 20 kPa PDMS. Images were taken on 30-day old cells, n/d = 1-2/4, and were stained with DAPI, ACTN2 (red) and HSPB7 (green). For cell area analysis, only the ACTN2 stain was analysed by CellPose 2.0

4.3.6.6 Protein localisation of mutant iPSC-CMs on PDMS

In the mouse model, homozygous mutants displayed an increased expression of filamin C and HspB7 at the intercalated disc. The intercalated discs were not found to regularly expressed or show regular morphology in iPSC-CMs so localisations were assessed independently and relative to actin or α-actinin only. To maximise the use of each image, all cardiomyocytes which were stained with actin or α-actinin were used for cell size imaging above.

The variant did not affect the localisation of filamin C (Figure 4-28), myotilin (Figure 4-29), HspB7 (Figure 4-30) or HspB1 (Figure 4-31) in the mutant iPSC-CMs cultured on 20 kPa PDMS. Staining of actinin-2 was displayed with striated lines in all samples and shown via intensity plots. Filamin C, myotilin, HspB7 and HspB1 showed evidence of regular Z-disc localisation, though high background staining of the FLNC antibodies made assessment difficult. Intensity plots show an increased abundance of myotilin at the Z-disk (Figure 4-29), however this is likely due to differences in image acquisition and quality.

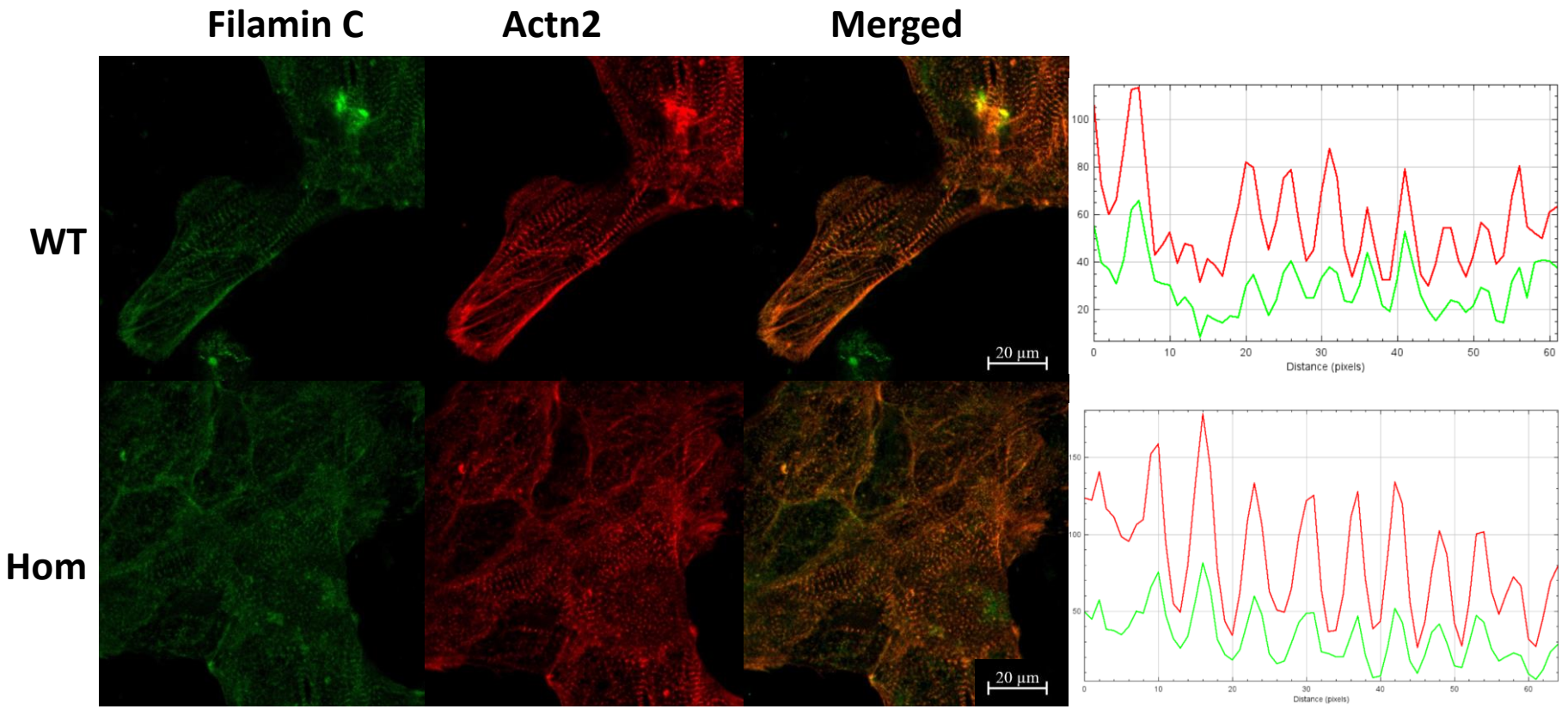

Figure 4-28 Immunofluorescent images of filamin C staining in WT and Hom iPSC-CMs cultured on 20 kPa PDMS. Images were taken on 30-day old cells, n/d = 1-2/4, and were stained with, ACTN2 (red) and Filamin C (green). Line intensity plots for the respective images on the right showing relative changes in FLNC localisation towards the Z-disk.

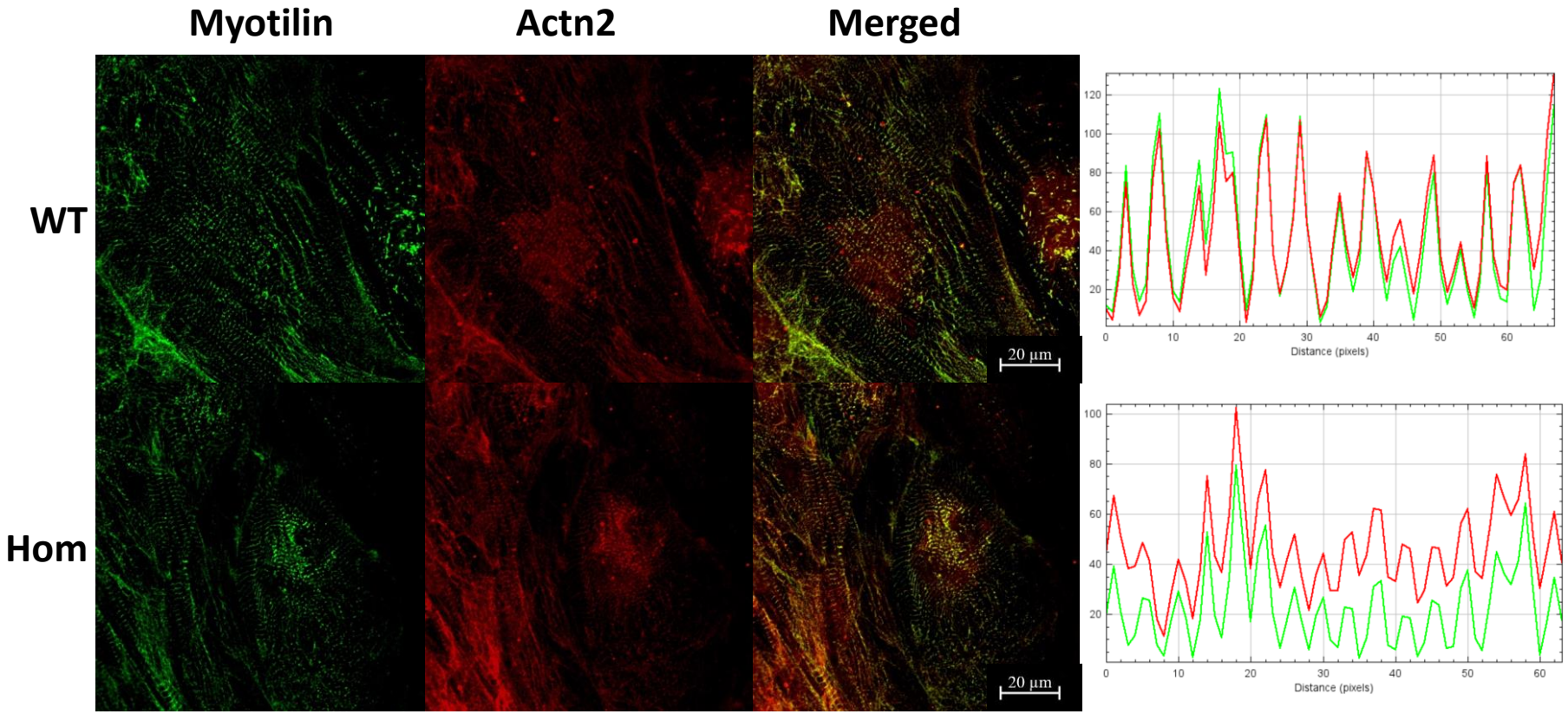

Figure 4-29 Immunofluorescent images of myotilin staining in WT and Hom iPSC-CMs cultured on 20 kPa PDMS. Images were taken on 30-day old cells, n/d = 1-2/4, and were stained with, ACTN2 (red) and myotilin (green). Line intensity plots for the respective images on the right showing relative changes in myotilin localisation towards the Z-disk.

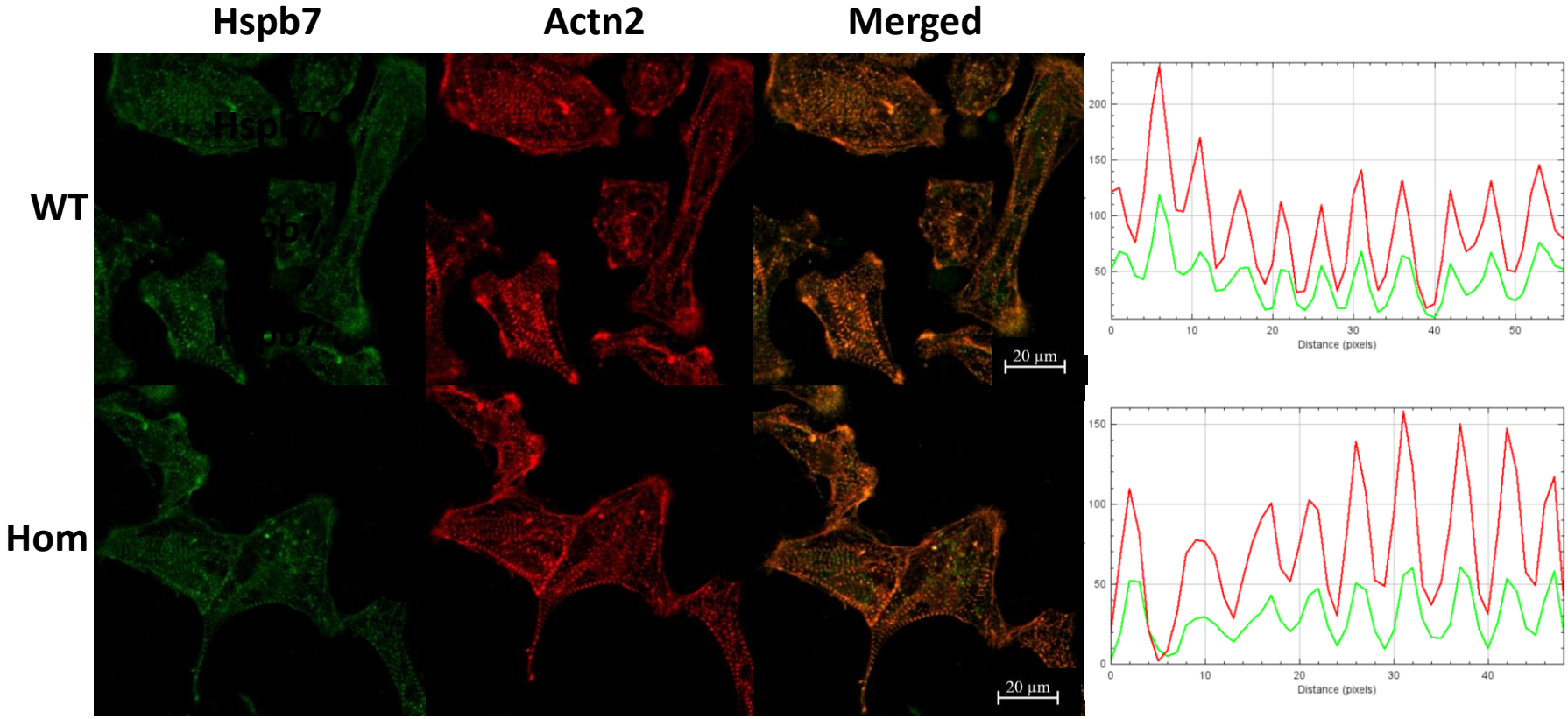

Figure 4-30 Immunofluorescent images of Hspb7 staining in WT and Hom iPSC-CMs cultured on 20 kPa PDMS. Images were taken on 30-day old cells, n/d = 1-2/4, and were stained with, ACTN2 (red) and Hspb7 (green). Line intensity plots for the respective images on the right showing relative changes in Hspb7 localisation towards the Z-disk.

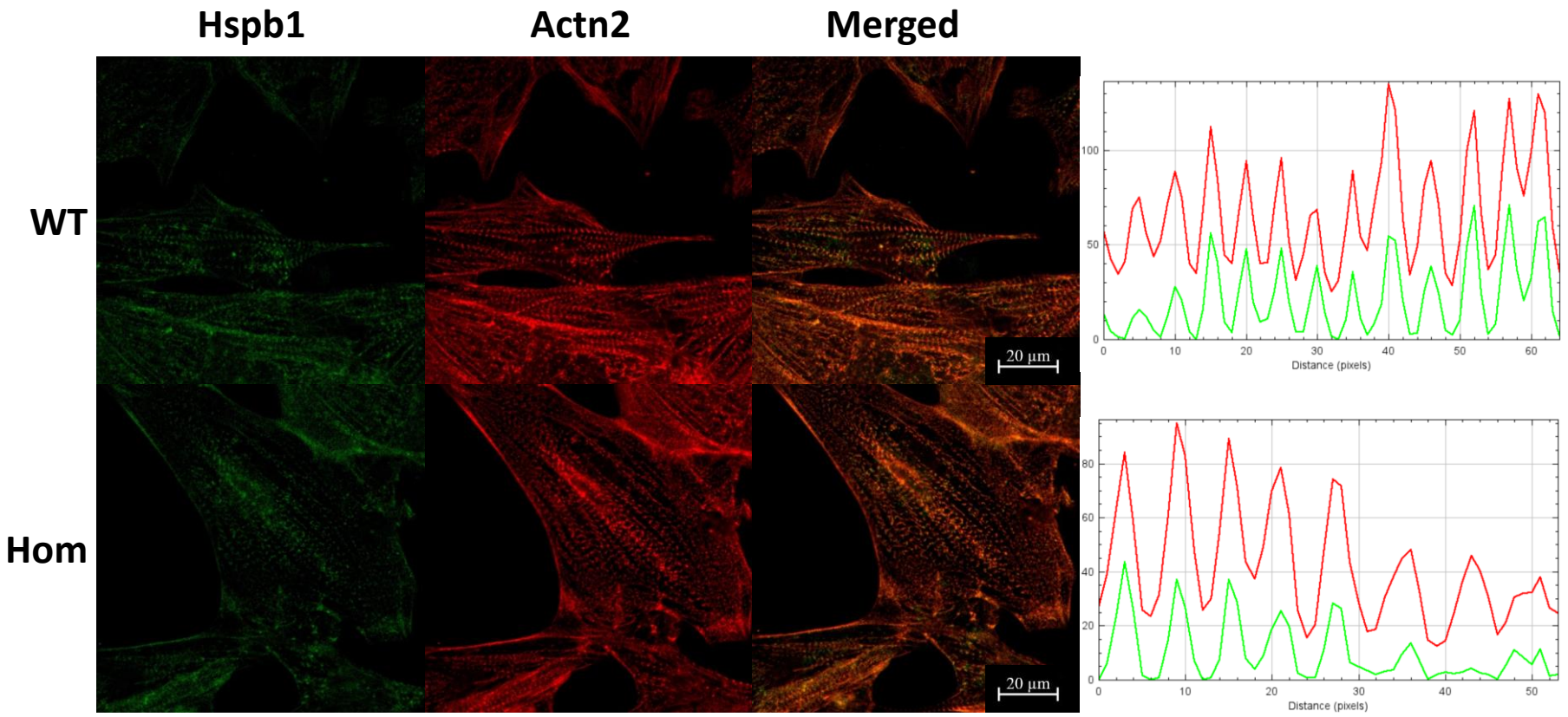

Figure 4-31 Immunofluorescent images of Hspb1 staining in WT and Hom iPSC-CMs cultured on 20 kPa PDMS. Images were taken on 30-day old cells, n/d = 1-2/4, and were stained with, ACTN2 (red) and Hspb1 (green). Line intensity plots for the respective images on the right showing relative changes in Hspb1 localisation towards the Z-disk.

4.4 Discussion

This chapter aimed to utilise the iPSC-CM as a model to better understand the contribution that the *FLNC* W2164C variant has towards a cardiomyopathy phenotype. With work already done in the mouse model (Chapter 3), a particular focus was to observe whether this human *in vitro* model can validate findings from the mouse model and provide additional insights. WT iPSC-CMs were assessed first to optimise the best experimental conditions. WT and mutant iPSC-CMs were tested under normal optimised culture conditions, ISO treatment and when cultured on PDMS surfaces of physiological stiffness.

4.4.1 Variant characterisation on iPSC-CMs on 2D-plastics and ISO treatment

4.4.1.1 Model validation

The iPSC-CM model was confirmed as a relevant model by conducting initial characterisation experiments. The WT kolf2 iPSC line successfully differentiated into spontaneously beating iPSC-CMs. These iPSC-CMs were found to expressed key cardiac markers, including filamin C, at transcript and protein level as they underwent 30 days of culture. The generated iPSC-CMs expressed the ventricular marker MLC2V at 94% and pan cardiac marker, cTnT at 96% when analysed by flow cytometry, confirming a high cardiomyocyte purity, comparable with other studies (91,366). MLC2V is usually found to be dominantly expressed in ventricular cardiomyocytes, whilst it is considerably lower in non-ventricular cardiac cells (367). Since neither MLC2V or cTnT is 100%, it is likely that non-ventricular and non-cardiomyocytes are influencing results, hence the need for a cardiac gene for relative expression in qPCR and immunoblotting.

As a proof of principle, when cultured on 2D tissue culture-treated plastics, iPSC-CMs displayed a drastic variability in myofibrillar organisation even within the same well. This makes studying myofibrillar arrangement difficult and subject to selection bias. Automated

analysis tools for studying sarcomere structural integrity were identified as a way to overcome these limitations and was used to a limited degree in this study (199). Despite the large batch-to-batch variability observed, the level of maturity due to time in culture plateaued between day 20 and day 30 – thus day 30 was chosen as the primary point of variant interrogation, a timepoint comparable with other studies (91,368). Mutant cardiomyocytes had comparable iPSC-CM differentiation success rates to WT cells (Table 4-2).

4.4.1.2 Effect of the *FLNC* W2164C variant

Filamin C is associated with maintaining sarcomere stability (369) and de novo sarcomere assembly with FLNC known to be expressed at early myocyte differentiation (128,156). The *FLNC* W2164C variant is located in a region involved in thin filament assembly, and therefore a mutant FLNC may have an impaired assembly process resulting in less mature sarcomeres. Day 20 was identified as a stable time point for measuring the effect of the variant on sarcomere assembly and therefore can inform on the potential development of the pathology the *FLNC* W2164C variant has on iPSC-CMs. As patients harbouring this variant present in adulthood, drastic changes in sarcomere assembly were not expected as this would be expected to be likened to paediatric disease. Filamin C has also been proposed as a fast myofibrillar repair responder protein (116).

A mutant FLNC may not operate properly in myofibrillar repair and affect the cardiomyocyte function, hence the majority of work investigating cardiomyocyte structure was carried out at day 30 post-sarcomere assembly when mature sarcomeres are formed. Though sarcomeres have been formed at this point, the sarcomere remains highly dynamic with sarcomere disassembly and reassembly.

At a structural level, the myofibrillar structure of the cardiomyocyte appeared consistently irregular with no indication of altered sarcomere formation or structure at day 30. Sarcomere lengths were unchanged when analysed both by Z-line detection and by SarcTrack, though the absolute values of sarcomere length differed between the method. This may be due to the nature of data acquisition, fixed cell imaging (Z-line detection) and live cell imaging (SarcTrack), perhaps due to initial characterisation normalised immunoblots to ACTN2, however, the ACTN2 levels at day 30 varied considerably especially in Hom iPSC-CMs. Alone this could indicate altered sarcomere stability, however, these cells continued to beat and immunofluorescence of ACTN2 in iPSC-CMs at this timepoint showed regular sarcomere structure across genotypes. In addition to this, the variant does not affect Z-disc architecture with both the Z-line length and mean sarcomere length remaining unaffected by the variant. It is likely that differences found by immunoblotting, are due to variabilities between iPSC-CM generation batches (370–373).

Confirming this at a molecular level, transcript interrogation of the variant at day 20 showed no changes in genes related to sarcomere development (*ACTN2*, *MYH7*) relative to wild-type samples, suggesting that the filamin C variant does not affect the development and early maintenance of the sarcomere.

The *FLNC* W2164C variant does not show evidence suggesting that sarcomere development, maintenance or stability are affected in 2D cultured at either day 20 or day 30.

4.4.1.3 *FLNC* W2164C variant on hypertrophy

The hallmark feature of HCM, is the enlargement of ventricular cardiac muscle cells (355). It was therefore expected that the HCM-associated *FLNC* W2164C variant should induce a change in cell area in Hom iPSC-CMs. To increase the likelihood of a genotype-related

phenotype, ISO was used to induce hypertrophy via β-adrenergic stimulation. By employing ISO, the idea was to mimic stress-induced cardiomyopathy as is used in mice as a chronic model of human advanced heart failure (169,365).

There were however no differences in cell area between WT and Hom. Though these cell areas are comparable between genotypes, the large degree of variation reported suggests room for improvement in measuring this parameter. Cell density is known to have a hypertrophic effect on cell size and especially in 2D culture cell area is affected by serum supplementation, time in culture (374,375). Previous studies reported that hypertrophy can be induced due to increased expression of hypoxia inducible factor 1-α (*HIF1A*) in iPSC-CMs cultured in the presence of glucose or lack of fatty acids in the culturing media due to (182,376–378), though this is not universally found (181,379). Using fatty acids in culturing media has been shown to mature iPSC-CMs, suppress *HIF1A*-induced hypertrophy and has allowed for an induction of hypertophy to be measured in response to pro-hypertrophic agents or genetic mutations (378). In the presence of an additional hypertrophic inducer, such as ISO and mechanical stretching, hypertrophic features may also be found in iPSC-CMs harbouring the Hom variant (182,378,380–382).

ISO incubation had a significant effect on cell size as determined by CellPose 2.0 proving the treatment worked, however there was no genotype related difference. While this method proved useful, less than 200 cells were analysed in total per genotype, with few differentiation batches and technical replicates. Other studies have analysed thousands of cells using FACs (91,375,383).

Variability within the transcript expression dataset is the dominating feature. For comparison, all trends observed in the mutant mouse were not replicated in the baseline

iPSC-CM study at either day 20 or day 30. Markers of the fetal gene programme and hypertrophic signalling were unaffected. Other hypertrophic markers could have been measured at transcript level, such as *CaMK II* (384) At the protein level, differences which were striking in the mouse proteomics and immunoblot data (e.g. upregulation of MYH7) were found to have no trends in Hom iPSC-CMs. Only XIRP1 expression was found to be downregulated in both Het and Hom iPSC-CMs. Low n-numbers, batch-to-batch variability and the use of a cardiac control which may be affected by the *FLNC* W2164C variant (ACTN2) may be factors into the contradictory findings in baseline iPSC-CMs.

The *FLNC* W2164C variant does not appear to affect the expression of markers related to cardiomyopathy at transcript or protein level in 2D cultured and ISO treated iPSC-CMs.

4.4.1.4 *FLNC* W2164C variant on cardiac function

Patients with hypertrophic cardiomyopathy have a thickening of the left ventricular wall which stiffens and patients experience diastolic dysfunction. Baseline cardiac output was measured in 2D plastic-cultured iPSC-CMs by SarcTrack and displayed no differences in any of the measured parameters. Consistent with the Z-disc line detection analysis, there were no differences in sarcomere lengths in either relaxed or contracted states. Since some of the measured iPSC-CMs had an intrinsic spontaneous beating rate above 1 Hz, all cells were paced at 2 Hz which may have introduced problems when observing phenotypes: Pacing at 2 Hz all may not allow the cells to completely relax in diastole, hence resulting in almost identical sarcomere lengths, contraction times and contraction percentages, and masking genotype effects. Interestingly, even though the pacing was at a high rate, a reasonable amount of variability is still observed when considering the contraction times and

percentages. Differences in these parameters may be linked to differences in intrinsic paces influencing how accustomed cells are to the higher pacing. Ideally it would be possible to make comparisons between cells that naturally beat at a similar rate but the endogenous beating rates of both genotypes were very variable and hence limited the ability to measure this. Contractile function was looked at simplistically by counting beats per minute in ISO treated iPSC-CMs. The beating frequencies under ISO treatment were not significantly different.

The *FLNC* W2164C variant does not appear to affect iPSC-CM cardiac function in the parameters measured on 2D cultured and ISO treated cells.

4.4.2 ISO characterisation assessment

The use of ISO in this study was primarily to induce a similar phenotypic effect on the molecular level as Ang-II had on the *FLNC* mutant mouse. Contrary to evidence found in mice, ISO treatment did not aggravate phenotypes either in the Het or Hom iPSC-CMs. To date, differences between mouse models and human iPSC-CM disease models have been reported previously and is not surprising given the stark physiological and molecular differences between the two models (383,384). While the differences could be explained by model differences as well as different modes of action between Ang-II and ISO (385), the contradictory findings with the mouse make interpretation difficult. This will be discussed in the Final Discussion chapter in greater detail.

4.4.3 PDMS characterisation

Cells which are cultured on overly rigid substrates, such as tissue culture plastics or glass, may employ a diverse panel of regulation mechanisms in order to compensate for the mechanical environment (386), and hence override any regulatory mechanisms that may lead

to a phenotype due to the *FLNC* variant itself. Given no differences were seen under normal 2D plastic culturing conditions and ISO treatment, iPSC-CMs were cultured on surfaces of physiological stiffnesses. This approach questioned whether iPSC-CMs were already mechanically compromised due to the high tensile forces induced by regular 2D culturing on plastics that masked a genotype-related phenotype. Therefore, PDMS surfaces were employed to reach physiologically healthy (20 kPa) and fibrotic (130 kPa) conditions. Culturing iPSC-CMs on physiological surfaces was also predicted to induce a more mature phenotype and hence aid in studying the effects of the *FLNC* variant in a system more equivalent to the adult heart.

4.4.3.1 Cardiac maturation on PDMS

Firstly, maturation of the iPSC-CMs was observed at a transcript level when on a PDMS surface compared to glass. This was seen with a reduction in titin isoform ratio *N2BA:N2B* on both 130 kPa and 20 kPa PDMS surfaces. While the isoform switch occurred to a significant degree in titin, the *MYH7:MYH6* isoform switch was not found to be significantly upregulated – likely due to the variability. Since HCM is a disease of altered energetics and a metabolic switch also occurs, the effect of surface tension was measured on genes involved in metabolism: *PDK4* and *HK2* (387). *PDK4*, which is involved in fatty acid oxidation, was significantly upregulated at a transcript level when on 130 kPa PDMS with a similar but non-significant trend observed in 20 kPa, indicating that metabolic maturation occurs in altered mechanical environments (388).

4.4.3.2 Hypertrophic induction on PDMS

Hypertrophy was measured in mutant iPSC-CMs cultured on PDMS. Surface tension has been known to influence iPSC-CM cell size (368). Unlike what was observed in the mouse

model and iPSC-CM model so far, morphological evidence of hypertrophy was observed in Hom cells. The cell area of Hom FLNC W2164C iPSC-CMs was significantly increased when cultured on 20 kPa PDMS surfaces relative to glass-cultured Hom iPSC-CMs.

Genotype differences started to be found after passaging cells onto either glass or PDMS. In Hom cells there is evidence of a reactivation of genes linked to the fetal gene programme (*NPPA, NPPB, MYH7, ACTA1*), an indicator of cardiac hypertrophy (389). This finding is consistent with findings in Chapter 3 and suggests that the *FLNC* variant may be inducing structural remodelling, although evidence of this was not interrogated for (390). Unlike the mouse model, genes linked to hypertrophic signalling (*ANKRD1, ANKRD2, FHL1*) were unchanged between WT and Hom regardless of their culturing substrate. The same was also observed with *MYOT* and *FLNC* both of which were found to be significantly upregulated in Hom mice both at saline and under Ang-II treatment.

Immunoblot data showed a stiffness dependent effect on protein expression. As also observed in the mutant mouse, *MYH7* transcript expression increases in Hom iPSC-CMs on 20kPa (Figure 3-17 & Figure 4-22). MYH7 is often found to increase in HCM (389). HSPB1 and HSPB7 expression is increased in Hom iPSC-CMs when exposed to fibrotic conditions and returning to WT levels at healthy mechanical conditions. This is not surprising since these heat shock proteins are known to respond to stress and carry cardioprotective properties (121,270). Since FLNC was not significantly increased in Hom iPSC-CMs, it could be that these heat shock proteins are upregulated in order to stabilise FLNC (242,270,391).

Protein localisation changes were observed in the mutant mouse. FLNC, MYOT and HSPB7 appeared to show increased abundance at the intercalated disc. This is a finding that is indicative of cardiac stress, as has been found in other models (107,154). When cultured on

glass and 20 kPa, no changes were observed in protein localisation. The interpretation of this is limited by the lack of successful intercalated disc staining. iPSC-CMs do not have fully mature intercalated discs (392) and in humans, the intercalated disc assembles postnatally (393,394). The intercalated disc was attempted to be displayed by N-cadherin, a transmembrane protein that mediates for cell-cell adhesion. The intercalated disc was not found to be consistent with the antibodies used in this thesis and hence limited comparable relocalisation assessment in this chapter.

Overall, culturing Hom iPSC-CMs on physiological surface stiffnesses displayed some aspects of a hypertrophic molecular phenotype, indicating that iPSC-CMs were sensitive to the mechanical culturing environment and helped unmask a Hom phenotype. However, genotype differences were also observed in iPSC-CMs cultured on glass as well as at fibrotic stiffness. This could be due to the more stringent iPSC-CM selection criteria resulting in less iPSC-CM quality driven phenotype-masking. Evidence of hypertrophy was not found on PDMS surfaces when analysed by CellPose 2.0.

4.4.3.3 Cardiac function on PDMS

Contractile function was looked at simplistically by counting beats per minute on PDMS-cultured cells. Similar to other studies, differences were observed when culturing iPSC-CMs on PDMS compared to glass (330). WT iPSC-CMs observed a stiffness-dependent reduction in beating frequency when cultured on glass (GPa+) and PDMS of 130 kPa and 20 kPa. Although Hom iPSC-CMs were also found to have significantly reduced beating frequencies between glass and 20 kPa PDMS, there were no differences found between genotypes at the same stiffness. The high stiffnesses of rigid glass surfaces may prevent cell-adherence and hence result in shorter contraction durations while the longer contraction durations of cells on softer PDMS surfaces may be due to cells being more adherent and pulling at the gel. The

induction of intrinsic cellular effects may be responsible for the changes in contractile function (395). The *FLNC* W2164C variant does not appear to affect beating frequency in this model on PDMS surfaces.

4.4.4 *FLNC* W2164C variant on energetics

A key finding in the mouse proteomics data was a significant reduction in the presence of proteins involved in mitochondrial function. HCM is a disease indicative of an energetic imbalance and mitochondrial dysfunction (396,397). Aberrant mitochondrial function may lead to an apoptotic or necrotic cell as reduced membrane potential may be central in the release of apoptotic factors (396,397).

In both the mouse and PDMS-treated iPSC-CM dataset, there was an induction of the fetal gene programme in mutants, indicative of a hypertrophic response (398). This induction may also correlate with a metabolic switch in order to meet with energetic demands and result in a mitochondrial adaptive response (284). It was hypothesised that the mutant iPSC-CMs would express lower membrane potential as a result of reduced expression of proteins involved in the electron transport chain, as suggested by the membrane-enriched fraction proteomics experiment (Figure 3-7).

Live-cell imaging of the 20 kPa PDMS-cultured Hom *FLNC* W2164C iPSC-CMs incubated with the membrane potential dye displayed no abnormal patterns in activated mitochondria. The total number of mitochondria detected via this method were also not significantly different in Hom iPSC-CMs. Although this measure is not a direct indicator of mitochondrial function, the fact that the number of activated and total mitochondria were unchanged in Hom cells, casts doubt onto whether the *FLNC* variant results in an energetic imbalance related to mitochondria number. While other iPSC-CM models of HCM have found evidence

of mitochondrial dysfunction, the methods used in this thesis did not detect any changes (91,399). Though more extensive techniques, such as the Seahorse system, can be used to directly assess mitochondrial energetics (400).

This assessment of membrane potential indicates that mitochondrial dysregulation is unlikely to be affected in the mutant iPSC-CMs.

4.4.5 Limitations

This chapter aimed to use the iPSC-CM model harbouring the *FLNC* W2164C variant to validate findings in the mouse model and provide additional insight which was not explored in the mutant mouse. While this was partially achieved, limitations to the approach of this study exist.

4.4.5.1 Variability

The key feature of this chapter highlights the stark variability that is present in iPSC-CMs which confounds interpretation. The variability between batches of differentiations means that with the relaxed selection criterion, the effect of the variant was not being isolated. Increasing n-numbers could improve this, however, the differentiation quality would still be measured rather than the variant itself specifically. The biggest cause of variability has been the iPSC-CM selection criteria. Despite having high percentage purity and multiple glucose-starvation rounds, a visual assessment of generated iPSC-CMs showed a range in levels of beating with some showing clusters of twitching and others beating as a full sheet.

A potential considerable impact to the variability observed in molecular studies is the cardiac control used, ACTN2. By simple PCR analysis it appeared to be a reasonable choice as a cardiac marker, however, mid-way through this work, proteomic analysis revealed α-actinin may be upregulated. Even though this was not found to be significant according to the

stringent criteria, efforts were made to correct the findings to cTnT wherever possible. It may however be more consistent to normalise protein analysis to total protein

ISO treatment functions by stimulating β1-adrenorceptors (401) and prior to testing this on mutant iPSC-CMs, it was hypothesised ISO treatment would induce a hypertrophic response in Hom iPSC-CM more than WT iPSC-CMs. ISO treatment in fact only appeared to exaggerate the variability that already existed. In iPSC-CMs, the expression of β1-adrenorceptors has been shown to alter in time (401,402). Different batches of iPSC-CMs are likely to differentially express this receptor representing sarcoplasmic reticulum immaturity (403) thus resulting in a batch-specific response to ISO rather than measuring the genotype effect.

Due to the troubling variability which had confounded interpretation, this led to a tightening of the iPSC-CM selection procedure for studying the effect of the variant in iPSC-CMs when cultured on PDMS surfaces of tuneable stiffness. For studying the effect of PDMS only iPSC-CMs which were beating as a full sheet were selected for passage and later study. While this did not eliminate the observed variability, a more stringent and defined cardiomyocyte quality control process aids in the iPSC-CM production consistency (370–372). The implementation of this quality control process contributed to the discovery of genotype differences which were comparable with the mutant mouse. Further morphological variability can be minimised by culturing cells on nanopatterned PDMS surfaces or engineered heart tissues (EHTs) (324,330).

4.4.5.2 Immaturity

Immaturity is a hallmark feature of iPSC-CMs: iPSC-CMs lack t-tubules (404,405), are small and round morphologically and resemble fetal CMs (361,406). They also display fetal-

like isoform expression (191). With most HCM cases affecting patients in later life, the immaturity of the cellular model makes relative findings difficult to judge. For instance, the induction of the fetal gene programme may be due to differences in maturation development rather than the reactivation of these genes as part of the pathogenic alterations.

4.5 Conclusion

Disease modelling is largely dependent on the model one uses. Human iPSC-CMs have been used as a disease model and have been shown to recapitulate phenotypes observed in the patient (407). Studies employing *in silico* models of iPSC-CM features call for caution over the clinical interpretation of iPSC-CM findings which have not been validated in alternative formats (408,409). Throughout the course of the iPSC-CM characterisation, variability dominated the findings thus confounding any interpretation. Efforts to limit this were reasonably successful, such having a characterised selection of cardiomyocytes for experimentation and using reference genes for relative expression calculations which should not be impacted by the *FLNC* missense variant. The use of PDMS surfaces of physiological stiffness successfully unmasked differences between genotypes and guided further experiments in investigating the *FLNC* variant in a mechano-sensing context (to be discussed in the next chapter). This chapter highlights the versatility of the iPSC-CM model, as well as providing an assessment of its use as a model to study cardiomyopathy variants alongside mouse models. Discerning whether the lack of differences is due to the limitations of the cellular model or if results reported in the mouse model are false positives is an element that introduces uncertainty into the impact of the *FLNC* W2164C variant. This will be discussed in further detail in the Final Discussion.

Chapter 5 : *FLNC* W2164C ON MECHANO-SENSING

5.1 Introduction

While the majority of HCM-causing disease genes are sarcomere genes, implicated in altered cardiomyocyte structure, a small subset affect genes involved in mechano-sensing, such as, Bcl2-associated athanogene 3 (*BAG3*) (391,410,411). Mechano-sensing is a process which allows the cardiac myocyte to respond appropriately to mechanical stress – in this case due to sarcomere contraction (98). Through constant contraction the sarcomere is under continuous mechanical, heat and oxidative stress. Cardiac muscle, in particular the cardiomyocyte, can sense and respond to mechanical load stress conditions in order to deliver consistent volumes of oxygenated blood to the body. This ensures the stability and subsequent function of the cardiomyocyte.

Sarcomere and cytoskeletal proteins such as filamin C change their conformation between folded and unfolded state (75,76) and accommodate the mechanical stress required for actin contraction (75,77). This continuous mechanical unfolding and refolding can result in irreversible damage due to exerted mechanical stress. In skeletal muscle, damaged proteins are recognised by the exposure of bindings sites during unfolding and are disposed of and replaced with a newly synthesised protein (59,88,412). The muscle homeostasis of filamin C is done via a mechanism called chaperone-assisted selective autophagy (CASA) (78). In skeletal muscle, filamin C is a target client of CASA, which is able to identify, remove and replace misfolded filamin C (59).

5.1.1 CASA

The CASA chaperone complex recognises protein misfolding and translates it into biochemical signals (76,79). This chaperone complex consists of BAG3, the key

cochaperone that initiates CASA and is coupled to the ubiquitin ligase named C-terminus of Hsc70-interacting protein (CHIP) (encoded by STIP1) (80), and molecular chaperones: heat shock proteins, especially HSPB8 and HSC70 (59,81,82). The BAG3 complex monitors the conformational state of filamins (and other sarcomere proteins) to recognise damaged proteins. When in an open conformation during filamin extension, hidden binding sites accessible by synaptopodin-2 are revealed (84,85). When filamins are damaged due to over-stretching, the BAG3 complex triggers filamin to be released from the myofilament into the cytosol for lysosomal degradation via CHIP/STUB-mediated ubiquitylation (86). This induces the recruitment of p62, an autophagic ubiquitin adaptor, for protein clearing through the formation of an autophagosome via LC3 (59). A new filamin is then synthesised and incorporated into the Z-disc to maintain regular skeletal myocyte function (59,83,412).

Though CASA has been found specifically in the skeletal muscle, these mechano-sensing mechanisms may not be limited to skeletal muscle and its myopathies. A CASA-like system may also exist in cardiac muscle and may provide insights into understanding the development of pathologic cardiac conditions. Variants in both cardiac filamin C and small HSPs (sHSPs) present in cardiomyopathies (92). Since they are both known to interact with each other via mechano-sensitive domains, aberrant chaperone-mediated mechano-sensing may be the basis of some cardiomyopathies (92).

The Coordinated Lysosomal Expression and Regulation (CLEAR) motif proteins may also be involved and activated by chaperone-mediated processes similar to CASA. As their name suggests, CLEAR proteins are known to be involved in the regulation of lysosomal protein expression (413).

So far, the mouse model equivalent of the FLNC W2164C missense variant has reported evidence of altered protein abundance and distribution. Since one of the roles of filamin C is to mediate the spatial and orientation of F-actin filaments through protein-protein interactions, a dysfunctional protein turnover of filamin C could have significant effects on the function of the cardiac myocyte and hence alter Z-disc organisation (110,111).

5.1.2 Hypothesis and aims

Since filamin C is thought to form a cardiac mechano-sensing complex at domain 20, this pathogenic variant is hypothesised to render its mechano-sensing functions to be constitutively active and thus cause a cardiac phenotype.

The objective of this chapter is to elucidate the role of the HCM-disease associated FLNC W2164C variant on mechano-sensing. In this study, this is achieved using both mouse and iPSC-CM models through the following aims:

- Assess for changes in mechano-sensing targets in the mutant mouse via unbiased proteomics analysis and targeted molecular follow-up
- Assess for changes in mechano-sensing targets in the mutant iPSC-CM model via targeted molecular characterisation and assessment of autophagic capacity

5.2 Results

5.2.1 CASA targeted proteomic analysis

In chapter 3, unbiased proteomics was carried out in WT and Hom FLNC mice. Proteomics profiling of CASA and lysosomal markers were interrogated in fractionated tissue as a sub-analysis (Table 5-1).

Using the relaxed threshold (fold-change = 2+ and Log(FDR) = +1.301), described in Chapter 3, proteins were identified which were significantly altered in Hom mice. When exploring the mouse proteome for CASA specific targets, 2 of the 3 main interactors, BAG3 and HSP70 (gene name: *Hsp12b*), were significantly upregulated in the membrane fraction in Hom mice. CASA-related proteins were identified based off two main publications by Martin et al 2021 (414) and Fang et al (415). In addition to an increase of the CASA client Flnc, additional proposed clients of CASA were also found to be significantly overexpressed (Sptan1, Xirp1) or under-expressed (Actn2) (414). Mitochondrial clients of CASA were also observed to be significantly under-expressed (Immt, Slc25a4, Uqcrc2) (414). The remaining CASA-linked proteins were located in the intermediate filament (Plec), actin cytoskeleton (Sorbs2), sarcomere (Myom2, Myh7) or elsewhere (Atp2a2, Cox6c) (414).

Additional targets were probed for (Table S3). Two HSPs associated with a cardioprotection and autophagic response were enriched in the Hom membrane fraction only (Hspb2, Hspd1/Hsp60). The activation of the CLEAR motif was also investigated using identified peptides (Table S3) (413). Proteins which are linked to CLEAR (Ctsd, Lamp1, Lamp2, Psap, Scarb2, Tpp1) showed no significant changes, nor were consistent trends observed in mouse proteomics data.

Table 5-1 List of proteins involved in CASA found to be increased/decreased in myofilament and membrane fraction proteomics analysis. Proteins were selected by their T-test fold change and -LogP value. The localisation, function and pathology association as according to Pubmed searches. Red and italics highlighted protein symbols represent the proteins that had a fold-change of greater than 2 and Log(FDR) =1.301. Abbreviations: ECM, extracellular matrix; ICD, intercalated disc.

Protein symbol	Protein Name	Function	Membrane Log2(Fold Change)	Membrane -Log10(FDR)	Myofilament Log2(Fold Change)	Myofilament -Log2(FDR)	Ref
CASA key proteins							
Bag3	Bcl2-associated athanogene 3	Chaperone for Hsp70 and Hsc70.	5.782	2.34	4.478	1.15	(228,229)
Hspa12b	Heat Shock Protein Family A Member 12B	Cardioprotection Molecular chaperone activity	3.544	1.71	0.786	0.21	(416)
Hspb8	Heat Shock Protein Beta-8	Cardioprotection Molecular chaperone activity	-0.786	0.49	3.358	0.95	(417)
Potential CASA clients							
Actn2	α-actinin 2	Crosslinks actin and titin from Z-disc	-7.284	2.93	1.403	0.18	(91,226,227)
Des	Desmin	Cytoskeletal support	-0.865	0.12	-2.863	0.41	(418)
Flnc	Filamin C	Cytoskeletal support Mechano-sensing	-1.888	0.39	9.210	6.96	(98,100,136,137)
Mybpc3	Myosin binding protein C3	Sarcomere organisation and maintenance	-3.198	0.71	1.859	0.21	(419,420)
Myom1	Myomesin 1	Sarcomere assemply Contractility regulation	-3.680	0.77	2.724	0.51	(421)
Myoz2	Myozenin 2 (calsarcin 1)	Inhibits pathological cardiac response by binding ACTN2	-0.336	0.17	3.530	0.71	(422)
Sptan1	αII spectrin	Actin crosslinking and molecular scaffold.	3.124	0.88	7.662	3.62	(262,263)
Xirp1	Xin Actin Binding Repeat Containing 2	Protects actin filaments from depolymerisation	0.211	0.09	3.570	1.50	(423,424)
Potential CASA interactors							

Actc1	Actin alpha cardiac muscle 1	Thin filament component	-4.281	0.59	-0.671	0.05	(425)
Alb	Albumin	Circulatory protein involved in maintaining fluid dynamics	4.145	0.66	0.0866	0.01	(426)
Atp2a2	Sarco-endoplasmic reticulum Ca^{2+} ATPase (SERCA2)	Ca^{2+} reuptake and Ca^{2+} signalling	-8.257	1.64	-3.800	0.62	(320,328)
Casq2	Calsequestrin 2	Storage and transport of Ca^{2+}	0.830	0.13	0.3615	0.06	(427)
Ckm	Creatine kinase M-type	Energetic homeostasis	0.643	0.08	-2.123	0.34	[428]
Col1a1	Collgen type I alpha 1 chain	Component of collagen	Undetected		3.475	1.12	[429]
Col6a3	Collagen type VI alpha 3 chain	Component of ECM	0.315	0.18	1.659	0.22	[430]
Cox6c	Cytochrome C oxidase subunit 6C	Oxidative phosphorylation	-7.345	1.86	0.118	0.01	[431]
Cryab	Crystallin Alpha B	Cardioprotection Molecular chaperone activity	-0.136	0.03	2.672	0.46	[432]
Dsp	Desmoplakin	Structural and mechanical support of junctions	-1.296	0.94	4.121	0.83	[433]
Fbn1	Fibrillin-1	Structural and mechanical support of ECM	-0.047	0.01	-0.331	0.05	[434]
Hadha	Mitochondrial trifuncional protein	Cardiolipin synthesis	-1.149	0.1	-6.572	1.30	[435]
Hspb1	Heat Shock Protein Beta-1	Cardioprotection Molecular chaperone activity	2.767	0.69	0.942	0.19	[107]
Immt	MIC60	Mitochondrial organisation, ATP generation, transportation, apoptosis	-7.197	2.03	1.324	0.18	[436]

Jup	Junction plakoglobin	Development and maintenance of the ICD	1.838	0.37	3.538	0.88	[437]
Ldb3	LIM domain binding 3	Z-disc structural integrity	0.540	0.07	1.031	0.13	[438]
Myh6	Myosin heavy chain 6	Cardiac contraction	-2.806	0.56	6.181	0.65	[439]
Myh7	Myosin heavy chain 7	Actin cross-linking Cytoskeleton organisation	-2.746	0.60	11.508	7.32	[254], [255]
Myl3	Myosin light chain 3	Regulates muscle contraction	-3.300	0.49	1.671	0.15	[440]
Myl12b	Myosin light chain 12B	Regulates muscle contraction	Undetected		2.148	0.90	[441]
Myom2	Myomesin-2	Sarcomere assemply Contractility regulation	-7.549	1.98	-0.449	0.05	[87], [421]
Nebl	Nebulette	Actin-binding protein	-0.094	0.08	0.543	0.07	[442]
Nnt	Nicotinamide nucleotide transhydrogenase	Heart development	3.829	0.41	3.119	0.44	[443]
Plec	Plectin	Scaffolding protein	-2.522	1.53	-4.315	0.65	[444]
Slc25a3	Mitochondrial phosphate transporter	Transports inorganic phosphate	-1.492	0.14	-1.607	0.33	[445]
Slc25a4	ADP/ATP Translocase 1	Associates with Bag3 for mitochondrial apoptosis regulation	-10.287	1.72	-4.696	0.63	[446]
Sorbs2	Sorbin and SH3 Domains-containing Protein 2	Cell adhesion and cytoskeletal formation	1.849	0.53	7.738	4.63	[259]
Stip1	Stress Induced Phosphoprotein 1	Molecular chaperone activities	-0.048	0.01	Undetected		[447]
Tnnc1	Troponin C1	Calcium binding	-2.508	0.48	3.638	0.49	[448]

Tnni3	Troponin I3	Binds to actin/tropomyosin	-2.046	0.4	4.689	0.66	[448]
Tpm1	Tropomyosin 1	Regulates muscle contraction	-1.951	0.24	4.861	0.55	[449]
Trap1	T3 Receptor Auxiliary Protein	Cardioprotection	-1.278	0.17	Undetected		[450]
Uqcrc1	Cytochrome b-c1 complex subunit 1	Mitochondrial respiration	-6.090	0.93	-4.010	0.68	[215]
Uqcrc2	Cytochrome b-c1 complex subunit 2	Mitochondrial respiration	-13.114	6.18	-4.333	0.70	[215]
Vim	Vimentin	Maintains cellular integrity	2.139	0.31	-0.110	0.01	[451]

5.2.2 CASA induction

The induction of CASA targets at transcript level was checked after mice underwent saline or chronic Ang-II treatment (Figure 5-1). As mentioned in Chapter 3, Ang-II treatment aims to challenge the mice via hypertension by acting within the renin-angiotensin-aldosterone system and promotes cardiac hypertrophy and remodelling in mice [310]. Ang-II mice are under pressure overload conditions and therefore may exhibit a greater mechano-sensing response. Ang-II treatment resulted in an increased transcript expression of Hspb1 for all genotypes. In control (saline) treated animals, Hspa8 and Hspb7 showed significant increases in Hom mice compared to WT though this effect was not significant in Ang-II treated mice. The gene encoding the protein Hsp70, Hspa1a, was significantly upregulated in Ang-II treated Hom mice relative to Ang-II treated WT mice.

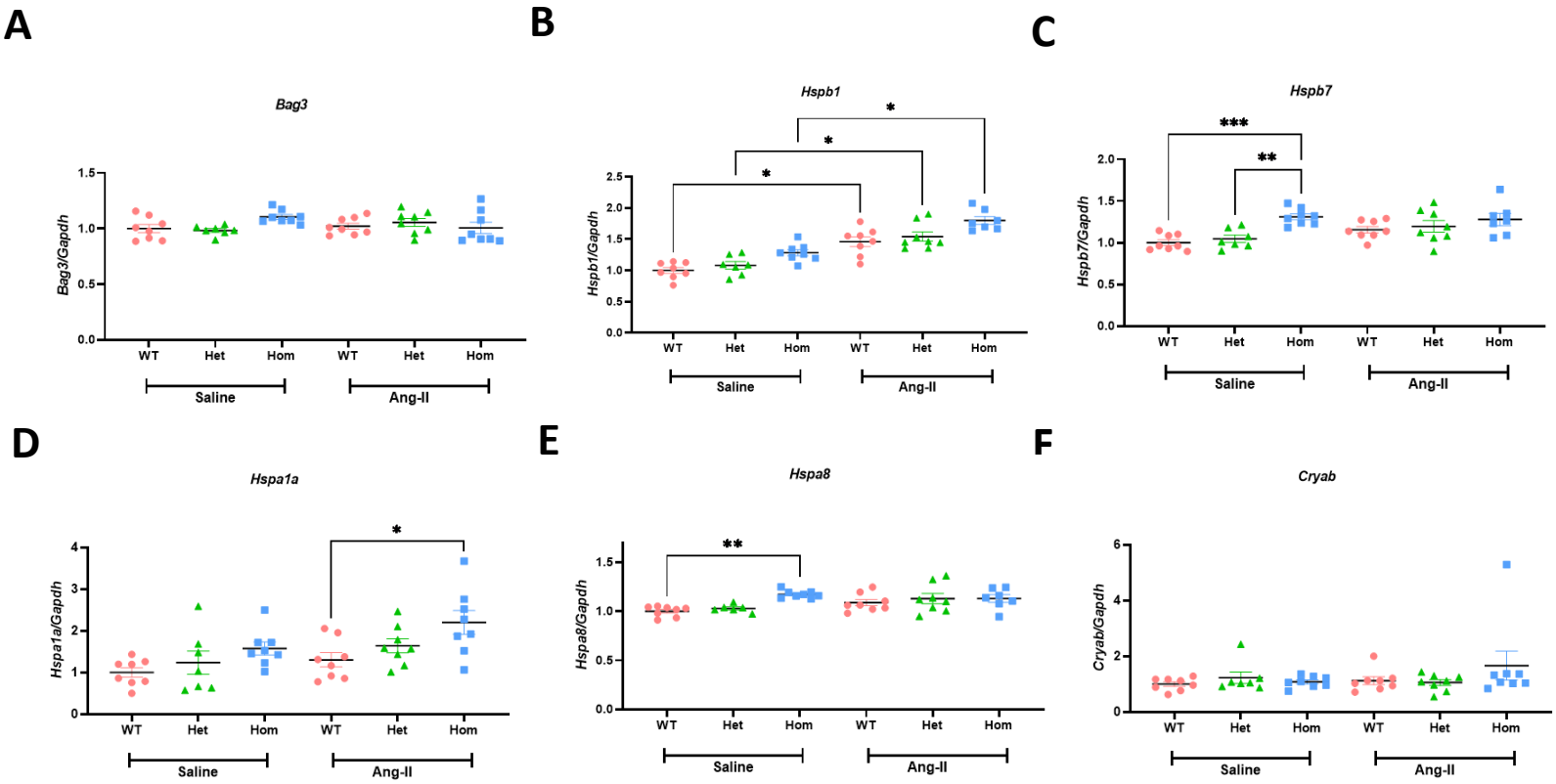

Figure 5-1 Assessment of changes at a transcript level in the heart of 14-week old FLNC W2165C mice under saline and AngII treatment. All measurements were normalised to Gapdh. Significant changes are observed and displayed with astericks. Data was not normally distributed and underwent a Kruskal-Wallis test followed by Wilcoxon rank sum test. n = 8, mixed sex. Significant changes are observed in the hearts of W2165C mice ($p<0.05$, *; $p<0.01$, **; $p<0.001$, ***; versus WT).

Analysis of proteins involved in CASA were also investigated, specifically by immunoblots in the myofilament and membrane fraction as well as whole tissue.

No significant changes of CASA-linked proteins were observed in whole tissue (Figure 5-2). The myofilament fraction showed an upregulation in Hom mice in 2 key proteins involved in filamin C binding and stabilisation: HSPB7 and XIRP2 while a key CASA interactor, BAG3, remained unchanged. HSPB1 trended towards upregulation in the Hom mouse myofilament fraction, but this did not reach significance (Figure 5-3). No significant changes were observed in HSPB1, HSPB7 and BAG3 in the membrane fraction (Figure 5-3).

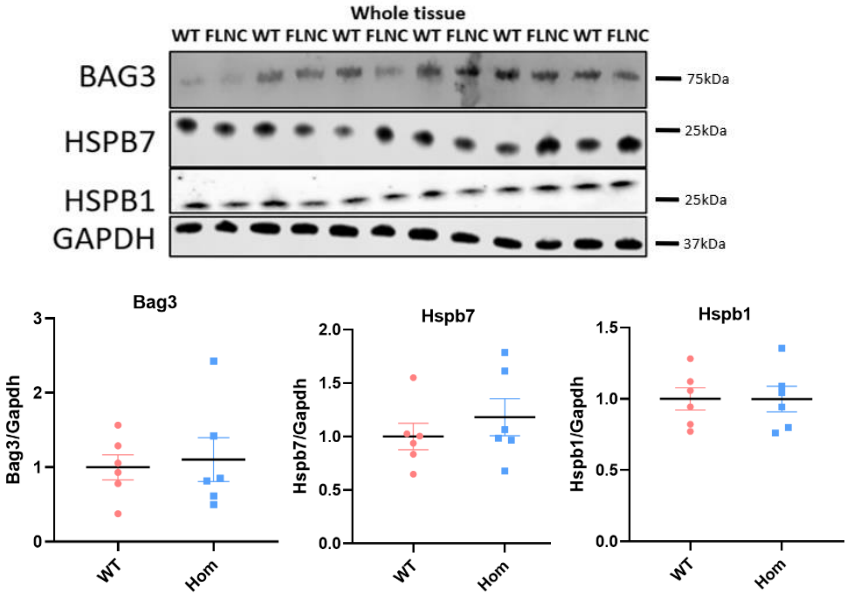

Figure 5-2 Assessment of changes at a protein level in the membrane fraction of heart tissue as well as whole tissue from 14-week old FLNC W2165C mice. A) BAG3, HSPB7, HSPB1 measured in the membrane fraction and normalised to vinculin as a membrane specific marker. BAG3, HSPB7, HSPB1 measured in the whole tissue and normalised to GAPDH. Significant changes are observed and displayed with asterisks. Data was not normally distributed and underwent Mann Whitney U test. n = 6, mixed sex.

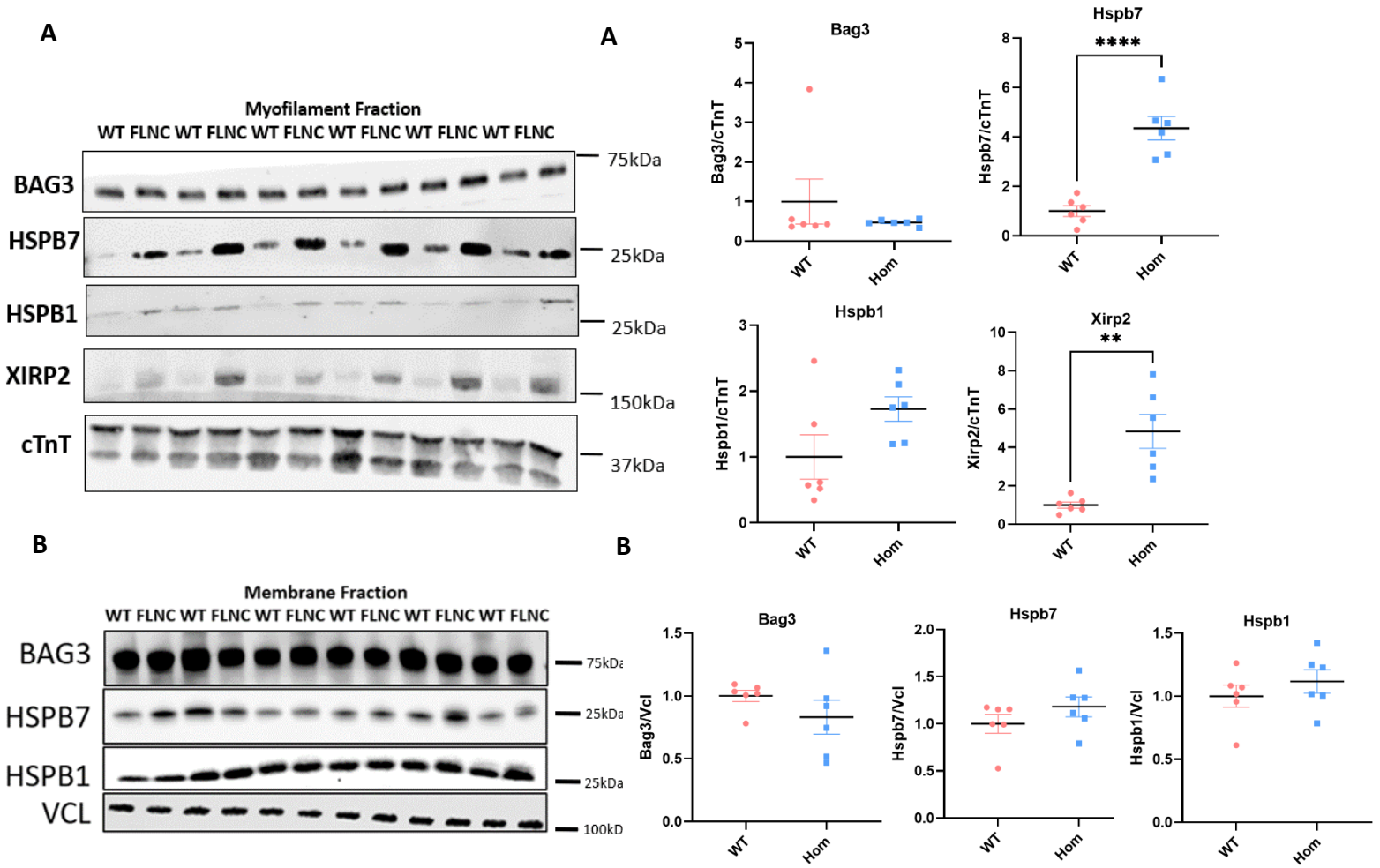

Figure 5-3 Assessment of changes at a protein level in the myofilament (A) and membrane (B) fraction of heart tissue from 14-week old FLNC W2165C mice. Myofilament measurements were normalised to cTnT and membrane measurements to vinculin (VCL). Data was not normally distributed and underwent Mann Whitney U test. n = 6, mixed sex. Significant changes are observed in the hearts of W2165C mice ($p<0.01$, **; $p<0.0001$, ****; versus WT).

5.2.3 CASA in iPSC-CMs

Due to the mechanical environment iPSC-CMs are under in regular 2D culturing conditions (Chapter 4) and its effect on the mechano-sensitive process of CASA, iPSC-CMs were cultured on surfaces of tuneable stiffnesses (Figure 5-4). iPSC-CMs that were cultured on 2 different stiffnesses, both compared to matched controls cultured on regular tissue-culture treated glass. The comparison between a healthy (20kPa) and fibrotic (130kPa) stiffness, enables one to observe if a CASA-like system is aggravated in a fibrotic environment.

An increased expression of heat shock proteins and co-chaperones was found in iPSC-CMs on PDMS of a physiological stiffness (20 kPa). Hom *FLNC* W2164C iPSC-CMs displayed significant transcript differences when changing culturing surface stiffness (*HSPB7, CRYAB, BAG3, HSPA1A, HSPA8*), this was absent in wild-type iPSC-CMs on surfaces of tuneable stiffness.

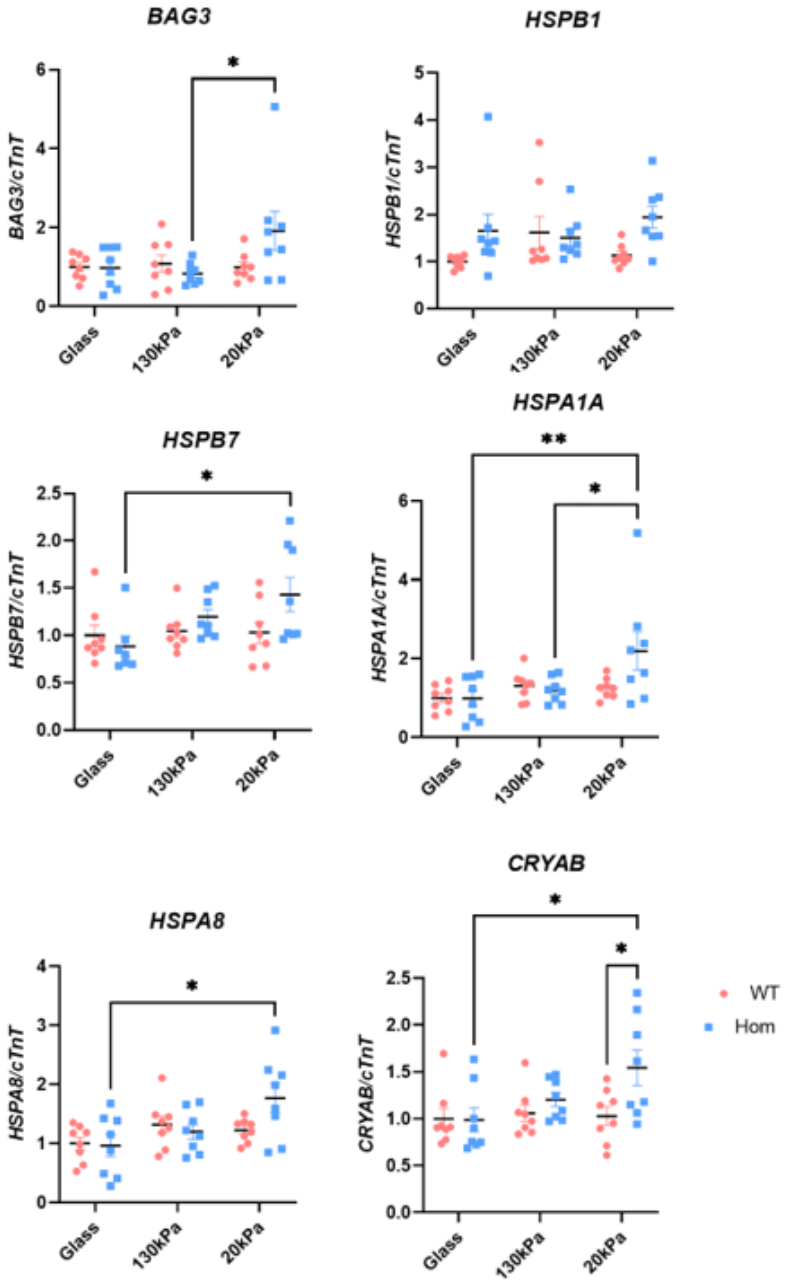

Figure 5-4 Assessment of changes at a transcript level of 30 days old FLNC W2164C iPSC-CMs on substrates of defined stiffness. All measurements were normalised to cTnT. Significant changes are observed and displayed with asterisks. Data underwent a two-way ANOVA. n/d = 2/4. Abbreviations: n/d = number of wells per differentiation/number of differentiation batches. Significant changes are observed in the hearts of W2165C mice ($p<0.05$, *; $p<0.01$, **; versus WT).

At protein level, CASA interactors (BAG3, HSP70), clients (Xirp1) and mechano-sensitive heat shock proteins (HSPB1, HSPB7) were measured in iPSC-CMs on 130 kPa and 20 kPa surfaces (Figure 5-5). Correlating with observations in transcript data, BAG3 trended towards an increase in Hom cells but this did not reach significance. HSPB1 and HSPB7 was found to significantly increase in Hom iPSC-CMs relative to WT cells on 130 kPa, but on 20 kPa substrates, both levels remained comparable to WT cells. No significant differences were observed in either XIRP1 or HSP70.

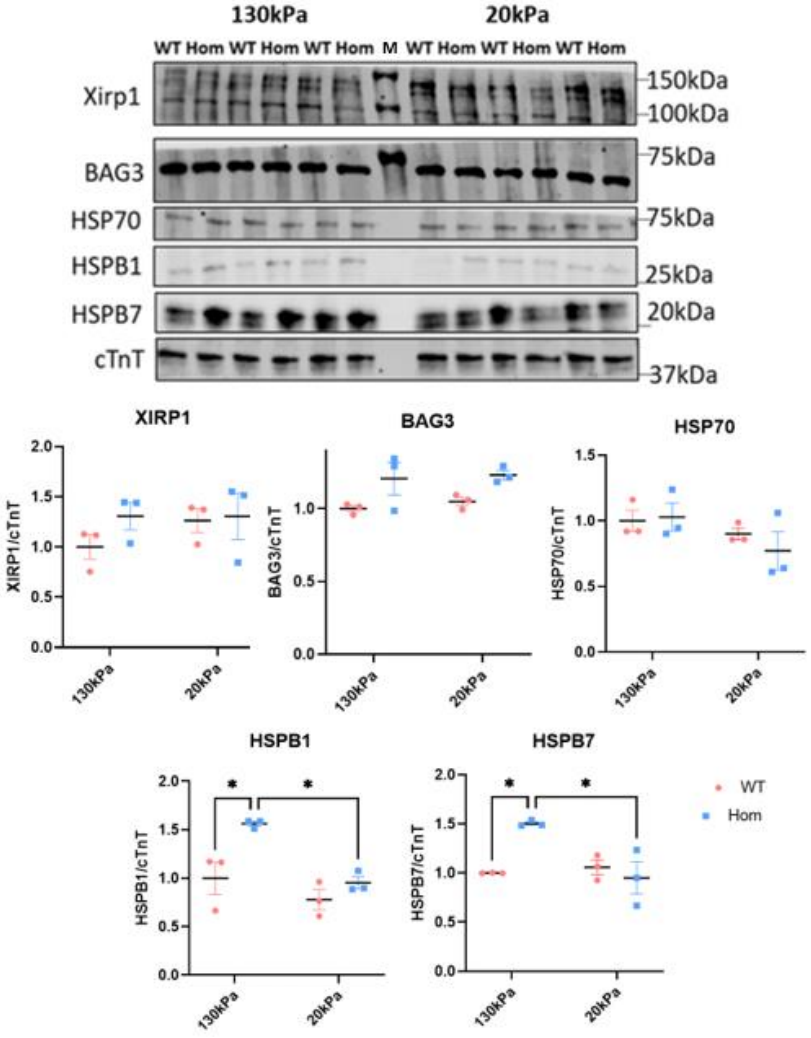

Figure 5-5 Assessment of changes at a protein level in CASA targets in 30-day old iPSC-CMs harbouring the FLNC W2164C variant cultured either on 130 kPa or PDMS of 20kPa stiffness. All measurements were normalised to cTnT. Significant changes are observed ($p<0.05$, *; versus WT). Data underwent a 2-way ANOVA. n/d = 1/3. Abbreviations: M = Marker; n/d = number of wells per differentiation/number of differentiation batches.

5.2.4 Autophagic flux in iPSC-CMs

The FLNC W2164C variant is hypothesised to affect CASA-dependent proteostasis, therefore mutant iPSC-CMs could display altered activity of autophagic pathways. An indirect indicator of CASA activity is evidence of autophagic activity. This was measured in iPSC-CMs cultured on 20 kPa PDMS surfaces by analysing the autophagic flux and measuring lysosomal content within live-cells.

Since autophagic pathways are highly dynamic, it is difficult to get steady-state measurements of autophagy markers, such as LC3 and p62, at either transcript or protein level [452]. LC3 exists in two forms: LC3-I is the cytosolic form which is converted into the membrane-bound form, LC3-II, in order to initiate autophagosome formation and elongation [453]. The ubiquitin-binding protein, p62, is the classical autophagic flux marker and is involved in targeting degradation of misfolded proteins during selective autophagy [453]. Autophagic flux experiments were setup by using chloroquine, which is known to inhibit autophagic flux in cells by decreasing the fusion of the autophagosome and lysosome [454]. In response to chloroquine treatment, Hom cells exhibited a significant increase in the level of LC3-II relative to LC3-I (Figure 5-6). WT cells did show a trend towards increase but this did not reach significance, suggesting that Hom iPSC-CMs are more sensitive to autophagic inhibition. With a range of variability, no significant genotype differences were found in p62 expression.

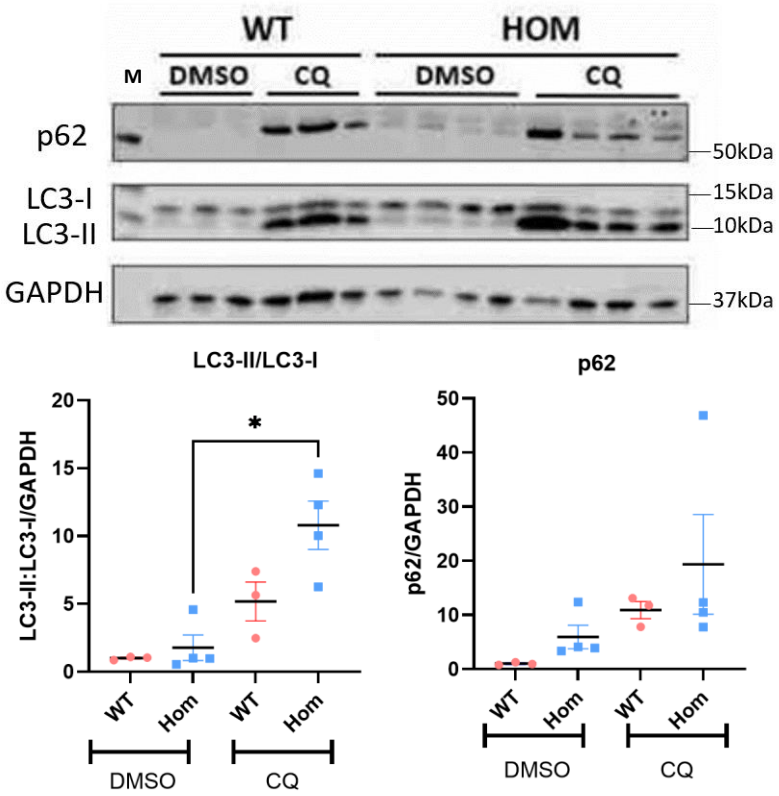

Figure 5-6 Assessment of changes at a protein level of 30 days old FLNC W2164C iPSC-CMs on 20 kPa stiffness under different DMSO or chloroquine (CQ) treatment. All measurements were normalised to GAPDH. Significant changes are observed and displayed with asterisks. Data underwent a Kruskal-Wallis test with multiple comparisons. n/d = 1/3-4. Significant changes are observed in mutant iPSC-CMs ($p<0.05$, *; versus WT). Abbreviations: M = Marker; n/d = number of wells per differentiation/number of differentiation batches.

5.2.5 Lysosome expression in iPSC-CMs

In response to processes such as autophagy and protein transport, the lysosomal machinery is activated to degrade intracellular molecules [455]. The size and/or number of organelles may change as a result of increased lysosomal protein levels in *FLNC* W2164C iPSC-CMs cultured on 20 kPa surfaces. The LysoTracker Deep Red dye was used to directly visualise lysosomes and show active lysosomal movement in live WT and Hom iPSC-CMs. There was evidence of active lysosomal movement of the LysoTracker in both WT and mutant iPSC-CM lines (Video 2), indicating that these acidic organelles were dynamically mobile [456]. Some videos demonstrate the movement along a linear path, other cells did not display this linear movement.

The quantification of LysoTracker staining showed no differences in size or number of LysoTracker structures (Figure 5-7). The LysoTracker particle number was calculated by field of view and was not normalised to the number of nuclei however so this result should be treated with caution.

Video 2 LysoTracker Deep Red labeling (red) videos of WT and Hom iPSC-CMs showing active lysosomal transport. (scale bar=20 μm).

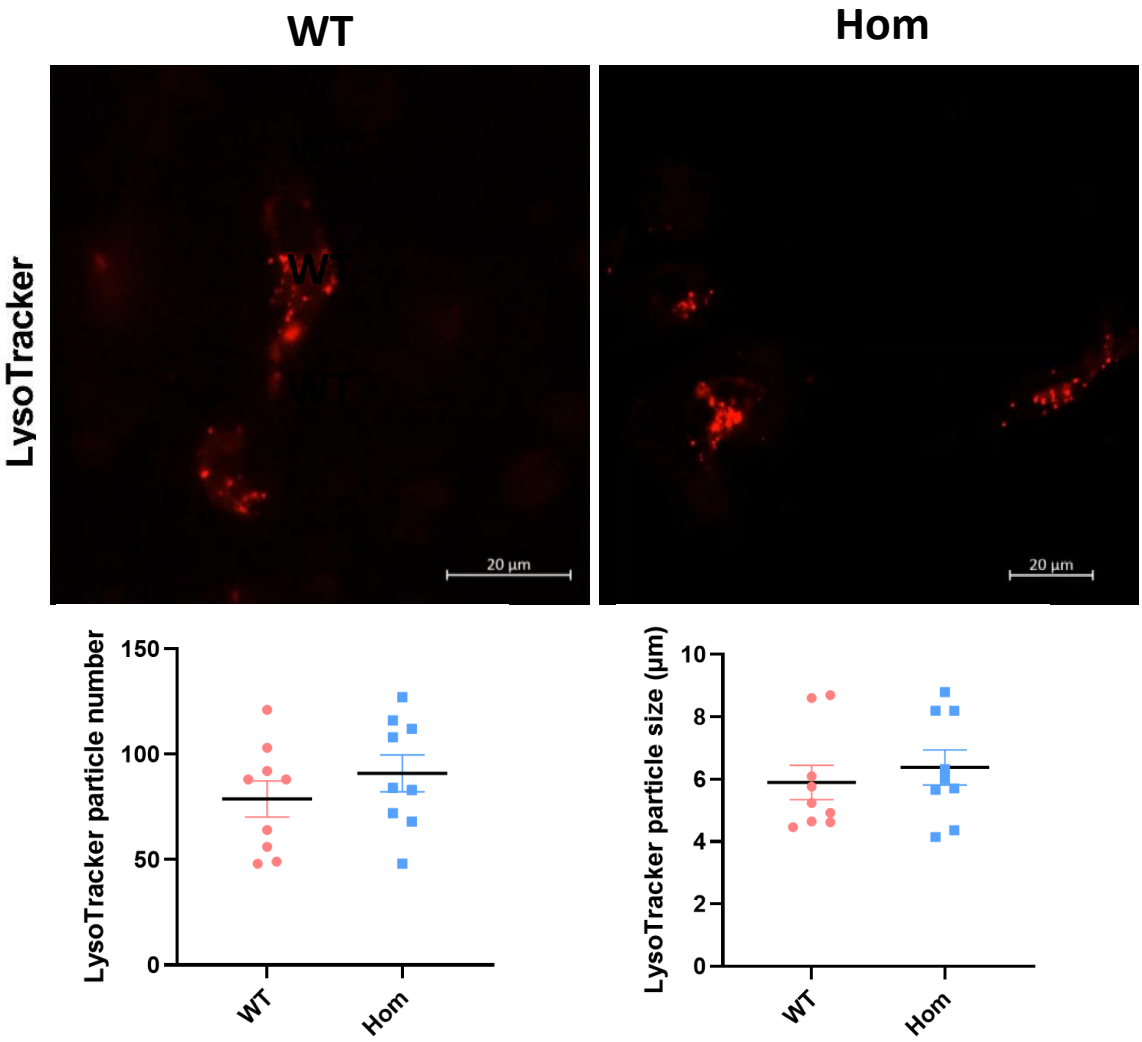

Figure 5-7 Confocal images of LysoTracker Deep Red labeling (red) show comparable lysosome content in Wild-type and mutant iPSC-CMs (scale bar=20 µm). Quantification of Lysotracker-stained particles. Quantification of Lysotracker-stained particle size. Student's t test, N/n/d = 3/1/3, age Day 30 ±1 day. Abbreviations: N/n/d = number of cells per well/number of wells per differentiation/number of differentiations.

5.3 Discussion

The previous chapters described a hypertrophic molecular response in mice and iPSC-CMs (induction of fetal gene programme). Evidence of altered proteostasis was first indicated in the mouse model in Chapter 3 with increased abundance and evidence of changed localisation of filamin C and its binding partners. This was interesting because pathogenic cardiac and skeletal myopathies have been implicated to affect proteostasis [59], [94], [107], [121], [457]. The exact mechanisms believed to cause altered proteostasis responses are not well defined in a cardiac setting, but molecular chaperones (BAG3, HSPB1, HSPB7, CRYAB) are likely to be implicated due to their involvement in maintaining cellular health through regulation of protein synthesis, folding, incorporation and degradation [59], [107], [121].

This chapter attempted to elucidate the contribution of mechano-sensing leading to impaired proteostasis and subsequent cardiomyopathic phenotypes. A CASA-like process was hypothesised to be constitutively active in mutant FLNC mice due to improper protein folding resulting in an overexposure of sites for CASA ligand-binding. To test whether CASA was over-activated in mutant mice and iPSC-CMs, general autophagic markers and lysosome expression were analysed in addition to specific investigation.

5.3.1 Induction of autophagy

Chaperone-mediated autophagy is the process for protein degradation which is based on the translocation of a targeted protein towards the lysosome membrane. Autophagic flux was determined in iPSC-CMs to assess the increased induction of autophagy in mutant cells.

Autophagy is involved in the degradation of proteins to ensure stasis. Measuring the rate of autophagy is possible by blocking a step in the autophagy pathway and measure the rate of

accumulation in the substrate which is inhibited in that step. This is often by blocking the degradation of LC3 using chloroquine [438].

LC3 is in the autophagy-related protein family which initiates the formation and lengthening of the autophagosome. It is post-translationally modified from LC3-I to form LC3-II once it is part of an autophagosome and therefore is a suitable metric for autophagy [438]. The level of LC3-II relative to LC3-I was assessed by immunoblot in iPSC-CMs during inhibition of LC3-II degradation (via chloroquine) under glucose deprivation as glucose is known to inhibit autophagy induction [458]. If autophagy is over-activated due to the *FLNC* W2164C variant, LC3-II should be increased.

Autophagic flux as measured by LC3-II trended towards upregulation after chloroquine treatment in both WT and *FLNC* W2164C iPSC-CMs. There was a significant upregulation of relative LC3-II in chloroquine-treated Hom cells compared to control Hom cells which was not present in the WT counterparts suggesting that mutant iPSC-CMs are more sensitive to autophagic inhibition and have a significantly increased autophagic flux. Although an upward trend in Hom cells, there was not a genotype effect on p62, an additional marker for autophagy.

Despite the lack of significance found in p62, the significant increase in LC3-II in Hom cells indicates that the presence of mutant FLNC has increased autophagic activity

5.3.2 Lysosomal activity

The depletion of proteins involved in autophagy initiation, phagophore nucleation, phagophore expansion, cargo sequestration, membrane sealing and autophagosome maturation may reflect an increase level of autophagy due to the consumption of such components [459]–[461]. Therefore, upon deeper inspection of the proteomics data,

CLEAR motif proteins were identified in both the myofilament and membrane fractions (Table 5-1).

Lysosomes play an instrumental role in the assembly and maintenance of the sarcomere through Z-disc protein turnover [360], [462]. Lysosomal proteins such as, LAMP2 (encoding lysosomal-associated membrane protein-2) have a central role in lysosome-mediated degradation, and murine studies have shown their essential role to Z-disc stability [59], [462]. A recent study demonstrated that a truncated FLNC protein, which results in FLNC accumulation, leads to an increase in lysosome expression [360]. Alongside the increased autophagic flux observed in mutant FLNC W2164C iPSC-CMs, increased lysosomal involvement may indicate an overactive response to prevent FLNC protein aggregation.

CLEAR motif proteins identified through the mouse proteomics data were lysosomal enzymes and proteins involved in mediating lysosomal acidification (Ctsd, Lamp1, Lamp2, Psap, Scarb2, Tpp1) [413]. CLEAR motif proteins are partially responsible for the regulation of lysosomal gene expression [413]. If there is an overactive induction in autophagic and lysosomal activity in order to present filamin C aggregation, CLEAR motif proteins would also increase with accumulation from the mutant filamin C protein. There was no evidence of lysosomal protein expression enrichment in the mouse proteome. Similar findings in lysosomal expression were found in homozygous *FLNC*-null iPSC-CMs or *FLNC* G1674C Hom iPSC-CMs, and could suggest that the lysosomal pathway is not overtly activated in by *FLNC* variants [360].

Live-cell imaging of lysosomes in iPSC-CMs failed to show genotype-related alterations with lysosome particle number and lysosome size as in other studies on the iPSC-CM

platform [360], [463]. Lysosomal motility also appeared to be unaffected, with both WT and Hom cells showing active lysosomal movement, however this was not assessed quantitatively. Due to technical difficulties in obtaining the data for lysosome particle number, the lysosome number could not be normalised to nuclear number and presents a major limitation to the interpretation of this work.

Cumulatively, this data does not show a direct lysosomal role in mice or iPSC-CMs carrying the homozygous FLNC W2164C variant. Additional work is being carried out to determine the autophagic flux status of mutant mice.

5.3.3 Activation of CASA

The activation of a chaperone-mediated autophagy system was measured by running a targeted interrogation on both models guided by the proteomics experiment.

Analysing the proteome of the mice showed a significant induction of key CASA complex proteins (Bag3, Hspa12b/Hsp70), CASA interactors (Sorbs2, Myh7) and clients (Actn2, Flnc, Sptan1, Xirp1) as defined my Martin et al. [414]. In response to proteotoxic stress, the CASA complex is found to upregulate and localise towards the sarcomere Z-disc [464].

At a proteome-wide level in the mutant mouse Bag3 and Hspa12b (a member of the Hsp70 family), were significantly upregulated. BAG3 is a highly expressed co-chaperone protein in the heart, in which its expression is induced by stress and is central to CASA [465], [466]. In response to stress, BAG3 plays an additional role in cardioprotection and aids in preventing cell death [467]. HSP70 is known to have cardioprotective functions that is involved in cardiac remodelling and maintains endothelial integrity in response to myocardial ischemia injury [416], [468], [469]. HSP70 activity is modulated by the BAG3 gene, therefore the co-upregulation is not surprising. Both proteins form a BAG3-HSP70

complex in response to stress and can inhibit the assembly of the apoptosome [467], [470]. An additional CASA interactor [414], HSPB1, was found to be significantly upregulated when probed for by immunoblotting. HSPB1 has been known to interact with the mechano-sensitive domain of FLNC and is involved in processing protein aggregates [107], [471]. HSPB2, which was found to be significantly upregulated in the membrane fraction of Hom mice (+3.395 fold relative to WT), is another heat shock protein which demonstrates weak binding to BAG3, acting as a binding competitor of HSPB8 [472].

The upregulation of CASA complexes correlates with the upregulation of CASA clients FLNC, SPTAN1 and XIRP1. XIRP1 directly interacts with FLNC in the region of Ig18-21 and earlier studies show an increased interaction of *FLNC* W2164C with XIRP1 [unpublished, Carin de Viliers' work], and may result in making filamin C less mobile and extending the half-life of the protein. The downregulation of ACTN2 observed in the membrane fraction proteomics data, however is not wholly understood, the high turnover of filamin C and increased activity of CASA may lead to poor incorporation of ACTN2 into the sarcomere without the stabilising effect of proper functioning FLNC. The function of mutant filamin C has not been assessed so interpretation of this result is limited.

BAG3 has been reported to modulate mitochondrial activity by promoting mitophagy in depolarised mitochondria [473]. Interestingly, one of the mitochondrial proteins identified in Chapter 3 as significantly under-expressed (Uqcrc2) is found in CASA complexes [414]. Alongside other mitochondrial proteins (Slc25a4), these reductions may be due to increased mitochondrial fragmentation from increased Bag3 levels [464]. Also found to be increased, Hsp60, facilitates the folding and degradation of mitochondrial proteins and its overexpression is associated with reduced mitochondrial cytochrome c hence potentially explaining the reduction of mitochondrial proteins observed in this work [474].

The transcription of heat shock proteins and CASA chaperones in both the Hom mouse (Hspa8, Hspb7, Hspa1a) and iPSC-CMs (HSPB7, CRYAB, BAG3, HSPA1A, HSPA8) showed increases relative to WT counterparts suggesting an increased level of chaperone activity. iPSC-CMs also showed a genotype response in 20kPa Hom cells with increased transcript in CASA related genes (BAG3, CRYAB, HSPA1A, HSPA8). The molecular phenotype appears to be induced by the variant itself rather than in response to changes between healthy (20 kPa) and fibrotic (130 kPa) conditions. Out of the proteins which underwent immunoblotting, these findings were not corroborated at a protein level, with one exception (HSPB7), indicating that some of these proteins may be under increased rates of turnover themselves.

Together with an increased level of autophagy occurring in iPSC-CMs as assayed by flux experiments (Figure 5-6), the significant changes observed from mouse proteome analysis indicate a possible induction of chaperone-mediated autophagy activity in the mutant cellular and mouse models. Strengthening this, a transcript induction of CASA interactors was also observed.

While this data does not show direct evidence of CASA involvement, this data suggests a potential role of CASA and future steps will include CASA-specific target probing via a co-immunoprecipitation experiment. This would allow one to measure changes in protein binding complexes between WT and mutant FLNC. Furthermore, other parameters, such as ubiquitination levels, can be informative to decipher whether a ubiquitin-dependent proteasome system is activated [475] or whether a different protein turnover system is employed such as macroautophagy, microautophagy or a different chaperone-mediated autophagy (CMA).

5.3.4 Role of heat shock proteins

The FLNC W2164C variant, located in the mechanosensitive region, was hypothesised to result in overactive chaperone-mediated autophagy due to an overexposed binding site of filamin C's Ig20. Aggregates were not observed in the mouse model or in iPSC-CMs, implying that there is adequate clearance of FLNC and its binding partners in the presence of the variant. The increased relative protein abundance (FLNC, MYOT) at the intercalated disc however is still not well understood. This thesis has identified an upregulation of a heat shock protein, HSPB7, which has not been previously implicated in CASA [107]. Heat shock proteins may play a mechano-sensing role in the phenotype observed in the FLNC W2164C variant.

HSP70, HSPB1, HSPB2, HSPB7 and HSPD1 (HSP60) were found to all significantly increase in mutant mice. The increased levels of apoptosis inducers, such as Hsp60, must be treated with caution as myopathy and congestive heart failure can lead to apoptosis as a secondary induction rather than the cause. While HSP70, HSPB1 and HSPB2 may interact with CASA machinery, HSPB7, was the only other validated protein to be significantly upregulated [414].

Together, with the lack of aggregation found in the mouse model, the increased myofilament expression of HSPB7 is a novel finding. HSPB7 was not expected to be upregulated as it normally binds to a different region of filamin C, the dimerization domain, Ig24 [133]. The expression of the chaperone HSPB7 increased significantly in the myofilament fraction and was found to localise closely to the intercalated disc as reported in Chapter 3. HSPB7, along with HSPB1, aids filamin C localisation and folding [107], [121]. In the absence of HSPB7, disrupted FLNC localisation, increased aggregation, cardiac myocyte dysfunction and

myopathy have been reported [121], [133], [246]. In addition, the lack of HSPB7 is associated with increased autophagy [133].

Within a chaperone-mediated autophagy context, it was proposed that HSPB7, along with HSPB8, could interact with BAG3 and aid in the transportation of denatured proteins to autophagosomes [268], [476], [477]. Recent data shows HSPB7 has been regularly reported to operate independent of machinery involved in CASA [272], [415]. In addition, a direct HSPB7-BAG3 interaction has been disproved [476], [478]. However, HSPB7 has also been reported to be involved in protein aggregate clearance [479], [480] and is found to increase in mouse models of dystrophy [481], [482]. While a knockout of HSPB7 is found to result in FLNC aggregates [133], [268], other studies have demonstrated that damaged FLNC is not cleared by HSPB7 alone [83]. There is no consensus of the action of HSPB7 on FLNC.

The increase of HSPB7 may represent a different mechanism of action for FLNC protein turnover resulting in the co-redistribution of HSPB7 and FLNC towards the intercalated disc. A BAG3-independent process has been proposed in which HSPB7 limits actin polymerisation to minimise protein aggregation, however, this has not been described *in vivo* [478].

With mutant FLNC known to be overextended, the domain 20 may be increasingly exposed and recognised for degradation. Structural analysis by collaborators demonstrated that the mutant FLNC has an extended native conformation and misses transition states between folding and unfolded conformations [unpublished – Benesch group]. The binding of HSPB1 to WT FLNC increases the energy required to unfold filamin C relative to HSPB1-mutFLNC, confirming that HSPB1 has a stabilising effect on WT FLNC [Figure 5-8 unpublished – Benesch group].

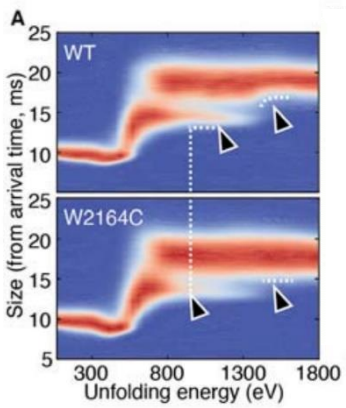

Figure 5-8 Coulomb force unfolding of WT and W2164C FLNC d18-21. Arrows point at differences in the unfolding pathways, with W2164C exhibiting destabilized intermediate states. **[Unpublished – Benesch Group, University of Oxford.**

HSPB7 may have increased off-target binding to the free cysteine residue in domain 20 of FLNC W2164C as HSPB7 is known to have disulphide-crosslinking properties [483]. If HSPB7 is binding to Ig20 instead of Ig24, it would make sense that HSPB7 expression at transcript and protein level is increased to ensure HSPB7 is performing the dimerization stabilisation properties in Ig24. In support for altered HSPB7 function in this variant, HSPB1 may be restricted in binding to Ig20 of mutant FLNC due to HSPB7 binding competition and hence impair the bind to Ig20 and hence result in a reduction of the energy needed to unfold mutant FLNC. While this is speculative, in the future, the technique of

hydrogen/deuterium exchange monitored mass spectrometry could be utilised to test if a disulphide bond forms between HSPB7 and a mutant construct of FLNC Ig20 [484].

5.4 Conclusion

To conclude, this data shows indirect evidence that the FLNC W2164C variant results in a chaperone-mediated autophagy which is constitutively active. The first indication of an active proteostasis system, was the lack of FLNC aggregation observed in mice and iPSC-CMs. Partners of CASA appear to be significantly affected in this variant, with HSPB7 posing as a player in a potential CASA-independent function. Further biochemical analysis is needed to understand the binding affinities of filamin C with heat shock proteins and measuring the mobility of mutant filamin C would be particularly informative as an indicator of protein turnover rate.

Chapter 6 : FINAL DISCUSSION

6.1 Summary of results

Every week, 12 people under the age of 35 die in the UK due to undiagnosed heart conditions, with inherited cardiomyopathies estimated to affect approximately 260 000 people in the UK alone [485]. Although diagnosis has been improved with the use of genetic screening which targets the known cardiomyopathy-associated genes (e.g. *MYH7, TTN, TNNT2, MYBPC3, FLNC*), the interpretation of the identified variants, such as *FLNC* missense variants remains a challenge as they are often classified as a variant of unknown significance.

FLNC is a novel disease gene encoding for the protein filamin C which possesses a unique Ig-like domain 20 [98]. This domain, within the mechano-sensitive region between d18-d21, may play a crucial role in relaying signals in response to mechanical stress via interaction with the stress-inducible heat shock protein B1 (HspB1) [270]. A missense variant in *FLNC* W2164C was found in this domain to co-segregate in a three-generation family affected by cardiomyopathy. This thesis attempted to characterise the effect of the potentially pathogenic *FLNC* W2164C missense variant in relation to cardiomyopathy using genetically modified mice and iPSC-CMs. The primary aims of this thesis were:

- Understand the role of an Ig20 missense variant in cardiomyopathy
- Interrogate the role of filamin C in mechano-sensing and how it is perturbed by W2164C
- Explore the use of iPSC-CMs in modelling this cardiomyopathy-related *FLNC* missense variant

6.1.1 Chapter 3: Mouse Model

In Chapter 3, the initial characterisation of the *FLNC* W2164C variant in a mouse model was undertaken: the cardiac morphology of the mice was described along with the molecular phenotype. Hypertrophy was not observed morphologically, however, an RCM phenotype was observed when measuring hypertrophy parameters (LVPW.d and LVAW.d) and considering atrial weight increased in mutant mice while ventricle weight/size remained unchanged. Increased atrial weight could represent impaired diastolic ventricular filling – however ventricular volumes were not altered. To confirm this, it would be beneficial to obtain colour Doppler, tissue Doppler and a long axis 4-chamber view ultrasound.

The RCM phenotype is in agreement with other studies highlighting the mutational hotspot with numerous RCM-associated missense variants in Ig20 [155], [486], [487] and in the intradomain insert [100].

Since filamin C re-localisation is observed in the presence of HCM- and RCM-related *FLNC* missense variants (*FLNC* V123A, V2297M), the quantity and distribution of filamin C and its binding partners were probed for in fractionated murine cardiac tissue via proteomics [98], [155]. Although this variant is heterozygous in patients, a mild phenotype was only observed in homozygous mice. Proteomics on these samples found mitochondrial proteins in the membrane fraction were less abundant in Hom mice, but also showed an increased abundance in some sarcomere proteins in the myofilament fraction (Flnc, Myh7, Myot). This finding was congruous with a molecular phenotype describing HCM as a disease of energetic deficiency and sarcomere disruption [284]. The mitochondrial differences, however, could not be validated by immunoblotting. Filamin C and its binding partner Hspb7 were found to be upregulated in the myofilament fraction and localised towards the intercalated disc.

Since at a transcript level, *FLNC* abundance remained the same between genotypes, it was proposed that any differences observed at protein level and localisation level are due to altered protein turnover. One such method of protein turnover, CASA, was probed for in Chapter 5 due to this process targeting filamin C as a client in skeletal muscle [59].

6.1.2 Chapter 4: Human-induced pluripotent stem cell-derived cardiomyocytes iPSC-CM model

Chapter 4 investigated this same variant in the cellular iPSC-CM model. With immaturity being a major concern in iPSC-CM research [488]–[490], an end point for experiments needed to be determined when cells reached a consistent cardiomyocyte structure and function which allowed for disease characterisation. This day was determined to be 30 days after differentiation induction. This time point has already been used in other studies of modelling cardiomyopathy in iPSC-CMs [360], [383]. Findings from the mouse model, namely upregulation of filamin C and its binding partners (such as myotilin), protein relocalisation (such as myotilin, HspB7), could not be recapitulated in the iPSC-CM model in plastic 2D culture or in the presence of ISO. This is likely due to the poor iPSC-CM selection criteria applied initially as discussed mentioned in Chapter 4.0. When cells were cultured on soft substrates using PDMS, however, a genotype-related phenotype was observed. Here, the cells were found be more mature at molecular level and showed a reduced beating frequency, associated with maturity, but were still found to have a disorganised myofibrillar arrangement and no genotype-related differences were observed at a morphological level. Homozygous cells cultured on 20 kPa PDMS showed an induction of markers for the fetal gene programme (*NPPA, NPPB, MYH7, ACTA1*). Unlike earlier observations in the mutant iPSC-CMs, on 2D plastics or on glass coverslips, the cells also

showed an induction of *HSPB7* at transcript level. This is likely due to a more stringent quality control process which was implemented later in the PhD to minimise variability.

6.1.3 Chapter 5: Effects of *FLNC* W2164C mutant on mechano-sensing

Chapter 5 specifically targeted the effect of the missense variant on mechano-sensing in both disease models. Markers which are implicated in mechano-sensing with filamin C were probed for at a transcript level by qPCR and protein level by immunoblotting in mutant mice and iPSC-CMs. Homozygous mice and iPSC-CMs were found to have an induction of HSPB7 both at a transcript and protein level.

Since there is no induction of the filamin C gene but a significant difference seen in proteomics data, it was hypothesised that this could be due to an impaired CASA complex resulting in altered autophagy activity. Autophagic flux and lysosomal content were measured in iPSC-CMs, however no significant differences were reported. This filamin C missense variant was not found to affect CASA or other forms of autophagy in the parameters measured in this study.

The summary of results can be split into three themes (Table 6-1):

- An evaluation of the cardiomyopathy-related missense *FLNC* W2164C variant
- The effect of *FLNC* W2164C to mechano-sensing
- An evaluation of models to study cardiomyopathy.

Table 6-1 Summary of changes observed in mutant mice and in mutant iPSC-CMs. Abbreviations: HW, heart weight; ICD, intercalated disc; NI, not investigated; ETC, electron transport chain.

	Mutant Mouse	**Mutant iPSC-CMs**
Heart measurements	Increased HW with Ang-II treatment (same in WT)	No changes in cell size or organisation
Hypertrophy markers	Fetal gene programme	Fetal gene programme
Protein localisation	FLNC/HSPB7/MYOT localised at ICD FLNC, MYOT colocalised	No changes observed
CASA and autophagy	Upregulation of CASA markers (Bag3, Hspa12a)	Increased autophagic flux Regular lysosomal activity
Energetic dysfunction	Downregulation of ETC components	No changes observed

6.2 *FLNC* W2164C and cardiomyopathy

Filamin C has been increasingly associated with cardiomyopathies independent of skeletal muscle involvement. Variant positioning has been reported to play a role in the cardiomyopathy subtype, however, a pathway has not been elucidated. Variants found between Ig18-21 have been proposed to play a role in altered mechano-sensing and -signalling. The *FLNC* variant assessed in this thesis lies within this region, at Ig20, and was found in a multi-generational family affected by cardiomyopathy.

Despite HCM being the primary cardiomyopathy in patients carrying this variant, morphological and contractile assessment in the mouse displayed a subtle phenotype resembling RCM, though this needs follow-up confirmation. The RCM phenotype is not surprising since other *FLNC* variants near *FLNC* W2164C have been reported in RCM patients [155], [491]. In partial agreement with the RCM filaminopathy, Tucker et al. described that filamin C protein continues to localise towards the ICD in RCM patients with

a *FLNC* V2297M missense variant , however, in contrast, the disappearance from the Z-disc described in their case was not observed in this thesis [155].

A molecular phenotype indicative of HCM was reported at transcript level in both models, and at a protein level in the mouse. By performing proteomics on fractionated tissue, genotype-specific alterations were identified at a protein level. Greater sensitivity was achieved in protein abundance changes between genotypes in fractionated samples. These changes guided follow-up experiments to determine whether changes were localised to the fraction, evidence of redistribution between fractions or if they were global changes. The increased level of HSPB7 in the myofilament fraction highlighted the importance of the fractionation, as immunoblot validation showed normal protein levels of HSPB7 in whole tissue and in the membrane fraction, and therefore is a fraction-specific upregulation.

6.3 *FLNC* W2164C to mechano-sensing

Mechano-sensing and -signalling have been proposed to be key functions of filamin C. The effect of the *FLNC* W2164C variant on this was briefly probed for. Although genes (and their transcribed proteins) implicated in proteostasis or mechano-sensing (*HSPB1*, *HSP70*, *HSPB7, FLNC*) were found to be increased in mutant mice and/or in iPSC-CMs, autophagic activation was not convincing in mutant iPSC-CMs. It could be that the variant is more readily refolded since it is found to be more elongated in the relaxed conformation [Elena Holden, unpublished, Justin Benesch group]. This would in turn result in an increased transcription of chaperones, such as *HSPB7,* but would not explain the protein re-localisation or increase in filamin C abundance. The *FLNC* W2164C variant clearly has an effect; however, the nature of this effect is unknown with no distinct pathway being identified in this work.

FLNC variants are found to possess a phenotypic spectrum of conditions: HCM [98], [141], DCM [99], [101], [140], RCM [100], [155] and atrial fibrillation [98], [141], [492]. Variants may act in conjunction with other genetic factors as described in a recent review on the impact of common variants to HCM and is likely to be the case for other cardiomyopathies [493]. In the mouse model, the *FLNC* W2164C variant was shown to induce a significant molecular phenotype indicative of HCM, though was not able to induce a consistent morphological or functional phenotype. This muted phenotype may suggest mouse-human differences or imply that additional genetic or environmental factors are involved that result in the patient found phenotype.

6.4 Models to study cardiomyopathy

Every model has its strengths and limitations. When data from different models are contradictory to each other, it is important to assess where data reliability and validity lie. The interpretation of such data therefore needs to be treated with caution.

Comparing findings between *in vivo* and *in vitro* models is difficult since there are intrinsic differences in how data is obtained and the conditions that are set. For instance, recording animal cardiac parameters required the mouse to be under general anaesthesia, which reduces heart rate, whereas iPSC-CMs were paced at a frequency above their intrinsic one. Both female and male mice were used for data collection, with sex-differences observed, whereas the iPSC-CM model was of male origin only with sex-differences also found to be present in other studies using the iPSC-CM model [494].

The molecular phenotype of iPSC-CMs when cultured on PDMS agreed with the molecular findings of the murine model; an induction of the fetal gene programme was observed in

both. This finding on the PDMS-coated iPSC-CMs may be due to a combination of the maturation effect of culturing cells on physiological stiffnesses as well as an improvement in the mechanical environment [330], [495]. Data generated beforehand was incongruent with the mouse findings and this made interpretation difficult. iPSC-CM data became comparable with the mouse model after improved quality control, and the maturation method of using PDMS were implemented.

By using both models, a molecular phenotype indicative of cardiomyopathy and altered autophagy was displayed in the mutants, however, iPSC-CMs failed to replicate the changes observed in the mouse model regarding protein localisation. This was in-part due to the lack of mature intercalated discs in 2D-cultured iPSC-CMs (Figure 8-1) [E.Ehler unpublished data]. For the purpose of validation, characterising both animal and cellular models has allowed for a more robust scientific approach and has identified deficiencies which would have otherwise been unnoticed with only one model. The deficiencies of the use of these models will be discussed in the following segment.

6.5 Study limitations

Trends were observed in this study indicating a hypertrophic response. This thesis benefits from the use of both mouse and iPSC-CM models to study cardiomyopathy. Though changes were identified and new hypotheses have been made, a specific molecular pathway was not identified. Attempts to gain insightful data on proposed protein interaction disruptions were unsuccessful, such as a co-immunoprecipitation of filamin C. No disease model is perfect, and while attempts were made to negate model weaknesses and optimise experimental methods, this thesis possesses limitations. These drawbacks will be discussed.

6.5.1 Mouse limitations

For financial and practical reasons, all work presented in the mouse model was done on mice of 14-weeks old, equivalent to a young adult [496]. Since this disease presents itself most severely in late-adulthood in humans, it is not a surprise that only a mild morphological and functional phenotype was observed. Multiple mouse models of cardiomyopathies have shown little or no phenotype when mice are around 3 months but develop phenotypes as they were aged or exposed to high fat diet [192], [497]–[499]. Further to this, clinically relevant electrical parameters were not measured in the mouse for this thesis, despite an altered protein content being observed at the intercalated disc, a site of cardiac conduction [500].

Given the importance sex plays in heart disease [501]–[504], all transcript and protein work is underpowered due to the combination of both sexes.

6.5.2 Proteomics thresholds

Setting a specified and stringent threshold is crucial for any -omics experiment in order to minimise false positives [505]. This was the case when analysing data from the proteomics experiment. Processing of the data with the aim of removing any contaminants or false reads minimised the impact of single samples skewing the data completely. Some proteins were not identified in some sample runs and therefore showed no quantified value for protein abundance, these are known as missing values. The minimum number of valid quantified values in at least one group, either WT or mutant, was set at a threshold of three. This resulted in a reduction of n-numbers from six to three samples in one group, and the other group as low as one sample for some of the identified proteins. This can have a large effect on the relative fold changes when comparing between WT and mutant and lead to exaggerated or disguised differences. Although six samples per group were used, the real

number per measurement is likely to be different and inconsistent between identified proteins, highlighting the need for validation. Data imputation of invalid values was used in an attempt to negate the negative effect of missing values which limits statistical power and interference as well as biological interpretation. The handling of missing values is not a standardised procedure [506], with multiple quality control thresholds and handling approaches in place to improve the handling process [506]–[508].

Being a label-free proteomics experiment, each sample was measured in a separate mass spectrometry run, therefore run conditions (including the temperature, column condition) may differ as well as the altered handling, losses in protein digestion/separation [506]. The effect of this could have been minimised by running a TMT-labelled proteomics experiment, where each sample is first chemically/metabolically labelled and combined into one sample for a single mass spectrometry run.

6.5.3 iPSC-CM limitations

Variability affected iPSC-CM results prior to use on PDMS. This rendered any definitive interpretation of the results difficult. The introduction of an iPSC-CM quality control process correlated with the use of PDMS as soft substrate. The quality control was determined at the point of cell harvest (day 30) by the following criteria: cells must be beating synchronously as a sheet (no clusters) at a beating rate between 30-90 times per minute, a comparative PCR was run on each differentiation batch for cardiac troponin T, data obtained from any batches which did not reach the threshold were excluded.

After quality control was implemented, genotype differences began to be observed, even in cells cultured on glass, which was hypothesised to mask phenotypes due to the rigid mechanical environment. This data did not entirely remove variability, but allowed for a

greater understanding behind the source of the variability. While this resulted in reduced variability in subsequent data, this data lies separate from all iPSC-CM data generated beforehand (e.g. contractility parameters from SarcTrack).

Immaturity of iPSC-CMs is a well-documented concern with their use in cardiovascular disease modelling. iPSC-CMs resemble fetal human cardiomyocytes regarding cardiac isoform expression and cell morphology [187]. Previous studies have suggested prolonged iPSC-CM culture improves maturation and better disease characterisation, however, the relative improvement from Day 30 to Day 90 is minimal [187], [189], [509]. The use of 3D cultures, in particular EHTs or engineered human myocardium (EHM), are found to mature the cells morphologically, functionally and molecularly [334], [510]. When these bioengineering approaches are coupled with electrical stimulation, enhanced cardiac gene expression improves along with structural and electrophysiological properties [511]–[514]. Maturation media have also been reported to improve the function of iPSC-CMs for disease modelling, such as media consisting of low glucose and high fatty acid content [515]. Additional maturation methods (e.g. co-cultures, biochemical cues) have also been described with limited success [324], [515].

For practical reasons regarding optimisation and the characterisation of individual or combined maturation methods, manipulating substrate stiffness with PDMS was the method chosen. The *FLNC* W2164C variant was proposed to have disrupted mechano-sensing properties. For mechano-sensing properties to be observed, it is important that the cultured cells are not mechanically compromised. The approach of using PDMS of varying surface stiffnesses, allowed for a potential unmasking of mechano-sensing phenotypes in Hom cells. Using this approach resulted in a maturation effect of sarcomere and metabolic markers on PDMS surfaces, though morphologically they remained unaltered. Nanopatterning or

creating microgrooves on PDMS surfaces has been attempted [516]. The benefit of this is mostly related to the cardiomyocyte appearance as well as the presence of more mature intercalated discs.

6.5.4 Inconsistencies across both models

As has been discussed previously in Chapter 3 and Chapter 4, both models carry their own limitations. The individual limitations of each model were minimised by comparing the mouse data with the data derived from the iPSC-CM model. When found in agreement, this strengthened the validity of the data, such as an altered proportion of HSPB7 and transcript markers of CASA. When the data from both models was contradictory, interpretation was limited and difficult to assess.

Further to this, treatments which attempted to induce a more striking phenotype differed between mouse and cellular models. The mouse underwent Ang-II treatment whereas the iPSC-CMs were treated with ISO. Both Ang-II and ISO increase the stress on the heart and are known to induce markers of cardiac hypertrophy, though for this induction they both have distinct mechanisms of action [385]. Due to the timeline of the work conducted in this thesis, the cardiac controls used for normalising immunoblotting data were different between the mouse model and PDMS-cultured iPSC-CMs. This was also influenced by using fraction specific controls in mouse cardiac tissue.

6.6 Future work

This thesis aimed to characterise the effect of the *FLNC* W2164C variant in order to better understand the role of filamin C to cardiomyopathy and the potential mechano-sensing functions of filamin C's Ig20. This was assessed in this thesis with molecular and functional experimentation, finding molecular trends in both models. This thesis has identified areas which require additional follow-up experiments to uncover the molecular functions that may lead to these trends.

Mutant mice of 14 weeks old proved to have a significant molecular phenotype, but only a subtle morphological and functional phenotype – even in the presence of Ang-II. This provides justification to age mice up to 18 months of age, closer to the equivalent age of disease presentation in humans, though ethics would still need to be approved to do so. Mice could undergo serial echocardiography readings at 6, 12 and 18 months to establish a phenotype timepoint in the first cohort before more in depth morphological and molecular study. Since this thesis did not touch on the electrical phenotype of either the mutant mice or iPSC-CMs, it would be of interest to follow this clinically relevant phenotype up in aged mice but also in the cellular model. Interrogation of the mouse and iPSC-CMs can be done, such as measuring the action potentials in iPSC-CMs and calcium conduction of mutant mouse hearts via optical mapping [170], [517], [518].

Physiological differences and iPSC-CM model limitations may have a role to play in the phenotypes observed in this thesis. As discussed in the introduction (1.5.3.1), patient phenotypic differences could be due to variant type and genetic location. It is possible that the phenotypic impact of the *FLNC* W2164C variant may be affected by the FLNC isoform expressed in the disease models. It is currently unknown whether *FLNC* isoform expression varies in these models compared to adult human cardiac tissue. An increased expression of

the more flexible longer FLNC may modify the ability of FLNC and key structures to respond to increased cellular stress [112]. Future work could assess the *FLNC* isoform expression levels in mutant mouse cardiac tissue and iPSC-CMs.

As mentioned in the previous section, this thesis considered the possibility that mutant filamin C may have altered proteostasis, however, to-date determining altered motility of the mutant protein has not proved successful. It is of interest, particularly because it is not clear whether this mutant results in increased or decreased protein turnover. Considering filamin C is already a highly mobile protein [116], it would be of interest to run a fluorescent recovery after photobleaching (FRAP) experiment to determine this [519]. A WT and mutant GFP-construct of filamin C would need to be transfected into sarcomere-containing cardiac cells. Images are taken to determine the initial fluorescence on a confocal laser scanning microscope before a region of interest is photobleached using a high intensity setting on the laser. The region of interest would be erased of fluorescence and sequential images taken to observe the diffusion of unbleached filamin C GFP-molecules from the surrounding area into the region of interest, the fluorescent recovery. The iPSC-CM model can be a good cellular model to use this experiment to display mobility changes in the *FLNC* W2164C variant.

Further to this, altered binding affinities have not been mentioned in this work. Collaborators have shown that compared to the WT protein, mutant filamin C has weaker binding to HSPB1 (Elena Holden in Justin Benesch group, Oxford University), which also correlated with an increased amount of energy required to unfold WT filamin C relative to mutant filamin C. A co-immunoprecipitation experiment on mouse tissue would be beneficial in determining the role of HSPB1, HSPB7 and even MYOT in the presence of the W2164C *FLNC* mutant. Although HSPB1 and HSPB7 levels may be increased as a cardioprotective

manner to stabilise mutant FLNC, another hypothesis was also formed. In Chapter 5, it was proposed that HSPB7, may in fact bind with a free cysteine residue in d20 and competitively prevent HSPB1 binding. With structural biology collaborators, the interaction between mutant FLNC and HSPB7 can be directly interrogated by expressing HSPB7 with *FLNC* W2164C protein fragments to measure any disulphide bond formations.

As already discussed in the limitations section, much of the iPSC-CM characterisation was done before a stringent quality control process was introduced. This meant many efforts to report or induce a phenotype were overwhelmed with variation from the initial differentiation itself. In addition, the use of PDMS substrates appeared to have a beneficial effect both for inducing cardiac maturation and a genotype-related phenotype. The iPSC-CM model could be used to its full potential by repeating these experiments, such as SarcTrack and ISO treatment, with this quality control process in place and where practically possible, on PDMS substrates of physiological stiffness. Further to this, additional techniques can be employed in the iPSC-CM model, such as high-resolution stochastic optical reconstruction microscopy [520] which can give a more details understanding of disrupted protein localisation.

6.7 Concluding remarks

The exact role of filamin C within a cardiac context is still largely unknown and this thesis focussed on elucidating the function of the mechano-sensing region of filamin C in the heart. This thesis evaluates the effect of a clinically-relevant *FLNC* variant found in patients affected by HCM with RCM features in two disease models (mouse and iPSC-CM) and adds to the work done on filaminopathies by previous researchers. This work supports the pathogenic role of the *FLNC* W2164C variant in cardiomyopathy. While a mechanism was not identified, targets and follow-up experiments have been identified to better elucidate the filamin C's role in cardiomyopathy and mechano-sensing pathways.

Genetically-edited iPSC-CMs for cardiovascular disease modelling hold potential to uncover pathologies which may otherwise be unknown in alternative models. This thesis demonstrates the deficiencies of many standard practices used in the culture of iPSC-CMs. The use of PDMS on the *FLNC* W2164C iPSC-CMs highlights the positive effect of manipulating the substrate stiffness on observable phenotypes. The field of iPSC-CMs is still in its relative infancy compared to animal use but it is rapidly developing with many maturation techniques being tested. Much work is still needed to be able to accurately study adult cardiovascular pathology and the continued use of iPSC-CMs will aide in the understanding of inherited cardiomyopathies and the mechano-sensing role filamin C plays in the heart.

Finally, the work presented here shows the benefit of using both murine and iPSC-CMs for modelling cardiovascular disease in order to overcome individual model deficiencies. Insight into disease mechanisms of cardiomyopathy variants may lead to an improved and personalised approach to treating patients with inherited cardiomyopathy.

Chapter 7 LIST OF REFERENCES

[1] J. J. V McMurray *et al.*, "ESC Guidelines for the diagnosis and treatment of acute and chronic heart failure 2012: The Task Force for the Diagnosis and Treatment of Acute and Chronic Heart Failure 2012 of the European Society of Cardiology. Developed in collaboration with the Heart," *Eur. Heart J.*, vol. 33, no. 14, pp. 1787–847, Jul. 2012, doi: 10.1093/eurheartj/ehs104.

[2] "bhf.org.uk - CVD Statistics UK Factsheet - Jan 2020."

[3] S. C. Greaves, A. H. G. Roche, J. M. Neutze, R. M. L. Whitlock, and A. M. O. Veale, "Inheritance of hypertrophic cardiomyopathy: A cross sectional and M mode echocardiographic study of 50 families," *Heart*, 1987, doi: 10.1136/hrt.58.3.259.

[4] H. Watkins, H. Ashrafian, and C. Redwood, "Inherited cardiomyopathies.," *N. Engl. J. Med.*, vol. 364, no. 17, pp. 1643–56, Apr. 2011, doi: 10.1056/NEJMra0902923.

[5] B. J. Maron *et al.*, "Contemporary definitions and classification of the cardiomyopathies: An American Heart Association Scientific Statement from the Council on Clinical Cardiology, Heart Failure and Transplantation Committee; Quality of Care and Outcomes Research and Functio," *Circulation*, 2006, doi: 10.1161/CIRCULATIONAHA.106.174287.

[6] S. Carlo, L. F. Rodríguez-Fernández, F. A. Benítez Ríos, N. J. Arciniegas-Medina, and H. Martínez-González, "Genetic Evaluation of Late-Onset Hypertrophic Cardiomyopathy: An Autobiographical Case Report," *Cureus*, Mar. 2022, doi: 10.7759/cureus.23349.

[7] K. Zaleta-Rivera *et al.*, "Allele-Specific Silencing Ameliorates Restrictive Cardiomyopathy Attributable to a Human Myosin Regulatory Light Chain Mutation.," *Circulation*, vol. 140, no. 9, pp. 765–778, 2019, doi: 10.1161/CIRCULATIONAHA.118.036965.

[8] P. A. Harvey and L. A. Leinwand, "Cellular mechanisms of cardiomyopathy," *J. Cell Biol.*, vol. 194, no. 3, pp. 355–365, Aug. 2011, doi: 10.1083/jcb.201101100.

[9] A. P. Burke, A. Farb, G. Tashko, and R. Virmani, "Arrhythmogenic Right Ventricular Cardiomyopathy and Fatty Replacement of the Right Ventricular Myocardium," *Circulation*, vol. 97, no. 16, pp. 1571–1580, Apr. 1998, doi: 10.1161/01.CIR.97.16.1571.

[10] J. A. Towbin, "Hypertrophic cardiomyopathy," *PACE - Pacing and Clinical Electrophysiology*. 2009, doi: 10.1111/j.1540-8159.2009.02381.x.

[11] B. J. Maron, J. M. Gardin, J. M. Flack, S. S. Gidding, T. T. Kurosaki, and D. E. Bild, "Prevalence of hypertrophic cardiomyopathy in a general population of young adults: Echocardiographic analysis of 4111 subjects in the CARDIA study," *Circulation*, 1995, doi: 10.1161/01.CIR.92.4.785.

[12] B. J. Maron, R. Mathenge, S. A. Casey, L. C. Poliac, and T. F. Longe, "Clinical profile of hypertrophic cardiomyopathy identified de novo in rural communities," *J. Am. Coll. Cardiol.*, 1999, doi: 10.1016/S0735-1097(99)00039-X.

[13] Y. Hada *et al.*, "Prevalence of hypertrophic cardiomyopathy in a population of adult japanese workers as detected by echocardiographic screening," *Am. J. Cardiol.*, 1987, doi: 10.1016/S0002-9149(87)80107-8.

[14] Y. Zou *et al.*, "Prevalence of idiopathic hypertrophic cardiomyopathy in China: A population-based echocardiographic analysis of 8080 adults," *Am. J. Med.*, 2004, doi: 10.1016/j.amjmed.2003.05.009.

[15] A. Vulpian, “Contribution à l’étude des rétrécissements de l’orifice ventriculo-aortique.,” *Arch Physiol*, vol. 3, pp. 220–222, 1868.

[16] D. TEARE, “Asymmetrical hypertrophy of the heart in young adults.,” *Br. Heart J.*, vol. 20, no. 1, pp. 1–8, Jan. 1958, doi: 10.1136/hrt.20.1.1.

[17] E. D. Wigle, H. Rakowski, B. P. Kimball, and W. G. Williams, “Hypertrophic cardiomyopathy: Clinical spectrum and treatment,” *Circulation*. 1995, doi: 10.1161/01.CIR.92.7.1680.

[18] A. HOLLMAN, J. F. GOODWIN, D. TEARE, and J. W. RENWICK, “A family with obstructive cardiomyopathy (asymmetrical hypertrophy).,” *Br. Heart J.*, 1960, doi: 10.1136/hrt.22.4.449.

[19] E. Braunwald, C. E. Seidman, and U. Sigwart, “Contemporary Evaluation and Management of Hypertrophic Cardiomyopathy,” *Circulation*, vol. 106, no. 11, pp. 1312–1316, Sep. 2002, doi: 10.1161/01.CIR.0000030314.11999.6A.

[20] R. Malik, M. S. Maron, H. Rastegar, and N. G. Pandian, “Hypertrophic cardiomyopathy with right ventricular outflow tract and left ventricular intracavitary obstruction,” *Echocardiography*, 2014, doi: 10.1111/echo.12543.

[21] V. J. Ferrans and E. R. Rodriguez, “Evidence of myocyte hyperplasia in hypertrophic cardiomyopathy and other disorders with myocardial hypertrophy?,” *Zeitschrift fur Kardiologie*. 1987, doi: 10.1007/978-3-642-85369-2_4.

[22] C. Y. Ho *et al.*, “Myocardial fibrosis as an early manifestation of hypertrophic cardiomyopathy,” *N. Engl. J. Med.*, 2010, doi: 10.1056/NEJMoa1002659.

[23] J. Davis *et al.*, “A Tension-Based Model Distinguishes Hypertrophic versus Dilated Cardiomyopathy,” *Cell*, vol. 165, no. 5, pp. 1147–1159, May 2016, doi: 10.1016/j.cell.2016.04.002.

[24] B. S. Burlew and K. T. Weber, “Connective tissue and the heart: Functional significance and regulatory mechanisms,” *Cardiol. Clin.*, 2000, doi: 10.1016/S0733-8651(05)70154-5.

[25] C. J. McLeod *et al.*, “Histologic characterization of hypertrophic cardiomyopathy with and without myofilament mutations.,” *Am. Heart J.*, vol. 158, no. 5, pp. 799–805, Nov. 2009, doi: 10.1016/j.ahj.2009.09.006.

[26] M. S. Maron *et al.*, “Hypertrophic Cardiomyopathy Is Predominantly a Disease of Left Ventricular Outflow Tract Obstruction,” *Circulation*, vol. 114, no. 21, pp. 2232–2239, Nov. 2006, doi: 10.1161/CIRCULATIONAHA.106.644682.

[27] P. Patel *et al.*, “Left Ventricular Outflow Tract Obstruction in Hypertrophic Cardiomyopathy Patients Without Severe Septal Hypertrophy,” *Circ. Cardiovasc. Imaging*, vol. 8, no. 7, Jul. 2015, doi: 10.1161/CIRCIMAGING.115.003132.

[28] M. S. Maron *et al.*, “Effect of Left Ventricular Outflow Tract Obstruction on Clinical Outcome in Hypertrophic Cardiomyopathy,” *N. Engl. J. Med.*, vol. 348, no. 4, pp. 295–303, Jan. 2003, doi: 10.1056/NEJMoa021332.

[29] C. Y. Ho *et al.*, “Study Design and Rationale of EXPLORER-HCM: Evaluation of Mavacamten in Adults With Symptomatic Obstructive Hypertrophic Cardiomyopathy.,” *Circ. Heart Fail.*, 2020, doi: 10.1161/CIRCHEARTFAILURE.120.006853.

[30] J. A. Jarcho *et al.*, “Mapping a Gene for Familial Hypertrophic Cardiomyopathy to Chromosome 14q1,” *N. Engl. J. Med.*, 1989, doi: 10.1056/NEJM198911163212005.

[31] S. D. Solomon *et al.*, “A locus for familial hypertrophic cardiomyopathy is closely linked to the cardiac myosin heavy chain genes, CRI-L436, and CRI-L329 on chromosome 14 at q11-q12,” *Am. J. Hum. Genet.*, 1990.

[32] H. Watkins, L. Thierfelder, D. S. Hwang, W. McKenna, J. G. Seidman, and C. E. Seidman, “Sporadic hypertrophic cardiomyopathy due to de novo myosin mutations,” *J. Clin. Invest.*, 1992, doi: 10.1172/JCI116038.

[33] H. Watkins *et al.*, “Mutations in the cardiac myosin binding protein–C gene on chromosome 11 cause familial hypertrophic cardiomyopathy,” *Nat. Genet.*, 1995, doi: 10.1038/ng1295-434.

[34] B. J. Maron and M. S. Maron, “Hypertrophic cardiomyopathy,” *The Lancet*. 2013, doi: 10.1016/S0140-6736(12)60397-3.

[35] C. E. Seidman and J. G. Seidman, “Identifying sarcomere gene mutations in hypertrophic cardiomyopathy: A personal history,” *Circ. Res.*, 2011, doi: 10.1161/CIRCRESAHA.110.223834.

[36] L. Thierfelder *et al.*, “α-tropomyosin and cardiac troponin T mutations cause familial hypertrophic cardiomyopathy: A disease of the sarcomere,” *Cell*, 1994, doi: 10.1016/0092-8674(94)90054-X.

[37] R. Tadros *et al.*, “Shared genetic pathways contribute to risk of hypertrophic and dilated cardiomyopathies with opposite directions of effect,” *Nat. Genet.*, vol. 53, no. 2, pp. 128–134, Feb. 2021, doi: 10.1038/s41588-020-00762-2.

[38] S. Marston *et al.*, “Evidence from human myectomy samples that MYBPC3 mutations cause hypertrophic cardiomyopathy through haploinsufficiency.,” *Circ. Res.*, vol. 105, no. 3, pp. 219–22, Jul. 2009, doi: 10.1161/CIRCRESAHA.109.202440.

[39] S. J. van Dijk *et al.*, “Cardiac myosin-binding protein C mutations and hypertrophic cardiomyopathy: haploinsufficiency, deranged phosphorylation, and cardiomyocyte dysfunction.,” *Circulation*, vol. 119, no. 11, pp. 1473–83, Mar. 2009, doi: 10.1161/CIRCULATIONAHA.108.838672.

[40] C. Redwood *et al.*, “Investigation of a truncated cardiac troponin T that causes familial hypertrophic cardiomyopathy: Ca(2+) regulatory properties of reconstituted thin filaments depend on the ratio of mutant to wild-type protein.,” *Circ. Res.*, vol. 86, no. 11, pp. 1146–52, Jun. 2000, doi: 10.1161/01.res.86.11.1146.

[41] R. Coppini *et al.*, “Clinical Phenotype and Outcome of Hypertrophic Cardiomyopathy Associated With Thin-Filament Gene Mutations,” *J. Am. Coll. Cardiol.*, vol. 64, no. 24, pp. 2589–2600, Dec. 2014, doi: 10.1016/j.jacc.2014.09.059.

[42] H. M. Viola and L. C. Hool, “Impaired calcium handling and mitochondrial metabolic dysfunction as early markers of hypertrophic cardiomyopathy,” *Arch. Biochem. Biophys.*, vol. 665, pp. 166–174, Apr. 2019, doi: 10.1016/j.abb.2019.03.006.

[43] J. A. Spudich, “Three perspectives on the molecular basis of hypercontractility caused by hypertrophic cardiomyopathy mutations,” *Pflügers Arch. - Eur. J. Physiol.*, vol. 471, no. 5, pp. 701–717, May 2019, doi: 10.1007/s00424-019-02259-2.

[44] N. Beraud *et al.*, “Mitochondrial dynamics in heart cells: very low amplitude high frequency fluctuations in adult cardiomyocytes and flow motion in non beating Hl-1 cells.,” *J. Bioenerg. Biomembr.*, vol. 41, no. 2, pp. 195–214, Apr. 2009, doi: 10.1007/s10863-009-9214-x.

[45] J. G. Crilley *et al.*, “Hypertrophic cardiomyopathy due to sarcomeric gene mutations is characterized by impaired energy metabolism irrespective of the degree of hypertrophy,” *J. Am. Coll. Cardiol.*, 2003, doi: 10.1016/S0735-1097(02)03009-7.

[46] S. Vakrou and M. R. Abraham, “Hypertrophic cardiomyopathy: a heart in need of an energy bar?,” *Front. Physiol.*, vol. 5, Aug. 2014, doi: 10.3389/fphys.2014.00309.

[47] R. Coppini, C. Ferrantini, A. Mugelli, C. Poggesi, and E. Cerbai, “Altered Ca2+ and Na+ Homeostasis in Human Hypertrophic Cardiomyopathy: Implications for Arrhythmogenesis,” *Front. Physiol.*, vol. 9, Oct. 2018, doi: 10.3389/fphys.2018.01391.

[48] M. Boyett, “The sinoatrial node, a heterogeneous pacemaker structure,” *Cardiovasc. Res.*, vol. 47, no. 4, pp. 658–687, Sep. 2000, doi: 10.1016/S0008-6363(00)00135-8.

[49] C. Castillo and A. Castellanos, “Retrograde activation of the his bundle in the human heart,” *Am. J. Cardiol.*, vol. 27, no. 3, pp. 264–271, Mar. 1971, doi: 10.1016/0002-9149(71)90301-8.

[50] D. W. Fawcett and N. S. McNutt, “THE ULTRASTRUCTURE OF THE CAT MYOCARDIUM,” *J. Cell Biol.*, vol. 42, no. 1, pp. 1–45, Jul. 1969, doi: 10.1083/jcb.42.1.1.

[51] M. Litviňuková *et al.*, “Cells of the adult human heart,” *Nature*, vol. 588, no. 7838, pp. 466–472, Dec. 2020, doi: 10.1038/s41586-020-2797-4.

[52] S. Doll *et al.*, “Region and cell-type resolved quantitative proteomic map of the human heart,” *Nat. Commun.*, vol. 8, no. 1, p. 1469, Dec. 2017, doi: 10.1038/s41467-017-01747-2.

[53] Y. Kanno and W. R. Loewenstein, “Low-resistance coupling between gland cells. Some observations on intercellular contact membranes and intercellular space [30],” *Nature*. 1964, doi: 10.1038/201194a0.

[54] B. R. Anderson and H. L. Granzier, “Titin-based tension in the cardiac sarcomere: molecular origin and physiological adaptations.,” *Prog. Biophys. Mol. Biol.*, vol. 110, no. 2–3, pp. 204–17, doi: 10.1016/j.pbiomolbio.2012.08.003.

[55] R. Knöll *et al.*, “The cardiac mechanical stretch sensor machinery involves a Z disc complex that is defective in a subset of human dilated cardiomyopathy.,” *Cell*, vol. 111, no. 7, pp. 943–55, Dec. 2002, doi: 10.1016/s0092-8674(02)01226-6.

[56] M.-L. Bang, J. Bogomolovas, and J. Chen, “Understanding the molecular basis of cardiomyopathy,” *Am. J. Physiol. Circ. Physiol.*, vol. 322, no. 2, pp. H181–H233, Feb. 2022, doi: 10.1152/ajpheart.00562.2021.

[57] L. Liu, K. Sun, X. Zhang, Y. Tang, and D. Xu, “Advances in the role and mechanism of BAG3 in dilated cardiomyopathy,” *Heart Fail. Rev.*, vol. 26, no. 1, pp. 183–194, Jan. 2021, doi: 10.1007/s10741-019-09899-7.

[58] G. R. Fedorchak, A. Kaminski, and J. Lammerding, “Cellular mechanosensing: Getting to the nucleus of it all,” *Prog. Biophys. Mol. Biol.*, vol. 115, no. 2–3, pp. 76–92, Aug. 2014, doi: 10.1016/j.pbiomolbio.2014.06.009.

[59] V. Arndt *et al.*, “Chaperone-Assisted Selective Autophagy Is Essential for Muscle Maintenance,” *Curr. Biol.*, vol. 20, no. 2, pp. 143–148, Jan. 2010, doi: 10.1016/j.cub.2009.11.022.

[60] F. Shaffer, R. McCraty, and C. L. Zerr, “A healthy heart is not a metronome: an integrative review of the heart’s anatomy and heart rate variability,” *Front. Psychol.*, vol. 5, Sep. 2014, doi: 10.3389/fpsyg.2014.01040.

[61] R. E. Peverill, “Understanding preload and preload reserve within the conceptual framework of a limited range of possible left ventricular end-diastolic volumes,” *Adv. Physiol. Educ.*, vol. 44, no. 3, pp. 414–422, Sep. 2020, doi: 10.1152/advan.00043.2020.

[62] G. Garoffolo and M. Pesce, “Mechanotransduction in the cardiovascular system: From developmental origins to homeostasis and pathology,” *Cells*, vol. 8, no. 12, 2019, doi: 10.3390/cells8121607.

[63] M. Gautel, “The sarcomeric cytoskeleton: who picks up the strain?,” *Curr. Opin. Cell Biol.*, vol. 23, no. 1, pp. 39–46, Feb. 2011, doi: 10.1016/j.ceb.2010.12.001.

[64] M. Yoshida *et al.*, “Weaving hypothesis of cardiomyocyte sarcomeres: discovery of periodic broadening and narrowing of intercalated disk during volume-load change.,” *Am. J. Pathol.*, vol. 176, no. 2, pp. 660–78, Feb. 2010, doi: 10.2353/ajpath.2010.090348.

[65] M. Hoshijima, “Mechanical stress-strain sensors embedded in cardiac cytoskeleton: Z disk, titin, and associated structures,” *Am. J. Physiol. Circ. Physiol.*, vol. 290, no. 4, pp. H1313–H1325, Apr. 2006, doi: 10.1152/ajpheart.00816.2005.

[66] T. Iskratsch, H. Wolfenson, and M. P. Sheetz, “Appreciating force and shape—the rise of mechanotransduction in cell biology.,” *Nat. Rev. Mol. Cell Biol.*, vol. 15, no. 12, pp. 825–33, 2014, doi: 10.1038/nrm3903.

[67] K. Jani and F. Schöck, “Molecular mechanisms of mechanosensing in muscle development,” *Dev. Dyn.*, vol. 238, no. 6, pp. 1526–1534, Jun. 2009, doi: 10.1002/dvdy.21972.

[68] A. Kocer, “Mechanisms of mechanosensing - mechanosensitive channels, function and re-engineering.,” *Curr. Opin. Chem. Biol.*, vol. 29, pp. 120–7, Dec. 2015, doi: 10.1016/j.cbpa.2015.10.006.

[69] J. S. Neves, A. M. Leite-Moreira, M. Neiva-Sousa, J. Almeida-Coelho, R. Castro-Ferreira, and A. F. Leite-Moreira, “Acute Myocardial Response to Stretch: What We (don’t) Know,” *Front. Physiol.*, vol. 6, Jan. 2016, doi: 10.3389/fphys.2015.00408.

[70] C. Caffarra Malvezzi, A. Cabassi, and M. Miragoli, “Mitochondrial mechanosensor in cardiovascular diseases.,” *Vasc. Biol. (Bristol, England)*, vol. 2, no. 1, pp. R85–R92, 2020, doi: 10.1530/VB-20-0002.

[71] P. Pandey *et al.*, “Cardiomyocytes Sense Matrix Rigidity through a Combination of Muscle and Non-muscle Myosin Contractions.,” *Dev. Cell*, vol. 45, no. 5, p. 661, 2018, doi: 10.1016/j.devcel.2018.05.016.

[72] B. Burke and C. L. Stewart, “Functional architecture of the cell’s nucleus in development, aging, and disease.,” *Curr. Top. Dev. Biol.*, vol. 109, pp. 1–52, 2014, doi: 10.1016/B978-0-12-397920-9.00006-8.

[73] K. Ohashi, S. Fujiwara, and K. Mizuno, “Roles of the cytoskeleton, cell adhesion and rho signalling in mechanosensing and mechanotransduction,” *J. Biochem.*, p. mvw082, Jan. 2017, doi: 10.1093/jb/mvw082.

[74] I. Olivotto, F. Cecchi, C. Poggesi, and M. H. Yacoub, “Developmental origins of hypertrophic cardiomyopathy phenotypes: a unifying hypothesis,” *Nat. Rev. Cardiol.*, vol. 6, no. 4, pp. 317–321, Apr. 2009, doi: 10.1038/nrcardio.2009.9.

[75] L. Rognoni, J. Stigler, B. Pelz, J. Ylänne, and M. Rief, “Dynamic force sensing of filamin revealed in single-molecule experiments,” *Proc. Natl. Acad. Sci. U. S. A.*, 2012, doi: 10.1073/pnas.1211274109.

[76] Y. Lad *et al.*, "Structural basis of the migfilin-filamin interaction and competition with integrin β tails," *J. Biol. Chem.*, 2008, doi: 10.1074/jbc.M802592200.

[77] F. Nakamura, M. Song, J. H. Hartwig, and T. P. Stossel, "Documentation and localization of force-mediated filamin A domain perturbations in moving cells," *Nat. Commun.*, 2014, doi: 10.1038/ncomms5656.

[78] A. J. Ehrlicher, F. Nakamura, J. H. Hartwig, D. A. Weitz, and T. P. Stossel, "Mechanical strain in actin networks regulates FilGAP and integrin binding to filamin A," *Nature*, 2011, doi: 10.1038/nature10430.

[79] S. S. Ithychanda and J. Qin, "Evidence for multisite ligand binding and stretching of filamin by integrin and migfilin," *Biochemistry*, 2011, doi: 10.1021/bi2003229.

[80] C. Zhang, Z. Xu, X. R. He, L. H. Michael, and C. Patterson, "CHIP, a cochaperone/ubiquitin ligase that regulates protein quality control, is required for maximal cardioprotection after myocardial infarction in mice," *Am. J. Physiol. - Hear. Circ. Physiol.*, 2005, doi: 10.1152/ajpheart.01122.2004.

[81] M. Gamerdinger, P. Hajieva, A. M. Kaya, U. Wolfrum, F. U. Hartl, and C. Behl, "Protein quality control during aging involves recruitment of the macroautophagy pathway by BAG3," *EMBO J.*, 2009, doi: 10.1038/emboj.2009.29.

[82] S. Carra, S. J. Seguin, H. Lambert, and J. Landry, "HspB8 chaperone activity toward poly(Q)-containing proteins depends on its association with Bag3, a stimulator of macroautophagy," *J. Biol. Chem.*, 2008, doi: 10.1074/jbc.M706304200.

[83] A. Ulbricht *et al.*, "Cellular mechanotransduction relies on tension-induced and chaperone-assisted autophagy," *Curr. Biol.*, 2013, doi: 10.1016/j.cub.2013.01.064.

[84] H. Chen, S. Chandrasekar, M. P. Sheetz, T. P. Stossel, F. Nakamura, and J. Yan, "Mechanical perturbation of filamin A immunoglobulin repeats 20-21 reveals potential non-equilibrium mechanochemical partner binding function," *Sci. Rep.*, 2013, doi: 10.1038/srep01642.

[85] J. Seppälä *et al.*, "Flexible structure of peptide-bound filamin a mechanosensor domain pair 20-21," *PLoS One*, 2015, doi: 10.1371/journal.pone.0136969.

[86] F. Ader *et al.*, "FLNC pathogenic variants in patients with cardiomyopathies: Prevalence and genotype-phenotype correlations," *Clin. Genet.*, 2019, doi: 10.1111/cge.13594.

[87] R. A. Kley *et al.*, "A Combined Laser Microdissection and Mass Spectrometry Approach Reveals New Disease Relevant Proteins Accumulating in Aggregates of Filaminopathy Patients," *Mol. Cell. Proteomics*, vol. 12, no. 1, pp. 215–227, Jan. 2013, doi: 10.1074/mcp.M112.023176.

[88] R. A. Kley *et al.*, "Impairment of protein degradation in myofibrillar myopathy caused by FLNC/filamin C mutations," *Autophagy*, 2013, doi: 10.4161/auto.22921.

[89] A. A. Ruparelia, V. Oorschot, G. Ramm, and R. J. Bryson-Richardson, "FLNC myofibrillar myopathy results from impaired autophagy and protein insufficiency," *Hum. Mol. Genet.*, 2016, doi: 10.1093/hmg/ddw080.

[90] A. T. L. Zech, S. R. Singh, S. Schlossarek, and L. Carrier, "Autophagy in cardiomyopathies," *Biochim. Biophys. Acta - Mol. Cell Res.*, vol. 1867, no. 3, p. 118432, Mar. 2020, doi: 10.1016/j.bbamcr.2019.01.013.

[91] A. T. L. Zech *et al.*, "ACTN2 Mutant Causes Proteopathy in Human iPSC-Derived

Cardiomyocytes," *Cells*, vol. 11, no. 17, p. 2745, Sep. 2022, doi: 10.3390/cells11172745.

[92] M. Ehsan, H. Jiang, K. L.Thomson, and K. Gehmlich, "When signalling goes wrong: pathogenic variants in structural and signalling proteins causing cardiomyopathies," *J. Muscle Res. Cell Motil.*, 2017, doi: 10.1007/s10974-017-9487-3.

[93] M. Sandri and J. Robbins, "Proteotoxicity: An underappreciated pathology in cardiac disease," *J. Mol. Cell. Cardiol.*, vol. 71, pp. 3–10, Jun. 2014, doi: 10.1016/j.yjmcc.2013.12.015.

[94] P. Tannous *et al.*, "Autophagy is an adaptive response in desmin-related cardiomyopathy," *Proc. Natl. Acad. Sci.*, vol. 105, no. 28, pp. 9745–9750, Jul. 2008, doi: 10.1073/pnas.0706802105.

[95] X. Wang and J. Robbins, "Proteasomal and lysosomal protein degradation and heart disease," *J. Mol. Cell. Cardiol.*, vol. 71, pp. 16–24, Jun. 2014, doi: 10.1016/j.yjmcc.2013.11.006.

[96] J. A. Towbin, "Inherited cardiomyopathies," *Circulation Journal*. 2014, doi: 10.1253/circj.CJ-14-0893.

[97] C. Lu *et al.*, "Molecular analysis of inherited cardiomyopathy using next generation semiconductor sequencing technologies," *J. Transl. Med.*, vol. 16, no. 1, p. 241, Dec. 2018, doi: 10.1186/s12967-018-1605-5.

[98] R. Valdés-Mas *et al.*, "Mutations in filamin C cause a new form of familial hypertrophic cardiomyopathy," *Nat. Commun.*, 2014, doi: 10.1038/ncomms6326.

[99] E. Reinstein *et al.*, "Congenital dilated cardiomyopathy caused by biallelic mutations in Filamin C," *Eur. J. Hum. Genet.*, 2016, doi: 10.1038/ejhg.2016.110.

[100] A. Brodehl *et al.*, "Mutations in FLNC are Associated with Familial Restrictive Cardiomyopathy," *Hum. Mutat.*, vol. 37, no. 3, pp. 269–279, Mar. 2016, doi: 10.1002/humu.22942.

[101] M. F. Ortiz-Genga *et al.*, "Truncating FLNC Mutations Are Associated With High-Risk Dilated and Arrhythmogenic Cardiomyopathies," *J. Am. Coll. Cardiol.*, 2016, doi: 10.1016/j.jacc.2016.09.927.

[102] Z. Razinia, T. Mäkelä, J. Ylänne, and D. A. Calderwood, "Filamins in Mechanosensing and Signaling," *Annu. Rev. Biophys.*, 2012, doi: 10.1146/annurev-biophys-050511-102252.

[103] A. Linnemann *et al.*, "The sarcomeric Z-disc component myopodin is a multiadapter protein that interacts with filamin and α-actinin," *Eur. J. Cell Biol.*, 2010, doi: 10.1016/j.ejcb.2010.04.004.

[104] P. F. M. van der Ven *et al.*, "Unusual splicing events result in distinct Xin isoforms that associate differentially with filamin c and Mena/VASP," *Exp. Cell Res.*, 2006, doi: 10.1016/j.yexcr.2006.03.015.

[105] Y. Feng and C. A. Walsh, "The many faces of filamin: A versatile molecular scaffold for cell motility and signalling," *Nature Cell Biology*. 2004, doi: 10.1038/ncb1104-1034.

[106] N. González-Morales, T. K. Holenka, and F. Schöck, "Filamin actin-binding and titin-binding fulfill distinct functions in Z-disc cohesion," *PLOS Genet.*, vol. 13, no. 7, p. e1006880, Jul. 2017, doi: 10.1371/journal.pgen.1006880.

[107] M. P. Collier *et al.*, "HspB1 phosphorylation regulates its intramolecular dynamics and

mechanosensitive molecular chaperone interaction with filamin C," *Sci. Adv.*, 2019, doi: 10.1126/sciadv.aav8421.

[108] M. Himmel, P. F. M. Van der Ven, W. Stöcklein, and D. O. Fürst, "The limits of promiscuity: Isoform-specific dimerization of filamins," *Biochemistry*, 2003, doi: 10.1021/bi026501+.

[109] J. B. Gorlin *et al.*, "Human endothelial actin-binding protein (ABP-280, nonmuscle filamin): A molecular leaf spring," *J. Cell Biol.*, 1990, doi: 10.1083/jcb.111.3.1089.

[110] T. P. Stossel *et al.*, "Filamins as integrators of cell mechanics and signalling," *Nature Reviews Molecular Cell Biology*. 2001, doi: 10.1038/35052082.

[111] G. M. Popowicz, M. Schleicher, A. A. Noegel, and T. A. Holak, "Filamins: promiscuous organizers of the cytoskeleton," *Trends in Biochemical Sciences*. 2006, doi: 10.1016/j.tibs.2006.05.006.

[112] S. W. Kong *et al.*, "Heart Failure-Associated Changes in RNA Splicing of Sarcomere Genes," *Circ. Cardiovasc. Genet.*, 2010, doi: 10.1161/CIRCGENETICS.109.904698.

[113] S. Molt *et al.*, "Aciculin interacts with filamin C and Xin and is essential for myofibril assembly, remodeling and maintenance," *J. Cell Sci.*, Jan. 2014, doi: 10.1242/jcs.152157.

[114] P. F. van der Ven *et al.*, "Indications for a novel muscular dystrophy pathway. gamma-filamin, the muscle-specific filamin isoform, interacts with myotilin.," *J. Cell Biol.*, vol. 151, no. 2, pp. 235–48, Oct. 2000, doi: 10.1083/jcb.151.2.235.

[115] P. F. M. Van Der Ven *et al.*, "Indications for a novel muscular dystrophy pathway: γ-Filamin, the muscle-specific filamin isoform, interacts with myotilin," *J. Cell Biol.*, vol. 151, no. 2, pp. 235–247, Oct. 2000, doi: 10.1083/jcb.151.2.235.

[116] Y. Leber *et al.*, "Filamin C is a highly dynamic protein associated with fast repair of myofibrillar microdamage," *Hum. Mol. Genet.*, 2016, doi: 10.1093/hmg/ddw135.

[117] A. A. Ruparelia, M. Zhao, P. D. Currie, and R. J. Bryson-Richardson, "Characterization and investigation of zebrafish models of filamin-related myofibrillar myopathy," *Hum. Mol. Genet.*, 2012, doi: 10.1093/hmg/dds231.

[118] S. Huelsmann, N. Rintanen, R. Sethi, N. H. Brown, and J. Ylänne, "Evidence for the mechanosensor function of filamin in tissue development," *Sci. Rep.*, vol. 6, no. 1, p. 32798, Sep. 2016, doi: 10.1038/srep32798.

[119] D. O. Fürst, L. G. Goldfarb, R. A. Kley, M. Vorgerd, M. Olivé, and P. F. M. Van Der Ven, "Filamin C-related myopathies: Pathology and mechanisms," *Acta Neuropathologica*. 2013, doi: 10.1007/s00401-012-1054-9.

[120] F. Raynaud *et al.*, "The calpain 1-α-actinin interaction," *Eur. J. Biochem.*, vol. 270, no. 23, pp. 4662–4670, Dec. 2003, doi: 10.1046/j.1432-1033.2003.03859.x.

[121] L. Y. Juo, W. C. Liao, Y. L. Shih, B. Y. Yang, A. B. Liu, and Y. T. Yan, "HSPB7 interacts with dimerized FLNC and its absence results in progressive myopathy in skeletal muscles," *J. Cell Sci.*, 2016, doi: 10.1242/jcs.179887.

[122] X. Zhou, J. Borén, and L. M. Akyürek, "Filamins in Cardiovascular Development," *Trends in Cardiovascular Medicine*. 2007, doi: 10.1016/j.tcm.2007.08.001.

[123] A. Van der Flier and A. Sonnenberg, "Structural and functional aspects of filamins," *Biochimica et Biophysica Acta - Molecular Cell Research*. 2001, doi: 10.1016/S0167-

4889(01)00072-6.

[124] Y. Tu, S. Wu, X. Shi, K. Chen, and C. Wu, “Migfilin and Mig-2 link focal adhesions to filamin and the actin cytoskeleton and function in cell shape modulation,” *Cell*, 2003, doi: 10.1016/S0092-8674(03)00163-6.

[125] L. Reimann *et al.*, “Myofibrillar Z-discs are a protein phosphorylation hot spot with protein kinase C (PKCα) modulating protein dynamics,” *Mol. Cell. Proteomics*, 2017, doi: 10.1074/mcp.M116.065425.

[126] D. A. Sequea, N. Sharma, E. B. Arias, and G. D. Cartee, “Greater filamin C, GSK3α, and GSK3β serine phosphorylation in insulin-stimulated isolated skeletal muscles of calorie restricted 24 month-old rats,” *Mech. Ageing Dev.*, 2013, doi: 10.1016/j.mad.2012.12.002.

[127] L. Reimann *et al.*, “Phosphoproteomics identifies dual-site phosphorylation in an extended basophilic motif regulating FILIP1-mediated degradation of filamin-C,” *Commun. Biol.*, 2020, doi: 10.1038/s42003-020-0982-5.

[128] M. Zhang, J. Liu, A. Cheng, S. M. DeYoung, and A. R. Saltiel, “Identification of CAP as a costameric protein that interacts with filamin C,” *Mol. Biol. Cell*, 2007, doi: 10.1091/mbc.E07-06-0628.

[129] I. Dalkilic, J. Schienda, T. G. Thompson, and L. M. Kunkel, “Loss of FilaminC (FLNc) Results in Severe Defects in Myogenesis and Myotube Structure,” *Mol. Cell. Biol.*, 2006, doi: 10.1128/mcb.00243-06.

[130] S. P. O’Brien, K. Seipel, Q. G. Medley, R. Bronson, R. Segal, and M. Streuli, “Skeletal muscle deformity and neuroanl disorder in Trio exchange factor-deficient mouse embryos,” *Proc. Natl. Acad. Sci. U. S. A.*, 2000, doi: 10.1073/pnas.97.22.12074.

[131] J. A. J. Verdonschot *et al.*, “ A Mutation Update for the FLNC gene in Myopathies and Cardiomyopathies ,” *Hum. Mutat.*, 2020, doi: 10.1002/humu.24004.

[132] Y. Zhou *et al.*, “Loss of Filamin C Is Catastrophic for Heart Function,” *Circulation*. 2020, doi: 10.1161/CIRCULATIONAHA.119.044061.

[133] E. J. Mercer, Y. F. Lin, L. Cohen-Gould, and T. Evans, “Hspb7 is a cardioprotective chaperone facilitating sarcomeric proteostasis,” *Dev. Biol.*, 2018, doi: 10.1016/j.ydbio.2018.01.005.

[134] V. Guergueltcheva *et al.*, “Distal myopathy with upper limb predominance caused by filamin C haploinsufficiency,” *Neurology*, 2011, doi: 10.1212/WNL.0b013e31823dc51e.

[135] J. Janssens *et al.*, “Investigating the role of filamin C in Belgian patients with frontotemporal dementia linked to GRN deficiency in FTLD-TDP brains,” *Acta Neuropathol. Commun.*, 2015, doi: 10.1186/s40478-015-0246-7.

[136] R. M. Duff *et al.*, “Mutations in the N-terminal actin-binding domain of filamin C cause a distal myopathy,” *Am. J. Hum. Genet.*, 2011, doi: 10.1016/j.ajhg.2011.04.021.

[137] V. M. *et al.*, “A mutation in the dimerization domain of filamin c causes a novel type of autosomal dominant myofibrillar myopathy.,” *Am. J. Hum. Genet.*, vol. 77, no. 2, pp. 297–304, Aug. 2005, doi: 10.1086/431959.

[138] R. A. Kley *et al.*, “Clinical and morphological phenotype of the filamin myopathy: A study of 31 German patients,” *Brain*, 2007, doi: 10.1093/brain/awm271.

[139] A. Janin *et al.*, “Truncating mutations on myofibrillar myopathies causing genes as

prevalent molecular explanations on patients with dilated cardiomyopathy," *Clin. Genet.*, 2017, doi: 10.1111/cge.13043.

[140] R. L. Begay *et al.*, "FLNC Gene Splice Mutations Cause Dilated Cardiomyopathy," *JACC: Basic to Translational Science*, vol. 1, no. 5. Elsevier Inc, pp. 344–359, Aug. 01, 2016, doi: 10.1016/j.jacbts.2016.05.004.

[141] J. Gómez *et al.*, "Screening of the Filamin C Gene in a Large Cohort of Hypertrophic Cardiomyopathy Patients," *Circ. Cardiovasc. Genet.*, 2017, doi: 10.1161/CIRCGENETICS.116.001584.

[142] C. L. Hall *et al.*, "Filamin C variants are associated with a distinctive clinical and immunohistochemical arrhythmogenic cardiomyopathy phenotype," *Int. J. Cardiol.*, 2019, doi: 10.1016/j.ijcard.2019.09.048.

[143] K. H. Schreiber and B. K. Kennedy, "When lamins go bad: Nuclear structure and disease," *Cell*. 2013, doi: 10.1016/j.cell.2013.02.015.

[144] C. G. Konersman *et al.*, "BAG3 myofibrillar myopathy presenting with cardiomyopathy," *Neuromuscul. Disord.*, 2015, doi: 10.1016/j.nmd.2015.01.009.

[145] H. Hartmannova *et al.*, "Isolated X-linked hypertrophic cardiomyopathy caused by a novel mutation of the four-and-a-half LIM domain 1 gene," *Circ. Cardiovasc. Genet.*, 2013, doi: 10.1161/CIRCGENETICS.113.000245.

[146] S. Bains, D. J. Tester, S. J. Asirvatham, P. A. Noseworthy, M. J. Ackerman, and J. R. Giudicessi, "A Novel Truncating Variant in FLNC-Encoded Filamin C May Serve as a Proarrhythmic Genetic Substrate for Arrhythmogenic Bileaflet Mitral Valve Prolapse Syndrome.," *Mayo Clin. Proc.*, vol. 94, no. 5, pp. 906–913, May 2019, doi: 10.1016/j.mayocp.2018.11.028.

[147] K. D. Mangum and S. J. Ferns, "A novel familial truncating mutation in the filamin C gene associated with cardiac arrhythmias.," *Eur. J. Med. Genet.*, vol. 62, no. 4, pp. 282–285, Apr. 2019, doi: 10.1016/j.ejmg.2018.08.006.

[148] D. Avila-Smirnow *et al.*, "Cardiac arrhythmia and late-onset muscle weakness caused by a myofibrillar myopathy with unusual histopathological features due to a novel missense mutation in FLNC," *Revue Neurologique*. 2016, doi: 10.1016/j.neurol.2016.07.017.

[149] A. Kiselev *et al.*, "De novo mutations in FLNC leading to early-onset restrictive cardiomyopathy and congenital myopathy," *Hum. Mutat.*, 2018, doi: 10.1002/humu.23559.

[150] T. Löwe *et al.*, "The pathomechanism of filaminopathy: Altered biochemical properties explain the cellular phenotype of a protein aggregation myopathy," *Hum. Mol. Genet.*, 2007, doi: 10.1093/hmg/ddm085.

[151] S. Kono *et al.*, "Dominant-negative effects of a novel mutation in the filamin myopathy," *Neurology*, 2010, doi: 10.1212/WNL.0b013e3181ec7fbd.

[152] G. Tasca *et al.*, "Novel FLNC mutation in a patient with myofibrillar myopathy in combination with late-onset cerebellar ataxia," *Muscle and Nerve*, 2012, doi: 10.1002/mus.23349.

[153] R. A. Kley *et al.*, "Pathophysiology of protein aggregation and extended phenotyping in filaminopathy," *Brain*, 2012, doi: 10.1093/brain/aws200.

[154] J. Schuld *et al.*, "Homozygous expression of the myofibrillar myopathy-associated p.W2710X filamin C variant reveals major pathomechanisms of sarcomeric lesion

formation," *Acta Neuropathol. Commun.*, 2020, doi: 10.1186/s40478-020-01001-9.

[155] N. R. Tucker *et al.*, "Novel Mutation in FLNC (Filamin C) Causes Familial Restrictive Cardiomyopathy," *Circ. Cardiovasc. Genet.*, 2017, doi: 10.1161/CIRCGENETICS.117.001780.

[156] P. F. M. Van Der Ven, W. M. J. Obermann, B. Lemke, M. Gautel, K. Weber, and D. O. Fürst, "Characterization of muscle filamin isoforms suggests a possible role of γ-Filamin/ABP-L in sarcomeric Z-disc formation," *Cell Motility and the Cytoskeleton*, vol. 45, no. 2. pp. 149–162, 2000, doi: 10.1002/(SICI)1097-0169(200002)45:2<149::AID-CM6>3.0.CO;2-G.

[157] R. Walsh *et al.*, "Quantitative approaches to variant classification increase the yield and precision of genetic testing in Mendelian diseases: The case of hypertrophic cardiomyopathy," *Genome Med.*, 2019, doi: 10.1186/s13073-019-0616-z.

[158] R. Hastings *et al.*, "Combination of Whole Genome Sequencing, Linkage, and Functional Studies Implicates a Missense Mutation in Titin as a Cause of Autosomal Dominant Cardiomyopathy with Features of Left Ventricular Noncompaction," *Circ. Cardiovasc. Genet.*, 2016, doi: 10.1161/CIRCGENETICS.116.001431.

[159] F. J. A. van den Bogaart *et al.*, "Widening the spectrum of filamin-C myopathy: Predominantly proximal myopathy due to the p.A193T mutation in the actin-binding domain of FLNC," *Neuromuscul. Disord.*, 2017, doi: 10.1016/j.nmd.2016.09.017.

[160] M. Dogan, "Electrophysiological changes during menstrual cycle," in *Sex and Cardiac Electrophysiology*, Elsevier, 2020, pp. 223–229.

[161] S. A. Said, R. Bloo, R. de Nooijer, and A. Slootweg, "Cardiac and non-cardiac causes of T-wave inversion in the precordial leads in adult subjects: A Dutch case series and review of the literature.," *World J. Cardiol.*, vol. 7, no. 2, pp. 86–100, Feb. 2015, doi: 10.4330/wjc.v7.i2.86.

[162] T. Istolahti *et al.*, "The prognostic significance of T-wave inversion according to ECG lead group during long-term follow-up in the general population," *Ann. Noninvasive Electrocardiol.*, vol. 26, no. 1, Jan. 2021, doi: 10.1111/anec.12799.

[163] H. Hayashi and M. Horie, "Biphasic P wave in inferior leads and the development of atrial fibrillation.," *J. arrhythmia*, vol. 31, no. 6, pp. 376–80, Dec. 2015, doi: 10.1016/j.joa.2015.06.00810.1016/j.joa.2015.06.008.

[164] M. J. Zema and P. Kligfield, "ECG poor R-wave progression: review and synthesis.," *Arch. Intern. Med.*, vol. 142, no. 6, pp. 1145–8, Jun. 1982, [Online]. Available: http://www.ncbi.nlm.nih.gov/pubmed/6212033.

[165] L. M. Ryerson and R. M. Giuffre, "QT intervals in metabolic dilated cardiomyopathy.," *Can. J. Cardiol.*, vol. 22, no. 3, pp. 217–20, Mar. 2006, doi: 10.1016/s0828-282x(06)70899-6.

[166] D. Barto, "Recognizing ST-segment elevation," *Nurs. Crit. Care*, vol. 11, no. 2, pp. 5–6, Mar. 2016, doi: 10.1097/01.CCN.0000480751.08226.ec.

[167] B. Musumeci *et al.*, "Left Ventricular Remodeling in Hypertrophic Cardiomyopathy: An Overview of Current Knowledge," *J. Clin. Med.*, vol. 10, no. 8, p. 1547, Apr. 2021, doi: 10.3390/jcm10081547.

[168] J. T. Maxwell, T. L. Domeier, and L. A. Blatter, "Dantrolene prevents arrhythmogenic Ca 2+ release in heart failure," *Am. J. Physiol. Circ. Physiol.*, vol. 302, no. 4, pp. H953–H963,

Feb. 2012, doi: 10.1152/ajpheart.00936.2011.

[169] Z. Zhao *et al.*, "Ion Channel Expression and Characterization in Human Induced Pluripotent Stem Cell-Derived Cardiomyocytes," *Stem Cells Int.*, 2018, doi: 10.1155/2018/6067096.

[170] M. J. Cumberland *et al.*, "Basic Research Approaches to Evaluate Cardiac Arrhythmia in Heart Failure and Beyond," *Front. Physiol.*, vol. 13, Feb. 2022, doi: 10.3389/fphys.2022.806366.

[171] N. Cao *et al.*, "In vitro differentiation of rat embryonic stem cells into functional cardiomyocytes," *Cell Res.*, vol. 21, no. 9, pp. 1316–1331, Sep. 2011, doi: 10.1038/cr.2011.48.

[172] S. Chlopcíková, J. Psotová, and P. Miketová, "Neonatal rat cardiomyocytes--a model for the study of morphological, biochemical and electrophysiological characteristics of the heart.," *Biomed. Pap. Med. Fac. Univ. Palacky. Olomouc. Czech. Repub.*, vol. 145, no. 2, pp. 49–55, Dec. 2001, [Online]. Available: http://www.ncbi.nlm.nih.gov/pubmed/12426771.

[173] M. H. Soonpaa *et al.*, "Absence of Cardiomyocyte Differentiation Following Transplantation of Adult Cardiac-Resident Sca-1 + Cells Into Infarcted Mouse Hearts," *Circulation*, vol. 138, no. 25, pp. 2963–2966, Dec. 2018, doi: 10.1161/CIRCULATIONAHA.118.035391.

[174] T. Vazin and W. J. Freed, "Human embryonic stem cells: Derivation, culture, and differentiation: A review," *Restor. Neurol. Neurosci.*, vol. 28, no. 4, pp. 589–603, 2010, doi: 10.3233/RNN-2010-0543.

[175] K. Takahashi and S. Yamanaka, "Induction of Pluripotent Stem Cells from Mouse Embryonic and Adult Fibroblast Cultures by Defined Factors," *Cell*, 2006, doi: 10.1016/j.cell.2006.07.024.

[176] K. Takahashi *et al.*, "Induction of pluripotent stem cells from adult human fibroblasts by defined factors.," *Cell*, vol. 131, no. 5, pp. 861–72, Nov. 2007, doi: 10.1016/j.cell.2007.11.019.

[177] K. R. Boheler, J. Czyz, D. Tweedie, H.-T. Yang, S. V Anisimov, and A. M. Wobus, "Differentiation of pluripotent embryonic stem cells into cardiomyocytes.," *Circ. Res.*, vol. 91, no. 3, pp. 189–201, Aug. 2002, doi: 10.1161/01.res.0000027865.61704.32.

[178] X. Lian *et al.*, "Directed cardiomyocyte differentiation from human pluripotent stem cells by modulating Wnt/β-catenin signaling under fully defined conditions," *Nat. Protoc.*, vol. 8, no. 1, pp. 162–175, Jan. 2013, doi: 10.1038/nprot.2012.150.

[179] P. W. Burridge *et al.*, "Chemically defned generation of human cardiomyocytes," *Nat. Methods*, 2014, doi: 10.1038/nMeth.2999.

[180] X. Lian *et al.*, "Robust cardiomyocyte differentiation from human pluripotent stem cells via temporal modulation of canonical Wnt signaling," *Proc. Natl. Acad. Sci. U. S. A.*, 2012, doi: 10.1073/pnas.1200250109.

[181] L. Han *et al.*, "Study familial hypertrophic cardiomyopathy using patient-specific induced pluripotent stem cells," *Cardiovasc. Res.*, vol. 104, no. 2, pp. 258–69, Nov. 2014, doi: 10.1093/cvr/cvu205.

[182] F. Lan *et al.*, "Abnormal calcium handling properties underlie familial hypertrophic cardiomyopathy pathology in patient-specific induced pluripotent stem cells.," *Cell Stem Cell*, vol. 12, no. 1, pp. 101–13, Jan. 2013, doi: 10.1016/j.stem.2012.10.010.

[183] Y. Chen *et al.*, “Engineering Human Stem Cell Lines with Inducible Gene Knockout using CRISPR/Cas9,” *Cell Stem Cell*, 2015, doi: 10.1016/j.stem.2015.06.001.

[184] Q. Ding, S. N. Regan, Y. Xia, L. A. Oostrom, C. A. Cowan, and K. Musunuru, “Enhanced efficiency of human pluripotent stem cell genome editing through replacing TALENs with CRISPRs,” *Cell Stem Cell*. 2013, doi: 10.1016/j.stem.2013.03.006.

[185] F. A. Ran, P. D. Hsu, J. Wright, V. Agarwala, D. A. Scott, and F. Zhang, “Genome engineering using the CRISPR-Cas9 system,” *Nat. Protoc.*, vol. 8, no. 11, pp. 2281–2308, Nov. 2013, doi: 10.1038/nprot.2013.143.

[186] J. D. Sander and J. K. Joung, “CRISPR-Cas systems for editing, regulating and targeting genomes,” *Nat. Biotechnol.*, vol. 32, no. 4, pp. 347–355, Apr. 2014, doi: 10.1038/nbt.2842.

[187] S. D. Lundy, W. Z. Zhu, M. Regnier, and M. A. Laflamme, “Structural and functional maturation of cardiomyocytes derived from human pluripotent stem cells,” *Stem Cells Dev.*, 2013, doi: 10.1089/scd.2012.0490.

[188] M. A. Argenziano, M. Burgos Angulo, M. Najari Beidokhti, J. Yang, A. C. Bertalovitz, and T. V. McDonald, “Generation of a heterozygous FLNC mutation-carrying human iPSC line, USFi002-A, for modeling dilated cardiomyopathy,” *Stem Cell Res.*, vol. 53, p. 102394, May 2021, doi: 10.1016/j.scr.2021.102394.

[189] T. Kamakura *et al.*, “Ultrastructural maturation of human-induced pluripotent stem cell-derived cardiomyocytes in a long-term culture.,” *Circ. J.*, vol. 77, no. 5, pp. 1307–14, 2013, doi: 10.1253/circj.cj-12-0987.

[190] A. Bizy and M. Klos, “Optimizing the Use of iPSC-CMs for Cardiac Regeneration in Animal Models,” *Animals*, vol. 10, no. 9, p. 1561, Sep. 2020, doi: 10.3390/ani10091561.

[191] C. C. Veerman, G. Kosmidis, C. L. Mummery, S. Casini, A. O. Verkerk, and M. Bellin, “Immaturity of Human Stem-Cell-Derived Cardiomyocytes in Culture: Fatal Flaw or Soluble Problem?,” *Stem Cells Dev.*, vol. 24, no. 9, pp. 1035–1052, May 2015, doi: 10.1089/scd.2014.0533.

[192] H. Jiang *et al.*, “Functional analysis of a gene-edited mouse model to gain insights into the disease mechanisms of a titin missense variant,” *Basic Res. Cardiol.*, vol. 116, no. 1, p. 14, Dec. 2021, doi: 10.1007/s00395-021-00853-z.

[193] S. Funakoshi *et al.*, “Generation of mature compact ventricular cardiomyocytes from human pluripotent stem cells,” *Nat. Commun.*, vol. 12, no. 1, p. 3155, Dec. 2021, doi: 10.1038/s41467-021-23329-z.

[194] J. Cox, M. Y. Hein, C. A. Luber, I. Paron, N. Nagaraj, and M. Mann, “Accurate proteome-wide label-free quantification by delayed normalization and maximal peptide ratio extraction, termed MaxLFQ,” *Mol. Cell. Proteomics*, 2014, doi: 10.1074/mcp.M113.031591.

[195] S. Tyanova *et al.*, “The Perseus computational platform for comprehensive analysis of (prote)omics data,” *Nature Methods*. 2016, doi: 10.1038/nmeth.3901.

[196] I. Shaikh *et al.*, “Differential gene expression analysis of HNSCC tumors deciphered tobacco dependent and independent molecular signatures,” *Oncotarget*, 2019, doi: 10.18632/oncotarget.27249.

[197] Y. Xie, W. Pan, and A. B. Khodursky, “A note on using permutation-based false discovery rate estimates to compare different analysis methods for microarray data,” *Bioinformatics*, 2005, doi: 10.1093/bioinformatics/bti685.

[198] C. Stringer, T. Wang, M. Michaelos, and M. Pachitariu, “Cellpose: a generalist algorithm for cellular segmentation,” *Nat. Methods*, vol. 18, no. 1, pp. 100–106, Jan. 2021, doi: 10.1038/s41592-020-01018-x.

[199] T. A. Morris *et al.*, “Striated myocyte structural integrity: Automated analysis of sarcomeric z-discs,” *PLoS Comput. Biol.*, vol. 16, no. 3, pp. 1–21, 2020, doi: 10.1371/journal.pcbi.1007676.

[200] C. N. Toepfer *et al.*, “SarcTrack,” *Circ. Res.*, vol. 124, no. 8, pp. 1172–1183, Apr. 2019, doi: 10.1161/CIRCRESAHA.118.314505.

[201] R. Apweiler *et al.*, “UniProt: The universal protein knowledgebase,” *Nucleic Acids Res.*, vol. 32, no. DATABASE ISS., Jan. 2004, doi: 10.1093/nar/gky092.

[202] M. Bern and D. Goldberg, “De novo analysis of peptide tandem mass spectra by spectral graph partitioning,” *J. Comput. Biol.*, vol. 13, no. 2, pp. 364–378, 2006, doi: 10.1089/cmb.2006.13.364.

[203] R. Wei *et al.*, “Missing Value Imputation Approach for Mass Spectrometry-based Metabolomics Data,” *Sci. Rep.*, vol. 8, no. 1, pp. 1–10, 2018, doi: 10.1038/s41598-017-19120-0.

[204] P. Berg, E. W. McConnell, L. M. Hicks, S. C. Popescu, and G. V. Popescu, “Evaluation of linear models and missing value imputation for the analysis of peptide-centric proteomics,” *BMC Bioinformatics*, vol. 20, no. Suppl 2, 2019, doi: 10.1186/s12859-019-2619-6.

[205] H. Choi and A. I. Nesvizhskii, “False discovery rates and related statistical concepts in mass spectrometry-based proteomics,” *J. Proteome Res.*, vol. 7, no. 1, pp. 47–50, 2008, doi: 10.1021/pr700747q.

[206] X. J. Du, “Gender modulates cardiac phenotype development in genetically modified mice,” *Cardiovasc. Res.*, vol. 63, no. 3, pp. 510–519, 2004, doi: 10.1016/j.cardiores.2004.03.027.

[207] C. Vilain *et al.*, “A novel NDUFV1 gene mutation in complex I deficiency in consanguineous siblings with brainstem lesions and Leigh syndrome,” *Clin. Genet.*, 2012, doi: 10.1111/j.1399-0004.2011.01743.x.

[208] K. B. Choksi, J. E. Nuss, J. H. DeFord, and J. Papaconstantinou, “Age-related alterations in oxidatively damaged proteins of mouse skeletal muscle mitochondrial electron transport chain complexes,” *Free Radic. Biol. Med.*, 2008, doi: 10.1016/j.freeradbiomed.2008.06.006.

[209] H. Ono, H. Nakamura, and M. Matsuzaki, “A NADH dehydrogenase ubiquinone flavoprotein is decreased in patients with dilated cardiomyopathy,” *Intern. Med.*, vol. 49, no. 19, pp. 2039–2042, 2010, doi: 10.2169/internalmedicine.49.3710.

[210] S. Choudhury *et al.*, “Role of AIF in cardiac apoptosis in hypertrophic cardiomyocytes from Dahl salt-sensitive rats,” *Cardiovasc. Res.*, 2010, doi: 10.1093/cvr/cvp261.

[211] Z. Xiong *et al.*, “Downregulation of AIF by HIF-1 contributes to hypoxia-induced epithelial-mesenchymal transition of colon cancer,” *Carcinogenesis*, 2016, doi: 10.1093/carcin/bgw089.

[212] L. Wischhof *et al.*, “A disease-associated Aifm1 variant induces severe myopathy in knockin mice,” *Mol. Metab.*, 2018, doi: 10.1016/j.molmet.2018.05.002.

[213] X. Lou *et al.*, “A Novel NDUFS3 mutation in a Chinese patient with severe Leigh

syndrome," *J. Hum. Genet.*, 2018, doi: 10.1038/s10038-018-0505-0.

[214] P. Wang, X. Cheng, Z. Fu, C. Zhou, W. Lu, and X. Xie, "Reduced expression of NDUFS3 and its clinical significance in serous ovarian cancer," *Int. J. Gynecol. Cancer*, 2013, doi: 10.1097/IGC.0b013e318287a90d.

[215] Y. Shang *et al.*, "Overexpression of UQCRC2 is correlated with tumor progression and poor prognosis in colorectal cancer," *Pathol. Res. Pract.*, 2018, doi: 10.1016/j.prp.2018.08.012.

[216] S. J. G. Hoefs *et al.*, "NDUFA10 mutations cause complex I deficiency in a patient with Leigh disease.," *Eur. J. Hum. Genet.*, vol. 19, no. 3, pp. 270–4, Mar. 2011, doi: 10.1038/ejhg.2010.204.

[217] A. Kinoshita *et al.*, "Carcinogenicity of dimethylarsinic acid in Ogg1-deficient mice," *Cancer Sci.*, vol. 98, no. 6, pp. 803–814, Jun. 2007, doi: 10.1111/j.1349-7006.2007.00475.x.

[218] S. Feldkirchner, J. Schessl, S. Müller, B. Schoser, and F. G. Hanisch, "Patient-specific protein aggregates in myofibrillar myopathies: Laser microdissection and differential proteomics for identification of plaque components," *Proteomics*, vol. 12, no. 23–24, pp. 3598–3609, 2012, doi: 10.1002/pmic.201100559.

[219] N. Kaludercic, A. Carpi, R. Menabò, F. Di Lisa, and N. Paolocci, "Monoamine oxidases (MAO) in the pathogenesis of heart failure and ischemia/reperfusion injury," *Biochim. Biophys. Acta - Mol. Cell Res.*, vol. 1813, no. 7, pp. 1323–1332, Jul. 2011, doi: 10.1016/j.bbamcr.2010.09.010.

[220] P. Riederer and G. Laux, "MAO-inhibitors in Parkinson's Disease.," *Exp. Neurobiol.*, vol. 20, no. 1, pp. 1–17, Mar. 2011, doi: 10.5607/en.2011.20.1.1.

[221] C. Wu, "Migfilin and its binding partners: From cell biology to human diseases," *J. Cell Sci.*, 2005, doi: 10.1242/jcs.01639.

[222] H. He *et al.*, "Migfilin regulates esophageal cancer cell motility through promoting GSK-3β-mediated degradation of β-catenin," *Mol. Cancer Res.*, 2012, doi: 10.1158/1541-7786.MCR-11-0419.

[223] Y. Jiao, Y. Li, P. Jiang, W. Han, and Y. Liu, "PGM5: A novel diagnostic and prognostic biomarker for liver cancer," *PeerJ*, 2019, doi: 10.7717/peerj.7070.

[224] A. M. Belkin and K. Burridge, "Expression and localization of the phosphoglucomutase-related cytoskeletal protein, aciculin, in skeletal muscle," *J. Cell Sci.*, 1994.

[225] S. Donkervoort *et al.*, "Cardiomyopathy in patients with ACTA1-myopathy," *Neuromuscul. Disord.*, vol. 25, p. S287, Oct. 2015, doi: 10.1016/j.nmd.2015.06.361.

[226] V. Gupta, M. Discenza, J. R. Guyon, L. M. Kunkel, and A. H. Beggs, "α-Actinin-2 deficiency results in sarcomeric defects in zebrafish that cannot be rescued by α-actinin-3 revealing functional differences between sarcomeric isoforms," *FASEB J.*, 2012, doi: 10.1096/fj.11-194548.

[227] O. Esue, Y. Tseng, and D. Wirtz, "α-Actinin and Filamin Cooperatively Enhance the Stiffness of Actin Filament Networks," *PLoS One*, vol. 4, no. 2, p. e4411, Feb. 2009, doi: 10.1371/journal.pone.0004411.

[228] J. Zhang *et al.*, "Overexpression of BAG3 attenuates hypoxia-induced cardiomyocyte apoptosis by inducing autophagy," *Cell. Physiol. Biochem.*, 2016, doi: 10.1159/000445641.

[229] E. Stürner and C. Behl, “The role of the multifunctional bag3 protein in cellular protein quality control and in disease,” *Frontiers in Molecular Neuroscience*. 2017, doi: 10.3389/fnmol.2017.00177.

[230] A. P. Landstrom, D. Dobrev, and X. H. T. Wehrens, “Calcium Signaling and Cardiac Arrhythmias,” *Circulation Research*. 2017, doi: 10.1161/CIRCRESAHA.117.310083.

[231] K. E. Orii *et al.*, “Genomic and mutational analysis of the mitochondrial trifunctional protein β-subunit (HADHB) gene in patients with trifunctional protein deficiency,” *Hum. Mol. Genet.*, 1997, doi: 10.1093/hmg/6.8.1215.

[232] F. Nakamura, J. H. Hartwig, T. P. Stossel, and P. T. Szymanski, “Ca2+ and Calmodulin Regulate the Binding of Filamin A to Actin Filaments,” *J. Biol. Chem.*, vol. 280, no. 37, pp. 32426–32433, Sep. 2005, doi: 10.1074/jbc.M502203200.

[233] Y. Huang *et al.*, “Variants in CAPZA2, a member of an F-actin capping complex, cause intellectual disability and developmental delay,” *Hum. Mol. Genet.*, vol. 29, no. 9, pp. 1537–1546, Jun. 2020, doi: 10.1093/hmg/ddaa078.

[234] K. Mukherjee *et al.*, “Actin capping protein CAPZB regulates cell morphology, differentiation, and neural crest migration in craniofacial morphogenesis†.,” *Hum. Mol. Genet.*, vol. 25, no. 7, pp. 1255–70, Apr. 2016, doi: 10.1093/hmg/ddw006.

[235] B. Yin *et al.*, “CRYAB protects cardiomyocytes against heat stress by preventing caspase-mediated apoptosis and reducing F-actin aggregation.,” *Cell Stress Chaperones*, vol. 24, no. 1, pp. 59–68, 2019, doi: 10.1007/s12192-018-0941-y.

[236] M. M. Rashid *et al.*, “Muscle LIM protein/CSRP3: a mechanosensor with a role in autophagy,” *Cell Death Discov.*, 2015, doi: 10.1038/cddiscovery.2015.14.

[237] E. Vafiadaki *et al.*, “Muscle lim protein isoform negatively regulates striated muscle actin dynamics and differentiation,” *FEBS J.*, 2014, doi: 10.1111/febs.12859.

[238] F. W. Friedrich *et al.*, “FHL2 expression and variants in hypertrophic cardiomyopathy,” *Basic Res. Cardiol.*, vol. 109, no. 6, p. 451, Nov. 2014, doi: 10.1007/s00395-014-0451-8.

[239] X. Chen and Y. Zhang, “Myocardial Cx43 expression in the cases of sudden death due to dilated cardiomyopathy,” *Forensic Sci. Int.*, 2006, doi: 10.1016/j.forsciint.2006.06.044.

[240] T. Bupha-Intr, K. M. Haizlip, and P. M. L. Janssen, “Temporal changes in expression of connexin 43 after load-induced hypertrophy in vitro,” *Am. J. Physiol. - Hear. Circ. Physiol.*, 2009, doi: 10.1152/ajpheart.01058.2008.

[241] R. Benndorf, J. L. Martin, S. L. Kosakovsky Pond, and J. O. Wertheim, “Neuropathy- and myopathy-associated mutations in human small heat shock proteins: Characteristics and evolutionary history of the mutation sites,” *Mutat. Res. Mutat. Res.*, vol. 761, pp. 15–30, Jul. 2014, doi: 10.1016/j.mrrev.2014.02.004.

[242] X. Hu, D. M. S. Van Marion, M. Wiersma, D. Zhang, and B. J. J. M. Brundel, “The protective role of small heat shock proteins in cardiac diseases: key role in atrial fibrillation,” *Cell Stress Chaperones*, vol. 22, no. 4, pp. 665–674, Jul. 2017, doi: 10.1007/s12192-017-0799-4.

[243] L. Ke *et al.*, “HSPB1, HSPB6, HSPB7 and HSPB8 Protect against RhoA GTPase-Induced Remodeling in Tachypaced Atrial Myocytes,” *PLoS One*, vol. 6, no. 6, p. e20395, Jun. 2011, doi: 10.1371/journal.pone.0020395.

[244] J. H. Grose *et al.*, “Characterization of the Cardiac Overexpression of HSPB2 Reveals

Mitochondrial and Myogenic Roles Supported by a Cardiac HspB2 Interactome," *PLoS One*, vol. 10, no. 10, p. e0133994, Oct. 2015, doi: 10.1371/journal.pone.0133994.

[245] M. Nakagawa, N. Tsujimoto, H. Nakagawa, T. Iwaki, Y. Fukumaki, and A. Iwaki, "Association of HSPB2, a member of the small heat shock protein family, with mitochondria," *Exp. Cell Res.*, 2001, doi: 10.1006/excr.2001.5362.

[246] T. Wu *et al.*, "HSPB7 is indispensable for heart development by modulating actin filament assembly," *Proc. Natl. Acad. Sci.*, vol. 114, no. 45, pp. 11956–11961, Nov. 2017, doi: 10.1073/pnas.1713763114.

[247] X. Sun, S. Siri, A. Hurst, and H. Qiu, "Heat Shock Protein 22 in Physiological and Pathological Hearts: Small Molecule, Large Potentials.," *Cells*, vol. 11, no. 1, 2021, doi: 10.3390/cells11010114.

[248] M. He *et al.*, "Genetic Variations in HSPA8 Gene Associated with Coronary Heart Disease Risk in a Chinese Population," *PLoS One*, vol. 5, no. 3, p. e9684, Mar. 2010, doi: 10.1371/journal.pone.0009684.

[249] "No Title."

[250] W. B. Holmes and C. L. Moncman, "Nebulette interacts with filamin C," *Cell Motil. Cytoskeleton*, vol. 65, no. 2, pp. 130–142, Feb. 2008, doi: 10.1002/cm.20249.

[251] R. J. Roberts, L. Hallee, and C. K. Lam, "The Potential of Hsp90 in Targeting Pathological Pathways in Cardiac Diseases," *J. Pers. Med.*, vol. 11, no. 12, p. 1373, Dec. 2021, doi: 10.3390/jpm11121373.

[252] A. Azad, G. Poloni, N. Sontayananon, H. Jiang, and K. Gehmlich, "The giant titin: how to evaluate its role in cardiomyopathies," *J. Muscle Res. Cell Motil.*, 2019, doi: 10.1007/s10974-019-09518-w.

[253] Q. Wang, J. L.-C. Lin, A. J. Erives, C.-I. Lin, and J. J.-C. Lin, "New insights into the roles of Xin repeat-containing proteins in cardiac development, function, and disease.," *Int. Rev. Cell Mol. Biol.*, vol. 310, pp. 89–128, 2014, doi: 10.1016/B978-0-12-800180-6.00003-7.

[254] M. Arad *et al.*, "Gene mutations in apical hypertrophic cardiomyopathy," *Circulation*, 2005, doi: 10.1161/CIRCULATIONAHA.105.547448.

[255] D. E. Dye, B. Azzarelli, H. H. Goebel, and N. G. Laing, "Novel slow-skeletal myosin (MYH7) mutation in the original myosin storage myopathy kindred," *Neuromuscul. Disord.*, 2006, doi: 10.1016/j.nmd.2006.03.011.

[256] S. M. Garvey, Y. Liu, S. E. Miller, and M. A. Hauser, "Myotilin overexpression enhances myopathology in the LGMD1A mouse model," *Muscle and Nerve*, 2008, doi: 10.1002/mus.20994.

[257] M. A. Hauser *et al.*, "Myotilin is mutated in limb girdle muscular dystrophy 1A," *Hum. Mol. Genet.*, 2000, doi: 10.1093/hmg/9.14.2141.

[258] T. Foroud *et al.*, "A mutation in myotilin causes spheroid body myopathy," *Neurology*, 2005, doi: 10.1212/01.wnl.0000188872.28149.9a.

[259] J. M. McLendon, X. Zhang, D. S. Matasic, B. London, and R. L. Boudreau, "Loss of SORBS2 in Cardiomyocytes Leads to Dilated Left Ventricle Cardiomyopathy in Mice," *FASEB J.*, vol. 34, no. S1, pp. 1–1, Apr. 2020, doi: 10.1096/fasebj.2020.34.s1.07385.

[260] S. R. Cunha and P. J. Mohler, "Obscurin targets ankyrin-B and protein phosphatase 2A to

the cardiac M-line," *J. Biol. Chem.*, 2008, doi: 10.1074/jbc.M806050200.

[261] D. Rossi *et al.*, "A novel FLNC frameshift and an OBSCN variant in a family with distal muscular dystrophy," *PLoS One*, 2017, doi: 10.1371/journal.pone.0186642.

[262] M. H. Derbala, A. S. Guo, P. J. Mohler, and S. A. Smith, "The role of βII spectrin in cardiac health and disease," *Life Sciences*. 2018, doi: 10.1016/j.lfs.2017.11.009.

[263] H. Saitsu *et al.*, "Dominant-Negative Mutations in α-II Spectrin Cause West Syndrome with Severe Cerebral Hypomyelination, Spastic Quadriplegia, and Developmental Delay," *Am. J. Hum. Genet.*, 2010, doi: 10.1016/j.ajhg.2010.04.013.

[264] A. Beqqali *et al.*, "CHAP is a newly identified Z-disc protein essential for heart and skeletal muscle function," *J. Cell Sci.*, 2010, doi: 10.1242/jcs.063859.

[265] C. T. Pappas *et al.*, "Knockout of Lmod2 results in shorter thin filaments followed by dilated cardiomyopathy and juvenile lethality," *Proc. Natl. Acad. Sci. U. S. A.*, 2015, doi: 10.1073/pnas.1508273112.

[266] S.-J. Jeong, J.-G. Park, and G. T. Oh, "Peroxiredoxins as Potential Targets for Cardiovascular Disease," *Antioxidants*, vol. 10, no. 8, p. 1244, Aug. 2021, doi: 10.3390/antiox10081244.

[267] R. Matsushima-Nishiwaki *et al.*, "Phosphorylated Heat Shock Protein 20 (HSPB6) Regulates Transforming Growth Factor-α-Induced Migration and Invasion of Hepatocellular Carcinoma Cells," *PLoS One*, vol. 11, no. 4, p. e0151907, Apr. 2016, doi: 10.1371/journal.pone.0151907.

[268] W. C. Liao, L. Y. Juo, Y. L. Shih, Y. H. Chen, and Y. T. Yan, "HSPB7 prevents cardiac conduction system defect through maintaining intercalated disc integrity," *PLoS Genet.*, 2017, doi: 10.1371/journal.pgen.1006984.

[269] L. Jing *et al.*, "Expression of Myopodin Induces Suppression of Tumor Growth and Metastasis," *Am. J. Pathol.*, 2004, doi: 10.1016/S0002-9440(10)63738-8.

[270] M. P. Collier and J. L. P. P. Benesch, "Small heat-shock proteins and their role in mechanical stress.," *Cell Stress Chaperones*, vol. 25, no. 4, pp. 601–613, 2020, doi: 10.1007/s12192-020-01095-z.

[271] S. Krief *et al.*, "Identification and characterization of cvHsp. A novel human small stress protein selectively expressed in cardiovascular and insulin-sensitive tissues," *J. Biol. Chem.*, vol. 274, no. 51, pp. 36592–36600, 1999, doi: 10.1074/jbc.274.51.36592.

[272] M. J. Vos *et al.*, "HSPB7 is the most potent polyQ aggregation suppressor within the HSPB family of molecular chaperones," *Hum. Mol. Genet.*, vol. 19, no. 23, pp. 4677–4693, 2010, doi: 10.1093/hmg/ddq398.

[273] J. N. Rauch *et al.*, "BAG3 Is a Modular, Scaffolding Protein that physically Links Heat Shock Protein 70 (Hsp70) to the Small Heat Shock Proteins," *J. Mol. Biol.*, vol. 429, no. 1, pp. 128–141, Jan. 2017, doi: 10.1016/j.jmb.2016.11.013.

[274] C. S. P. Lam *et al.*, "Sex differences in heart failure," *Eur. Heart J.*, vol. 40, no. 47, pp. 3859–3868, 2019, doi: 10.1093/eurheartj/ehz835.

[275] L. L. A. M. Nijenkamp *et al.*, "Sex Differences at the Time of Myectomy in Hypertrophic Cardiomyopathy," *Circ. Hear. Fail.*, vol. 11, no. 6, pp. 1–13, 2018, doi: 10.1161/CIRCHEARTFAILURE.117.004133.

[276] B. Van Driel, L. Nijenkamp, R. Huurman, M. Michels, and J. Van Der Velden, “Sex differences in hypertrophic cardiomyopathy: New insights,” *Curr. Opin. Cardiol.*, vol. 34, no. 3, pp. 254–259, 2019, doi: 10.1097/HCO.0000000000000612.

[277] R. López-Vilella *et al.*, “The Female Sex Confers Different Prognosis in Heart Failure: Same Mortality but More Readmissions,” *Front. Cardiovasc. Med.*, vol. 8, Mar. 2021, doi: 10.3389/fcvm.2021.618398.

[278] R. D. Patten, “Models of gender differences in cardiovascular disease,” *Drug Discov. Today Dis. Model.*, vol. 4, no. 4, pp. 227–232, 2007, doi: 10.1016/j.ddmod.2007.11.002.

[279] J. T. Lightfoot, “Sex hormones’ regulation of rodent physical activity: A review,” *Int. J. Biol. Sci.*, vol. 4, no. 3, pp. 126–132, 2008, doi: 10.7150/ijbs.4.126.

[280] A.-R. Niță, G. A. Knock, and R. J. Heads, “Signalling mechanisms in the cardiovascular protective effects of estrogen: With a focus on rapid/membrane signalling.,” *Curr. Res. Physiol.*, vol. 4, no. March, pp. 103–118, 2021, doi: 10.1016/j.crphys.2021.03.003.

[281] S. Horiuchi, “Postmenopausal Acceleration of Age-Related Mortality Increase,” *Journals Gerontol. Ser. A Biol. Sci. Med. Sci.*, vol. 52A, no. 1, pp. B78–B92, Jan. 1997, doi: 10.1093/gerona/52A.1.B78.

[282] A. Iorga, C. M. Cunningham, S. Moazeni, G. Ruffenach, S. Umar, and M. Eghbali, “The protective role of estrogen and estrogen receptors in cardiovascular disease and the controversial use of estrogen therapy,” *Biol. Sex Differ.*, vol. 8, no. 1, p. 33, Dec. 2017, doi: 10.1186/s13293-017-0152-8.

[283] J. Piquereau *et al.*, “Mitochondrial dynamics in the adult cardiomyocytes: Which roles for a highly specialized cell?,” *Front. Physiol.*, 2013, doi: 10.3389/fphys.2013.00102.

[284] H. Ashrafian, C. Redwood, E. Blair, and H. Watkins, “Hypertrophic cardiomyopathy:a paradigm for myocardial energy depletion,” *Trends Genet.*, vol. 19, no. 5, pp. 263–268, May 2003, doi: 10.1016/S0168-9525(03)00081-7.

[285] J. Van Der Velden *et al.*, “Metabolic changes in hypertrophic cardiomyopathies: Scientific update from the working group of myocardial function of the European Society of Cardiology,” *Cardiovasc. Res.*, vol. 114, no. 10, pp. 1273–1280, 2018, doi: 10.1093/cvr/cvy147.

[286] D. C. Fuhrmann and B. Brüne, “Mitochondrial composition and function under the control of hypoxia,” *Redox Biology*. 2017, doi: 10.1016/j.redox.2017.02.012.

[287] T. Liu, L. Chen, E. Kim, D. Tran, B. S. Phinney, and A. A. Knowlton, “Mitochondrial proteome remodeling in ischemic heart failure,” *Life Sci.*, vol. 101, no. 1–2, pp. 27–36, Apr. 2014, doi: 10.1016/j.lfs.2014.02.004.

[288] T. Hou *et al.*, “NDUFAB1 confers cardio-protection by enhancing mitochondrial bioenergetics through coordination of respiratory complex and supercomplex assembly,” *Cell Res.*, vol. 29, no. 9, pp. 754–766, Sep. 2019, doi: 10.1038/s41422-019-0208-x.

[289] G. Roy-Choudhury and M. M. Daadi, “Assay for Assessing Mitochondrial Function in iPSC-Derived Neural Stem Cells and Dopaminergic Neurons,” 2019, pp. 161–173.

[290] W. A. Ng, I. L. Grupp, A. Subramaniam, and J. Robbins, “Cardiac myosin heavy chain mRNA expression and myocardial function in the mouse heart.,” *Circ. Res.*, vol. 68, no. 6, pp. 1742–1750, Jun. 1991, doi: 10.1161/01.RES.68.6.1742.

[291] E. M. McNally, R. Kraft, M. Bravo-Zehnder, D. A. Taylor, and L. A. Leinwand, “Full-

length rat alpha and beta cardiac myosin heavy chain sequences," *J. Mol. Biol.*, vol. 210, no. 3, pp. 665–671, Dec. 1989, doi: 10.1016/0022-2836(89)90141-1.

[292] K. Harada, T. Sugaya, K. Murakami, Y. Yazaki, and I. Komuro, "Angiotensin II type 1A receptor knockout mice display less left ventricular remodeling and improved survival after myocardial infarction," *Circulation*, vol. 100, no. 20, pp. 2093–2099, Nov. 1999, doi: 10.1161/01.CIR.100.20.2093.

[293] L. E. Waspe, C. P. Ordahl, and P. C. Simpson, "The cardiac β-myosin heavy chain isogene is induced selectively in α1-adrenergic receptor-stimulated hypertrophy of cultured rat heart myocytes," *J. Clin. Invest.*, vol. 85, no. 4, pp. 1206–1214, 1990, doi: 10.1172/JCI114554.

[294] S. Chugh *et al.*, "Pilot study identifying myosin heavy chain 7, desmin, insulin-like growth factor 7, and annexin A2 as circulating biomarkers of human heart failure," *Proteomics*, 2013, doi: 10.1002/pmic.201200455.

[295] P. J. Reiser, M. A. Portman, X. H. Ning, and C. S. Moravec, "Human cardiac myosin heavy chain isoforms in fetal and failing adult atria and ventricles," *Am. J. Physiol. - Hear. Circ. Physiol.*, 2001, doi: 10.1152/ajpheart.2001.280.4.h1814.

[296] T.-F. Chiu *et al.*, "Association of Plasma Concentration of Small Heat Shock Protein B7 With Acute Coronary Syndrome," *Circ. J.*, vol. 76, no. 9, pp. 2226–2233, 2012, doi: 10.1253/circj.CJ-12-0238.

[297] D. Selcen and A. G. Engel, "Mutations in myotilin cause myofibrillar myopathy," *Neurology*, 2004, doi: 10.1212/01.WNL.0000123576.74801.75.

[298] J. Wang, D. K. Dube, B. Mittal, J. M. Sanger, and J. W. Sanger, "Myotilin dynamics in cardiac and skeletal muscle cells," *Cytoskeleton*, 2011, doi: 10.1002/cm.20542.

[299] A. Wyttenbach, "Role of heat shock proteins during polyglutamine neurodegeneration: Mechanisms and hypothesis," *Journal of Molecular Neuroscience*. 2004, doi: 10.1385/jmn:23:1-2:069.

[300] H. Sun, C. Gao, and Y. Wang, "A H(a)rd Way to Adapt in Cardiac Hypertrophy," *Circ. Res.*, vol. 117, no. 6, pp. 484–486, Aug. 2015, doi: 10.1161/CIRCRESAHA.115.307164.

[301] V. P. M. van Empel *et al.*, "Downregulation of apoptosis-inducing factor in harlequin mutant mice sensitizes the myocardium to oxidative stress-related cell death and pressure overload-induced decompensation.," *Circ. Res.*, vol. 96, no. 12, 2005, doi: 10.1161/01.RES.0000172081.30327.28.

[302] R. Ferrari, "Mitochondria and the heart," *Eur. Heart J.*, 2011, doi: 10.1093/eurheartj/ehr406.

[303] B. J. Haubner *et al.*, "In vivo cardiac role of migfilin during experimental pressure overload," *Cardiovasc. Res.*, vol. 106, no. 3, pp. 398–407, Jun. 2015, doi: 10.1093/cvr/cvv125.

[304] W. Van Eldik *et al.*, "Z-disc protein CHAPb induces cardiomyopathy and contractile dysfunction in the postnatal heart," *PLoS One*, 2017, doi: 10.1371/journal.pone.0189139.

[305] N. J. Haywood *et al.*, "Hypertrophic cardiomyopathy mutations in the calponin-homology domain of ACTN2 affect actin binding and cardiomyocyte Z-disc incorporation," *Biochem. J.*, 2016, doi: 10.1042/BCJ20160421.

[306] C. T. Pappas, G. P. Farman, R. M. Mayfield, J. P. Konhilas, and C. C. Gregorio, "Cardiac-specific knockout of Lmod2 results in a severe reduction in myofilament force production

and rapid cardiac failure," *J. Mol. Cell. Cardiol.*, 2018, doi: 10.1016/j.yjmcc.2018.08.009.

[307] H. Watkins *et al.*, "Mutations in the Genes for Cardiac Troponin T and α-Tropomyosin in Hypertrophic Cardiomyopathy," *N. Engl. J. Med.*, 1995, doi: 10.1056/NEJM199504203321603.

[308] F. Pasquale, P. Syrris, J. P. Kaski, J. Mogensen, W. J. McKenna, and P. Elliott, "Long-term outcomes in hypertrophic cardiomyopathy caused by mutations in the cardiac troponin T gene," *Circ. Cardiovasc. Genet.*, 2012, doi: 10.1161/CIRCGENETICS.111.959973.

[309] S. J. Forrester *et al.*, "Angiotensin II signal transduction: An update on mechanisms of physiology and pathophysiology," *Physiol. Rev.*, vol. 98, no. 3, pp. 1627–1738, 2018, doi: 10.1152/physrev.00038.2017.

[310] L. T. Mccollum, P. E. Gallagher, and E. Ann Tallant, "Angiotensin-(1-7) attenuates angiotensin II-induced cardiac remodeling associated with upregulation of dual-specificity phosphatase 1," *Am. J. Physiol. - Hear. Circ. Physiol.*, vol. 302, no. 3, pp. 801–810, 2012, doi: 10.1152/ajpheart.00908.2011.

[311] J. van der Velden *et al.*, "Animal models and animal-free innovations for cardiovascular research: current status and routes to be explored. Consensus document of the ESC Working Group on Myocardial Function and the ESC Working Group on Cellular Biology of the Heart," *Cardiovasc. Res.*, Jan. 2022, doi: 10.1093/cvr/cvab370.

[312] D. Schüttler *et al.*, "A practical guide to setting up pig models for cardiovascular catheterization, electrophysiological assessment and heart disease research," *Lab Anim. (NY).*, vol. 51, no. 2, pp. 46–67, Feb. 2022, doi: 10.1038/s41684-021-00909-6.

[313] J. Mitcheson, "Cultured adult cardiac myocytes Future applications, culture methods, morphological and electrophysiological properties," *Cardiovasc. Res.*, vol. 39, no. 2, pp. 280–300, Aug. 1998, doi: 10.1016/S0008-6363(98)00128-X.

[314] A. Pezhouman *et al.*, "Isolation and characterization of human embryonic stem cell-derived heart field-specific cardiomyocytes unravels new insights into their transcriptional and electrophysiological profiles," *Cardiovasc. Res.*, vol. 118, no. 3, pp. 828–843, Feb. 2022, doi: 10.1093/cvr/cvab102.

[315] P. Menasché, "Cell Therapy With Human ESC-Derived Cardiac Cells: Clinical Perspectives," *Front. Bioeng. Biotechnol.*, vol. 8, Oct. 2020, doi: 10.3389/fbioe.2020.601560.

[316] R. Cohn *et al.*, "A Contraction Stress Model of Hypertrophic Cardiomyopathy due to Sarcomere Mutations," *Stem Cell Reports*, 2019, doi: 10.1016/j.stemcr.2018.11.015.

[317] N. Sun *et al.*, "Patient-specific induced pluripotent stem cells as a model for familial dilated cardiomyopathy," *Sci. Transl. Med.*, 2012, doi: 10.1126/scitranslmed.3003552.

[318] Y. Wang *et al.*, "Genome editing of isogenic human induced pluripotent stem cells recapitulates long QT phenotype for drug testing," *J. Am. Coll. Cardiol.*, 2014, doi: 10.1016/j.jacc.2014.04.057.

[319] L. Wang *et al.*, "Generation and Characterization of a Human iPSC Cardiomyocyte Model of Troponin T I79N Linked Hypertrophic Cardiomyopathy," *Biophys. J.*, 2017, doi: 10.1016/j.bpj.2016.11.577.

[320] H. S. Hwang *et al.*, "Comparable calcium handling of human iPSC-derived cardiomyocytes generated by multiple laboratories," *J. Mol. Cell. Cardiol.*, 2015, doi: 10.1016/j.yjmcc.2015.05.003.

[321] G. M. Roth, D. M. Bader, and E. R. Pfaltzgraff, “Isolation and Physiological Analysis of Mouse Cardiomyocytes,” *J. Vis. Exp.*, no. 91, Sep. 2014, doi: 10.3791/51109.

[322] J. Lewandowski *et al.*, “The impact of in vitro cell culture duration on the maturation of human cardiomyocytes derived from induced pluripotent stem cells of myogenic origin.,” *Cell Transplant.*, vol. 27, no. 7, pp. 1047–1067, 2018, doi: 10.1177/0963689718779346.

[323] Y. Jiang, P. Park, S. M. Hong, and K. Ban, “Maturation of cardiomyocytes derived from human pluripotent stem cells: Current strategies and limitations,” *Molecules and Cells*. 2018, doi: 10.14348/molcells.2018.0143.

[324] R. E. Ahmed, T. Anzai, N. Chanthra, and H. Uosaki, “A Brief Review of Current Maturation Methods for Human Induced Pluripotent Stem Cells-Derived Cardiomyocytes.,” *Front. cell Dev. Biol.*, vol. 8, p. 178, 2020, doi: 10.3389/fcell.2020.00178.

[325] S. S. Parikh *et al.*, “Thyroid and Glucocorticoid Hormones Promote Functional T-Tubule Development in Human-Induced Pluripotent Stem Cell-Derived Cardiomyocytes.,” *Circ. Res.*, vol. 121, no. 12, pp. 1323–1330, Dec. 2017, doi: 10.1161/CIRCRESAHA.117.311920.

[326] Y. Horikoshi *et al.*, “Fatty Acid-Treated Induced Pluripotent Stem Cell-Derived Human Cardiomyocytes Exhibit Adult Cardiomyocyte-Like Energy Metabolism Phenotypes.,” *Cells*, vol. 8, no. 9, 2019, doi: 10.3390/cells8091095.

[327] X. Yang *et al.*, “Fatty Acids Enhance the Maturation of Cardiomyocytes Derived from Human Pluripotent Stem Cells.,” *Stem cell reports*, vol. 13, no. 4, pp. 657–668, 2019, doi: 10.1016/j.stemcr.2019.08.013.

[328] S. Martewicz, E. Serena, S. Zatti, G. Keller, and N. Elvassore, “Substrate and mechanotransduction influence SERCA2a localization in human pluripotent stem cell-derived cardiomyocytes affecting functional performance.,” *Stem Cell Res.*, vol. 25, pp. 107–114, 2017, doi: 10.1016/j.scr.2017.10.011.

[329] C. O. Heras-Bautista *et al.*, “The influence of physiological matrix conditions on permanent culture of induced pluripotent stem cell-derived cardiomyocytes,” *Biomaterials*, 2014, doi: 10.1016/j.biomaterials.2014.05.027.

[330] A. Körner, M. Mosqueira, M. Hecker, and N. D. Ullrich, “Substrate Stiffness Influences Structural and Functional Remodeling in Induced Pluripotent Stem Cell-Derived Cardiomyocytes,” *Front. Physiol.*, vol. 12, no. August, 2021, doi: 10.3389/fphys.2021.710619.

[331] R. Ma *et al.*, “Electrical Stimulation Enhances Cardiac Differentiation of Human Induced Pluripotent Stem Cells for Myocardial Infarction Therapy.,” *Antioxid. Redox Signal.*, vol. 28, no. 5, pp. 371–384, 2018, doi: 10.1089/ars.2016.6766.

[332] S. Yoshida, K. Sumomozawa, K. Nagamine, and M. Nishizawa, “Hydrogel Microchambers Integrated with Organic Electrodes for Efficient Electrical Stimulation of Human iPSC-Derived Cardiomyocytes.,” *Macromol. Biosci.*, vol. 19, no. 6, p. e1900060, 2019, doi: 10.1002/mabi.201900060.

[333] C. E. Rupert and K. L. K. Coulombe, “IGF1 and NRG1 Enhance Proliferation, Metabolic Maturity, and the Force-Frequency Response in hESC-Derived Engineered Cardiac Tissues.,” *Stem Cells Int.*, vol. 2017, p. 7648409, 2017, doi: 10.1155/2017/7648409.

[334] W. H. Zimmermann, C. Fink, D. Kralisch, U. Remmers, J. Weil, and T. Eschenhagen, “Three-dimensional engineered heart tissue from neonatal rat cardiac myocytes,”

Biotechnol. Bioeng., vol. 68, no. 1, pp. 106–114, Apr. 2000, doi: 10.1002/(SICI)1097-0290(20000405)68:1<106::AID-BIT13>3.0.CO;2-3.

[335] T. J. Herron *et al.*, "Extracellular Matrix–Mediated Maturation of Human Pluripotent Stem Cell–Derived Cardiac Monolayer Structure and Electrophysiological Function," *Circ. Arrhythmia Electrophysiol.*, vol. 9, no. 4, Apr. 2016, doi: 10.1161/CIRCEP.113.003638.

[336] S. Yoshida *et al.*, "Maturation of Human Induced Pluripotent Stem Cell-Derived Cardiomyocytes by Soluble Factors from Human Mesenchymal Stem Cells," *Mol. Ther.*, vol. 26, no. 11, pp. 2681–2695, Nov. 2018, doi: 10.1016/j.ymthe.2018.08.012.

[337] C. Y. Huang *et al.*, "Enhancement of human iPSC-derived cardiomyocyte maturation by chemical conditioning in a 3D environment," *J. Mol. Cell. Cardiol.*, vol. 138, pp. 1–11, Jan. 2020, doi: 10.1016/j.yjmcc.2019.10.001.

[338] H. Masumoto *et al.*, "The myocardial regenerative potential of three-dimensional engineered cardiac tissues composed of multiple human iPS cell-derived cardiovascular cell lineages," *Sci. Rep.*, vol. 6, no. 1, p. 29933, Jul. 2016, doi: 10.1038/srep29933.

[339] I. Y. Shadrin *et al.*, "Cardiopatch platform enables maturation and scale-up of human pluripotent stem cell-derived engineered heart tissues," *Nat. Commun.*, vol. 8, no. 1, p. 1825, Dec. 2017, doi: 10.1038/s41467-017-01946-x.

[340] E. Giacomelli *et al.*, "Human-iPSC-Derived Cardiac Stromal Cells Enhance Maturation in 3D Cardiac Microtissues and Reveal Non-cardiomyocyte Contributions to Heart Disease," *Cell Stem Cell*, vol. 26, no. 6, pp. 862-879.e11, Jun. 2020, doi: 10.1016/j.stem.2020.05.004.

[341] N. Huebsch *et al.*, "Miniaturized iPS-Cell-Derived Cardiac Muscles for Physiologically Relevant Drug Response Analyses," *Sci. Rep.*, 2016, doi: 10.1038/srep24726.

[342] S. Funakoshi *et al.*, "Enhanced engraftment, proliferation, and therapeutic potential in heart using optimized human iPSC-derived cardiomyocytes.," *Sci. Rep.*, vol. 6, p. 19111, Jan. 2016, doi: 10.1038/srep19111.

[343] J. S. Sham, S. N. Hatem, and M. Morad, "Species differences in the activity of the Na(+)-Ca2+ exchanger in mammalian cardiac myocytes.," *J. Physiol.*, vol. 488, no. 3, pp. 623–631, 1995, doi: 10.1113/jphysiol.1995.sp020995.

[344] R. H. Waterston *et al.*, "Initial sequencing and comparative analysis of the mouse genome," *Nature*, vol. 420, no. 6915, pp. 520–562, 2002, [Online]. Available: http://www.nature.com/nature/journal/v420/n6915/full/nature01262.html.

[345] A. C. Gomes, I. Falcão-Pires, A. L. Pires, C. Brás-Silva, and A. F. Leite-Moreira, "Rodent models of heart failure: an updated review," *Heart Fail. Rev.*, vol. 18, no. 2, pp. 219–249, Mar. 2013, doi: 10.1007/s10741-012-9305-3.

[346] R. Zhu, A. Blazeski, E. Poon, K. D. Costa, L. Tung, and K. R. Boheler, "Physical developmental cues for the maturation of human pluripotent stem cell-derived cardiomyocytes," *Stem Cell Res. Ther.*, vol. 5, no. 1, pp. 1–18, 2014, doi: 10.1186/scrt507.

[347] B. Hinz B., "Matrix Mechanics And Regulation Of The Fibroblast Phenotype," *Periodontol. 2000*, 2013, doi: 10.1111/prd.12030.

[348] B. Bhana *et al.*, "Influence of substrate stiffness on the phenotype of heart cells," *Biotechnol. Bioeng.*, 2010, doi: 10.1002/bit.22647.

[349] N. Thavandiran *et al.*, "Design and formulation of functional pluripotent stem cell-derived cardiac microtissues," *Proc. Natl. Acad. Sci. U. S. A.*, 2013, doi: 10.1073/pnas.1311120110.

[350] A. J. S. Ribeiro *et al.*, “Contractility of Single cardiomyocytes differentiated from pluripotent stem cells depends on physiological shape and substrate stiffness,” *Proc. Natl. Acad. Sci. U. S. A.*, 2015, doi: 10.1073/pnas.1508073112.

[351] M. Ö. Öztürk-Öncel *et al.*, “Impact of Poly(dimethylsiloxane) Surface Modification with Conventional and Amino Acid-Conjugated Self-Assembled Monolayers on the Differentiation of Induced Pluripotent Stem Cells into Cardiomyocytes,” *ACS Biomater. Sci. Eng.*, vol. 7, no. 4, pp. 1539–1551, Apr. 2021, doi: 10.1021/acsbiomaterials.0c01434.

[352] J. Fu, Y. J. Chuah, J. Liu, S. Y. Tan, and D.-A. Wang, “Respective Effects of Gelatin-Coated Polydimethylsiloxane (PDMS) Substrates on Self-renewal and Cardiac Differentiation of Induced Pluripotent Stem Cells (iPSCs),” *ACS Biomater. Sci. Eng.*, vol. 4, no. 12, pp. 4321–4330, Dec. 2018, doi: 10.1021/acsbiomaterials.8b00993.

[353] J. Fu, Y. J. Chuah, W. T. Ang, N. Zheng, and D.-A. Wang, “Optimization of a polydopamine (PD)-based coating method and polydimethylsiloxane (PDMS) substrates for improved mouse embryonic stem cell (ESC) pluripotency maintenance and cardiac differentiation,” *Biomater. Sci.*, vol. 5, no. 6, pp. 1156–1173, 2017, doi: 10.1039/C7BM00266A.

[354] Q. Tu *et al.*, “Surface modification of poly(dimethylsiloxane) and its applications in microfluidics-based biological analysis,” *Rev. Anal. Chem.*, vol. 31, no. 3–4, Jan. 2012, doi: 10.1515/revac-2012-0016.

[355] I. Mirsky and W. W. Parmley, “Assessment of passive elastic stiffness for isolated heart muscle and the intact heart,” *Circ. Res.*, vol. 33, no. 2, pp. 233–243, 1973, doi: 10.1161/01.RES.33.2.233.

[356] R. Gaetani, E. A. Zizzi, M. A. Deriu, U. Morbiducci, M. Pesce, and E. Messina, “When Stiffness Matters: Mechanosensing in Heart Development and Disease,” *Front. Cell Dev. Biol.*, vol. 8, no. May, pp. 1–16, 2020, doi: 10.3389/fcell.2020.00334.

[357] H. Kanai, “Propagation of spontaneously actuated pulsive vibration in human heart wall and in vivo viscoelasticity estimation,” *IEEE Trans. Ultrason. Ferroelectr. Freq. Control*, vol. 52, no. 11, pp. 1931–1942, 2005, doi: 10.1109/TUFFC.2005.1561662.

[358] A. J. Engler *et al.*, “Elasticity : Scar-Like Rigidity Inhibits Beating,” *J. Cell Sci.*, vol. 121, no. Pt 22, pp. 3794–3802, 2009, doi: 10.1242/jcs.029678.Embryonic.

[359] W. C. Oliver and G. M. Pharr, “Measurement of hardness and elastic modulus by instrumented indentation: Advances in understanding and refinements to methodology,” *J. Mater. Res.*, vol. 19, no. 1, pp. 3–20, 2004, doi: 10.1557/jmr.2004.19.1.3.

[360] R. Agarwal *et al.*, “Filamin C Cardiomyopathy Variants Cause Protein and Lysosome Accumulation,” *Circ. Res.*, pp. 751–766, 2021, doi: 10.1161/CIRCRESAHA.120.317076.

[361] I. Karakikes, M. Ameen, V. Termglinchan, and J. C. Wu, “Human Induced Pluripotent Stem Cell–Derived Cardiomyocytes,” *Circ. Res.*, vol. 117, no. 1, pp. 80–88, Jun. 2015, doi: 10.1161/CIRCRESAHA.117.305365.

[362] A. Skorska *et al.*, “Monitoring the maturation of the sarcomere network: a super-resolution microscopy-based approach,” *Cell. Mol. Life Sci.*, vol. 79, no. 3, p. 149, Mar. 2022, doi: 10.1007/s00018-022-04196-3.

[363] G. Olivetti *et al.*, “Myocyte cellular hypertrophy is responsible for ventricular remodelling in the hypertrophied heart of middle aged individuals in the absence of cardiac failure,” *Cardiovasc. Res.*, vol. 28, no. 8, pp. 1199–1208, Aug. 1994, doi: 10.1093/cvr/28.8.1199.

[364] T. D. Vu and T. Kofidis, “Biomaterials and cells for cardiac tissue engineering,” in *Cardiac Regeneration and Repair*, Elsevier, 2014, pp. 127–179.

[365] M. D. Lemoine *et al.*, “Human Induced Pluripotent Stem Cell-Derived Engineered Heart Tissue as a Sensitive Test System for QT Prolongation and Arrhythmic Triggers,” *Circ. Arrhythmia Electrophysiol.*, vol. 11, no. 7, pp. 1–15, 2018, doi: 10.1161/CIRCEP.117.006035.

[366] S. Hamad *et al.*, “Generation of human induced pluripotent stem cell-derived cardiomyocytes in 2D monolayer and scalable 3D suspension bioreactor cultures with reduced batch-to-batch variations,” *Theranostics*, vol. 9, no. 24, pp. 7222–7238, 2019, doi: 10.7150/thno.32058.

[367] A. Bizy *et al.*, “Myosin light chain 2-based selection of human iPSC-derived early ventricular cardiac myocytes,” *Stem Cell Res.*, 2013, doi: 10.1016/j.scr.2013.09.003.

[368] J. Li, X. Feng, and X. Wei, “Modeling hypertrophic cardiomyopathy with human cardiomyocytes derived from induced pluripotent stem cells,” *Stem Cell Res. Ther.*, vol. 13, no. 1, p. 232, Dec. 2022, doi: 10.1186/s13287-022-02905-0.

[369] T. G. Thompson *et al.*, “Filamin 2 (FLN2): A muscle-specific sarcoglycan interacting protein,” *J. Cell Biol.*, 2000, doi: 10.1083/jcb.148.1.115.

[370] T. K. Pullinger and J. Q. X. Gong, “To their own beat: modelling variability in induced pluripotent stem cell-derived cardiomyocytes,” *J. Physiol.*, vol. 597, no. 20, pp. 5047–5048, Oct. 2019, doi: 10.1113/JP278739.

[371] J. Yang, M. A. Argenziano, M. Burgos Angulo, A. Bertalovitz, M. N. Beidokhti, and T. V. McDonald, “Phenotypic Variability in iPSC-Induced Cardiomyocytes and Cardiac Fibroblasts Carrying Diverse LMNA Mutations,” *Front. Physiol.*, vol. 12, Dec. 2021, doi: 10.3389/fphys.2021.778982.

[372] D. C. Kernik *et al.*, “A computational model of induced pluripotent stem-cell derived cardiomyocytes incorporating experimental variability from multiple data sources,” *J. Physiol.*, vol. 597, no. 17, pp. 4533–4564, Sep. 2019, doi: 10.1113/JP277724.

[373] K. Ufford *et al.*, “Myofibrillar Structural Variability Underlies Contractile Function in Stem Cell-Derived Cardiomyocytes,” *Stem Cell Reports*, vol. 16, no. 3, pp. 470–477, Mar. 2021, doi: 10.1016/j.stemcr.2021.01.007.

[374] M. Uesugi, A. Ojima, T. Taniguchi, N. Miyamoto, and K. Sawada, “Low-density plating is sufficient to induce cardiac hypertrophy and electrical remodeling in highly purified human iPS cell-derived cardiomyocytes,” *J. Pharmacol. Toxicol. Methods*, vol. 69, no. 2, pp. 177–188, Mar. 2014, doi: 10.1016/j.vascn.2013.11.002.

[375] D. Mosqueira, K. Lis-Slimak, and C. Denning, “High-Throughput Phenotyping Toolkit for Characterizing Cellular Models of Hypertrophic Cardiomyopathy In Vitro.,” *Methods Protoc.*, vol. 2, no. 4, Oct. 2019, doi: 10.3390/mps2040083.

[376] K. M. Ng *et al.*, “Empagliflozin Ammeliorates High Glucose Induced-Cardiac Dysfuntion in Human iPSC-Derived Cardiomyocytes,” *Sci. Rep.*, vol. 8, no. 1, pp. 1–13, 2018, doi: 10.1038/s41598-018-33293-2.

[377] C. Deisl, M. Fine, O. W. Moe, and D. W. Hilgemann, “Hypertrophy of human embryonic stem cell–derived cardiomyocytes supported by positive feedback between Ca2+ and diacylglycerol signals,” *Pflügers Arch. - Eur. J. Physiol.*, vol. 471, no. 8, pp. 1143–1157, Aug. 2019, doi: 10.1007/s00424-019-02293-0.

[378] W. E. Knight *et al.*, “Maturation of Pluripotent Stem Cell-Derived Cardiomyocytes Enables Modeling of Human Hypertrophic Cardiomyopathy,” *Stem Cell Reports*, vol. 16, no. 3, pp. 519–533, Mar. 2021, doi: 10.1016/j.stemcr.2021.01.018.

[379] A. Tanaka *et al.*, “Endothelin-1 Induces Myofibrillar Disarray and Contractile Vector Variability in Hypertrophic Cardiomyopathy–Induced Pluripotent Stem Cell–Derived Cardiomyocytes,” *J. Am. Heart Assoc.*, vol. 3, no. 6, Dec. 2014, doi: 10.1161/JAHA.114.001263.

[380] E. Ovchinnikova *et al.*, “Modeling Human Cardiac Hypertrophy in Stem Cell-Derived Cardiomyocytes,” *Stem Cell Reports*, vol. 10, no. 3, pp. 794–807, 2018, doi: 10.1016/j.stemcr.2018.01.016.

[381] K. Bourque *et al.*, “Measuring hypertrophy in neonatal rat primary cardiomyocytes and human iPSC-derived cardiomyocytes,” *Methods*, vol. 203, pp. 447–464, Jul. 2022, doi: 10.1016/j.ymeth.2021.12.006.

[382] E. M. Higgins, J. M. Bos, S. M. Dotzler, C. John Kim, and M. J. Ackerman, “MRAS Variants Cause Cardiomyocyte Hypertrophy in Patient-Specific Induced Pluripotent Stem Cell-Derived Cardiomyocytes,” *Circ. Genomic Precis. Med.*, vol. 12, no. 11, Nov. 2019, doi: 10.1161/CIRCGEN.119.002648.

[383] C. N. Toepfer *et al.*, “Myosin Sequestration Regulates Sarcomere Function, Cardiomyocyte Energetics, and Metabolism, Informing the Pathogenesis of Hypertrophic Cardiomyopathy,” *Circulation*, vol. 141, no. 10, pp. 828–842, Mar. 2020, doi: 10.1161/CIRCULATIONAHA.119.042339.

[384] J. G. W. W. Smith *et al.*, “Isogenic Pairs of hiPSC-CMs with Hypertrophic Cardiomyopathy/LVNC-Associated ACTC1 E99K Mutation Unveil Differential Functional Deficits,” *Stem Cell Reports*, vol. 11, no. 5, pp. 1226–1243, Nov. 2018, doi: 10.1016/j.stemcr.2018.10.006.

[385] K. Agostinucci *et al.*, “Divergent Cardiac Effects of Angiotensin II and Isoproterenol Following Juvenile Exposure to Doxorubicin,” *Front. Cardiovasc. Med.*, vol. 9, Mar. 2022, doi: 10.3389/fcvm.2022.742193.

[386] M. Goßmann *et al.*, “Integration of mechanical conditioning into a high throughput contractility assay for cardiac safety assessment.,” *J. Pharmacol. Toxicol. Methods*, vol. 105, p. 106892, Sep. 2020, doi: 10.1016/j.vascn.2020.106892.

[387] S. Vučković *et al.*, “Characterization of cardiac metabolism in iPSC-derived cardiomyocytes: lessons from maturation and disease modeling,” *Stem Cell Res. Ther.*, vol. 13, no. 1, p. 332, Dec. 2022, doi: 10.1186/s13287-022-03021-9.

[388] A. C. Cardoso *et al.*, “Mitochondrial Substrate Utilization Regulates Cardiomyocyte Cell Cycle Progression.,” *Nat. Metab.*, vol. 2, no. 2, pp. 167–178, 2020, [Online]. Available: http://www.ncbi.nlm.nih.gov/pubmed/32617517.

[389] N. M. Stege, R. A. de Boer, M. P. van den Berg, and H. H. W. Silljé, “The Time Has Come to Explore Plasma Biomarkers in Genetic Cardiomyopathies,” *Int. J. Mol. Sci.*, vol. 22, no. 6, p. 2955, Mar. 2021, doi: 10.3390/ijms22062955.

[390] H. Taegtmeyer, S. Sen, and D. Vela, “Return to the fetal gene program,” *Ann. N. Y. Acad. Sci.*, vol. 1188, no. 1, pp. 191–198, Feb. 2010, doi: 10.1111/j.1749-6632.2009.05100.x.

[391] M. J. Ranek, M. J. Stachowski, J. A. Kirk, and M. S. Willis, “The role of heat shock proteins and co-chaperones in heart failure,” *Philos. Trans. R. Soc. B Biol. Sci.*, vol. 373,

no. 1738, p. 20160530, Jan. 2018, doi: 10.1098/rstb.2016.0530.

[392] M. Gherghiceanu *et al.*, "Cardiomyocytes derived from human embryonic and induced pluripotent stem cells: comparative ultrastructure," *J. Cell. Mol. Med.*, vol. 15, no. 11, pp. 2539–2551, Nov. 2011, doi: 10.1111/j.1582-4934.2011.01417.x.

[393] M. Delmar, "Connexin43 regulates sodium current; ankyrin-G modulates gap junctions: the intercalated disc exchanger," *Cardiovasc. Res.*, vol. 93, no. 2, pp. 220–222, Feb. 2012, doi: 10.1093/cvr/cvr343.

[394] A. Vreeker, L. van Stuijvenberg, T. J. Hund, P. J. Mohler, P. G. J. Nikkels, and T. A. B. van Veen, "Assembly of the Cardiac Intercalated Disk during Pre- and Postnatal Development of the Human Heart," *PLoS One*, vol. 9, no. 4, p. e94722, Apr. 2014, doi: 10.1371/journal.pone.0094722.

[395] E. D. van Deel *et al.*, "In vitro model to study the effects of matrix stiffening on Ca 2+ handling and myofilament function in isolated adult rat cardiomyocytes," *J. Physiol.*, vol. 595, no. 14, pp. 4597–4610, Jul. 2017, doi: 10.1113/JP274460.

[396] A. Saraste and K. Pulkki, "Morphologic and biochemical hallmarks of apoptosis," *Cardiovasc. Res.*, vol. 45, no. 3, pp. 528–537, 2000, doi: 10.1016/S0008-6363(99)00384-3.

[397] J. D. Ly, D. R. Grubb, and A. Lawen, "The mitochondrial membrane potential (δψm) in apoptosis; an update," *Apoptosis*, vol. 8, no. 2, pp. 115–128, 2003, doi: 10.1023/A:1022945107762.

[398] L. Binó *et al.*, "Hypoxia favors myosin heavy chain beta gene expression in an Hif-1alpha-dependent manner," *Oncotarget*, 2017, doi: 10.18632/oncotarget.19016.

[399] S. Li *et al.*, "Mitochondrial Dysfunctions Contribute to Hypertrophic Cardiomyopathy in Patient iPSC-Derived Cardiomyocytes with MT-RNR2 Mutation," *Stem Cell Reports*, vol. 10, no. 3, pp. 808–821, 2018, doi: 10.1016/j.stemcr.2018.01.013.

[400] D. M. Lyra-Leite *et al.*, "Mitochondrial function in engineered cardiac tissues is regulated by extracellular matrix elasticity and tissue alignment," *Am. J. Physiol. Circ. Physiol.*, vol. 313, no. 4, pp. H757–H767, Oct. 2017, doi: 10.1152/ajpheart.00290.2017.

[401] G. Jung *et al.*, "Time-dependent evolution of functional vs. remodeling signaling in induced pluripotent stem cell-derived cardiomyocytes and induced maturation with biomechanical stimulation," *FASEB J.*, vol. 30, no. 4, pp. 1464–1479, Apr. 2016, doi: 10.1096/fj.15-280982.

[402] A. Signalling *et al.*, "Age-Dependent Maturation of iPSC-CMs Leads to the Enhanced Compartmentation of," *Cells*, 2020.

[403] F. Pillekamp *et al.*, "Contractile properties of early human embryonic stem cell-derived cardiomyocytes: beta-adrenergic stimulation induces positive chronotropy and lusitropy but not inotropy.," *Stem Cells Dev.*, vol. 21, no. 12, pp. 2111–21, Aug. 2012, doi: 10.1089/scd.2011.0312.

[404] C. Kane and C. M. Terracciano, "Induced pluripotent stem cell-derived cardiac myocytes to understand and test calcium handling: Pie in the sky?," *J. Mol. Cell. Cardiol.*, vol. 89, pp. 376–378, Dec. 2015, doi: 10.1016/j.yjmcc.2015.10.023.

[405] S. Li, G. Chen, and R. A. Li, "Calcium signalling of human pluripotent stem cell-derived cardiomyocytes," *J. Physiol.*, vol. 591, no. 21, pp. 5279–5290, Nov. 2013, doi: 10.1113/jphysiol.2013.256495.

[406] R. Schick *et al.*, “Functional abnormalities in induced pluripotent stem cell-derived cardiomyocytes generated from titin-mutated patients with dilated cardiomyopathy,” *PLoS One*, 2018, doi: 10.1371/journal.pone.0205719.

[407] H. Wu *et al.*, “Modelling diastolic dysfunction in induced pluripotent stem cell-derived cardiomyocytes from hypertrophic cardiomyopathy patients,” *Eur. Heart J.*, vol. 40, no. 45, pp. 3685–3695, Dec. 2019, doi: 10.1093/eurheartj/ehz326.

[408] J. T. Koivumäki *et al.*, “Structural Immaturity of Human iPSC-Derived Cardiomyocytes: In Silico Investigation of Effects on Function and Disease Modeling,” *Front. Physiol.*, vol. 9, Feb. 2018, doi: 10.3389/fphys.2018.00080.

[409] F. Margara, Y. Psaras, Z. J. Wang, and M. Schmid, “Human iPSC-CMs and in-silico technologies define mechanisms and accelerate targeted pharmacogenetics in hypertrophic cardiomyopathy,” *bioRxiv Prepr.*, pp. 1–34, 2022, doi: 10.1101/2022.06.08.495324.

[410] F. Domínguez *et al.*, “Dilated Cardiomyopathy Due to BLC2-Associated Athanogene 3 (BAG3) Mutations,” *J. Am. Coll. Cardiol.*, vol. 72, no. 20, pp. 2471–2481, Nov. 2018, doi: 10.1016/j.jacc.2018.08.2181.

[411] T. Knezevic *et al.*, “BAG3: a new player in the heart failure paradigm,” *Heart Fail. Rev.*, vol. 20, no. 4, pp. 423–434, Jul. 2015, doi: 10.1007/s10741-015-9487-6.

[412] A. Ulbricht and J. Höhfeld, “Tension-induced autophagy: May the chaperone be with you,” *Autophagy*, 2013, doi: 10.4161/auto.24213.

[413] M. Sardiello *et al.*, “A Gene Network Regulating Lysosomal Biogenesis and Function,” *Science (80-.).*, vol. 325, no. 5939, pp. 473–477, Jul. 2009, doi: 10.1126/science.1174447.

[414] T. G. Martin *et al.*, “Cardiomyocyte contractile impairment in heart failure results from reduced BAG3-mediated sarcomeric protein turnover,” *Nat. Commun.*, vol. 12, no. 1, p. 2942, Dec. 2021, doi: 10.1038/s41467-021-23272-z.

[415] X. Fang *et al.*, “Loss-of-function mutations in co-chaperone BAG3 destabilize small HSPs and cause cardiomyopathy,” *J. Clin. Invest.*, vol. 127, no. 8, pp. 3189–3200, Jul. 2017, doi: 10.1172/JCI94310.

[416] J. Li *et al.*, “HSPA12B attenuates cardiac dysfunction and remodelling after myocardial infarction through an eNOS-dependent mechanism,” *Cardiovasc. Res.*, vol. 99, no. 4, pp. 674–684, Sep. 2013, doi: 10.1093/cvr/cvt139.

[417] D. Morin *et al.*, “Hsp22 overexpression induces myocardial hypertrophy, senescence and reduced life span through enhanced oxidative stress,” *Free Radic. Biol. Med.*, vol. 137, pp. 194–200, Jun. 2019, doi: 10.1016/j.freeradbiomed.2019.04.035.

[418] R. Schröder and B. Schoser, “Myofibrillar myopathies: A clinical and myopathological guide: Mini-symposium: Protein aggregate myopathies,” 2009, doi: 10.1111/j.1750-3639.2009.00289.x.

[419] H. Morita *et al.*, “Shared genetic causes of cardiac hypertrophy in children and adults,” *N. Engl. J. Med.*, 2008, doi: 10.1056/NEJMoa075463.

[420] J. P. Kaski *et al.*, “Prevalence of sarcomere protein gene mutations in preadolescent children with hypertrophic cardiomyopathy,” *Circ. Cardiovasc. Genet.*, 2009, doi: 10.1161/CIRCGENETICS.108.821314.

[421] C. Hang *et al.*, “Knockout of MYOM1 in human cardiomyocytes leads to myocardial atrophy via impairing calcium homeostasis,” *J. Cell. Mol. Med.*, vol. 25, no. 3, pp. 1661–

1676, Feb. 2021, doi: 10.1111/jcmm.16268.

[422] A. Osio *et al.*, “Myozenin 2 Is a Novel Gene for Human Hypertrophic Cardiomyopathy,” *Circ. Res.*, vol. 100, no. 6, pp. 766–768, Mar. 2007, doi: 10.1161/01.RES.0000263008.66799.aa.

[423] S. Kebir *et al.*, “Sarcomeric lesions and remodeling proximal to intercalated disks in overload-induced cardiac hypertrophy,” *Exp. Cell Res.*, vol. 348, no. 1, pp. 95–105, Oct. 2016, doi: 10.1016/j.yexcr.2016.09.008.

[424] L. Huang *et al.*, “Critical Roles of Xirp Proteins in Cardiac Conduction and Their Rare Variants Identified in Sudden Unexplained Nocturnal Death Syndrome and Brugada Syndrome in Chinese Han Population.,” *J. Am. Heart Assoc.*, vol. 7, no. 1, 2018, doi: 10.1161/JAHA.117.006320.

[425] E. A. Despond and J. F. Dawson, “Classifying Cardiac Actin Mutations Associated With Hypertrophic Cardiomyopathy,” *Front. Physiol.*, vol. 9, Apr. 2018, doi: 10.3389/fphys.2018.00405.

[426] D. M. Gopal *et al.*, “Serum albumin concentration and heart failure risk,” *Am. Heart J.*, vol. 160, no. 2, pp. 279–285, Aug. 2010, doi: 10.1016/j.ahj.2010.05.022.

[427] U. Gergs *et al.*, “Alterations of protein expression of phospholamban, ZASP and plakoglobin in human atria in subgroups of seniors,” *Sci. Rep.*, 2019, doi: 10.1038/s41598-019-42141-w.

[428] G. T. Schuyler and L. R. Yarbrough, “Changes in myosin and creatine kinase mRNA levels with cardiac hypertrophy and hypothyroidism,” *Basic Res. Cardiol.*, vol. 85, no. 5, pp. 481–494, Sep. 1990, doi: 10.1007/BF01931494.

[429] X. Hua *et al.*, “Multi-level transcriptome sequencing identifies COL1A1 as a candidate marker in human heart failure progression,” *BMC Med.*, vol. 18, no. 1, p. 2, Dec. 2020, doi: 10.1186/s12916-019-1469-4.

[430] J. Wang and W. Pan, “The Biological Role of the Collagen Alpha-3 (VI) Chain and Its Cleaved C5 Domain Fragment Endotrophin in Cancer,” *Onco. Targets. Ther.*, vol. Volume 13, pp. 5779–5793, Jun. 2020, doi: 10.2147/OTT.S256654.

[431] B.-X. Tian, W. Sun, S.-H. Wang, P.-J. Liu, and Y.-C. Wang, “Differential expression and clinical significance of COX6C in human diseases.,” *Am. J. Transl. Res.*, vol. 13, no. 1, pp. 1–10, 2021, [Online]. Available: http://www.ncbi.nlm.nih.gov/pubmed/33527004.

[432] A. Ruparelia, R. Vaz, and R. Bryson-Richardso, “Myofibrillar Myopathies and the Z-Disk Associated Proteins,” in *Skeletal Muscle - From Myogenesis to Clinical Relations*, InTech, 2012.

[433] D. Ma *et al.*, “Generation of patient-specific induced pluripotent stem cell-derived cardiomyocytes as a cellular model of arrhythmogenic right ventricular cardiomyopathy,” *Eur. Heart J.*, vol. 34, no. 15, pp. 1122–1133, Apr. 2013, doi: 10.1093/eurheartj/ehs226.

[434] J. Aalders *et al.*, “Effects of fibrillin mutations on the behavior of heart muscle cells in Marfan syndrome,” *Sci. Rep.*, vol. 10, no. 1, p. 16756, Dec. 2020, doi: 10.1038/s41598-020-73802-w.

[435] J. W. Miklas *et al.*, “TFPa/HADHA is required for fatty acid beta-oxidation and cardiolipin re-modeling in human cardiomyocytes,” *Nat. Commun.*, vol. 10, no. 1, p. 4671, Dec. 2019, doi: 10.1038/s41467-019-12482-1.

[436] Y. Feng, N. B. Madungwe, and J. C. Bopassa, “Mitochondrial inner membrane protein, Mic60/mitofilin in mammalian organ protection,” *J. Cell. Physiol.*, vol. 234, no. 4, pp. 3383–3393, Apr. 2019, doi: 10.1002/jcp.27314.

[437] P. Ruiz *et al.*, “Targeted mutation of plakoglobin in mice reveals essential functions of desmosomes in the embryonic heart.,” *J. Cell Biol.*, vol. 135, no. 1, pp. 215–225, Oct. 1996, doi: 10.1083/jcb.135.1.215.

[438] Y. Kabeya, “LC3, a mammalian homologue of yeast Apg8p, is localized in autophagosome membranes after processing,” *EMBO J.*, vol. 19, no. 21, pp. 5720–5728, Nov. 2000, doi: 10.1093/emboj/19.21.5720.

[439] S. Schiaffino and C. Reggiani, “Molecular diversity of myofibrillar proteins: gene regulation and functional significance.,” *Physiol. Rev.*, vol. 76, no. 2, pp. 371–423, Apr. 1996, doi: 10.1152/physrev.1996.76.2.371.

[440] D. P. S. Osborn *et al.*, “Autosomal recessive cardiomyopathy and sudden cardiac death associated with variants in MYL3,” *Genet. Med.*, vol. 23, no. 4, pp. 787–792, Apr. 2021, doi: 10.1038/s41436-020-01028-2.

[441] J. Sun *et al.*, “Distinct Roles of Smooth Muscle and Non-muscle Myosin Light Chain-Mediated Smooth Muscle Contraction,” *Front. Physiol.*, vol. 11, Dec. 2020, doi: 10.3389/fphys.2020.593966.

[442] A. Perrot *et al.*, “Mutations in NEBL encoding the cardiac Z-disk protein nebulette are associated with various cardiomyopathies,” *Arch. Med. Sci.*, vol. 2, pp. 263–278, 2016, doi: 10.5114/aoms.2016.59250.

[443] M. N. Bainbridge *et al.*, “Loss of Function Mutations in NNT Are Associated With Left Ventricular Noncompaction,” *Circ. Cardiovasc. Genet.*, vol. 8, no. 4, pp. 544–552, Aug. 2015, doi: 10.1161/CIRCGENETICS.115.001026.

[444] S. M. Perez, L. T. Brinton, and K. A. Kelly, “Plectin in Cancer: From Biomarker to Therapeutic Target,” *Cells*, vol. 10, no. 9, p. 2246, Aug. 2021, doi: 10.3390/cells10092246.

[445] L. Rochette, A. Meloux, M. Zeller, G. Malka, Y. Cottin, and C. Vergely, “Mitochondrial SLC25 Carriers: Novel Targets for Cancer Therapy,” *Molecules*, vol. 25, no. 10, p. 2417, May 2020, doi: 10.3390/molecules25102417.

[446] C.-P. Hsiao, D. Wang, A. Kaushal, and L. Saligan, “Mitochondria-Related Gene Expression Changes Are Associated With Fatigue in Patients With Nonmetastatic Prostate Cancer Receiving External Beam Radiation Therapy,” *Cancer Nurs.*, vol. 36, no. 3, pp. 189–197, May 2013, doi: 10.1097/NCC.0b013e318263f514.

[447] V. Joshi, A. Amanullah, A. Upadhyay, R. Mishra, A. Kumar, and A. Mishra, “A Decade of Boon or Burden: What Has the CHIP Ever Done for Cellular Protein Quality Control Mechanism Implicated in Neurodegeneration and Aging?,” *Front. Mol. Neurosci.*, vol. 9, Oct. 2016, doi: 10.3389/fnmol.2016.00093.

[448] R. Hassoun *et al.*, “De Novo Missense Mutations in TNNC1 and TNNI3 Causing Severe Infantile Cardiomyopathy Affect Myofilament Structure and Function and Are Modulated by Troponin Targeting Agents.,” *Int. J. Mol. Sci.*, vol. 22, no. 17, Sep. 2021, doi: 10.3390/ijms22179625.

[449] L. M. Dorsch *et al.*, “The effect of tropomyosin variants on cardiomyocyte function and structure that underlie different clinical cardiomyopathy phenotypes,” *Int. J. Cardiol.*, vol. 323, pp. 251–258, Jan. 2021, doi: 10.1016/j.ijcard.2020.08.101.

[450] F. Mastorci, L. Sabatino, C. Vassalle, and A. Pingitore, “Cardioprotection and Thyroid Hormones in the Clinical Setting of Heart Failure,” *Front. Endocrinol. (Lausanne).*, vol. 10, Jan. 2020, doi: 10.3389/fendo.2019.00927.

[451] K. M. Ridge, J. E. Eriksson, M. Pekny, and R. D. Goldman, “Roles of vimentin in health and disease,” *Genes Dev.*, vol. 36, no. 7–8, pp. 391–407, Apr. 2022, doi: 10.1101/gad.349358.122.

[452] “No Title.”

[453] I. Tanida, “Autophagosome Formation and Molecular Mechanism of Autophagy,” *Antioxid. Redox Signal.*, vol. 14, no. 11, pp. 2201–2214, Jun. 2011, doi: 10.1089/ars.2010.3482.

[454] M. Mauthe *et al.*, “Chloroquine inhibits autophagic flux by decreasing autophagosome-lysosome fusion.,” *Autophagy*, vol. 14, no. 8, pp. 1435–1455, 2018, doi: 10.1080/15548627.2018.1474314.

[455] J. Pu, C. M. Guardia, T. Keren-Kaplan, and J. S. Bonifacino, “Mechanisms and functions of lysosome positioning.,” *J. Cell Sci.*, vol. 129, no. 23, pp. 4329–4339, 2016, doi: 10.1242/jcs.196287.

[456] C. M. Guardia, G. G. Farías, R. Jia, J. Pu, and J. S. Bonifacino, “BORC Functions Upstream of Kinesins 1 and 3 to Coordinate Regional Movement of Lysosomes along Different Microtubule Tracks,” *Cell Rep.*, vol. 17, no. 8, pp. 1950–1961, Nov. 2016, doi: 10.1016/j.celrep.2016.10.062.

[457] P. M. McLendon and J. Robbins, “Desmin-related cardiomyopathy: an unfolding story,” *Am. J. Physiol. Circ. Physiol.*, vol. 301, no. 4, pp. H1220–H1228, Oct. 2011, doi: 10.1152/ajpheart.00601.2011.

[458] C. Karabiyik, M. Vicinanza, S. M. Son, and D. C. Rubinsztein, “Glucose starvation induces autophagy via ULK1-mediated activation of PIKfyve in an AMPK-dependent manner,” *Dev. Cell*, vol. 56, no. 13, pp. 1961-1975.e5, Jul. 2021, doi: 10.1016/j.devcel.2021.05.010.

[459] I. Dikic and Z. Elazar, “Mechanism and medical implications of mammalian autophagy,” *Nat. Rev. Mol. Cell Biol.*, vol. 19, no. 6, pp. 349–364, Jun. 2018, doi: 10.1038/s41580-018-0003-4.

[460] C. Pohl and I. Dikic, “Cellular quality control by the ubiquitin-proteasome system and autophagy,” *Science (80-.).*, vol. 366, no. 6467, pp. 818–822, Nov. 2019, doi: 10.1126/science.aax3769.

[461] J. S. Stephan, Y.-Y. Yeh, V. Ramachandran, S. J. Deminoff, and P. K. Herman, “The Tor and PKA signaling pathways independently target the Atg1/Atg13 protein kinase complex to control autophagy,” *Proc. Natl. Acad. Sci.*, vol. 106, no. 40, pp. 17049–17054, Oct. 2009, doi: 10.1073/pnas.0903316106.

[462] F. Samad *et al.*, “Malignant cardiac phenotypic expression of Danon disease (LAMP2 cardiomyopathy),” *Int. J. Cardiol.*, vol. 245, pp. 201–206, Oct. 2017, doi: 10.1016/j.ijcard.2017.06.031.

[463] K.-M. Ng *et al.*, “Amelioration of X-Linked Related Autophagy Failure in Danon Disease With DNA Methylation Inhibitor,” *Circulation*, vol. 134, no. 18, pp. 1373–1389, Nov. 2016, doi: 10.1161/CIRCULATIONAHA.115.019847.

[464] M. T. Quintana *et al.*, “Cardiomyocyte-Specific Human Bcl2-Associated Anthanogene 3 P209L Expression Induces Mitochondrial Fragmentation, Bcl2-Associated Anthanogene 3 Haploinsufficiency, and Activates p38 Signaling,” *Am. J. Pathol.*, vol. 186, no. 8, pp. 1989–

2007, Aug. 2016, doi: 10.1016/j.ajpath.2016.03.017.

[465] W. Mizushima and J. Sadoshima, “BAG3 plays a central role in proteostasis in the heart,” *Journal of Clinical Investigation*. 2017, doi: 10.1172/JCI95839.

[466] T. Arimura, T. Ishikawa, S. Nunoda, S. Kawai, and A. Kimura, “Dilated cardiomyopathy-associated BAG3 mutations impair Z-disc assembly and enhance sensitivity to apoptosis in cardiomyocytes,” *Hum. Mutat.*, 2011, doi: 10.1002/humu.21603.

[467] M. G. Pagliuca, R. Lerose, S. Cigliano, and A. Leone, “Regulation by heavy metals and temperature of the human BAG-3 gene, a modulator of Hsp70 activity,” *FEBS Lett.*, vol. 541, no. 1–3, pp. 11–15, Apr. 2003, doi: 10.1016/S0014-5793(03)00274-6.

[468] Q. Kong *et al.*, “HSPA12B Attenuated Acute Myocardial Ischemia/reperfusion Injury via Maintaining Endothelial Integrity in a PI3K/Akt/mTOR-dependent Mechanism,” *Sci. Rep.*, vol. 6, no. 1, p. 33636, Dec. 2016, doi: 10.1038/srep33636.

[469] M. Fan *et al.*, “Endothelial cell HSPA12B and yes-associated protein cooperatively regulate angiogenesis following myocardial infarction,” *JCI Insight*, vol. 5, no. 18, Sep. 2020, doi: 10.1172/jci.insight.139640.

[470] C. Garrido, S. Gurbuxani, L. Ravagnan, and G. Kroemer, “Heat Shock Proteins: Endogenous Modulators of Apoptotic Cell Death,” *Biochem. Biophys. Res. Commun.*, vol. 286, no. 3, pp. 433–442, Aug. 2001, doi: 10.1006/bbrc.2001.5427.

[471] C. C. Gonçalves, I. Sharon, T. M. Schmeing, C. H. I. Ramos, and J. C. Young, “The chaperone HSPB1 prepares protein aggregates for resolubilization by HSP70,” *Sci. Rep.*, vol. 11, no. 1, p. 17139, Dec. 2021, doi: 10.1038/s41598-021-96518-x.

[472] F. F. Morelli *et al.*, “An interaction study in mammalian cells demonstrates weak binding of HSPB2 to BAG3, which is regulated by HSPB3 and abrogated by HSPB8,” *Cell Stress Chaperones*, vol. 22, no. 4, pp. 531–540, Jul. 2017, doi: 10.1007/s12192-017-0769-x.

[473] F. G. Tahrir *et al.*, “Evidence for the Role of BAG3 in Mitochondrial Quality Control in Cardiomyocytes,” *J. Cell. Physiol.*, vol. 232, no. 4, pp. 797–805, Apr. 2017, doi: 10.1002/jcp.25476.

[474] Y. Duan, H. Tang, K. Mitchell-silbaugh, X. Fang, Z. Han, and K. Ouyang, “Heat Shock Protein 60 in Cardiovascular Physiology and Diseases,” *Front. Mol. Biosci.*, vol. 7, Apr. 2020, doi: 10.3389/fmolb.2020.00073.

[475] N. Xu *et al.*, “Ube2v1 Positively Regulates Protein Aggregation by Modulating Ubiquitin Proteasome System Performance Partially Through K63 Ubiquitination,” *Circ. Res.*, vol. 126, no. 7, pp. 907–922, Mar. 2020, doi: 10.1161/CIRCRESAHA.119.316444.

[476] U. Esslinger *et al.*, “Exome-wide association study reveals novel susceptibility genes to sporadic dilated cardiomyopathy,” *PLoS One*, vol. 12, no. 3, p. e0172995, Mar. 2017, doi: 10.1371/journal.pone.0172995.

[477] T. S. Wales, D. Yang, G. John, F. Ali, A. Blais, and J. C. McDermott, “Regulation of Hspb7 by MEF2 and AP-1: implications for Hspb7 in muscle atrophy,” *J. Cell Sci.*, Jan. 2016, doi: 10.1242/jcs.190009.

[478] X. Fang, J. Bogomolovas, C. Trexler, and J. Chen, “The BAG3-dependent and -independent roles of cardiac small heat shock proteins,” *JCI insight*. 2019, doi: 10.1172/jci.insight.126464.

[479] E. V. Mymrikov, M. Daake, B. Richter, M. Haslbeck, and J. Buchner, “The Chaperone

Activity and Substrate Spectrum of Human Small Heat Shock Proteins," *J. Biol. Chem.*, vol. 292, no. 2, pp. 672–684, Jan. 2017, doi: 10.1074/jbc.M116.760413.

[480] E. Eenjes, J. M. Dragich, H. H. Kampinga, and A. Yamamoto, "Distinguishing aggregate formation and aggregate clearance using cell based assays," *J. Cell Sci.*, Jan. 2016, doi: 10.1242/jcs.179978.

[481] P. Doran, G. Martin, P. Dowling, H. Jockusch, and K. Ohlendieck, "Proteome analysis of the dystrophin-deficient MDX diaphragm reveals a drastic increase in the heat shock protein cvHSP," *Proteomics*, vol. 6, no. 16, pp. 4610–4621, Aug. 2006, doi: 10.1002/pmic.200600082.

[482] H. Brinkmeier and K. Ohlendieck, "Chaperoning heat shock proteins: Proteomic analysis and relevance for normal and dystrophin-deficient muscle," *PROTEOMICS - Clin. Appl.*, vol. 8, no. 11–12, pp. 875–895, Dec. 2014, doi: 10.1002/prca.201400015.

[483] L. K. Muranova, V. M. Shatov, A. V. Slushchev, and N. B. Gusev, "Quaternary Structure and Hetero-Oligomerization of Recombinant Human Small Heat Shock Protein HspB7 (cvHsp)," *Int. J. Mol. Sci.*, vol. 22, no. 15, p. 7777, Jul. 2021, doi: 10.3390/ijms22157777.

[484] S. Mysling, R. Salbo, M. Ploug, and T. J. D. Jørgensen, "Electrochemical Reduction of Disulfide-Containing Proteins for Hydrogen/Deuterium Exchange Monitored by Mass Spectrometry," *Anal. Chem.*, vol. 86, no. 1, pp. 340–345, Jan. 2014, doi: 10.1021/ac403269a.

[485] M. Papadakis, S. Sharma, S. Cox, M. N. Sheppard, V. F. Panoulas, and E. R. Behr, "The magnitude of sudden cardiac death in the young: a death certificate-based review in England and Wales.," *Europace*, vol. 11, no. 10, pp. 1353–8, Oct. 2009, doi: 10.1093/europace/eup229.

[486] J. Schubert, M. Tariq, G. Geddes, S. Kindel, E. M. Miller, and S. M. Ware, "Novel pathogenic variants in filamin C identified in pediatric restrictive cardiomyopathy," *Hum. Mutat.*, 2018, doi: 10.1002/humu.23661.

[487] A. Roldán-Sevilla *et al.*, "Missense Mutations in the FLNC Gene Causing Familial Restrictive Cardiomyopathy," *Circ. Genomic Precis. Med.*, vol. 12, no. 3, Mar. 2019, doi: 10.1161/CIRCGEN.118.002388.

[488] X. Sun and S. S. Nunes, "Bioengineering Approaches to Mature Human Pluripotent Stem Cell-Derived Cardiomyocytes," *Front. Cell Dev. Biol.*, vol. 5, Mar. 2017, doi: 10.3389/fcell.2017.00019.

[489] R. R. Besser, M. Ishahak, V. Mayo, D. Carbonero, I. Claure, and A. Agarwal, "Engineered Microenvironments for Maturation of Stem Cell Derived Cardiac Myocytes," *Theranostics*, vol. 8, no. 1, pp. 124–140, 2018, doi: 10.7150/thno.19441.

[490] D. Rajamohan *et al.*, "Current status of drug screening and disease modelling in human pluripotent stem cells.," *Bioessays*, vol. 35, no. 3, pp. 281–98, Mar. 2013, doi: 10.1002/bies.201200053.

[491] Z. Mao and F. Nakamura, "Structure and Function of Filamin C in the Muscle Z-Disc.," *Int. J. Mol. Sci.*, vol. 21, no. 8, Apr. 2020, doi: 10.3390/ijms21082696.

[492] I. V. Düzen *et al.*, "Leukocyte TRP channel gene expressions in patients with non-valvular atrial fibrillation," *Sci. Rep.*, vol. 7, no. 1, p. 9272, Dec. 2017, doi: 10.1038/s41598-017-10039-0.

[493] A. R. Harper *et al.*, "Common genetic variants and modifiable risk factors underpin

hypertrophic cardiomyopathy susceptibility and expressivity," *Nat. Genet.*, vol. 53, no. 2, pp. 135–142, Feb. 2021, doi: 10.1038/s41588-020-00764-0.

[494] J. Huo, F. Wei, C. Cai, B. Lyn-Cook, and L. Pang, "Sex-Related Differences in Drug-Induced QT Prolongation and Torsades de Pointes: A New Model System with Human iPSC-CMs," *Toxicol. Sci.*, Sep. 2018, doi: 10.1093/toxsci/kfy239.

[495] M. L. Rodriguez *et al.*, "Substrate Stiffness, Cell Anisotropy, and Cell–Cell Contact Contribute to Enhanced Structural and Calcium Handling Properties of Human Embryonic Stem Cell-Derived Cardiomyocytes," *ACS Biomater. Sci. Eng.*, vol. 5, no. 8, pp. 3876–3888, Aug. 2019, doi: 10.1021/acsbiomaterials.8b01256.

[496] N. Geifman and E. Rubin, "The Mouse Age Phenome Knowledgebase and Disease-Specific Inter-Species Age Mapping," *PLoS One*, vol. 8, no. 12, p. e81114, Dec. 2013, doi: 10.1371/journal.pone.0081114.

[497] S. Marston, O. Copeland, K. Gehmlich, S. Schlossarek, L. Carrier, and L. Carrrier, "How do MYBPC3 mutations cause hypertrophic cardiomyopathy?," *J. Muscle Res. Cell Motil.*, vol. 33, no. 1, pp. 75–80, May 2012, doi: 10.1007/s10974-011-9268-3.

[498] X. J. Du, X. M. Gao, B. Wang, G. L. Jennings, E. A. Woodcock, and A. M. Dart, "Age-dependent cardiomyopathy and heart failure phenotype in mice overexpressing beta(2)-adrenergic receptors in the heart.," *Cardiovasc. Res.*, vol. 48, no. 3, pp. 448–54, Dec. 2000, doi: 10.1016/s0008-6363(00)00187-5.

[499] H. Zeng, V. R. Vaka, X. He, G. W. Booz, and J. Chen, "High-fat diet induces cardiac remodelling and dysfunction: assessment of the role played by <scp>SIRT</scp> 3 loss," *J. Cell. Mol. Med.*, vol. 19, no. 8, pp. 1847–1856, Aug. 2015, doi: 10.1111/jcmm.12556.

[500] A. G. Kleber and J. E. Saffitz, "Role of the intercalated disc in cardiac propagation and arrhythmogenesis," *Front. Physiol.*, vol. 5, Oct. 2014, doi: 10.3389/fphys.2014.00404.

[501] L. Mosca, E. Barrett-Connor, and N. K. Wenger, "Sex/gender differences in cardiovascular disease prevention: what a difference a decade makes.," *Circulation*, vol. 124, no. 19, pp. 2145–54, Nov. 2011, doi: 10.1161/CIRCULATIONAHA.110.968792.

[502] A. H. E. M. Maas and Y. E. A. Appelman, "Gender differences in coronary heart disease.," *Neth. Heart J.*, vol. 18, no. 12, pp. 598–602, Dec. 2010, doi: 10.1007/s12471-010-0841-y.

[503] H. Den Ruijter, "Sex and Gender Matters to the Heart," *Front. Cardiovasc. Med.*, vol. 7, Nov. 2020, doi: 10.3389/fcvm.2020.587888.

[504] S. H. Bots, S. A. E. Peters, and M. Woodward, "Sex differences in coronary heart disease and stroke mortality: a global assessment of the effect of ageing between 1980 and 2010," *BMJ Glob. Heal.*, vol. 2, no. 2, p. e000298, Mar. 2017, doi: 10.1136/bmjgh-2017-000298.

[505] A. M. Hawkridge, "CHAPTER 1. Practical Considerations and Current Limitations in Quantitative Mass Spectrometry-based Proteomics," 2014, pp. 1–25.

[506] K. A. McGurk *et al.*, "The use of missing values in proteomic data-independent acquisition mass spectrometry to enable disease activity discrimination," *Bioinformatics*, vol. 36, no. 7, pp. 2217–2223, Apr. 2020, doi: 10.1093/bioinformatics/btz898.

[507] C. Lazar, L. Gatto, M. Ferro, C. Bruley, and T. Burger, "Accounting for the Multiple Natures of Missing Values in Label-Free Quantitative Proteomics Data Sets to Compare Imputation Strategies," *J. Proteome Res.*, vol. 15, no. 4, pp. 1116–1125, Apr. 2016, doi: 10.1021/acs.jproteome.5b00981.

[508] B.-J. M. Webb-Robertson *et al.*, “Review, Evaluation, and Discussion of the Challenges of Missing Value Imputation for Mass Spectrometry-Based Label-Free Global Proteomics,” *J. Proteome Res.*, vol. 14, no. 5, pp. 1993–2001, May 2015, doi: 10.1021/pr501138h.

[509] F. B. Bedada *et al.*, “Acquisition of a quantitative, stoichiometrically conserved ratiometric marker of maturation status in stem cell-derived cardiac myocytes.,” *Stem cell reports*, vol. 3, no. 4, pp. 594–605, Oct. 2014, doi: 10.1016/j.stemcr.2014.07.012.

[510] M. Tiburcy *et al.*, “Defined engineered human myocardium with advanced maturation for applications in heart failure modeling and repair,” *Circulation*, 2017, doi: 10.1161/CIRCULATIONAHA.116.024145.

[511] D. Zhang, I. Y. Shadrin, J. Lam, H. Q. Xian, H. R. Snodgrass, and N. Bursac, “Tissue-engineered cardiac patch for advanced functional maturation of human ESC-derived cardiomyocytes,” *Biomaterials*, 2013, doi: 10.1016/j.biomaterials.2013.04.026.

[512] A. Mihic *et al.*, “The effect of cyclic stretch on maturation and 3D tissue formation of human embryonic stem cell-derived cardiomyocytes,” *Biomaterials*, 2014, doi: 10.1016/j.biomaterials.2013.12.052.

[513] S. S. Nunes *et al.*, “Biowire: A platform for maturation of human pluripotent stem cell-derived cardiomyocytes,” *Nat. Methods*, 2013, doi: 10.1038/nmeth.2524.

[514] R. A. Li *et al.*, “Bioengineering an electro-mechanically functional miniature ventricular heart chamber from human pluripotent stem cells,” *Biomaterials*, 2018, doi: 10.1016/j.biomaterials.2018.02.024.

[515] D. A. M. Feyen *et al.*, “Metabolic Maturation Media Improve Physiological Function of Human iPSC-Derived Cardiomyocytes,” *Cell Rep.*, vol. 32, no. 3, p. 107925, Jul. 2020, doi: 10.1016/j.celrep.2020.107925.

[516] M. Ermis, E. Antmen, and V. Hasirci, “Micro and Nanofabrication methods to control cell-substrate interactions and cell behavior: A review from the tissue engineering perspective,” *Bioact. Mater.*, vol. 3, no. 3, pp. 355–369, Sep. 2018, doi: 10.1016/j.bioactmat.2018.05.005.

[517] C. O’Shea *et al.*, “Cardiac optical mapping - State-of-the-art and future challenges.,” *Int. J. Biochem. Cell Biol.*, vol. 126, p. 105804, 2020, doi: 10.1016/j.biocel.2020.105804.

[518] B. Vandendriessche, E. Sieliwonczyk, M. Alaerts, B. L. Loeys, D. Snyders, and D. Schepers, “Optical Mapping in hiPSC-CM and Zebrafish to Resolve Cardiac Arrhythmias,” *Hearts*, vol. 1, no. 3, pp. 181–199, Dec. 2020, doi: 10.3390/hearts1030018.

[519] E. A. J. Reits and J. J. Neefjes, “From fixed to FRAP: measuring protein mobility and activity in living cells,” *Nat. Cell Biol.*, vol. 3, no. 6, pp. E145–E147, Jun. 2001, doi: 10.1038/35078615.

[520] M. Klevanski, F. Herrmannsdoerfer, S. Sass, V. Venkataramani, M. Heilemann, and T. Kuner, “Automated highly multiplexed super-resolution imaging of protein nano-architecture in cells and tissues,” *Nat. Commun.*, vol. 11, no. 1, p. 1552, Dec. 2020, doi: 10.1038/s41467-020-15362-1.

[521] M. Haase and G. Fitze, “HSP90AB1: Helping the good and the bad,” *Gene*, vol. 575, no. 2, pp. 171–186, Jan. 2016, doi: 10.1016/j.gene.2015.08.063.

[522] O. M. Grbovic *et al.*, “V600E B-Raf requires the Hsp90 chaperone for stability and is degraded in response to Hsp90 inhibitors,” *Proc. Natl. Acad. Sci.*, vol. 103, no. 1, pp. 57–62, Jan. 2006, doi: 10.1073/pnas.0609973103.

[523] M. P. Mayer and B. Bukau, “Hsp70 chaperones: cellular functions and molecular mechanism.,” *Cell. Mol. Life Sci.*, vol. 62, no. 6, pp. 670–84, Mar. 2005, doi: 10.1007/s00018-004-4464-6.

[524] J. Mi *et al.*, “Inhibition of heat shock protein family A member 8 attenuates spinal cord ischemia–reperfusion injury via astrocyte NF-κB/NLRP3 inflammasome pathway,” *J. Neuroinflammation*, vol. 18, no. 1, p. 170, Dec. 2021, doi: 10.1186/s12974-021-02220-0.

[525] P. R. Dores-Silva, D. M. Cauvi, V. T. R. Kiraly, J. C. Borges, and A. De Maio, “Human HSPA9 (mtHsp70, mortalin) interacts with lipid bilayers containing cardiolipin, a major component of the inner mitochondrial membrane,” *Biochim. Biophys. Acta - Biomembr.*, vol. 1862, no. 11, p. 183436, Nov. 2020, doi: 10.1016/j.bbamem.2020.183436.

[526] G.-C. Fan and E. G. Kranias, “Small heat shock protein 20 (HspB6) in cardiac hypertrophy and failure,” *J. Mol. Cell. Cardiol.*, vol. 51, no. 4, pp. 574–577, Oct. 2011, doi: 10.1016/j.yjmcc.2010.09.013.

[527] L. Lin *et al.*, “HSP60 in heart failure: abnormal distribution and role in cardiac myocyte apoptosis,” *Am. J. Physiol. Circ. Physiol.*, vol. 293, no. 4, pp. H2238–H2247, Oct. 2007, doi: 10.1152/ajpheart.00740.2007.

[528] Y. Cheng *et al.*, “Expression and location of HSP60 and HSP10 in the heart tissue of heat-stressed rats,” *Exp. Ther. Med.*, vol. 12, no. 4, pp. 2759–2765, Oct. 2016, doi: 10.3892/etm.2016.3650.

[529] P. Wu *et al.*, “Myocardial Upregulation of Cathepsin D by Ischemic Heart Disease Promotes Autophagic Flux and Protects Against Cardiac Remodeling and Heart Failure,” *Circ. Hear. Fail.*, vol. 10, no. 7, Jul. 2017, doi: 10.1161/CIRCHEARTFAILURE.117.004044.

[530] X. Ma *et al.*, “Impaired autophagosome clearance contributes to cardiomyocyte death in ischemia/reperfusion injury.,” *Circulation*, vol. 125, no. 25, pp. 3170–81, Jun. 2012, doi: 10.1161/CIRCULATIONAHA.111.041814.

[531] E.-L. Eskelinen, “Roles of LAMP-1 and LAMP-2 in lysosome biogenesis and autophagy,” *Mol. Aspects Med.*, vol. 27, no. 5–6, pp. 495–502, Oct. 2006, doi: 10.1016/j.mam.2006.08.005.

[532] R. J. Tamargo, A. Velayati, E. Goldin, and E. Sidransky, “The role of saposin C in Gaucher disease,” *Mol. Genet. Metab.*, vol. 106, no. 3, pp. 257–263, Jul. 2012, doi: 10.1016/j.ymgme.2012.04.024.

[533] S. Heybrock *et al.*, “Lysosomal integral membrane protein-2 (LIMP-2/SCARB2) is involved in lysosomal cholesterol export,” *Nat. Commun.*, vol. 10, no. 1, p. 3521, Dec. 2019, doi: 10.1038/s41467-019-11425-0.

[534] J. S. Beebe, D. S. Darling, and W. W. Chin, “3,5,3′-Triiodothyronine Receptor Auxiliary Protein (TRAP) Enhances Receptor Binding by Interactions within the Thyroid Hormone Response Element,” *Mol. Endocrinol.*, vol. 5, no. 1, pp. 85–93, Jan. 1991, doi: 10.1210/mend-5-1-85.

Chapter 8 Appendix

Table S 1 Recipes of buffers and solutions

Buffer	Composition
2X SDS sample buffer	100mM, Tris-HCl (pH 6.8); 4% w/v, sodium dodecyl sulfate; 0.2% w/v, bromophenol blue; 200mM, dithiothreitol; 20% v/v, glycerol
Lysis Buffer 1	50mM, Tris-Base (pH 7.5); 2mM, EDTA; 5mM, EGTA; 5mM, dithiothreitol; 0.05% w/v, digitonin; 1 tablet, protease inhibitor; 1 tablet, phosphatase inhibitor
Lysis Buffer 2	1mM, Tris-Base (pH 7.5); 2mM, EDTA; 5mM, EGTA; 5mM, dithiothreitol; 10% v/v, triton-X-100; 0.05% w/v, digitonin; 1 tablet, protease inhibitor; 1 tablet, phosphatase inhibitor

Table S 2 List of commercial products

Products	Company and catalogue number
4-15% Polyacrylamide gels	BioRad #415-076
B27™ Supplement	Gibco #17504-044
B27™ Supplement, minus insulin	Gibco #A18956-01
CHIR-99021	Selleck #S2924
DNAse I	NEB #M0303S
Dulbecco's Modified Eagle Medium/F12	Gibco #11320033
cOmplete™, EDTA-free Protease Inhibitor Cocktail	Roche #4693132001
Fetal bovine serum	Gibco #A4766801
FuGENE6®	Promega #E2691
IWR1	Selleck #S7086
JC-10 Mitochondrial Membrane Potential Kit	Sigma-Aldrich #MAK159
KnockOut™ Serum Replacement	Gibco #10828010
LysoTracker Red DND-99	Invitrogen #L7528
mFreSR	STEMCELL #05855
mTeSR Plus	STEMCELL #100-0276
Opti-MEM™ I Reduced Serum Medium	Gibco #31985062
PBS, pH7.4	Gibco #10010023
Reduced Growth Factor, Phenol Red-free Matrigel	Corning #356231
RPMI-1640	Gibco #11875-093
RPMI-1640, no glucose	Gibco #11879020
TaqMan™ Fast Advanced Master Mix	Applied Biosystems #AA35
Thiazovivin	Selleck #S1456
Nitrocellulose transfer stacks	
TRIzol™	Invitrogen #15596026
TrypLE™ Express Enzyme (1X), no phenol red	Gibco
Tween-20 (Polyoxyethylene-20-Sorbitan Monolaurate)	VWR #9005-64-5
Vitronectin (VTN-N) Recombinant Human Protein, Truncated	Gibco #A14700
Y-27632 (Dihydrochloride)	STEMCELL #72302

Table S3 List of heat shock proteins and CLEAR motif proteins with their relative abundance in myofilament and membrane fraction proteomics analysis. Proteins were selected by their T-test fold change and -LogP value. The localisation, function and pathology association as according to Pubmed searches. Red and italics highlighted protein symbols represent the proteins that had a fold-change of greater than 2 and Log(FDR) =1.301. Abbreviations: ECM, extracellular matrix; ICD, intercalated disc.

Protein symbol	Protein Name	Function	Membrane Log2(Fold Change)	Membrane -Log10(FDR)	Myofilament Log2(Fold Change)	Myofilament -Log2(FDR)	Ref
Heat shock proteins							
Hsp90ab1	Heat Shock Protein 90 Alpha Beta Family Member 1	Cardioprotection Molecular chaperone activity	-0.472	0.08	-0.411	0.08	[521]
Hsp90b1	Heat Shock Protein 90 Beta Family Member 1	Cardioprotection Molecular chaperone activity	-0.299	0.04	-1.391	0.45	[522]
Hspa5	Heat Shock Protein Family A Member 5	Refolds denatured proteins	-1.625	0.23	-2.985	0.73	[523]
Hspa8	Heat Shock Protein Family A Member 8	Cardioprotection Molecular chaperone activity	3.221	0.58	0.703	0.10	[524]
Hspa9	Heat Shock Protein Family A Member 9	Cell proliferation control	-1.757	0.26	-2.617	0.61	[525]
Hspb2	Heat Shock Protein Beta-2	Cardioprotection Molecular chaperone activity	*3.395*	*2.65*	Undetected		[244], [245]
Hspb6	Heat Shock Protein Beta-6	Cardioprotection Molecular chaperone activity	3.273	0.72	2.450	0.53	[526]
Hspb7	Heat Shock Protein Beta-7	Cardioprotection Molecular chaperone activity	1.503	0.36	*4.640*	*3.07*	[121], [133], [246], [268]
Hspd1	Heat Shock Protein Family D Member 1	Cardioprotection Molecular chaperone activity	*5.146*	*1.41*	-1.771	0.37	[474], [527]
Hspe1	Heat Shock Protein Family E Member 1	Cardioprotection Molecular chaperone activity	2.532	0.47	-0.328	0.09	[474], [528]

Xirp2	Xin Actin Binding Repeat Containing 2	Protects actin filaments from depolymerisation	Undetected		Undetected		[423], [424]
CLEAR Proteins							
Ctsd	Cathepsin D	Lysosomal protease	1.593	0.28	-0.402	0.25	[529]
Lamp1	Lysosomal-associated membrane protein 1	Maintain lysosomal catabolism	0.300	0.05	Undetected		[530], [531]
Lamp2	Lysosomal-associated membrane protein 2	Maintain lysosomal catabolism	0.141	0.04	Undetected		[530], [531]
Psap	Prosaposin	Lysosomal lysosomal degradation	-2.177	0.58	Undetected		[532]
Scarb2	Lysosomal integral membrane protein type-2	Lysosomal organisation	-2.239	0.91	Undetected		[533]
Tpp1	Tripeptidyl Peptidase 1	Lysosomal protease	-0.498	0.11	Undetected		[534]

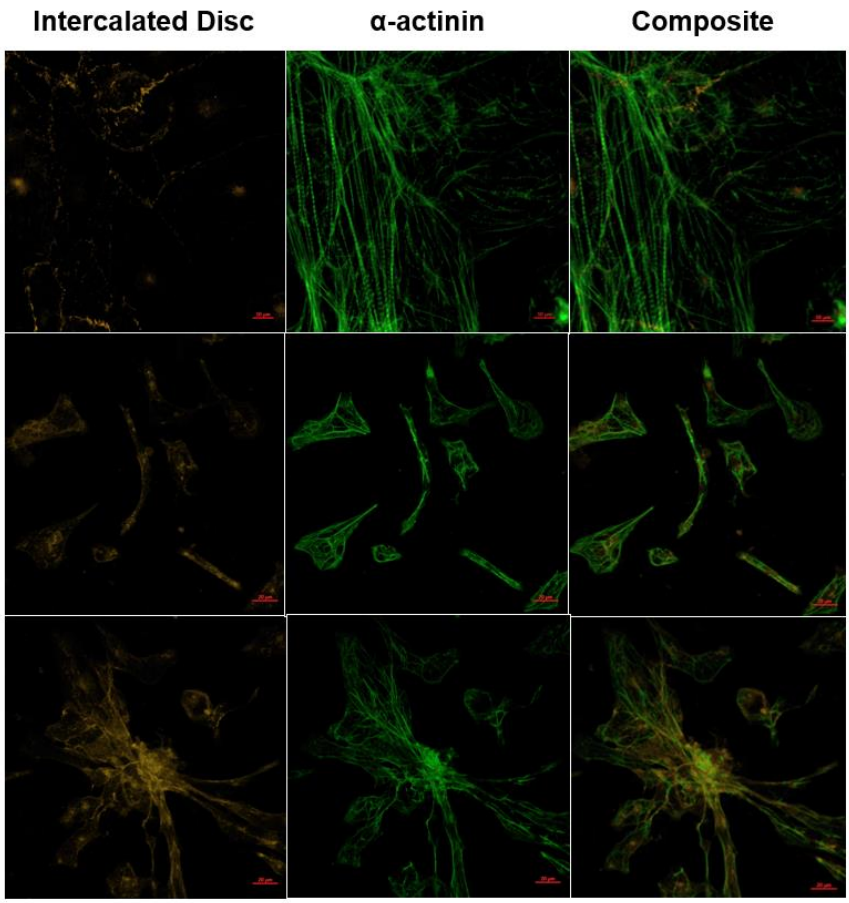

Figure 8-1 The intercalated disc formation within the generated iPSC-CMs in this study. Stained with plakoglobin as the intercalated disc marker on day 30 iPSC-CMs.